

DIRUTHENIUM ARYLS: STRUCTURE, BONDING, AND REACTIVITY

by

Adharsh Raghavan

A Dissertation

Submitted to the Faculty of Purdue University

In Partial Fulfillment of the Requirements for the degree of

Doctor of Philosophy



Department of Chemistry

West Lafayette, Indiana

August 2020

THE PURDUE UNIVERSITY GRADUATE SCHOOL
STATEMENT OF COMMITTEE APPROVAL

Dr. Tong Ren, Chair

Department of Chemistry

Dr. Suzanne C. Bart

Department of Chemistry

Dr. Christopher Uyeda

Department of Chemistry

Dr. Jonathan Wilker

Department of Chemistry

Approved by:

Dr. Christine A. Hrycyna

To Trillian

ACKNOWLEDGMENTS

I am where I am today thanks in major part to my parents, Jeyanthi and Raghavan. They have sacrificed so much in their own lives so that the lives of their progeny would stand enriched. This has resulted in the opening of so many doors that would otherwise have remained closed. For their selfless, unconditional, and unwavering support, I thank them.

During these five years, there have been two people who have stood by me through thick and thin, whose support I see as a big contributor to my mental well-being. I cannot imagine getting through some of my darker times without the help and constant support of both Ganesh and Saranya. Words can try, but will ultimately fail to capture how empty the last five years of my life would have been without Saranya. I have come to lean and depend on her kindness, endless patience, and even mere existence, to get through life on a daily basis. I owe her a huge debt of gratitude for breaking down walls that I had built around myself, and for giving me the confidence to be nothing but myself around her and others. In Ganesh, I have found a friend for life, and in Saranya, I have found myself. For this, I thank them.

August of 2017 marked one of the most important months of my life, when I brought home Trillian, who was then barely three months old. I am amazed by how, no matter how much love I gave her, she always gave back more. She grew to be an introvert just like me, but we had a very special bond. Her presence brightened my life, and she would not stay in a room devoid of me. Losing her was a heart-rending experience. I always thought I had more time with her, that we would grow old together and that she would move with me. What was asked of her, a mere 3-year-old, was extremely unfair. Yet she braved through it all. She fought a valiant fight, and I am so proud of her for being strong and giving me strength that I never knew I had. Without her, the last three years would have meant far less. For this, I thank her and dedicate this dissertation to her.

The Bart group was the first ‘home’ for me in the States. Since joining her group in 2015 and despite leaving it in early 2017, Suzanne has played a big role in my professional career. I have always deeply admired Suzanne as a person and as a scientist. It was from her that I learnt how to perform rigorous science and, how to leave no stone unturned in its pursuit. Her passion for fundamental science is contagious, and I wish I had caught it earlier than I actually did. As a mentor and advisor, Suzanne has been so supportive, and has gone above and beyond to help me with my career goals. For helping me level up, I thank her. Another Bart group member who has

had a positive influence on me is Caleb Tatebe. What started out as a mentor-mentee relationship has happily ended up becoming a friendship that I cherish. Apart from our shared love for The Beatles, Pokémon and football, from which we have both derived many happy memories during grad school, I deeply admire his commitment to achieve a work-life balance. For all that he has taught me, knowingly or unknowingly, I thank Caleb.

After leaving the Bart group, I joined Dr. Ren's group in April of 2017. This was obviously a career-defining moment for me. But little did I know that I would end up falling in love with a completely new field, let alone that I would consider building a career in it. Dr. Ren's constant support and encouragement to pursue a line of research completely different from what the rest of the group was doing, allowed me to explore and find my own comfort zone. During this period, I started defining myself as a physical inorganic chemist. I owe him a huge debt of gratitude for taking me under his wing and mentoring me, while treating me as a colleague and respecting my professional opinion in many matters. This has enabled me to rebuild my confidence over the years, and to trust in myself. For his continued support and confidence in my abilities, I thank him.

I would also like to thank Pradeep and Neha for everything they did to help me during two crucial transitions – India to the US, and Bart lab to Ren lab. Their support has been an invaluable asset to me during these difficult times, and I do not know if I can ever thank them enough for this. There are some Ren lab members, both present and past, that I wish to thank: Susie, for her advice, for proofreading my documents, and for all the discussions we have had on chemistry, broad aspects of science in academia, the justice system and politics, for being a supportive colleague, and for bringing Trillian into my life; Sean for being my first mentor in the Ren lab; Ashley for being such an easy person to talk to, and indulging my sweet tooth, and livening up the lab atmosphere. Special thanks to Dr. Matthias Zeller for teaching me crystallography and answering any and all questions that I had, patiently and comprehensively

Over the last couple of years, during which my decision to stay in academia slowly crystallized, I have started mentally taking notes on how to run a research group by looking towards both of my mentors, Suzanne and Tong. I have had a unique experience in grad school because of this. Although I would do things differently if I had the chance to go back in time (who would not?), I will not trade the lessons I have learnt for anything else. I hope I have found my calling, and I thank everyone who has helped me get here, for, far from being a one-man show, all of this has been a collaborative effort.

TABLE OF CONTENTS

LIST OF TABLES	9
LIST OF FIGURES	10
LIST OF SCHEMES.....	13
LIST OF ABBREVIATIONS.....	14
ABSTRACT.....	15
CHAPTER 1. MONOARYL COMPLEXES OF DIRUTHENIUM(II,III)	17
1.1 Abstract.....	17
1.2 Introduction.....	17
1.3 Results and Discussion	20
1.3.1 Synthesis	20
1.3.2 Mass Spectrometry	21
1.3.3 Molecular structures	22
1.3.4 Electronic absorption spectroscopy	26
1.3.5 Electrochemistry	28
1.3.6 Magnetism	31
1.3.7 Density Functional Theory Calculations.	32
1.4 Conclusion	34
1.5 Experimental Details.....	35
1.6 Supporting Information.....	41
CHAPTER 2. BISARYL COMPLEXES OF DIRUTHENIUM(III,III).....	51
2.1 Abstract.....	51
2.2 Introduction.....	51
2.3 Results and Discussion	53
2.3.1 Synthesis	53
2.3.2 Molecular Structures.....	54
2.3.3 Electrochemistry	58
2.3.4 Electronic Absorption Spectroscopy.	60
2.3.5 Density Functional Theory Calculations.	61
2.4 Conclusion	66

2.5	Experimental Section	67
2.6	Supporting Information.....	70
CHAPTER 3. REACTIVITY OF DIRUTHENIUM MONOARYLS		80
3.1	Abstract	80
3.2	Introduction.....	80
3.3	Results and Discussion	82
3.3.1	Reactivity with neutral substrates (CO).....	82
3.3.2	Reactivity with anionic substrates (CN ⁻ , RC≡C-C≡C ⁻ and HC≡C ⁻)	88
	CN ⁻	89
	R-C≡C-C≡C ⁻ (R = TMS, H).....	90
	HC≡C ⁻	93
3.3.3	UV-Vis/NIR and IR absorption spectroscopy	97
3.3.4	Electrochemistry	98
3.4	Conclusion	100
3.5	Experimental Section	101
3.6	Supporting Information.....	105
CHAPTER 4. MISCELLANEOUS		114
4.1	Abstract.....	114
4.2	Results and Discussion	114
4.2.1	Redox chemistry and spectroelectrochemistry of Ru ₂ (II,III) monoaryls.....	114
4.2.2	Improved ground state and excited state DFT calculations of Ru ₂ (II,III) and Ru ₂ (III,III) monoaryls	118
	Ground state calculations	118
	Excited state calculations	120
4.2.3	Phenylene bridged diruthenium complexes of the form [Ru ₂ (ap) ₄]-Ar-[Ru ₂ (ap) ₄]. Ru ₂ (II,III) termini bridged by a mixed phenylene/polyynediyl unit (-C ₆ H ₄ -C≡C-C≡C-C ₆ H ₄ -)	141
	Ru ₂ (II,III) bridged by a phenylene unit (-C ₆ H ₄ -).....	146
4.3	Conclusions and Future Directions.....	147
4.4	Supporting Information.....	149
REFERENCES		158

VITA..... 168
PUBLICATIONS..... 169

LIST OF TABLES

Table 1.1. Selected Bond Lengths (Å) and Angles (deg) for compounds 1–6	23
Table 1.2. Electrochemical data from DPV (in V vs. Fc ⁺⁰)	29
Table 2.1. Selected Bond Lengths (Å) and Angles (deg) for Compounds 7–9	55
Table 2.2. Electrode Potentials (V, vs. Fc ⁺⁰) for Ru ₂ (<i>dmba</i>) ₄ X ₂	59
Table 2.3. Natural transition orbitals derived from TD-DFT calculations. Transitions are noted as NTO1 → NTO2.	64
Table 3.1. Redox potentials (V, versus Fc ⁺⁰) for (Y)[Ru ₂ (<i>ap</i>) ₄](C ₆ H ₄ -4-NMe ₂) in THF.	99
Table 3.2. Voltammery and IR spectroscopy of Ru ₂ –CO complexes in the literature.	100
Table 4.1. Comparison between experimental and DFT-optimized (improved) structural parameters	119
Table 4.2. Natural transition orbitals* derived from TD-DFT analysis of 1'	122
Table 4.3. Natural transition orbitals* derived from TD-DFT analysis of 4'	126
Table 4.4. Natural transition orbitals* derived from TD-DFT analysis of [1'] ⁺	131
Table 4.5. Redox potentials of compounds 14a and 15 (from DPV)*	145

LIST OF FIGURES

Figure 1.1. ESI-MS of 1 . Red (top): calculated; Blue (bottom): experimental.	22
Figure 1.2. Dihedral angle (θ), defined as the angle between the lines C1–C2 and Ru2–Nx.....	23
Figure 1.3. Structural plot of 1 at 30% probability level. One of the two molecules (A) present in the asymmetric unit was selected. Hydrogens omitted for clarity.	24
Figure 1.4. Structural plot of 2 at 30% probability level. Solvent molecules and hydrogens omitted for clarity.....	24
Figure 1.5. Structural plot of 3 at 30% probability level. Solvent molecules and hydrogens omitted for clarity.....	25
Figure 1.6. Structural plot of 4 at 30% probability level. Solvent molecules, disordered ligand and hydrogens omitted for clarity.....	25
Figure 1.7. Structural plot of 5 at 30% probability level. Aryl ligand is disordered around the C_2 axis.	26
Figure 1.8. Structural plot of 6 at 30% probability level. Solvent molecules, disordered ligands and hydrogens omitted for clarity.....	26
Figure 1.9. Vis-NIR absorption spectra of compounds 1–6 and $Ru_2(ap)_4Cl$ recorded in THF. ...	27
Figure 1.10. Representation of HOMO in 1 and 2 , $\pi(Ru_2/Ar)$	28
Figure 1.11. Cyclic (CV, black) and differential pulse (DPV, red) voltammograms of compounds 1–6 (1.0 mM) recorded in a 0.10 M CH_2Cl_2 solution of Bu_4NPF_6 at a scan rate of 0.10 V/s.	29
Figure 1.12. Hammett plot of redox potentials ($E(Ru_2^{6+/5+})$) versus σ_x for compounds 1–6 . The circles are the measured potentials, the solid line is the least-squares fit.	30
Figure 1.13. SQUID magnetometry of 1 from 2–300 K, courtesy of Dr. Fang Yuan. Curves simulated for $D = 76 \text{ cm}^{-1}$, $g_{\parallel} = 1.9500$, $g_{\perp} = 2.0265$	32
Figure 1.14. Frontier molecular orbital diagrams for 1' and 6' from DFT calculations.....	34
Figure 2.1. Structural plot of 7 at the 30% probability level. One of the two disordered moieties (A) present in the asymmetric unit was selected. Hydrogens are omitted for clarity.	56
Figure 2.2. Structural plot of 8 at the 30% probability level. Hydrogens are omitted for clarity.	56
Figure 2.3. Structural plot of 9 at the 30% probability level. Solvent molecules and hydrogens are omitted for clarity.	57
Figure 2.4. Distorted coordination geometry in 7–9 . $\alpha_{ave} \approx 79.7^\circ$, $\beta_{ave} \approx 95.2^\circ$, $\gamma_{ave} \approx 152^\circ$	57
Figure 2.5. Cyclic (black) and differential pulse (gray) voltammograms of compounds 7–9 (1.0 mM) recorded in 0.10 M nBu_4NPF_6 in CH_2Cl_2 at a scan rate of 0.10 V/s.....	59
Figure 2.6. Vis–NIR spectra of compounds 7–9 in THF.	60

Figure 2.7. Frontier MO diagram of 8' obtained from DFT calculations; isovalue = 0.03.....	62
Figure 2.8. HOMO – 4 for the optimized structure 8' ; a $\pi^*(\text{Ru-Ru})$ orbital with σ -bonding character.....	63
Figure 2.9. Experimental curve (black), fit peaks (blue, dashed) and cumulative fit curve (red) obtained from Gaussian deconvolution of the electronic absorption spectrum of 8 in THF.....	66
Figure 3.1. Spacefill model of 1 viewed perpendicular to the Ru–Ru–aryl axis (left) and down the Ru–Ru axis (right).....	81
Figure 3.2. UV-Vis/NIR spectrum of 1 (black dotted line), 4 freshly prepared by exposure of 1 for varying lengths of time.	83
Figure 3.3. Cyclic voltammogram of compound 1 under N_2 (black dotted line), 4 freshly prepared by purging the electrochemical cell with CO (violet line, 0 min), and subsequent scans recorded after the electrochemical cell was purged with N_2 for varying lengths of time.....	84
Figure 3.4. Molecular structure of compound 10 . Solvent molecules and hydrogens are omitted for clarity. Selected bond lengths (\AA) and angles (deg): Ru1–Ru2, 2.5060(3); Ru1–C1, 2.053(2); Ru2–C53, 1.877(2); Ru2–Ru1–C1, 155.61(6); Ru1–Ru2–C53, 169.50(7).....	85
Figure 3.5. SQUID magnetometry of 10 from 2–300 K, courtesy of Dr. Fang Yuan.	86
Figure 3.6. Frontier MO plots from ground-state DFT calculations of 4	87
Figure 3.7. Net unpaired electron density calculated from the difference between α and β -spin electron densities in 10' , represented at isovalue = 0.003. The unpaired electron is predominantly localized on the δ^* orbital, per the electronic configuration described in the text.	88
Figure 3.8. ^1H NMR spectrum of 11 in CDCl_3 at 293 K.	89
Figure 3.9. Molecular structure of compound 11 . Solvent molecules and hydrogens are omitted for clarity. Selected bond lengths (\AA) and angles (deg): Ru1–Ru2, 2.4857(7); Ru1–C1, 2.077(7); Ru2–C53, 2.021(7); Ru2–Ru1–C1, 155.61(6); Ru1–Ru2–C53, 169.50(7).....	90
Figure 3.10. ^1H NMR spectrum of 12 in CDCl_3 at 293 K.	91
Figure 3.11. Molecular structure of compound 12 . Solvent molecules and hydrogens are omitted for clarity. Selected bond lengths (\AA) and angles (deg): Ru1–Ru2, 2.4887(5); Ru1–C1, 2.046(2); Ru2–C53, 1.977(2); Ru2–Ru1–C1, 153.99(6); Ru1–Ru2–C53, 166.22(6).....	92
Figure 3.12. ^1H NMR spectrum of 12a in CDCl_3 at 293 K.	93
Figure 3.13. Molecular structure of compound 13 . Solvent molecules and hydrogens are omitted for clarity. Selected bond lengths (\AA) and angles (deg): Ru1–Ru2, 2.4887(5); Ru1–C1, 2.058(4); Ru2–C53, 2.005(4); Ru2–Ru1–C1, 156.02(9); Ru1–Ru2–C53, 166.45(9).....	94
Figure 3.14. ^1H NMR spectrum of 13 in CDCl_3 at 293 K.	95
Figure 3.15. VT-NMR spectrum of 13 in CDCl_3 . Black asterisks represent solvent impurities (THF and CH_2Cl_2). Equivalent peaks are denoted by matching shapes and colors.	95

Figure 3.16. VT-NMR spectrum of 13 in CDCl ₃ , shown here are the peaks corresponding to the acetylide (C≡C–H) proton.	96
Figure 3.17. Vis/NIR absorption spectrum of compounds 10–13 (and 1 included for comparison) measured in THF.	97
Figure 3.18. CV (black) and DPV (red) of compounds 10–13 recorded in 0.1 M TBAP THF solution. [Ru ₂] = 1 mM.	98
Figure 4.1. UV-Vis/NIR absorption spectrum of 1 and 1 ⁺ , and 2 and 2 ⁺	116
Figure 4.2. Oxidation of 2 to [2] ⁺ (left) and oxidation of [2] ⁺ to [2] ²⁺ (right).	117
Figure 4.3. The oxidation of compound 2 to [2] ⁺ and [2] ²⁺ , and subsequent reduction of [2] ²⁺ to [2] ⁺ upon removal of the positive bias.	117
Figure 4.4. Similarities between the chemical and electrochemical oxidation of 2	118
Figure 4.5. TD-DFT calculated UV-Vis/NIR spectrum of [1'] in THF.	121
Figure 4.6. TD-DFT calculated UV-Vis/NIR spectrum of [4'] in THF.	121
Figure 4.7. TD-DFT calculated UV-Vis/NIR spectrum of [1'] ⁺ in THF.	131
Figure 4.8. Molecular structure of 14 represented at the 30% probability level (one of the two disordered TIPS moieties shown). Hydrogens and solvents have been removed for clarity.	143
Figure 4.9. HR-MS spectrum of 15 in an acetone solution; CID performed for peaks at m/z = 1958 ± 15.	144
Figure 4.10. CV and DPV of compounds 14a and 15 recorded in 0.2 M TBAP THF solution. [14a] = 1 mM, [15] < 1mM due to solubility issues.	145
Figure 4.11. ESI-MS of the crude reaction mixture of Scheme 4.5 at low fragmentation voltages. Isotopic distribution characteristic of (Ru ₂) ₂ corresponding to [16] ²⁺ (m/z = 1834.0/2 = 917, left). Side-product Ru ₂ (ap) ₄ (Ph) (compound 4 , right).	147

LIST OF SCHEMES

Scheme 1.1. Reported M_2 -Aryl complexes derived from or containing a paddlewheel motif	18
Scheme 1.2. Synthesis of 2-anilinopyridine	20
Scheme 1.3. Synthesis of $Ru_2(ap)_4Cl$	20
Scheme 1.4. Synthesis of $Ru_2(ap)_4Ar$ (compounds 1–6).....	21
Scheme 2.1. Synthesis of N,N'-dimethylbenzamidine (<i>Hdmba</i>)	53
Scheme 2.2. Synthesis of $Ru_2(dmba)_4Cl_2$	53
Scheme 2.3. Synthesis of $Ru_2(dmba)_4Ar_2$	54
Scheme 3.1. Synthesis of 10 from the reaction between 1 and CO.	83
Scheme 3.2. Synthesis of 11–13 from the reaction between 1 , Y and O_2	88
Scheme 4.1. Synthesis of [1]PF ₆ and [2]PF ₆	114
Scheme 4.2. Retrosynthesis for 15	142
Scheme 4.3. Syntheses of 14 and 14a	142
Scheme 4.4. Synthesis of 15 through a modified Eglinton reaction.	144
Scheme 4.5. Synthesis of 16 from $Ru_2(ap)_4Cl$ and 1,4-dilithiobenzene.	146

LIST OF ABBREVIATIONS

<i>ap</i> =	2-anilinopyridinate
<i>dmba</i> =	N,N'-dimethylbenzamidinate
Ar =	Aryl
NMR =	Nuclear magnetic resonance
UV-Vis/NIR =	Ultraviolet-visible/Near infrared
IR =	Infrared
XRD =	X-ray diffraction
DFT =	Density functional theory
MO =	Molecular orbital
HOMO =	Highest occupied MO
LUMO =	Lowest unoccupied MO
SOMO =	Singly occupied MO
TD-DFT =	Time-dependent DFT
ESI-MS =	Electrospray ionization mass spectrometry
HR <i>n</i> ESI-MS =	High-resolution nano ESI-MS
SQUID =	Superconducting quantum interference device
CV =	Cyclic Voltammogram/Voltammetry
DPV =	Differential pulse voltammogram/voltammetry
TMS =	trimethylsilyl
TIPS =	triisopropylsilyl
Fc ⁺ /Fc =	Ferrocenium/Ferrocene
QRE =	Quasi reference electrode
ROS =	Restricted Open-Shell

ABSTRACT

The chemistry of metal–metal (M–M) multiply bonded compounds has fascinated inorganic chemists for a period spanning more than five decades. Since the elucidation of the quadruple bond by Cotton in 1964, thousands of compounds featuring M–M bonds have been isolated and studied. Of these, dinuclear units supported by four bidentate ligands forming a ‘paddlewheel’ motif represent a class of compounds that present unique molecular and electronic structures, and useful electrochemical and magnetic properties.

Over the last two and a half decades, our laboratory has focused on studying diruthenium paddlewheel complexes for their ease of preparation, rich electrochemical properties, and remarkable stability. We have isolated a vast number of diverse diruthenium alkynyls in multiple oxidation states, bearing different paddlewheel (equatorial) ligand systems and studied their molecular and electronic structures. Taking advantage of the extended conjugation that exists between the Ru₂ core and the poly-alkynyl ligand motif, we have also found applications for them in prototypical flash-memory devices. At this juncture, we sought to expand the organometallic chemistry of Ru₂ to complexes featuring Ru–aryl linkages.

The ‘aryl anion’ is, based on pK_a, twenty orders of magnitude more basic than the corresponding acetylide. Arguably, this difference should result in a more electron-rich dinuclear core with new electronic structures waiting to be explored. Although kinetically more reactive than metal–alkynyls, metal–aryls are still more stable than the corresponding metal–alkyls. However, for second-row transition metals like ruthenium, kinetic instability issues are somewhat more suppressed than for their first-row counterparts.

Armed with the knowledge that it was reasonable to expect somewhat stable metal–aryl complexes, the synthesis and characterization, and analyses of molecular and electronic structures of diruthenium aryls were attempted. By employing relatively simple lithium-halogen exchange reactions, both mono and bis-aryl complexes of diruthenium have been isolated. Additionally, two different oxidation states of diruthenium have been accessed, namely Ru₂(II,III) and Ru₂(III,III), by judiciously modifying the paddlewheel ligands. Following this, preliminary reactivity studies of Ru₂(II,III) monoaryls of the form Ru₂(*ap*)₄Ar were performed, which yielded surprising results. This work led to the conclusion that the diruthenium–aryl interaction is an example of a metal–

metal–ligand interaction that can bring reactivity to the distal metal site. Moreover, it was found that even minor changes in axial ligands can bring about major upheavals in electronic structure.

Computational investigations into the electronic structure of the above-mentioned compounds have faced many a barrier because of the complexity of the system. The deep mixing of the metal–metal and metal–ligand valence manifolds is more easily isolated into its constituent parts in the case of relatively simple structures such as the monoaryls, $\text{Ru}_2^{\text{II,III}}\text{L}_4\text{Ar}$. However, electronic structure calculations are fraught with difficulties in the case of heavily distorted axially disubstituted mono and bis-aryls, $(\text{X})\text{Ru}_2^{\text{III,III}}\text{L}_4\text{Ar}$ and $\text{Ru}_2^{\text{III,III}}\text{L}_4\text{Ar}_2$, respectively. $\text{Ru}_2^{\text{III,III}}\text{L}_4\text{Ar}_2$ complexes present an interesting case of second order Jahn-Teller distortion (SOJT), which has been adequately modeled. However, the more heavily distorted case of $\text{XRu}_2(\text{ap})_4\text{Ar}$ ($\text{X} = \text{CCH}, \text{CN}, \text{CO}, \text{etc.}$) pose greater computational challenges, such as low-lying excited states, spin-admixed ground states and difficulties in isolating metal and ligand contributions to the valence manifold.

Our investigations into diruthenium aryls began as a mere curiosity that arose out of a serendipitous discovery. Two years later, our continued efforts in this direction have yielded rather fruitful results. The unusual structures and associated complex bonding motifs in these systems have taught us about the importance of metal–metal–ligand interactions as more than just a sum of metal–metal and metal–ligand parts.

CHAPTER 1. MONOARYL COMPLEXES OF DIRUTHENIUM(II,III)

Reprinted (adapted) with permission from Raghavan, A., Mash, B. L., Ren, T., *Inorganic Chemistry*, **2019**, 58, 2618–2626. Copyright 2019, American Chemical Society.

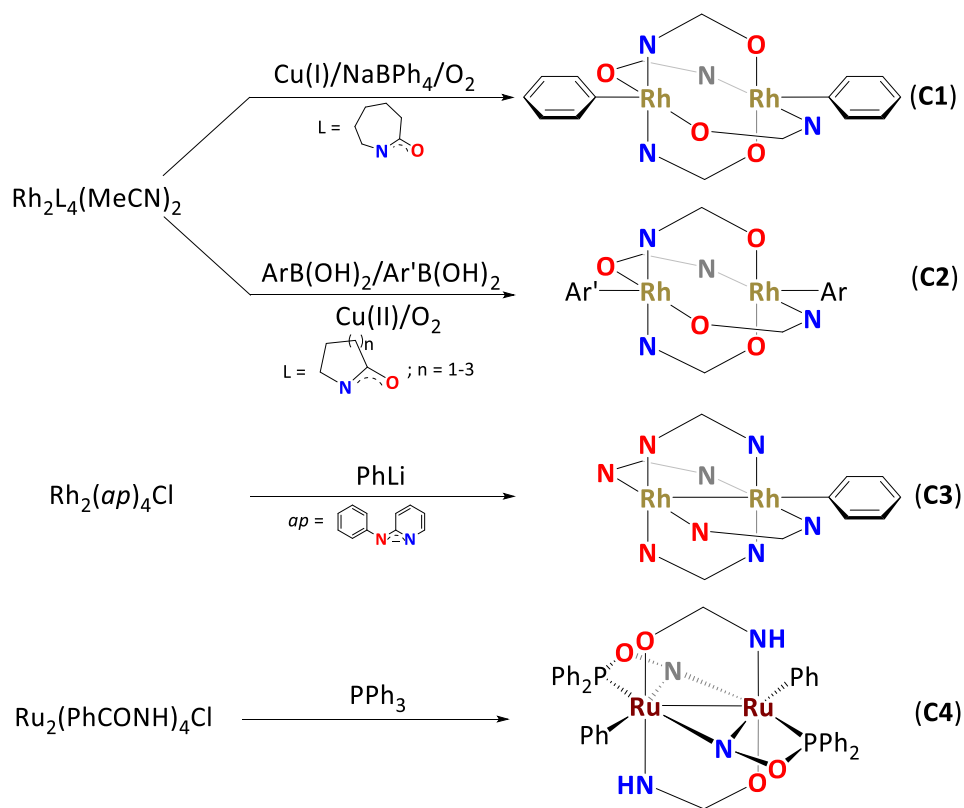
1.1 Abstract

The synthesis and characterization of monoaryl complexes of diruthenium paddlewheel complexes are described here. Compounds of the form $\text{Ru}_2(\text{ap})_4(\text{Ar})$ (ap = 2-anilinopyridinate; Ar = aryl) were synthesized by simple lithium-halogen exchange reactions between the readily prepared $\text{Ru}_2(\text{II,III})$ starting material, $\text{Ru}_2(\text{ap})_4\text{Cl}$, and the corresponding aryllithium, LiAr . The resultant monoaryl $\text{Ru}_2(\text{ap})_4(\text{C}_6\text{H}_4\text{-4-X})$ type compounds (X = NMe_2 (**1**); $\text{N,N}-(\text{C}_6\text{H}_4\text{-4-OMe})_2$ (**2**); $t\text{Bu}$ (**3**); H (**4**); Br (**5**); CF_3 (**6**)) were characterized by electrospray ionization mass spectrometry (ESI-MS), electronic absorption spectroscopy, voltammetry, and magnetism studies, and their molecular structures established by single crystal X-ray diffraction (XRD) analysis. Electrochemical data showed that σ -aryls are strongly electron donating axial ligands; a range of electronically distinct *para* substituents on the aryl moiety allowed for a closer inspection of the extent of electronic conjugation across the diruthenium paddlewheel core and the axial ligand. Furthermore, their electronic structures were modeled by density functional theory (DFT) calculations.

1.2 Introduction

Diruthenium paddlewheel complexes have been extensively studied since the isolation of $\text{Ru}_2(\text{acetate})_4\text{Cl}$ in 1966 by Wilkinson.¹ The ease of replacement of the acetate ligand has led to the isolation of Ru_2 complexes bearing a variety of different bidentate ligands.² With these paddlewheel ligands controlling both the sterics and electronics at the ruthenium centers, axial ligands can be systematically introduced/varied. One of the commonly used paddlewheel ligands is 2-anilinopyridinate (ap). $\text{Ru}_2(\text{ap})_4\text{Cl}$, first synthesized in 1985 by Cotton and Chakravarty, has served as an extremely stable and useful starting material in diruthenium chemistry.³ In fact the earliest example of an organometallic diruthenium paddlewheel complex came from the Cotton group in 1986, namely, $\text{Ru}_2(\text{ap})_4(\text{C}\equiv\text{CPh})$, bearing this ligand in the equatorial sites.⁴ Since then,

there has been a lot of interest to study $\text{Ru}_2\text{L}_4(\text{C}\equiv\text{CR})_n$ type complexes ($n = 1$ or 2). Because of the extended conjugation along the Ru_2 -poly-alkynyl chains and the robust redox states of the Ru_2^{n+} ($n = 4, 5$ or 6) core, the wire-like characteristics of these molecules, many of which are based on $[\text{Ru}_2(\text{ap})_4]$, have been studied by several laboratories including ours.⁵⁻⁹ This has enabled the incorporation of $\text{Ru}_2(\text{ap})_4$ -alkynyl molecules in non-volatile flash memory devices.^{10,11} It is noteworthy that all structurally characterized organometallic diruthenium paddlewheel complexes feature either one or two alkynyl axial ligand(s), or smaller ligands like CN^- ¹² or CO .¹³ All of these are examples of *sp*-hybridized carbons directly bonded to ruthenium. Specifically, the $\text{Ru}-\text{Ru}-\text{C}_{\text{aryl}}$ bond in a paddlewheel complex is a much sought-after target, since nothing is known about the bonding, structure and reactivity of these species.



Scheme 1.1. Reported M_2 -Aryl complexes derived from or containing a paddlewheel motif

The existence of $\text{Rh}-\text{Rh}-\text{C}_{\text{aryl}}$ bonds in paddlewheel compounds has indeed been documented by the laboratories of Doyle and Bear and Kadish. Doyle and co-workers first reported the synthesis and characterization of a bis(phenyl)dirhodium(III) compound formed *via* oxidation

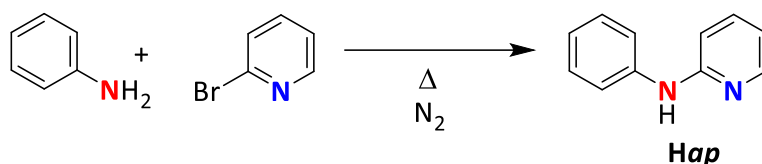
of a Rh₂(II,III) species in the presence of NaBPh₄ (Scheme 1.1, **C1**).¹⁴ The compound was diamagnetic, as expected from Rh₂⁶⁺. However, the disappearance of the Rh–Rh bond was unexpected; this denoted a change in the electronic structure of the Rh₂ core. Since then, other reagents like arylboronic acids have been employed to introduce a wider range of substituents in the axial sites of Rh₂(III,III) caprolactamates (Scheme 1.1, **C2**).^{15–19} The electronic configuration of Rh₂⁶⁺ in these compounds has been established as $\pi^4\delta^2\pi^*4\delta^*2$. In 2009, Bear and Kadish reported the synthesis of mono-aryl and mono-alkyl compounds Rh₂(*ap*)₄(C₆H₅) and Rh₂(*ap*)₄(CH₃) from Rh₂(*ap*)₄Cl using large excesses of phenyllithium and methyllithium, respectively (Scheme 1.1, **C3**).²⁰ However, product isolation required a rigorously inert atmosphere and sequestration from any light source to avoid decomposition of the relatively unstable compounds.

Despite the similarity between dirhodium and diruthenium paddlewheel complexes, it is noteworthy that there is no precedent in literature for diruthenium compounds bearing axial σ -aryl ligands. The only example of a diruthenium aryl compound comes from the Cotton group (Scheme 1.1, **C4**).^{21,22} The compound with the formula Ru₂Ph₂(PhCONH)₂[Ph₂POC(Ph)N]₂ was prepared from the reaction between Ru₂(PhCONH)₄Cl and PPh₃, and the transfer of a Ph group from the axially coordinated PPh₃ to Ru was accompanied by a structural rearrangement from a paddlewheel to an edge-sharing bioctahedral motif. It was of interest to us to synthesize diruthenium compounds containing aryl ligands in the axial positions, while leaving the paddlewheel motif unchanged. The classic technique used to forge Ru–C \equiv C bonds involves using LiC \equiv CR formed *via* lithiation of the corresponding alkyne, HC \equiv CR. Hence, the well-documented lithium-halogen exchange reaction was employed for the introduction of an aryl ligand (Ar); this resulted in a series of Ru₂(*ap*)₄(Ar) in relatively high yield (Scheme 1.4). The [Ru₂(*ap*)₄]⁺ system was chosen because it offers certain advantages over other paddlewheel systems. Axially substituted [Ru₂(*ap*)₄] compounds are very easy to synthesize and are exceptionally stable, in addition to having excellent redox properties. Moreover, the four *ap* ligands are always arranged in a polar (4,0) fashion wherein all four pyridyl nitrogens are coordinated to one ruthenium center and all four anilide nitrogens to the other (see Scheme 1.4); the (3,1) and (2,2) isomers are never formed.² This important structural feature prevents coordination of ligands spanning more than one dimension at the vacant ruthenium site and should allow for the exclusive isolation of monoaryl Ru₂(II,III) complexes.

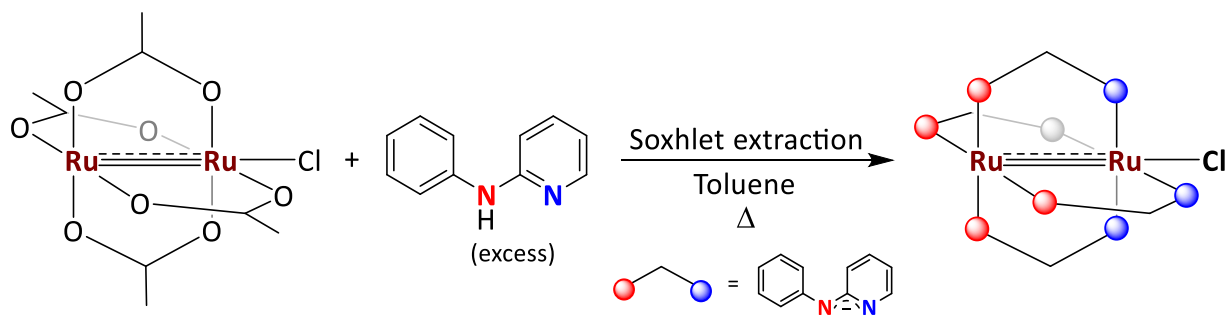
1.3 Results and Discussion

1.3.1 Synthesis

The precursor for the deprotonated *ap* ligand, *Hap*, was prepared from the reaction between 2-bromopyridine and aniline, as outlined in Scheme 1.2, and the Ru₂(II,III) starting material, Ru₂(*ap*)₄Cl, from the reaction between Ru₂(OAc)₄Cl and *Hap*, per Scheme 1.3.



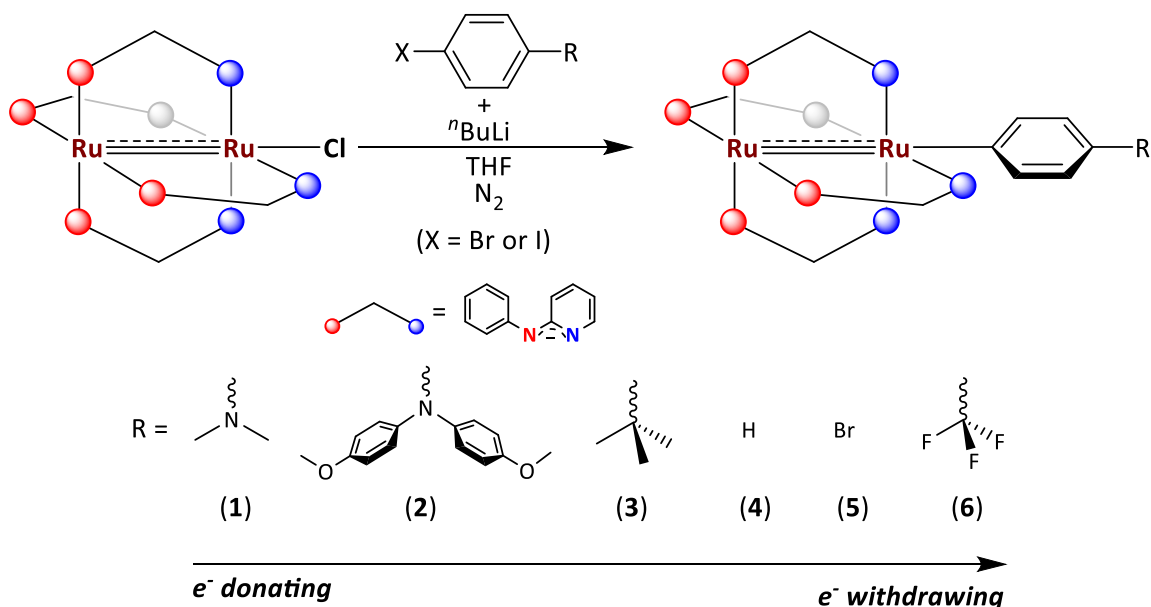
Scheme 1.2. Synthesis of 2-anilinopyridine



Scheme 1.3. Synthesis of Ru₂(*ap*)₄Cl

The reaction between Ru₂(*ap*)₄Cl and LiAr resulted in the formation of Ru₂(*ap*)₄(Ar) and LiCl (Scheme 1.4). The reactions were instantaneous and were accompanied by easily identifiable color changes. Work-up of the reaction mixtures and purification of the products were done under ambient conditions, using column chromatography or by simple recrystallization techniques; products were isolated in yields ranging from 30–95%. Since [Ru₂(*ap*)₄]-based compounds either decompose when exposed to the acidic surface of silica or become irretrievably adsorbed onto it, the silica used for thin-layer chromatography and column chromatography were deactivated with triethylamine prior to use. The isolated compounds **1–6** are stable both in solution (THF) and solid state under ambient conditions, with no noticeable decomposition over a few months. The effective magnetic moments of compounds **1–6** (determined using Evans method) range from 3.4 to 4.1 μ_B ,

which are in agreement with a $S = 3/2$ ground state. Although their paramagnetism precluded characterization by NMR spectroscopy, compounds **1–6** were analyzed using ESI-MS, electronic absorption spectroscopy, cyclic and differential pulse voltammetry, room temperature magnetism studies, single crystal XRD studies, and DFT calculations.



Scheme 1.4. Synthesis of $\text{Ru}_2(\text{ap})_4\text{Ar}$ (compounds **1–6**)

It must be noted that the lithium-halogen exchange reaction does have its limitations in terms of functional group tolerance. For instance, it was of interest to us to install a nitro ($-\text{NO}_2$) substituent in the aryl ring. However, all attempts to form $\text{Li-C}_6\text{H}_4\text{-4-NO}_2$ failed. A brief explanation is offered in the Experimental Section.

1.3.2 Mass Spectrometry

Ruthenium has a characteristic isotopic distribution that is easily captured and identified by mass spectrometry. With two ruthenium atoms, this effect is even more pronounced. As a representative example, the mass spectrum (ESI-MS) of compound **1** is shown in Figure 1.1. The reaction between $\text{Ru}_2(\text{ap})_4\text{Cl}$ and LiAr was monitored by ESI-MS, noting the disappearance of the cluster of characteristic $\text{Ru}_2(\text{ap})_4\text{Cl}$ peaks roughly centered around an m/z value of 914.4 and the appearance of the corresponding $\text{Ru}_2(\text{ap})_4\text{Ar}$ cluster of peaks.

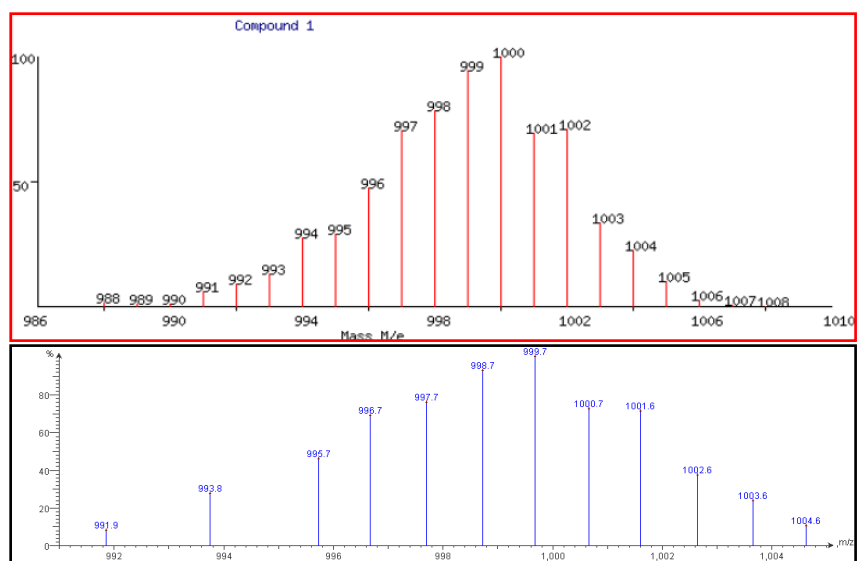


Figure 1.1. ESI-MS of 1. Red (top): calculated; Blue (bottom): experimental.

1.3.3 Molecular structures

The molecular structures of compounds **1–6** determined via single crystal XRD studies are shown in Figures **1–6**; selected bond lengths and angles are given in Table 1.1. The bridging *ap* ligands retain the (4,0) arrangement present in $\text{Ru}_2(\text{ap})_4\text{Cl}$. The most unique feature of these complexes is obviously the Ru–C bond. Compounds **1–6** feature the very first examples of $\text{Ru}_2\text{–C}(sp^2)$ bonds among paddlewheel complexes. Whereas Ru–C bond lengths in mono- and bis-alkynyl complexes average between 1.85–2.1 Å,² compounds **1–6** all have bond lengths greater than 2.13 Å. A similar lengthening of the M–C bond is observed in the dirhodium paddlewheels $\text{Rh}_2(\text{ap})_4(\text{C}\equiv\text{CH})$ (Rh–C = 2.021 Å) and $\text{Rh}_2(\text{ap})_4(\text{Ph})$ (Rh–C = 2.108 Å).²⁰ This increase in bond length is attributed to (i) the change in hybridization of the ipso carbon from *sp* ($r_{\text{covalent}} = 69$ pm) to sp^2 ($r_{\text{covalent}} = 73$ pm)²³ and (ii) the significant increase in sterics at the axial site from the linear $\text{C}\equiv\text{C}$ to the two-dimensional aryl. Although there is a trend of decreasing electron-donating ability of the para substituent upon going from compound **1** to compound **6**, there is no apparent manifestation of this in the Ru–C, or the Ru–Ru bond lengths.

Ru–Ru bond lengths for the compounds range from 2.3347(7) Å to 2.3423(5) Å, and are significantly elongated from $\text{Ru}_2(\text{ap})_4\text{Cl}$ (2.275(6) Å). But this is not unusual in Ru_2^{5+} compounds; σ -alkynyl complexes $\text{Ru}_2(\text{ap})_4((\text{C}\equiv\text{C})_n\text{R})$ ($n = 1, 2$) have Ru–Ru bond lengths of *ca.* 2.32–2.33 Å.⁷ This is attributed to the stronger electron-donor effect of the axial alkynyl ligand compared to

chloro. The fact that it increases from 2.319(2) Å in $\text{Ru}_2(\text{ap})_4(\text{C}\equiv\text{CPh})$, to 2.3380(5) Å in $\text{Ru}_2(\text{ap})_4(\text{Ph})$ (**4**) is indicative of the even stronger electron-donating ability of the aryl ligand in comparison to alkynyl. Such an effect is also seen in the case of $\text{Rh}_2(\text{ap})_4(\text{C}\equiv\text{CH})$ ($\text{Rh-Rh} = 2.439$ Å) vs. $\text{Rh}_2(\text{ap})_4(\text{Ph})$ ($\text{Rh-Rh} = 2.470$ Å).²⁰

Not unlike alkynyls, the aryl ligands retain conjugation between the diruthenium core and the axial ligand, and this is supported by the consistent linearity of the Ru–Ru–C angles and planarity of the aryl ligands (Table 1.1). Except in the case of compounds **3** and **6**, the aryl ligands are approximately coplanar with the plane containing $\text{N}_x\text{–Ru}_2\text{–N}_y$ (Figure 1.2). The two-dimensional nature of the aryl ligand is in stark contrast to the one-dimensional nature of the alkynyl ligand. This unique feature reduces the 4-fold axial symmetry observed in mono- and bis-alkynyl paddlewheel species to 2-fold, the effect of which can be seen in the electronic absorption spectra (see below).

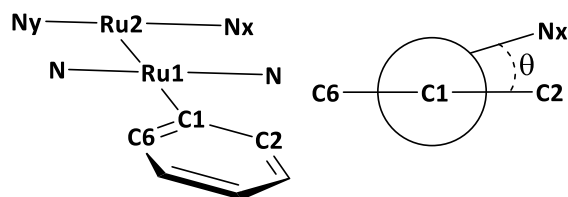


Figure 1.2. Dihedral angle (θ), defined as the angle between the lines C1–C2 and Ru2–Nx.

Table 1.1. Selected Bond Lengths (Å) and Angles (deg) for compounds **1–6**.

	1^a	2	3	4^b	5	6^b
Ru1–Ru2	2.3347(7)	2.338(1)	2.3423(5)	2.3380(5)	2.3375(4)	2.3373(5)
Ru1–C1	2.214(3)	2.260(8)	2.190(4)	2.16(1)	2.216(5)	2.22(1)
Ru2–Ru1–C1	179.3(1)	177.8(2)	175.51(9)	173.9(3)	176.3(4)	177.9(3)
Ru1–N1	2.105(6)	2.103(8)	2.112(3)	2.104(4)	2.124(2)	2.132(4)
Ru1–N3	2.102(5)	2.118(9)	2.135(3)	2.117(4)	(Ru1–N2) 2.107(2)	2.158(9)
Ru1–N5	2.106(5)	2.118(8)	2.138(3)	2.122(4)		2.128(4)
Ru1–N7	2.109(5)	2.103(9)	2.098(3)	2.128(4)		2.106(3)
Ru2–N2	2.041(5)	2.050(7)	2.043(3)	2.062(4)	(Ru2–N3) 2.0320(19)	2.043(3)

Table 1.1 continued

Ru2–N4	2.046(5)	2.019(9)	2.041(2)	2.055(4)	2.0485(18)	2.040(4)
Ru2–N6	2.037(5)	2.045(7)	2.033(3)	2.024(4)		2.032(2)
Ru2–N8	2.051(5)	2.034(9)	2.036(2)	2.018(4)		2.038(3)
θ^c	-1.60	+4.26	-11.7	-3.79	+3.77	+10.6

^a One of the two molecules present in the asymmetric unit was chosen (Molecule A). Molecule B can be found in the corresponding CIF file. Any structural differences between A and B were deemed insignificant. ^b major moiety chosen from disordered axial ligands. ^c θ is defined per Figure 1.2.

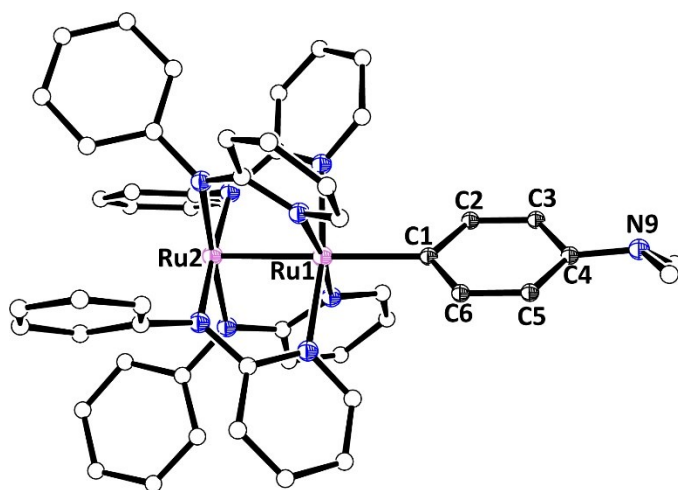


Figure 1.3. Structural plot of **1** at 30% probability level. One of the two molecules (A) present in the asymmetric unit was selected. Hydrogens omitted for clarity.

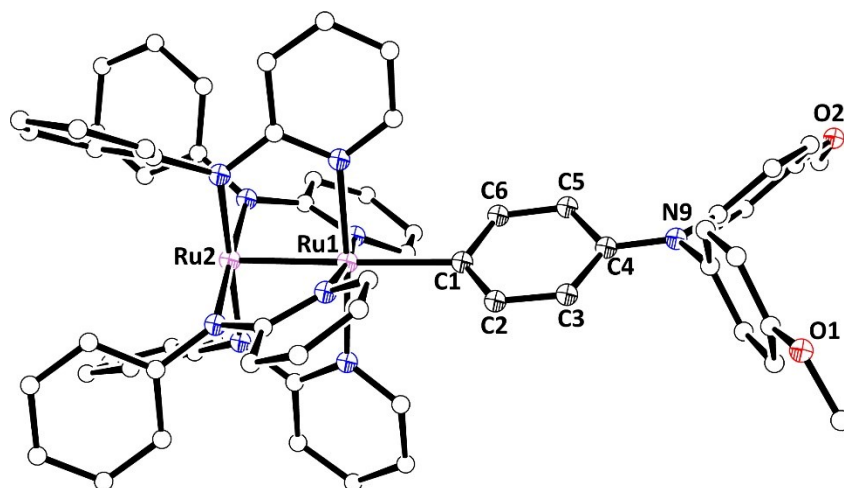


Figure 1.4. Structural plot of **2** at 30% probability level. Solvent molecules and hydrogens omitted for clarity.

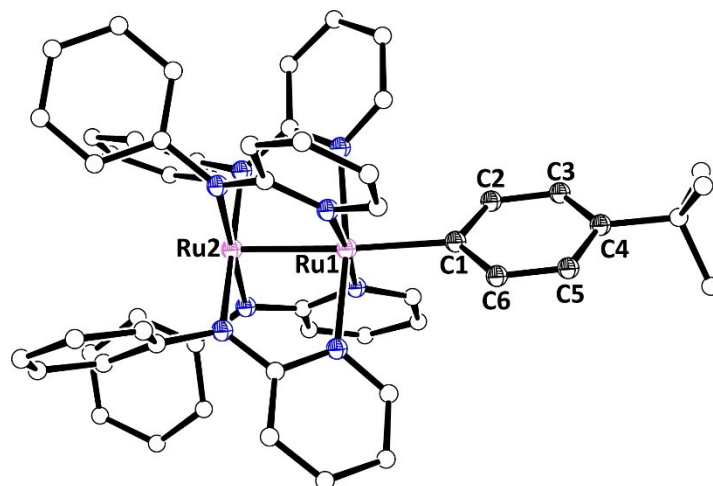


Figure 1.5. Structural plot of **3** at 30% probability level. Solvent molecules and hydrogens omitted for clarity.

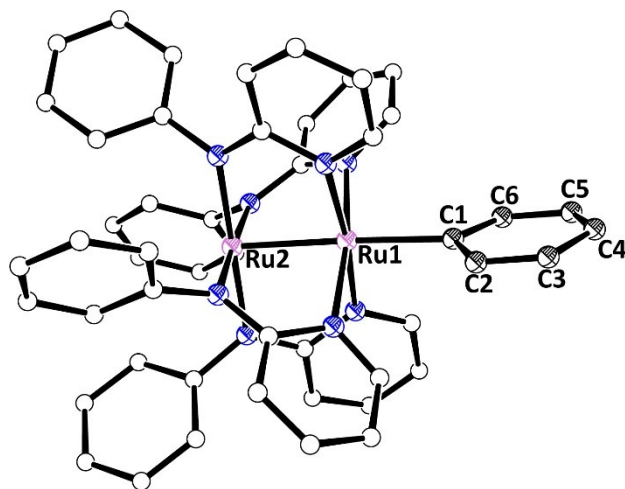


Figure 1.6. Structural plot of **4** at 30% probability level. Solvent molecules, disordered ligand and hydrogens omitted for clarity.

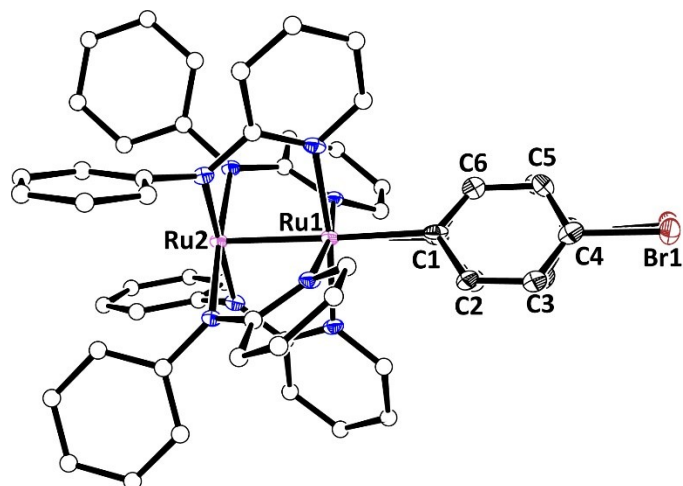


Figure 1.7. Structural plot of **5** at 30% probability level. Aryl ligand is disordered around the C_2 axis.

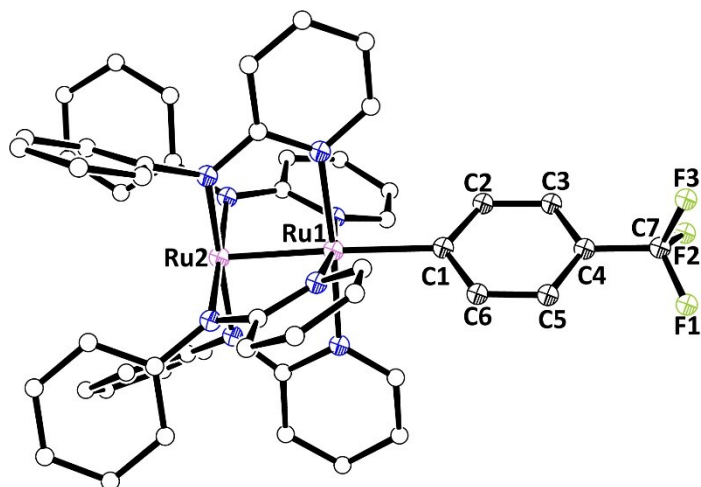


Figure 1.8. Structural plot of **6** at 30% probability level. Solvent molecules, disordered ligands and hydrogens omitted for clarity.

1.3.4 Electronic absorption spectroscopy

Compounds **1–6** are all intensely colored, a characteristic feature of diruthenium paddlewheels. The major features in the electronic absorption spectra of compounds **1–6** agree with those of reported Ru_2^{5+} alkynyl compounds. Figure 1.9 shows an overlay of the visible/near infrared (Vis-NIR) absorption spectra of compounds **1–6**, and $\text{Ru}_2(\text{ap})_4\text{Cl}$. Compounds **1–6** all undergo at least two major electronic transitions that are characteristic of Ru_2^{5+} , one at *ca.* 460 nm and the other around 820 nm. Overall, the relative energies of the major absorptions are not very

different from the ones seen in the starting material, $\text{Ru}_2(\text{ap})_4\text{Cl}$ (415 nm, 754 nm), or in mono σ -alkynyl complexes for example, $\text{Ru}_2(\text{ap})_4(\text{C}\equiv\text{CPh})$ (415 nm, 764 nm)⁴ and $\text{Ru}_2(\text{ap})_4(\text{C}\equiv\text{CH})$ (466 nm, 749 nm).²⁴ The spectra of compounds **1–6** also display some subtle but unique features attributed to the axial aryl ligands.

It is well established that the ground state configuration of $\text{Ru}_2(\text{ap})_4\text{L}_{\text{ax}}$ is $\sigma^2\pi^4\delta^2\pi^*2\delta^{*1,2}$, and the open shell nature of this type molecules makes the assignment of transitions challenging. A recent study by Berry and coworkers based on both magnetic circular dichroism (MCD) spectroscopy and DFT calculations suggested that the peaks at 770 and 430 nm for $\text{Ru}_2(\text{ap})_4\text{Cl}$ should be assigned as $\delta \rightarrow \pi^*$ and $\delta \rightarrow \delta^*$ transitions, respectively.²⁵ It is believed that the same assignment holds true for $\text{Ru}_2(\text{ap})_4\text{Ar}$ compounds reported here, namely, the peak at *ca.* 460 nm being $\delta \rightarrow \delta^*$, and the broad peak around 820 nm being $\delta \rightarrow \pi^*$. Furthermore, the latter assignment is consistent with the broad and even double-humped feature (compounds **1** and **2**). The attachment of aryl reduces the 4-fold axial symmetry of the $\text{Ru}_2(\text{ap})_4$ core to 2-fold, which removes the degeneracy of $\pi^*(\text{Ru}_2)$, resulting in two energetically distinct $\delta \rightarrow \pi^*$ transitions. Conversely, the 4-fold axial symmetry is preserved in the $\text{Ru}_2(\text{ap})_4(\text{C}_2\text{R})$ type compounds, where a single low energy absorption has been consistently observed.

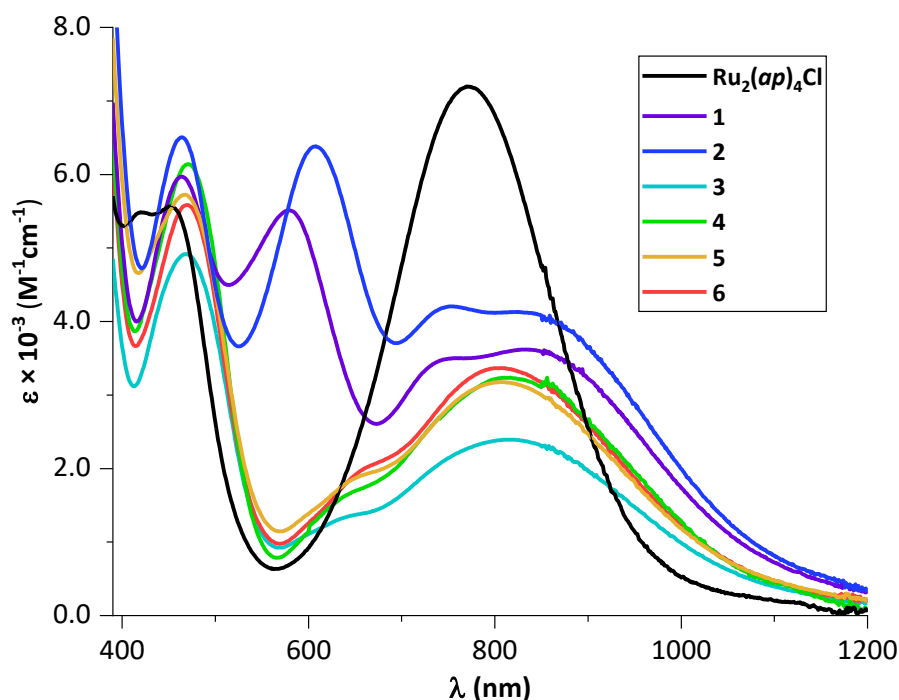


Figure 1.9. Vis-NIR absorption spectra of compounds **1–6** and $\text{Ru}_2(\text{ap})_4\text{Cl}$ recorded in THF.

Compounds **1** and **2** display an additional intense absorption at 579 nm and 607 nm, respectively, which is the primary source of the vastly different colors of **1** (dark grey) and **2** (blue-green) in comparison to those of compounds **3–6** (olive-green). This transition has its origin in the amino-substituent of the aryl ligand, considering that it is absent in those aryl ligands lacking an electron-donor. This is supported by ground state DFT calculations of **1** (see discussion below), which reveals a high-energy $\pi(\text{Ar})$ orbital that is extensively mixed with $\pi(\text{Ru}_2)$ in SOMO – 3 (aka HOMO, Figure 1.10). Therefore, the assignment for this transition is the dipole-allowed $\pi(\text{Ru}_2/\text{Ar}) \rightarrow \pi^*(\text{Ru}_2/\text{Ar})$. On the contrary, for compound **6**, HOMO is completely localized on the $[\text{Ru}_2(\text{ap})_4]$ core, because the corresponding $\pi(\text{Ar})$ orbital is likely buried at a much lower energy.

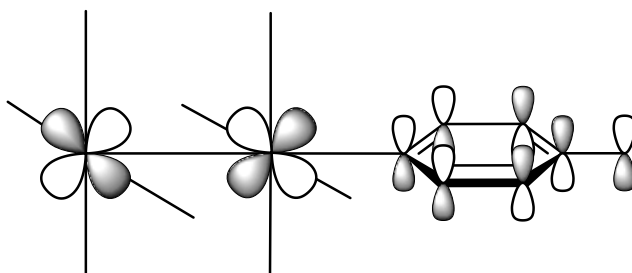


Figure 1.10. Representation of HOMO in **1** and **2**, $\pi(\text{Ru}_2/\text{Ar})$.

1.3.5 Electrochemistry

The redox properties of compounds **1–6** were analyzed by voltammetry; results are plotted in Figure 1.11 and tabulated in Table 1.2. All compounds exhibit a reversible one-electron oxidation (**B**), corresponding to $\text{Ru}_2^{6+/5+}$, between -0.24 and -0.38 V (potentials are reported against the ferrocium/ferrocene couple ($\text{Fc}^{+/0}$)) and a reversible one-electron reduction (**A**) corresponding to $\text{Ru}_2^{5+/4+}$, between -1.47 and -1.62 V. Compounds **1** and **2** exhibit three additional reversible one-electron oxidation events (**C**, **D** and **E**), and the oxidation at *ca.* 0.13 V (**C**) is attributed to the amine functionality. Two reversible one-electron oxidations at more positive potentials (**D** and **E**) occur within 0.14 V of each other and are likely Ru_2 -centered in analogy to those described for $\text{Ru}_2(\text{ap})_4(\text{C}_2\text{R})$.²⁴ For compounds **3–6**, both the one-electron reduction **A** and the first one-electron oxidation **B** are reversible. However, oxidation events beyond couple **B** (**D** and **E**) are either quasi-reversible or irreversible. While the cause of the diverse behavior of compounds **3–6** at more positive potentials is not straightforward, it is noteworthy that **1** and **2** are

electrochemically robust even at higher potentials. The redox robustness of compounds **1** and **2** may be attributed to the ability of $-NR_2$ groups in stabilizing $Ru_2(ap)_4$ core at higher oxidation states through extensive conjugation.

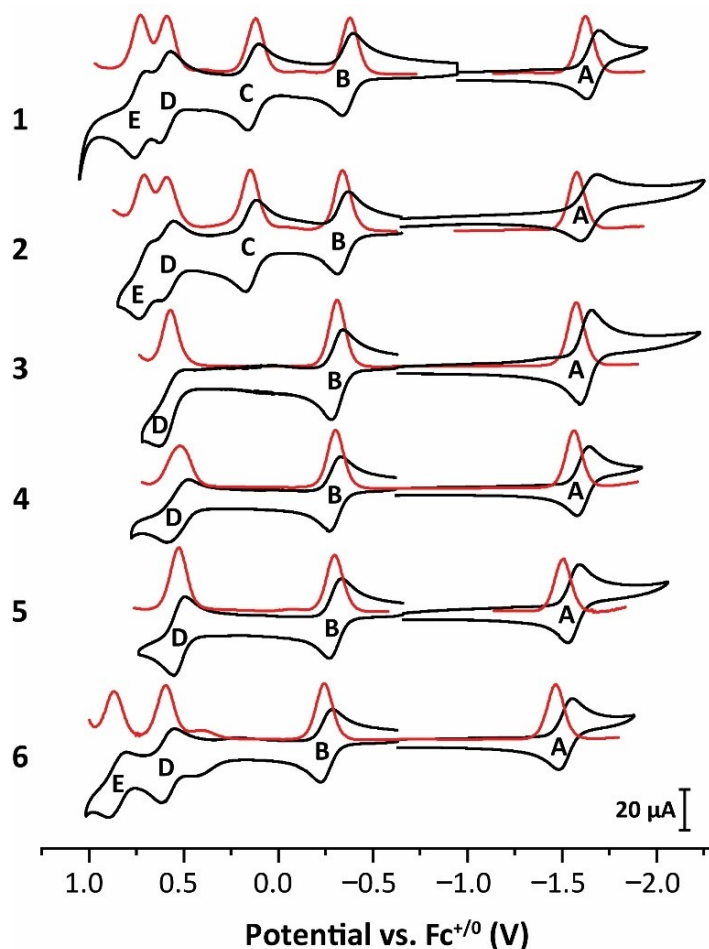


Figure 1.11. Cyclic (CV, black) and differential pulse (DPV, red) voltammograms of compounds **1–6** (1.0 mM) recorded in a 0.10 M CH_2Cl_2 solution of Bu_4NPF_6 at a scan rate of 0.10 V/s.

Table 1.2. Electrochemical data from DPV (in V vs. Fc^{+0})

Compound	A	B	C	D	E
1	-1.62	-0.38	0.12	0.59	0.73
2	-1.58	-0.34	0.15	0.59	0.71
3	-1.57	-0.31	–	0.57	–
4	-1.56	-0.30	–	0.52	–

Table 1.2 continued

5	-1.50	-0.29	-	0.53	-
6	-1.47	-0.24	-	0.59	0.87

It is clear from Table 1.2 that the potentials for reversible couples **A** and **B** shift anodically in the order **1–6**, following the trend of decreasing electron donating / increasing electron withdrawing character of the *para* substituent. The trend is further quantified through a linear fit of the first oxidation potential ($E(\mathbf{B})$) versus the Hammett constant of the substituents (Figure 1.11),^{26–28} which yields a reactivity constant (ρ) of *ca.* 98 mV (Equation 1.1). Similar results were obtained from Hammett plots of $E(\mathbf{A})$ ($\rho \approx 107$ mV). Previously, the reactivity constants for the series $\text{Ru}_2(\text{dmba})_4(\text{C}\equiv\text{C}-\text{C}_6\text{H}_4-4-\text{X})_2$ were determined to be 121 mV and 86 mV for the first oxidation and reduction couples, respectively. The values of ρ are comparable between the two series, reflecting a similar impact of the *para* aryl substituents.

$$E_{\frac{1}{2}}(X) = \rho\sigma_X + E_{\frac{1}{2}}(H) \dots (\text{Eq. 1.1})$$

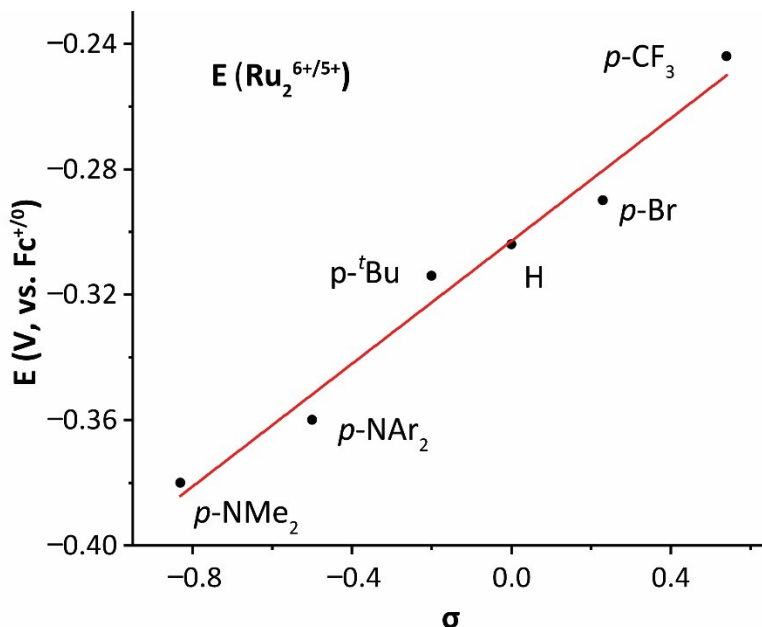


Figure 1.12. Hammett plot of redox potentials ($E(\text{Ru}_2^{6+/5+})$) versus σ_x for compounds **1–6**. The circles are the measured potentials, the solid line is the least-squares fit.

Compared to Ru₂(ap)₄Cl the strongly nucleophilic Ar⁻ axial ligand cathodically shifts both the E_{1/2}(Ru₂^{6+/5+}) and E_{1/2}(Ru₂^{5+/4+}) potentials of Ru₂(ap)₄Ar by an average of 350 mV and 300 mV, respectively. Further, the strong e⁻-donor properties of the aryl ligands are reflected in the cathodic shift of the corresponding E_{1/2} values compared to alkynyls. For instance, compared to Ru₂(ap)₄(C₂Ph),²⁹ the E_{1/2}(Ru₂^{6+/5+}) of Ru₂(ap)₄(Ph) (**4**) is cathodically shifted by 87 mV, and E_{1/2}(Ru₂^{5+/4+}) by 130 mV (see Table 1.S1). As expected, this cathodic shift increases as the *para*-substituent on the aryl ligand becomes more electron-donating.

1.3.6 Magnetism

Evans method³⁰ magnetic susceptibility measurements yielded effective magnetic moments (μ_{eff}) of 3.4– 4.1 μ_B, suggesting a quartet ground state for compounds **1–6** (S = 3/2), which is very common for the Ru₂(II,III) oxidation state. The electronic configuration is thus in agreement with the expected σ²π⁴δ²(π*δ*)³. To further characterize the paramagnetic nature of these complexes, superconducting quantum interference device (SQUID) magnetometry measurements in the temperature range of 2–300 K were performed on compound **1** as a representative example.

One of the characteristic features of S = 3/2 Ru₂(II,III) systems is the exceptionally large zero-field splitting (ZFS) energy.^{25,31–33} This effect is so large, that other contributors to the spin Hamiltonian (coupling to nearest neighbors, temperature-independent paramagnetism) can be treated as negligible. This is evident from Figure 1.13, where the experimental data has been fitted using the Van-Vleck equations Eq 1.2–1.4.³⁴

$$\chi_{\parallel} = \frac{N_A g_{\parallel}^2 \beta^2}{k_B T} \cdot \left\{ \frac{1 + 9e^{-\frac{2D}{k_B T}}}{4 \left(1 + e^{-\frac{2D}{k_B T}} \right)} \right\} \dots (Eq 1.2)$$

$$\chi_{\perp} = \frac{N_A g_{\perp}^2 \beta^2}{k_B T} \cdot \left\{ \frac{4 + \left(\frac{6k_B T}{D} \right) \left(1 - e^{-\frac{2D}{k_B T}} \right)}{4 \left(1 + e^{-\frac{2D}{k_B T}} \right)} \right\} \dots (Eq 1.3)$$

$$\chi_{total} = \frac{1}{3} (\chi_{\parallel} + 2 \cdot \chi_{\perp}) \dots (Eq 1.4)$$

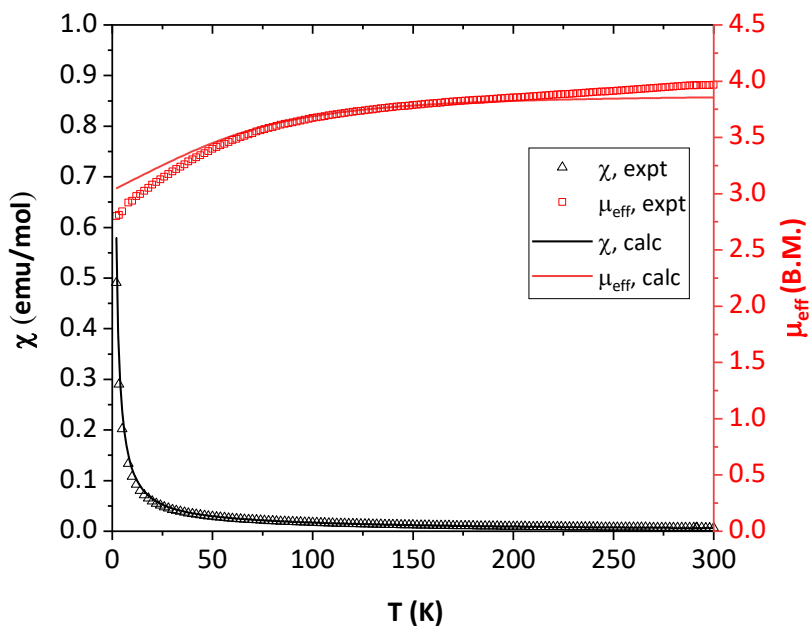


Figure 1.13. SQUID magnetometry of **1** from 2–300 K, courtesy of Dr. Fang Yuan. Curves simulated for $D = 76 \text{ cm}^{-1}$, $g_{\parallel} = 1.9500$, $g_{\perp} = 2.0265$.

The relatively large ZFS ($D = 76\text{cm}^{-1}$) is indicative of the pseudo-axiality of the molecule, while the goodness of fit suggests that all other effects like intermolecular exchange and temperature independent magnetism (TIP), including the contribution of the rhombic component of ZFS (E) are minor.

1.3.7 Density Functional Theory Calculations.

In order to gain further insight into the electronic structure of these compounds, the molecular orbitals of compounds **1** and **6**, two compounds at the opposite ends of the donicity of *para*-substituents, were computed using restricted open-shell (ROS) DFT. One of the advantages of the ROS formalism is that it does not suffer from spin-contamination because the ROS wavefunction is an eigenfunction of the $\langle S^2 \rangle_{\text{exact}}$ operator. This is not the case with unrestricted DFT calculations. Unfortunately, many analytic techniques are unavailable to ROS calculations (for instance, calculation of force constants, excited states, etc. cannot be done using the Gaussian16 package using the ROS formalism). As a result, the only practical utility of ROS DFT is the computation of ground state geometries and molecular orbitals.

The optimized geometries of **1** and **6** were based on their respective crystal structures as initial input geometries. Calculations were performed using the B3LYP functional,^{35–38} and frequency analyses were done to ensure stationary points; resultant structures, namely **1'** and **6'**, are shown in Figure 1.S6, along with optimized metric parameters in Table 1.S8. The bond lengths of the optimized structures are in decent agreement with the respective crystal structures. The optimized Ru–Ru bond lengths (*ca.* 2.39 Å) are *ca.* 0.06 Å longer than the experimental bond lengths (*ca.* 2.33 Å) while the optimized Ru–C bond lengths (*ca.* 2.17 Å for **1'** and 2.19 Å for **6'**) are shorter than the experimental values (*ca.* 2.21 Å for **1** and 2.22 for **6**). These are attributed to: i) the underestimation of Ru–Ru interactions by the B3LYP functional,³⁹ ii) neglect of dispersion correction, iii) neglect of solvent model and iv) smaller basis sets with relatively little polarization. The calculated bond angles were found to be in good agreement with experiment (Table 1.S8).

In agreement with magnetism data and the expected electronic configuration, DFT calculations support an electronic configuration of $\sigma^2\pi^4\delta^2\pi^*\delta^*$. Figure 1.13 clearly shows that the three singly occupied MOs of **1'** and **6'** (SOMO, SOMO – 1, and SOMO – 2) have δ^* , π^* and π^* and character, respectively. The introduction of the aryl ring, as previously described, causes the $\pi^*(Ru_2)$ orbitals to lose their degeneracy, giving rise to the double-humped feature seen in the electronic absorption spectra. Whereas SOMO – 1 has contributions from both the diruthenium core and the aryl ligand, SOMO – 2 has no contribution from the latter, owing to the coplanarity of the d_{yz} orbitals and aryl ligand. DFT calculations support this argument; there is a small but significant difference between the energies of SOMO – 1 and SOMO – 2 (80 meV for **1** and 30 meV for **6**), both of which have $\pi^*(Ru_2)$ character. Both SOMO and LUMO are completely localized on $[Ru_2(ap)_4]$, hence the constant SOMO–LUMO energy gap of 1.74 eV. The crucial difference between **1** and **6** is reflected in their respective HOMO orbitals. As mentioned previously, due to the presence of an electron-donating nitrogen in the *para* position of the aryl ring in **1** (and **2**), HOMO is of $\pi(Ru_2)/\pi(Ar)$ character. On the contrary, HOMO in the case of **6** is localized on $[Ru_2(ap)_4]$.

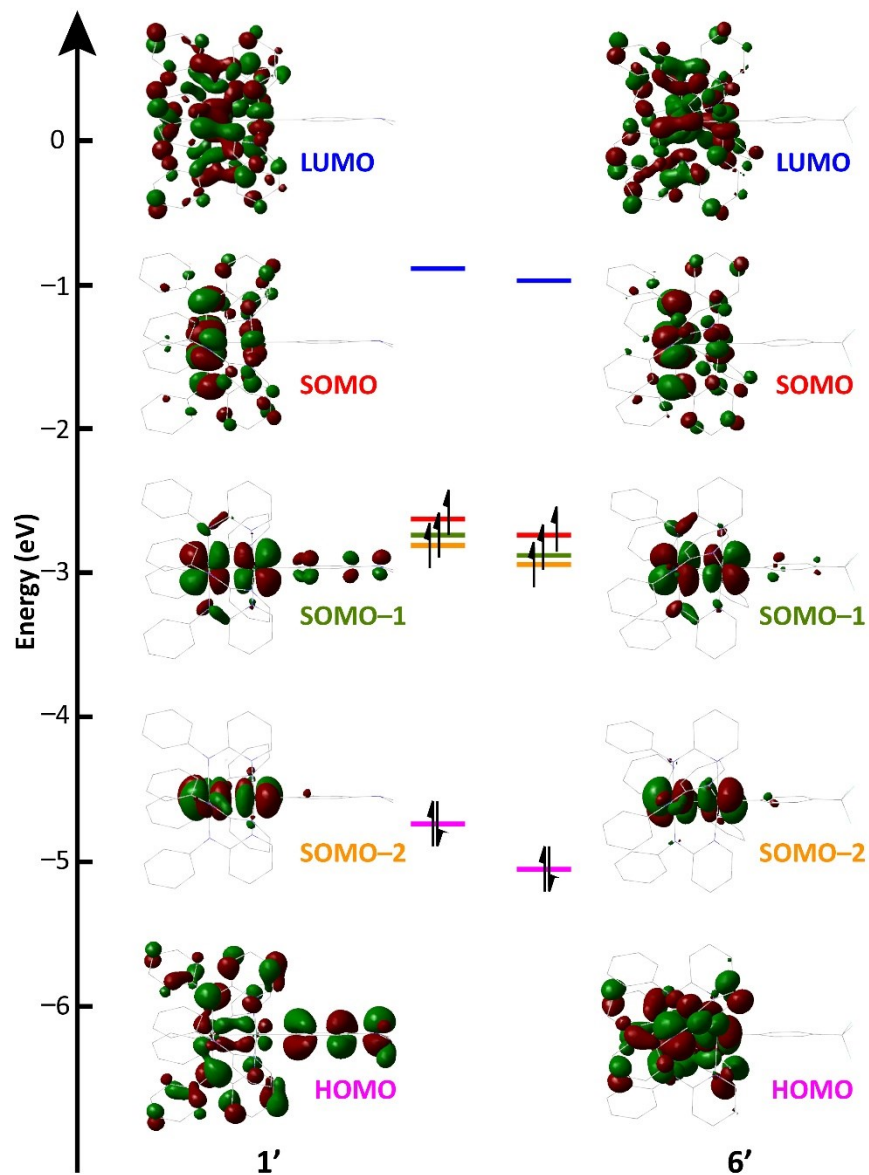


Figure 1.14. Frontier molecular orbital diagrams for **1'** and **6'** from DFT calculations

1.4 Conclusion

In conclusion, the first examples of diruthenium paddlewheel complexes with σ -aryl ligands in the axial sites have been isolated. The paddlewheel compounds are in the Ru_2^{5+} oxidation state and support up to four electrochemically reversible oxidations and one reversible reduction, thereby attesting to the remarkable redox stability of such species. Such a quality is highly desired for compounds as the active species in molecular wires/devices.⁴⁰ Additionally, electrochemical

studies show that it is possible to tune the reduction potentials of the complexes by altering the substituent on the axial ligand. Overall, the significant cathodic shift in reduction potentials in comparison to their σ -alkynyl counterparts establishes the stronger electron-donor character of the aryl ligand. DFT calculations suggest that the aryl ligand has a significant role to play in modulating the electronic structure of the overall complex. The $\sigma(\text{Ru}_2)$ bond is retained to a certain extent as allowed by the formation of a competing $\sigma(\text{Ru}-\text{C})$ bond, and the high-lying π -manifold of the aryl ligand deeply mixes with that of the Ru_2 unit.

The findings mentioned here outline the preliminary study of monoaryl Ru_2 complexes, and will be supported by data on the reactivity of the vacant ruthenium site in these complexes (Chapter 3) along with some additional spectroscopic and computational data (Chapter 4).

1.5 Experimental Details

General. $\text{Ru}_2(\text{ap})_4\text{Cl}^{3,24}$ and $\text{TPA}(\text{OMe})_2\text{Br}^{41}$ (4-bromo-*N,N*-bis(4-methoxyphenyl)aniline) were prepared using literature methods. $n\text{BuLi}$ (2.5 M in hexanes) was purchased from Sigma-Aldrich. All other halogenated arene precursors were purchased from commercial sources. Tetrahydrofuran was freshly distilled over sodium/benzophenone, while dichloromethane was freshly distilled over CaH_2 prior to use. All reactions were performed under dry N_2 atmosphere implementing standard Schlenk procedures unless otherwise noted. UV-Vis/NIR spectra were obtained with a JASCO V-670 spectrophotometer in THF solutions. ^1H NMR spectra were recorded on a Varian Inova 300 spectrometer operating at 300 MHz. Effective magnetic moments (at 25°C) were calculated by Evans method, using ferrocene as the standard. Cyclic and differential pulse voltammograms were recorded in 0.1 M [$n\text{Bu}_4\text{N}$][PF_6] solution (CH_2Cl_2 , N_2 -degassed) on a CHI620A voltammetric analyzer with a glassy carbon working electrode (diameter = 2 mm), a Pt-wire auxiliary electrode, and a Ag/AgCl QRE. The concentration of Ru_2 -species is always *ca.* 1.0 mM. The $\text{Fc}^{+1/0}$ couple was observed at *ca.* 0.417 ± 0.017 V (vs Ag/AgCl) at the noted experimental conditions. Electrospray ionization mass spectra (ESI-MS) were collected on an Advion expression^L mass spectrometer with an *m/z* range of 10–2000. Elemental analyses were performed by Atlantic Microlab, Inc. DC temperature-dependent magnetization was measured from 2–300 K using zero-field-cooling (ZFC) mode on a Quantum Design MPMS-3 SQUID magnetometer. Compound **1** was measured under a magnetic field of 1000 Oe with a cooling rate of 2 K/min. The whole magnetic measurement was done under vacuum of a few torr.

Synthesis of Ru₂(ap)₄(C₆H₄-4-NMe₂) (1). 4-Bromo-*N,N*-dimethylaniline (220 mg, 1.1 mmol) was dissolved in 10 mL THF and treated with 0.44 mL of 2.5 M ⁿBuLi (1.1 mmol) at 0°C for 15 min. The aryllithium solution was cannula transferred to a 15 mL THF solution of Ru₂(ap)₄Cl (100 mg, 0.11 mmol). Immediate color change from dark green to black was observed. The reaction mixture was stirred at room temperature for 2 h. After removal of solvents, the residue was re-dissolved in a mixture of benzene and ethyl acetate, and the resulting solution as filtered through a deactivated (w/ triethylamine) silica gel pad. The filtrate was collected, solvents were removed, and product was recrystallized from a 1:20 (v:v) CH₂Cl₂:hexanes mixture at -20°C, as a black microcrystalline solid. Yield: 90 mg, 82%. Crystals suitable for X-ray diffraction analysis were grown by layering hexanes over a concentrated solution of **1** in benzene/toluene = 1/1 (v/v).

Data for **1**. Anal. Found (Calcd.) for C₅₂H₄₈N₉ORu₂ (**1**·H₂O): C, 61.02 (61.40); H, 4.63 (4.76); N, 12.07 (12.39). ESI-MS (m/z, based on ¹⁰¹Ru): [M⁺] = 999.7. UV-Vis (in THF) λ, nm, (ε, M⁻¹cm⁻¹): 464 (5900), 579 (5500), 754 (3500), 831 (3600). R_f (1/5 THF/hexanes (v/v); silica gel deactivated with NEt₃) = 0.32. μ_{eff} (25°C) (Evans method) = 3.9 μ_B. Electrochemistry (CH₂Cl₂, vs. Fc⁺⁰), E_{1/2}/V, ΔE_p/mV, i_{forward}/i_{backward}: -0.38, 56, 1.09; 0.12, 57, 1.018; 0.59, 60, ; 0.73, 56, ; -1.62, 63, 1.2.

Synthesis of Ru₂(ap)₄(C₆H₄-4-*N,N*-(C₆H₄-4-OMe)₂) (2). 4-Bromo-*N,N*-bis(4-methoxyphenyl)aniline (1.35 g, 3.5 mmol) was dissolved in 15 mL THF and treated with 1.4 mL of 2.5 M ⁿBuLi (3.5 mmol) at -78°C for 15 min. The temperature was subsequently raised to 0°C, and at this point, a 100 mL THF solution of Ru₂(ap)₄Cl (400 mg, 0.44 mmol) was cannula transferred over to the aryllithium solution. Immediate color change to deep blue-green was observed. The reaction mixture was stirred at room temperature for 2h. After removal of solvent, a blue-green solid was recrystallized from a 1:15 (v:v) THF:hexanes mixture at -20°C. The precipitate was collected on a frit, and rinsed first with hexanes, then cold methanol until the filtrate ran clear. The green residual solid was dried under vacuum. Yield: 491 mg, 95%. Crystals suitable for X-ray diffraction analysis were grown by layering hexanes over a concentrated solution of **2** in EtOAc/benzene = 1/1 (v/v).

Data for **2**. Anal. Found (Calcd.) for C₆₄H₅₆N₉O₃Ru₂ (**2**·H₂O): C, 63.97 (63.97); H, 4.75 (4.69); N, 10.26 (10.49). ESI-MS (m/z, based on ¹⁰¹Ru): [M⁺] = 1183.4. UV-Vis (in THF) λ, nm, (ε, M⁻¹cm⁻¹): 464 (6500), 607 (6400), 753 (4200), 822 (4100). R_f (1/5 THF/hexanes (v/v); silica gel deactivated with NEt₃) = 0.2. μ_{eff} (25°C) (Evans method) = 3.8 μ_B. Electrochemistry

(CH₂Cl₂, vs. Fc⁺⁰), E_{1/2}/V, ΔE_p/mV, i_{forward}/i_{backward}: -0.34, 55, 1.18; 0.15, 59, 1.08; 0.59, 59, ; 0.71, 62, ; -1.58, 1.13.

Synthesis of Ru₂(ap)₄(C₆H₄-4-^tBu) (3). 1-Bromo-4-(tert-butyl)benzene (0.218 mL, 1.3 mmol) was dissolved in *ca.* 15 mL THF and treated with 0.5 mL of 2.5 M ⁿBuLi (1.3 mmol) at 0°C for 15 min. At this point, a 30 mL THF solution of Ru₂(ap)₄Cl (115 mg, 0.13 mmol) was cannula transferred over to the aryllithium solution. Immediate color change from dark green to brown-green was observed. The reaction mixture was stirred at room temperature for 2h, during which the solution had acquired a red-brown color. Upon exposure to air, the color of the solution changed back to brown-green. After removal of solvent, a green solid was recrystallized from a 1:15 (v:v) THF:hexanes mixture at -20°C. The precipitate was collected on a frit, and rinsed first with n-pentane, then cold methanol until the filtrate ran clear. The olive-green residual solid was dried under vacuum. Yield: 85 mg, 67%. Crystals suitable for X-ray diffraction analysis were grown by layering methanol over a concentrated solution of **3** in THF.

Data for **3**. Anal. Found (Calcd.) for C₅₄H₅₃N₈O₂Ru₂·(3·2H₂O): C, 61.94 (61.88); H, 4.80 (5.09); N, 10.63 (10.69). ESI-MS (m/z, based on ¹⁰¹Ru): [M⁺] = 1012.2. UV-Vis (in THF) λ, nm, (ε, M⁻¹cm⁻¹): 468 (4900), 643 (1300, sh), 815 (2400). R_f (1/5 THF/hexanes (v/v); silica gel deactivated with NEt₃) = 0.5. μ_{eff} (25°C) (Evans method) = 3.4 μ_B. Electrochemistry (CH₂Cl₂, vs. Fc⁺⁰), E_{1/2}/V, ΔE_p/mV, i_{forward}/i_{backward}: -0.31, 57, 1.08; 0.57, irrev.; -1.58, 62, 0.960;

Synthesis of Ru₂(ap)₄(Ph) (4). Bromobenzene (0.092 mL, 0.87 mmol) was dissolved in *ca.* 10 mL THF and treated with 0.35 mL of 2.5 M ⁿBuLi (0.87 mmol) at 0°C for 15 min. The aryllithium solution was cannula transferred to a 20 mL THF solution of Ru₂(ap)₄Cl (100 mg, 0.11 mmol). Immediate color change from dark green to red-brown was observed. The reaction mixture was stirred at room temperature for 2 h. Upon exposure to air, the color of the solution changed from red-brown to green-brown. After removal of solvent, the crude product mixture was subjected to purification by column chromatography on deactivated (w/ triethylamine) silica. The light green band was eluted (w/ EtOAc/hexanes), and an olive-green microcrystalline solid was isolated. Yield: 32 mg, 30%. Crystals suitable for X-ray diffraction analysis were grown by layering methanol over a concentrated solution of **4** in THF/benzene = 2/1 (v/v).

Data for **4**. Anal. Found (Calcd.) for C₅₄H₅₁N₈O₃Ru₂ (4·H₂O·EtOAc): C, 61.69 (60.06); H, 4.89 (4.84); N, 10.51 (10.55). ESI-MS (m/z, based on ¹⁰¹Ru): [M⁺] = 956.1. UV-Vis (in THF) λ, nm (ε, M⁻¹cm⁻¹): 471 (6100), 647 (1700, sh), 812 (3200). R_f (1/5 THF/hexanes (v/v); silica gel

deactivated with NEt_3) = 0.39. μ_{eff} (25°C) (Evans method) = 4.0 μ_B . Electrochemistry (CH_2Cl_2 , vs. $\text{Fc}^{+/0}$), $E_{1/2}/V$, $\Delta E_p/mV$, $i_{\text{forward}}/i_{\text{backward}}$: -0.30, 57, 1.08; 0.52, 117, 1.37; -1.56, 61, 1.09.

Synthesis of $\text{Ru}_2(\text{ap})_4(\text{C}_6\text{H}_4\text{-4-Br})$ (5**).** 1-Bromo-4-iodobenzene (832 mg, 2.9 mmol) was dissolved in *ca.* 25 mL of THF was treated with 1.2 mL of 2.5 M $n\text{BuLi}$ (1.4 mmol) at -78°C for 15 min. The temperature was subsequently raised to 0°C , and at this point, a 100 mL THF solution of $\text{Ru}_2(\text{ap})_4\text{Cl}$ (400 mg, 0.44 mmol) was cannula transferred over to the aryllithium solution. Immediate color change to deep blue-green was observed. The reaction mixture was stirred at room temperature for 2 h. After removal of solvent, the residue was re-dissolved (partially) in hexanes and an olive green solid precipitated out at -20°C . The precipitate was collected on a frit, rinsed with hexanes and cold methanol, and dried under vacuum to afford an olive-green product. Yield: 180 mg, 80%. Crystals suitable for X-ray diffraction analysis were grown by layering hexanes over a concentrated solution of **5** in THF/benzene = 2/1 (v/v).

Data for **5**. Anal. Found (Calcd.) for $\text{C}_{55}\text{H}_{50}\text{BrCl}_2\text{N}_8\text{O}_2\text{Ru}_2$ (**5**·2 H_2O ·MeOH): C, 55.41 (55.53); H, 3.99 (4.39); N, 9.64 (10.16). ESI-MS (m/z , based on ^{101}Ru): $[\text{M}^+]$ = 1034.9. UV-Vis (in THF) λ , nm, (ϵ , $\text{M}^{-1}\text{cm}^{-1}$): 467 (5700), 650 (1900, sh), 805 (3200). R_f (1/5 THF/hexanes (v/v); silica gel deactivated with NEt_3) = 0.39. μ_{eff} (25°C) (Evans method) = 3.7 μ_B . Electrochemistry (CH_2Cl_2 , vs. $\text{Fc}^{+/0}$), $E_{1/2}/V$, $\Delta E_p/mV$, $i_{\text{forward}}/i_{\text{backward}}$: -0.29, 68, 1.04; 0.53, 63, 1.27; -1.50, 64, 1.06.

Synthesis of $\text{Ru}_2(\text{ap})_4(\text{C}_6\text{H}_4\text{-4-CF}_3)$ (6**).** 4-Bromobenzotrifluoride (0.11 mL, 0.77 mmol) was taken in a Schlenk flask and degassed thrice *via* cycles of freeze/pump/thaw, dissolved in *ca.* 10 mL THF and treated with 0.3 mL of 2.5 M $n\text{BuLi}$ at -78°C for 15 min. The aryllithium solution was cannula transferred to a 15 mL THF solution of $\text{Ru}_2(\text{ap})_4\text{Cl}$ (100 mg, 0.11 mmol). Immediate color change from dark green to red-brown was observed. The reaction mixture was stirred at room temperature for 4 h. After 4 h, the color of the solution turned green-brown. After removal of solvent, the crude product mixture was subjected to purification by column chromatography on deactivated (w/ triethylamine) silica. The green band was eluted, and an olive-green solid was isolated. Yield: 52 mg, 46%. Crystals suitable for X-ray diffraction analysis were grown by layering methanol over a concentrated solution of **6** in THF/benzene = 2/1 (v/v).

Data for **6**. Anal. Found (Calcd.) for $\text{C}_{55}\text{H}_{48}\text{F}_3\text{N}_8\text{ORu}_2$ (**6**·THF): C, 60.76 (60.26); H, 4.68 (4.41); N, 10.47 (10.22). ESI-MS (m/z , based on ^{101}Ru): $[\text{M}^+]$ = 1024.8. UV-Vis (in THF) λ , nm, (ϵ , $\text{M}^{-1}\text{cm}^{-1}$): 470 (5600), 661 (2000, sh), 805 (3400). R_f (1/5 THF/hexanes (v/v); silica gel deactivated with NEt_3) = 0.43. μ_{eff} (25°C) (Evans method) = 4.1 μ_B . Electrochemistry (CH_2Cl_2 , vs.

$Fc^{+/0}$), $E_{1/2}/V$, $\Delta E_p/mV$, $i_{forward}/i_{backward}$: -0.24, 62, 1.12; 0.59, 68, 0.90; 0.87, 93, 1.84; -1.47, 64, 1.02.

Attempted synthesis of $Ru_2(ap)_4(C_6H_4-4-NO_2)$. 4-Iodonitrobenzene (408 mg, 1.6 mmol) was dissolved in 20 mL THF and treated with 0.65 mL of 2.5 M *n*BuLi (1.6 mmol) at $-78\text{ }^\circ\text{C}$. The pale yellow color of the solution instantaneously turned deep purple. Upon cannula transfer of $Ru_2(ap)_4Cl$ in THF (100 mg, 0.11 mmol) to the aryllithium solution, a color change to deep red was noted, and this color remained unchanged for the entire duration of the procedure (12 h, under dinitrogen). After the reaction was stopped and exposed to ambient conditions for work-up, the color of the reaction mixture immediately changed to green, reminiscent of starting material. Analysis of the mixture by both TLC and ESI-MS revealed $Ru_2(ap)_4Cl$ to be the only diruthenium compound in the mixture. The results were found to be similar upon replacing 4-iodonitrobenzene with 4-bromonitrobenzene. The explanation we offer is as follows:

-NO₂ groups are notoriously difficult to handle in the presence of reactive nucleophilic reagents, like alkyllithiums or Grignard reagents. The famous Bartoli indole synthesis makes use of this reactivity of the -NO₂ group towards synthesis of indoles. In the presence of other, more reactive centres in the molecule, the nitro group can potentially remain just a spectator, as can be seen from the work on $LiC\equiv C-C_6H_4-4-NO_2$ by Peng. In Peng's work, in the presence in $HC\equiv C^-$ moiety, the alkyllithium reagent selectively deprotonates the alkynyl proton, while the nitro group is unaffected. Unfortunately, for both 4-iodonitrobenzene and 4-bromonitrobenzene, the -NO₂ functional group is more reactive than the C-X bond (X=halogen), so the butyllithium proceeds to react with the former. The nature of the interaction between the product(s) of this reaction and $Ru_2(ap)_4Cl$ is unclear, and we were unable to isolate any product under the conditions described for other compounds in the manuscript. Any product that may have formed immediately reverted to starting material ($Ru_2(ap)_4Cl$). This precluded the synthesis of -NO₂ substituted $Ru_2(ap)_4(aryl)$.

X-ray Crystallographic Analysis. Single crystal X-ray diffraction data for compounds **1**–**6** at 100 K were collected on a Bruker AXS D8 Quest CMOS diffractometer using Mo-K α radiation ($\lambda = 0.71073\text{ \AA}$). Data was collected and processed using APEX3,⁴² and the structures were solved using SHELXTL suite of programs^{43,44} and refined using Shelxl2016.^{45,46}

Computational Methods. Geometry optimizations of structures **1** and **6** based on the respective crystal structures were done using restricted open-shell density DFT at the B3LYP level. The basis set DGDZVP^{47,48} was used for ruthenium, and 6-31G*^{49–53} was used for all other atoms.

Frequency analyses were carried out for both the optimized structures **1'** and **6'**, and stationary points were confirmed. All calculations were carried out with Gaussian 16, rev. A.03.⁵⁴

1.6 Supporting Information

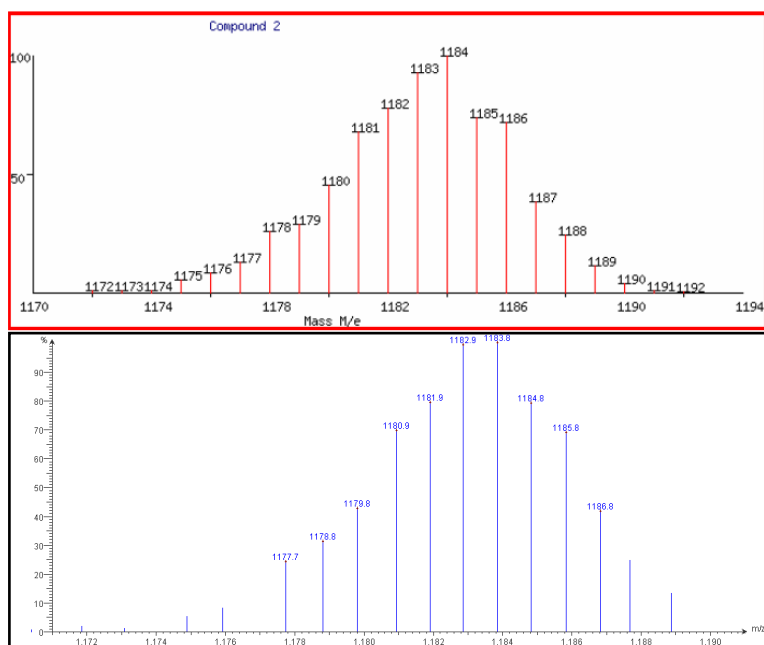


Figure 1.S1. ESI-MS⁺ spectrum of **2**. Red:(top) Calculated. Black(bottom): Experimental

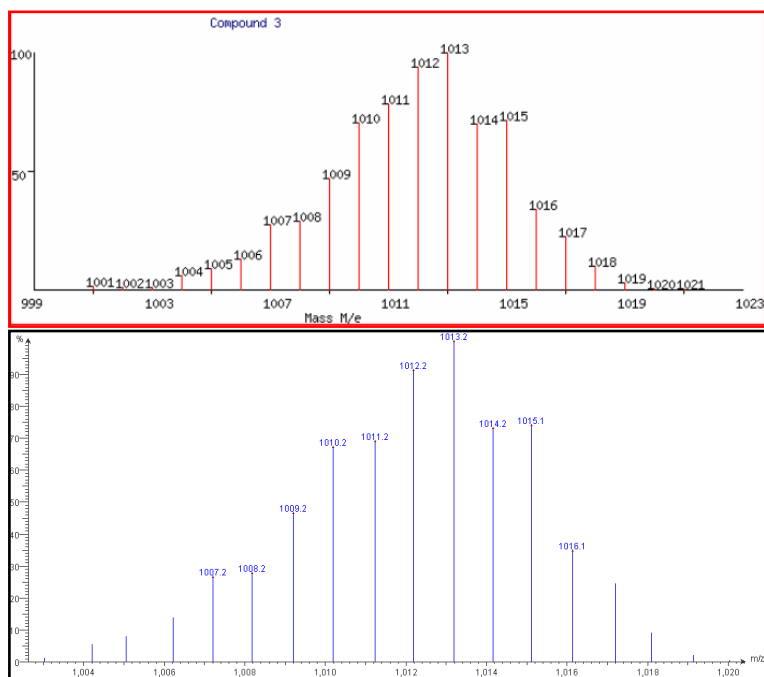


Figure 1.S2. ESI-MS⁺ spectrum of **3**. Red:(top) Calculated. Black(bottom): Experimental

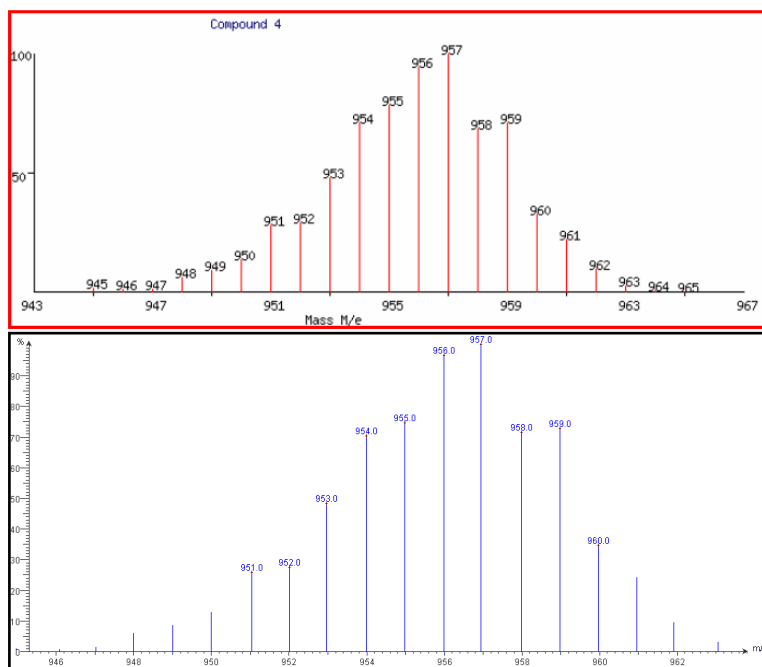


Figure 1.S3. ESI-MS⁺ spectrum of **4**. Red:(top) Calculated. Black(bottom): Experimental

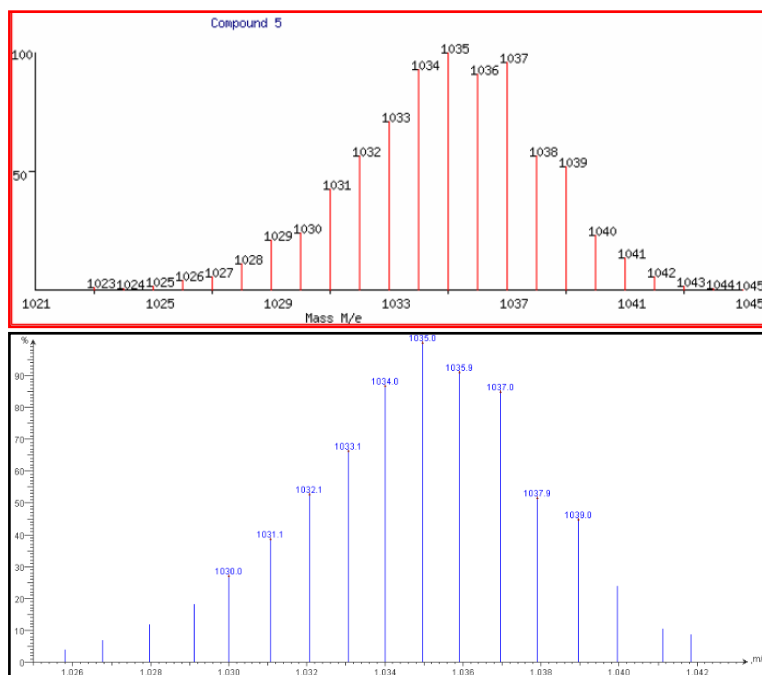


Figure 1.S4. ESI-MS⁺ spectrum of **5**. Red:(top) Calculated. Black(bottom): Experimental

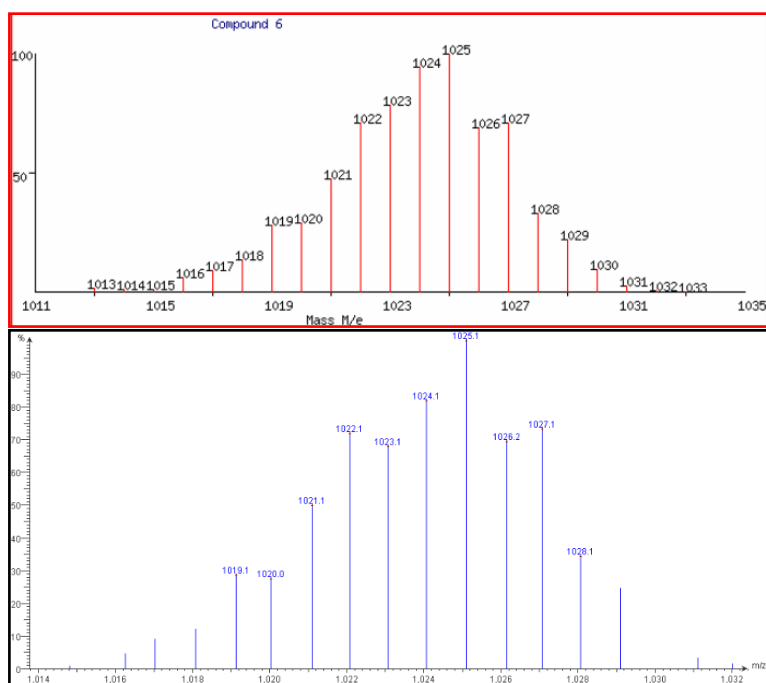


Figure 1.S5. ESI-MS⁺ spectrum of **6**. Red:(top) Calculated. Black(bottom): Experimental

Table 1.S1. Electrochemical data from DPV (in V vs. Ag/AgCl)

Compound	1+/0	2+/1+	3+/2+	4+/3+	0/1-
1	0.052	0.552	1.022	1.162	-1.188
2	0.088	0.578	1.018	1.138	-1.152
3	0.094	0.974	-	-	-1.166
4	0.100	0.920	-	-	-1.160
5	0.146	0.966	-	-	-1.064
6	0.160	0.990	1.270	-	-1.070
Ru ₂ (<i>ap</i>) ₄ Cl	0.457	1.430	-	-	-0.834
Ru ₂ (<i>ap</i>) ₄ (C≡CPh)	0.187	-	-	-	-1.036

Table 1.S2. Crystallographic details for Ru₂(ap)₄(C₆H₄-4-NMe₂) (1)

Ru ₂ (ap) ₄ (C ₆ H ₄ -4-NMe ₂) (1)	
Crystal data	
Chemical formula	C ₅₂ H ₄₆ N ₉ Ru ₂
<i>M</i> _r	999.12
Crystal system, space group	Triclinic, <i>P</i> $\bar{1}$
Temperature (K)	293
<i>a</i> , <i>b</i> , <i>c</i> (Å)	16.424 (3), 16.863 (3), 17.097 (3)
α , β , γ (°)	83.69 (3), 73.13 (3), 88.24 (3)
<i>V</i> (Å ³)	4503.9 (17)
<i>Z</i>	4
Radiation type	Mo <i>K</i> α
μ (mm ⁻¹)	0.72
Crystal size (mm)	0.80 × 0.35 × 0.02
Data collection	
Diffractometer	Bruker AXS D8 Quest CMOS diffractometer
Absorption correction	Multi-scan <i>SADABS</i> 2016/2: Krause, L., Herbst-Irmer, R., Sheldrick G.M. & Stalke D. (2015). <i>J. Appl. Cryst.</i> 48 3-10.
<i>T</i> _{min} , <i>T</i> _{max}	0.529, 0.746
No. of measured, independent and observed [<i>I</i> > 2 σ (<i>I</i>)] reflections	26716, 26716, 17494
<i>R</i> _{int}	?
($\sin \theta/\lambda$) _{max} (Å ⁻¹)	0.718
Refinement	
<i>R</i> [<i>F</i> ² > 2 σ (<i>F</i> ²)], <i>wR</i> (<i>F</i> ²), <i>S</i>	0.057, 0.172, 1.04
No. of reflections	26716
No. of parameters	1215
No. of restraints	300
H-atom treatment	H-atom parameters constrained
Δ) _{max} , Δ) _{min} (e Å ⁻³)	2.26, -1.83

Table 1.S3. Crystallographic details for Ru₂(ap)₄(C₆H₄-4-N,N-(C₆H₄-4-OMe)₂) (2)

Ru ₂ (ap) ₄ (C ₆ H ₄ -4-N,N-(C ₆ H ₄ -4-OMe) ₂) (2)	
Crystal data	
Chemical formula	C ₆₄ H ₅₄ N ₉ O ₂ Ru ₂ ·1.267(C ₇ H ₈)
<i>M</i> _r	1300.39
Crystal system, space group	Triclinic, <i>P</i> $\bar{1}$
Temperature (K)	150
<i>a</i> , <i>b</i> , <i>c</i> (Å)	10.529 (2), 17.601 (5), 18.593 (5)
α , β , γ (°)	76.754 (10), 75.344 (5), 72.989 (6)
<i>V</i> (Å ³)	3142.6 (14)
<i>Z</i>	2
Radiation type	Mo <i>K</i> α
μ (mm ⁻¹)	0.54
Crystal size (mm)	0.20 × 0.20 × 0.02
Data collection	
Diffractometer	Bruker AXS D8 Quest CMOS diffractometer
Absorption correction	Multi-scan <i>SADABS</i> 2016/2: Krause, L., Herbst-Irmer, R., Sheldrick G.M. & Stalke D. (2015). <i>J. Appl. Cryst.</i> 48 3-10.
<i>T</i> _{min} , <i>T</i> _{max}	0.057, 0.093
No. of measured, independent and observed [<i>I</i> > 2 σ (<i>I</i>)] reflections	71434, 71434, 43599
<i>R</i> _{int}	?
(sin θ/λ) _{max} (Å ⁻¹)	0.610
Refinement	
<i>R</i> [<i>F</i> ² > 2 σ (<i>F</i> ²)], <i>wR</i> (<i>F</i> ²), <i>S</i>	0.085, 0.245, 1.04
No. of reflections	71434
No. of parameters	906
No. of restraints	561
H-atom treatment	H-atom parameters constrained
Δ) _{max} , Δ) _{min} (e Å ⁻³)	4.20, -1.99

Table 1.S4. Crystallographic details for Ru₂(ap)₄(C₆H₄-4-^tBu) (**3**)

Ru ₂ (ap) ₄ (C ₆ H ₄ -4- ^t Bu) (3)	
Crystal data	
Chemical formula	C ₅₄ H ₄₉ N ₈ Ru ₂ ·C ₄ H ₈ O
<i>M</i> _r	1084.25
Crystal system, space group	Triclinic, <i>P</i> $\bar{1}$
Temperature (K)	150
<i>a</i> , <i>b</i> , <i>c</i> (Å)	10.2618 (3), 16.2462 (5), 16.6654 (5)
α , β , γ (°)	105.6624 (8), 99.1061 (9), 107.7249 (8)
<i>V</i> (Å ³)	2459.08 (13)
<i>Z</i>	2
Radiation type	Cu <i>K</i> α
μ (mm ⁻¹)	5.36
Crystal size (mm)	0.2 × 0.2 × 0.2
Data collection	
Diffractometer	Bruker AXS D8 Quest CMOS diffractometer
Absorption correction	Multi-scan <i>SADABS</i> 2016/2: Krause, L., Herbst-Irmer, R., Sheldrick G.M. & Stalke D., <i>J. Appl. Cryst.</i> 48 (2015) 3-10
<i>T</i> _{min} , <i>T</i> _{max}	0.048, 0.179
No. of measured, independent and observed [<i>I</i> > 2 σ (<i>I</i>)] reflections	53010, 10546, 9293
<i>R</i> _{int}	0.053
(<i>sin</i> θ / λ) _{max} (Å ⁻¹)	0.641
Refinement	
<i>R</i> [<i>F</i> ² > 2 σ (<i>F</i> ²)], <i>wR</i> (<i>F</i> ²), <i>S</i>	0.049, 0.152, 1.20
No. of reflections	10546
No. of parameters	672
No. of restraints	166
H-atom treatment	H-atom parameters constrained
Δ _{max} , Δ _{min} (e Å ⁻³)	1.37, -1.00

Table 1.S5. Crystallographic details for Ru₂(ap)₄(Ph) (4)

Ru ₂ (ap) ₄ (Ph) (4)	
Crystal data	
Chemical formula	C ₅₀ H ₄₁ N ₈ Ru ₂ ·0.5(C ₆ H ₆)
<i>M</i> _r	995.10
Crystal system, space group	Monoclinic, <i>P</i> 2 ₁ / <i>c</i>
Temperature (K)	150
<i>a</i> , <i>b</i> , <i>c</i> (Å)	13.0307 (10), 18.9714 (15), 18.4273 (12)
β (°)	101.255 (2)
<i>V</i> (Å ³)	4467.8 (6)
<i>Z</i>	4
Radiation type	Mo <i>K</i> α
μ (mm ⁻¹)	0.72
Crystal size (mm)	0.22 × 0.14 × 0.12
Data collection	
Diffractometer	Bruker AXS D8 Quest CMOS diffractometer
Absorption correction	Multi-scan <i>SADABS</i> 2016/2: Krause, L., Herbst-Irmer, R., Sheldrick G.M. & Stalke D., <i>J. Appl. Cryst.</i> 48 (2015) 3-10
<i>T</i> _{min} , <i>T</i> _{max}	0.115, 0.164
No. of measured, independent and observed [<i>I</i> > 2σ(<i>I</i>)] reflections	114193, 11089, 8664
<i>R</i> _{int}	0.071
(sin θ/λ) _{max} (Å ⁻¹)	0.667
Refinement	
<i>R</i> [<i>F</i> ² > 2σ(<i>F</i> ²)], <i>wR</i> (<i>F</i> ²), <i>S</i>	0.065, 0.189, 1.02
No. of reflections	11089
No. of parameters	638
No. of restraints	234
H-atom treatment	H-atom parameters constrained
	$w = 1/[\sigma^2(F_o^2) + (0.099P)^2 + 15.994P]$ where $P = (F_o^2 + 2F_c^2)/3$
Δ _{max} , Δ _{min} (e Å ⁻³)	3.02, -1.55

Table 1.S6. Crystallographic details for Ru₂(ap)₄(C₆H₄-4-Br) (5)

Ru ₂ (ap) ₄ (C ₆ H ₄ -4-Br) (5)	
Crystal data	
Chemical formula	C ₅₀ H ₄₀ BrN ₈ Ru ₂
<i>M</i> _r	1034.95
Crystal system, space group	Monoclinic, <i>C2/c</i>
Temperature (K)	150
<i>a</i> , <i>b</i> , <i>c</i> (Å)	20.3051 (15), 15.0295 (9), 16.8602 (9)
β (°)	109.437 (2)
<i>V</i> (Å ³)	4852.1 (5)
<i>Z</i>	4
Radiation type	Mo <i>K</i> α
μ (mm ⁻¹)	1.49
Crystal size (mm)	0.60 × 0.25 × 0.25
Data collection	
Diffractometer	Bruker AXS D8 Quest CMOS diffractometer
Absorption correction	Multi-scan <i>SADABS</i> 2016/2: Krause, L., Herbst-Irmer, R., Sheldrick G.M. & Stalke D., <i>J. Appl. Cryst.</i> 48 (2015) 3-10
<i>T</i> _{min} , <i>T</i> _{max}	0.617, 0.747
No. of measured, independent and observed [<i>I</i> > 2σ(<i>I</i>)] reflections	69000, 4962, 4353
<i>R</i> _{int}	0.036
(sin θ/λ) _{max} (Å ⁻¹)	0.625
Refinement	
<i>R</i> [<i>F</i> ² > 2σ(<i>F</i> ²)], <i>wR</i> (<i>F</i> ²), <i>S</i>	0.027, 0.071, 1.13
No. of reflections	4962
No. of parameters	308
No. of restraints	46
H-atom treatment	H-atom parameters constrained
	$w = 1/[\sigma^2(F_o^2) + (0.0265P)^2 + 12.3942P]$ where $P = (F_o^2 + 2F_c^2)/3$
Δ _{max} , Δ _{min} (e Å ⁻³)	1.38, -0.85

Table 1.S7. Crystallographic details for Ru₂(ap)₄(C₆H₄-4-CF₃) (6)

Ru ₂ (ap) ₄ (C ₆ H ₄ -4-CF ₃) (6)	
Crystal data	
Chemical formula	C ₅₀ H ₄₀ BrN ₈ Ru ₂
<i>M</i> _r	1034.95
Crystal system, space group	Monoclinic, <i>C2/c</i>
Temperature (K)	150
<i>a</i> , <i>b</i> , <i>c</i> (Å)	20.3051 (15), 15.0295 (9), 16.8602 (9)
β (°)	109.437 (2)
<i>V</i> (Å ³)	4852.1 (5)
<i>Z</i>	4
Radiation type	Mo <i>K</i> α
μ (mm ⁻¹)	1.49
Crystal size (mm)	0.60 × 0.25 × 0.25
Data collection	
Diffractometer	Bruker AXS D8 Quest CMOS diffractometer
Absorption correction	Multi-scan <i>SADABS</i> 2016/2: Krause, L., Herbst-Irmer, R., Sheldrick G.M. & Stalke D., <i>J. Appl. Cryst.</i> 48 (2015) 3-10
<i>T</i> _{min} , <i>T</i> _{max}	0.617, 0.747
No. of measured, independent and observed [<i>I</i> > 2σ(<i>I</i>)] reflections	69000, 4962, 4353
<i>R</i> _{int}	0.036
(sin θ/λ) _{max} (Å ⁻¹)	0.625
Refinement	
<i>R</i> [<i>F</i> ² > 2σ(<i>F</i> ²)], <i>wR</i> (<i>F</i> ²), <i>S</i>	0.027, 0.071, 1.13
No. of reflections	4962
No. of parameters	308
No. of restraints	46
H-atom treatment	H-atom parameters constrained
	$w = 1/[\sigma^2(F_o^2) + (0.0265P)^2 + 12.3942P]$ where $P = (F_o^2 + 2F_c^2)/3$
Δ _{max} , Δ _{min} (e Å ⁻³)	1.38, -0.85

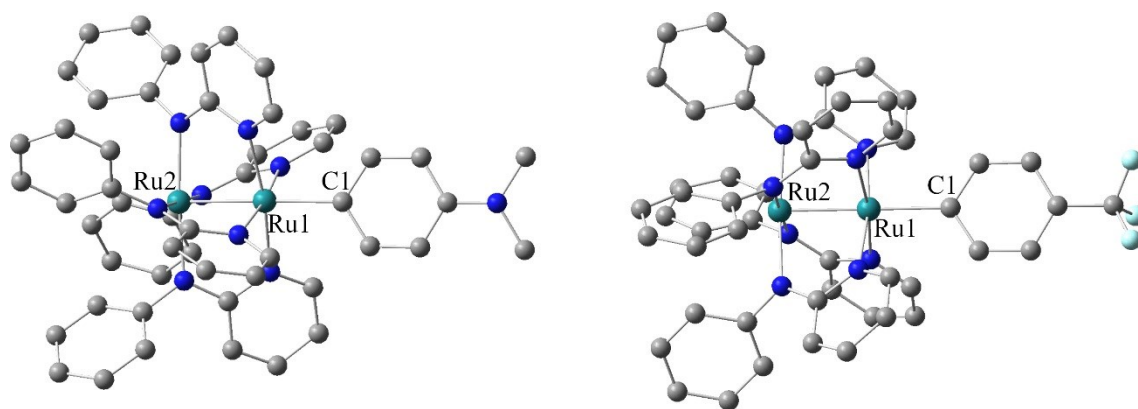


Figure 1.S6. DFT optimized structures **1'** (left) and **6'** (right).

Table 1.S8. Comparison of selected geometric parameters of **1**, **1'**, **6** and **6'**.

Bond metric	1 (crystal)	1' (DFT)	6 (crystal)	6' (DFT)
Ru1–Ru2 (Å)	2.3347(7)	2.3955	2.3373(5)	2.3918
Ru1–C1 (Å)	2.214(3)	2.1736	2.22(1)	2.1905
Ru2–Ru1–C1 (°)	179.3(1)	178.64	177.9(3)	179.90

CHAPTER 2. BISARYL COMPLEXES OF DIRUTHENIUM(III,III)

Reprinted (adapted) with permission from Raghavan, A., Ren, T., *Organometallics*, **2019**, *38*, 3888–3896. Copyright 2019, American Chemical Society.

2.1 Abstract

Aryls (Ar^-) fall into a class of both σ - and π - donating electron-rich ligands that is underexplored as such in the field of metal-metal bonding. Herein is described the isolation of bisaryl diruthenium(III) paddlewheel complexes, enabled by a decrease in the steric bulk around the diruthenium axial sites and an increase in the basicity of the bridging equatorial ligands. Compounds of the form $\text{Ru}_2(\text{dmba})_4\text{Ar}_2$ ($\text{dmba} = N,N'$ -dimethylbenzamidinate, $\text{Ar} = \text{C}_6\text{H}_4$ -4- t Bu (**7**), Ph (**8**) or C_6H_3 -3,5-(OCH_3)₂ (**9**)) were synthesized *via* a lithium-halogen exchange reaction between $\text{Ru}_2(\text{dmba})_4\text{Cl}_2$ and excess LiAr , and characterized using ESI-MS, electronic absorption spectroscopy, cyclic and differential pulse voltammetry and ^1H NMR spectroscopy. The molecular structures of compounds **7–9** were established using single-crystal XRD analysis and their electronic structures (both ground and excited state) analyzed using DFT calculations.

2.2 Introduction

The discovery of $\text{Ru}_2(\text{ap})_4(\text{C}\equiv\text{CPh})$ by Cotton and Chakravarty⁴ has inspired extensive investigation of the organometallic chemistry of di- and triruthenium paddlewheel complexes bearing axial mono- and bisalkynyls,^{7,55–60} and their potential applications as molecular wires in electronic devices have been explored by our laboratory.^{9–11,61} Besides Ru_2 -alkynyls, other aspects of di- and tri-ruthenium compounds vigorously pursued in recent years include C–H activation,⁶² aerobic and peroxy oxidation catalysis,^{63–65} magnetism,^{66,67} and devices based on metal-strings.^{68,69} Compared to alkynyls, aryls can be classified as σ - and π -donating ligands with a stronger electron-donating ability that may lead to Ru_2 compounds with frontier orbitals energetically distinctive from those based of Ru_2 alkynyl compounds. In this context $\text{M}_2\text{L}_4(\text{aryl})_n$ compounds, whose chemistry remains largely unexplored, are intriguing targets. Currently, there are very few examples of bimetallic aryl complexes either derived from and/or containing a paddlewheel motif (Scheme 1.1, Chapter 1).

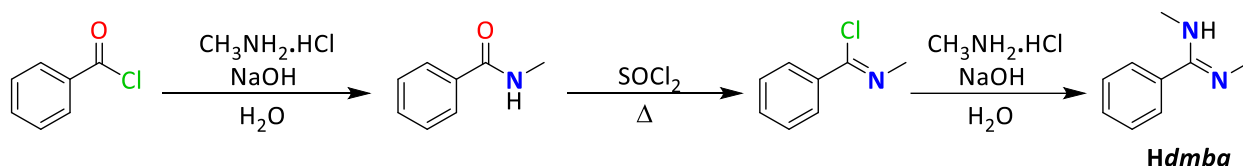
Of particular import is the example of a bis(phenyl) dirhodium(III) paddlewheel complex formed by oxidative arylation of a Rh₂(II,III) species (Scheme 1.1, **C1**).¹⁴ This was the very first example of an unambiguously characterized Rh₂⁶⁺ species in the literature. Since then, the Doyle group has investigated other bisaryl complexes of the form the Rh₂(L)₄(Ar¹)(Ar²) formed in the presence of the corresponding aryl boronic acids (Scheme 1.1, **C2**).^{17–19} Compounds like these present very interesting molecular and electronic structures; the cleavage of the Rh–Rh bond as a result of a drastic change in the electronic structure of the Rh₂ core to $\pi^4\delta^2\pi^*4\delta^*2$ is a particularly noteworthy feature. Spectroscopic evidence suggested the existence of significant π -interactions between the aryl ring and the HOMO–LUMO manifold of the dirhodium core. Even in the absence of an M–M bond, it was found that in the case of unsymmetrical bisaryl dirhodium species such as **C2**, there is electronic communication between the two rhodium centers through the paddlewheel ligand. Such intricate electronic structure properties are important to study, in order to better understand the properties of M–M bonding in general.

In this context, the first examples of diruthenium(II,III) paddlewheel monoaryls prepared by metathesis with aryllithiums were discussed (compounds **1–6**, Chapter 1). These compounds are remarkably stable under ambient conditions and exhibit rich electrochemical properties by supporting up to four reversible oxidations and one reversible reduction. This electron-richness and extended conjugation across the Ru₂ core and aryl ligand prompted us to attempt the isolation of diruthenium aryls in higher oxidation states, and to expand their chemistry to include bisaryl species. In order to isolate bisaryls, the relatively uncommon Ru₂(III,III) oxidation state needs to be accessed. Starting from Ru₂(*ap*)₄Cl, while it is possible to synthesize both Ru₂(II,III) and Ru₂(III,III) mono- and bisalkynyl species,^{70,71} the steric repulsion between the aryl moiety and the flanking Ph groups of the *ap* ligand precludes the formation of Ru₂(*ap*)₄Ar₂-type bisaryl compounds. The ideal bridging ligand for this purpose must provide both a viable Ru₂(III,III) starting point and a sterically less demanding axial coordination site. Out of the few structurally characterized examples of Ru₂^{III,III}L₄X₂-type compounds that exist in the literature, only a small subset of L-type ligands satisfy the above requirements.² Keeping these considerations in mind, the highly basic and sterically accommodating bidentate ligand *dmba* was chosen. Our laboratory has successfully handled [Ru₂(*dmba*)₄]²⁺ chemistry with a variety of axial ligands. In this chapter, the synthesis and characterization of three new bisaryl diruthenium complexes of the formula Ru₂(*dmba*)₄Ar₂ (Ar = C₆H₄-4-*t*Bu, **7**; Ph, **8**; C₆H₃-3,5-(OCH₃)₂, **9**) are presented.

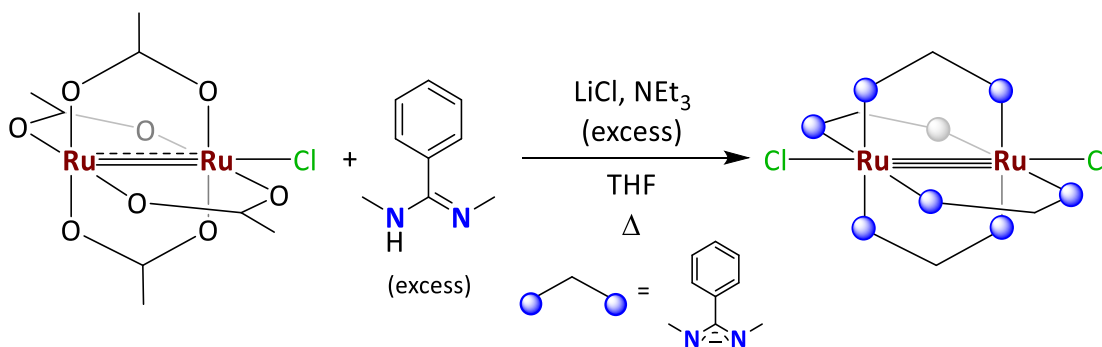
2.3 Results and Discussion

2.3.1 Synthesis

The synthesis of *Hdmba* (N,N'-dimethylbenzamidine) was accomplished in three steps as outlined in Scheme 2.1, and the Ru₂(III,III) starting material, Ru₂(*dmba*)₄Cl₂, was prepared from the reaction between Ru₂(OAc)₄Cl, *Hdmba*, a weak base (NEt₃) and LiCl according to Scheme 2.2.

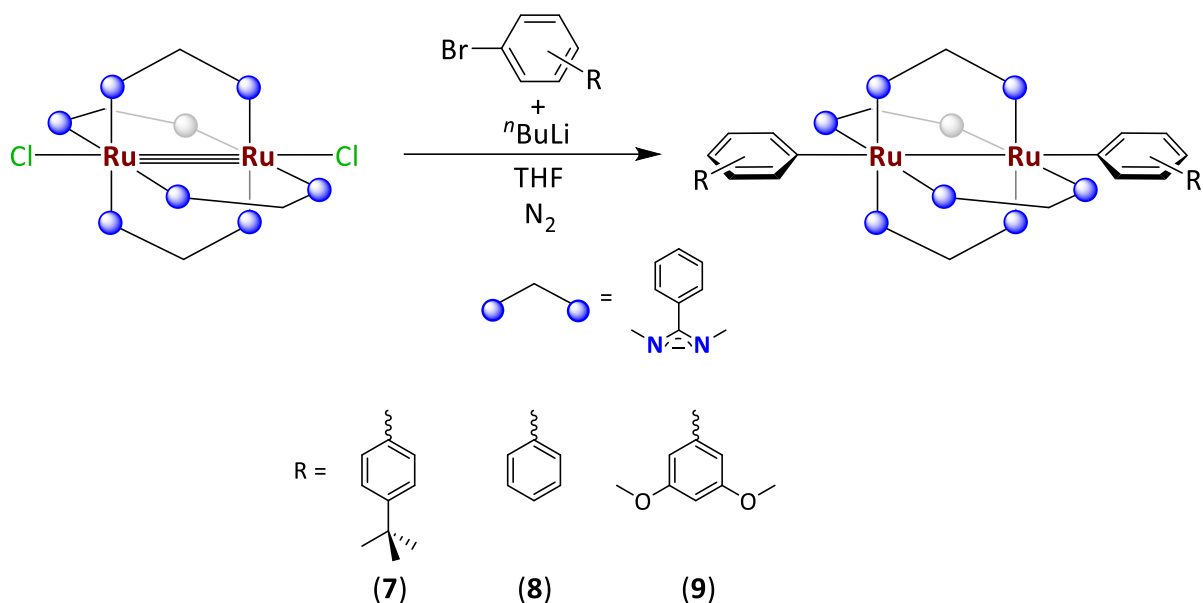


Scheme 2.1. Synthesis of N,N'-dimethylbenzamidine (*Hdmba*)



Scheme 2.2. Synthesis of Ru₂(*dmba*)₄Cl₂

The facile preparation of Ru₂(*dmba*)₄(C₂R)₂ from Ru₂(*dmba*)₄Cl₂ prompted us to attempt the synthesis of Ru₂(*dmba*)₄(Ar)₂ under conditions similar to those for Ru₂(*ap*)₄Ar. The reactions between LiAr and Ru₂(*dmba*)₄Cl₂ (Scheme 2.3) were accompanied by a rapid color change from brown to deep red. The consumption of Ru₂ starting material was confirmed by thin-layer chromatography (TLC) and ESI-MS. Purification of compounds **7–9** was done by filtration of the reaction mixture through a triethylamine-deactivated silica plug, elution of a red-orange band, followed by recrystallization and washing with cold methanol and hexanes.



Scheme 2.3. Synthesis of $\text{Ru}_2(\text{dmba})_4\text{Ar}_2$

The isolated compounds **7–9** are stable in both solution and solid state under ambient conditions. Like their bis(alkynyl) counterparts, $\text{Ru}_2(\text{dmba})_4\text{Ar}_2$ compounds have a singlet ground state and thus exhibit ^1H NMR spectra in the normal diamagnetic window. Further characterization was done using ESI-MS, UV-Vis/NIR absorption spectroscopy, cyclic and differential pulse voltammetry, DFT calculations, and single-crystal XRD analysis.

2.3.2 Molecular Structures

Single-crystal XRD analysis established the molecular structures of all three compounds; selected bond lengths are listed in Table 2.1 and the structures are plotted in Figures 2.1–2.3. All three compounds crystallize in the $\text{P}\bar{1}$ space group, and each of the individual molecules has an inversion center at the mid-point of the Ru–Ru bond. The average Ru–Ru bond distance in **7–9** is 2.4989[6] Å, significantly longer than that found in $\text{Ru}_2(\text{dmba})_4\text{Cl}_2$ (Ru–Ru = 2.3228(6) Å). The much stronger σ -donating Ar^- ligands engage the Ru d_z^2 orbitals to form strong Ru–C σ bonds, forcing a change in electronic configuration from $\sigma^2\pi^4\delta^2(\pi^*)^2$ to $\pi^4\delta^2(\pi^*)^4$ that is supported by the diamagnetism of **7–9**. The absence of a formal σ bond between the metal centers has also been noted by Chisholm and co-workers for bisalkyl ditungsten and dimolybdenum paddlewheel

complexes of the form $M_2(O_2CR')_4R_2$. These formally d^3-d^3 systems bearing M–M triple bonds have the electronic configuration of $\pi^4\delta^2$.⁷²

Indeed, Ru–Ru bond lengths found here are comparable to $Ru_2(dmba)_4(C\equiv CR)_2$ species (ave. 2.45 Å) with the same electronic configuration.^{73,74} This effect is also seen in the significant shortening of the Ru–C bond in compounds **7–9** (ave. 2.071[4] Å) in comparison to those in $Ru_2(ap)_4Ar$ species (ave. 2.21 Å, Chapter 1). The Ru–C(sp^2) bond lengths here are slightly longer than the corresponding Ru–C(sp) bond lengths in $Ru_2(dmba)_4(C\equiv CR)_2$ compounds (ave. 1.97 Å). The argument here is the same provided for the pairs of $Rh_2(ap)_4(C\equiv CH)$ vs. $Rh_2(ap)_4(Ph)$ ²⁰ and $Ru_2(ap)_4(C\equiv CR)$ vs. $Ru_2(ap)_4(Ar)$: (i) ipso carbon hybridization change from sp to sp^2 is accompanied by expansion of $r_{\text{covalent, ipso-C}}$ from 69 pm to 73 pm,²³ and (ii) increase in steric bulk at the axial site. Despite being electronically distinct, the 4-^tBu and 3,5-(OCH₃)₂ substituents do not significantly influence either the Ru–Ru or the Ru–C bond lengths because the aryl ligand π -orbitals are involved in neither the net single δ bond, nor the Ru–C σ bonds.

Table 2.1. Selected Bond Lengths (Å) and Angles (deg) for Compounds **7–9**.

	7	8	9
Ru1–Ru2	2.5099(5)	2.4940(3)	2.4928(3)
Ru1–C1	2.078(4)	2.068(1)	2.068(1)
Ru2–Ru1–C1	153.6(1)	152.42(3)	151.23(4)
Ru1–N1	1.99(2)	2.018(1)	2.096(1)
Ru1–N3	2.109(6)	2.0227(9)	2.020(1)
Ru2–N2	2.100(7)	2.1072(9)	2.018(1)
Ru2–N4	2.04(2)	2.1161(8)	2.099(1)

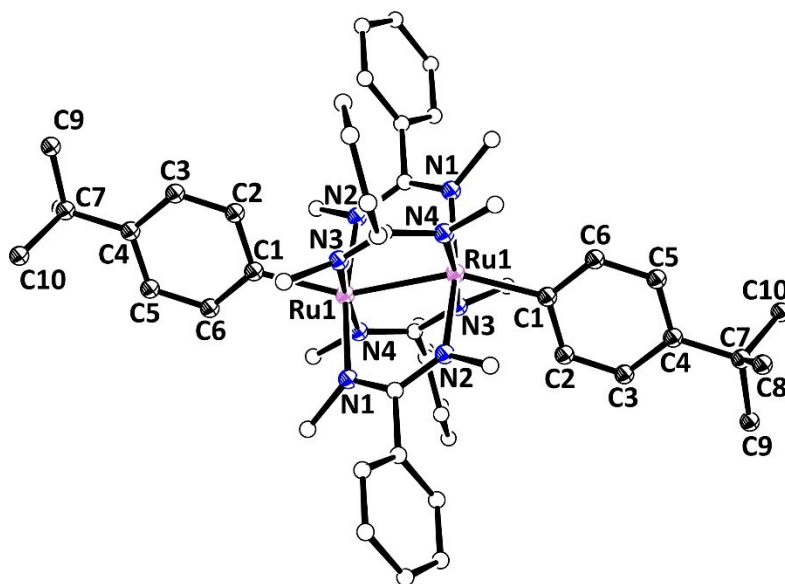


Figure 2.1. Structural plot of **7** at the 30% probability level. One of the two disordered moieties (A) present in the asymmetric unit was selected. Hydrogens are omitted for clarity.

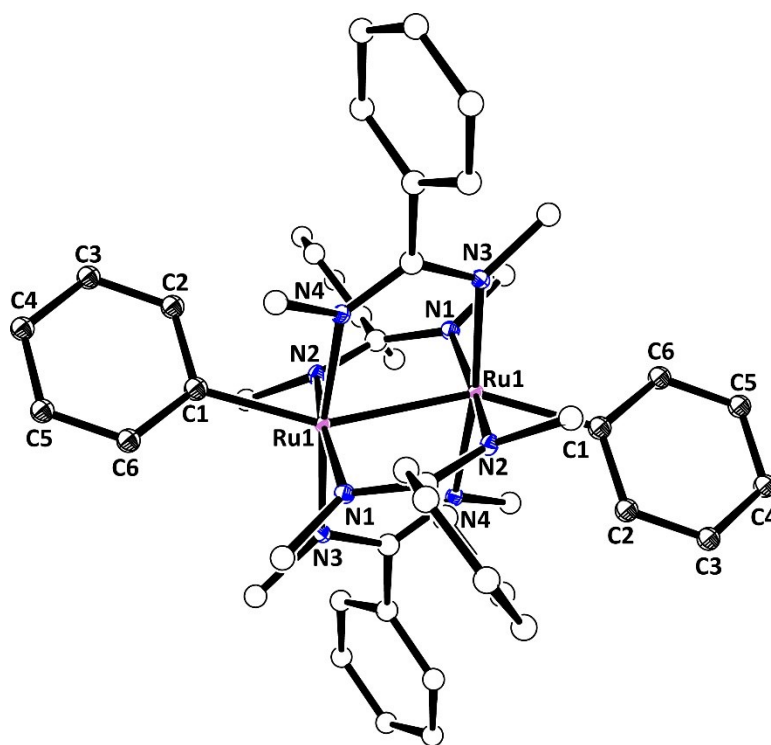


Figure 2.2. Structural plot of **8** at the 30% probability level. Hydrogens are omitted for clarity.

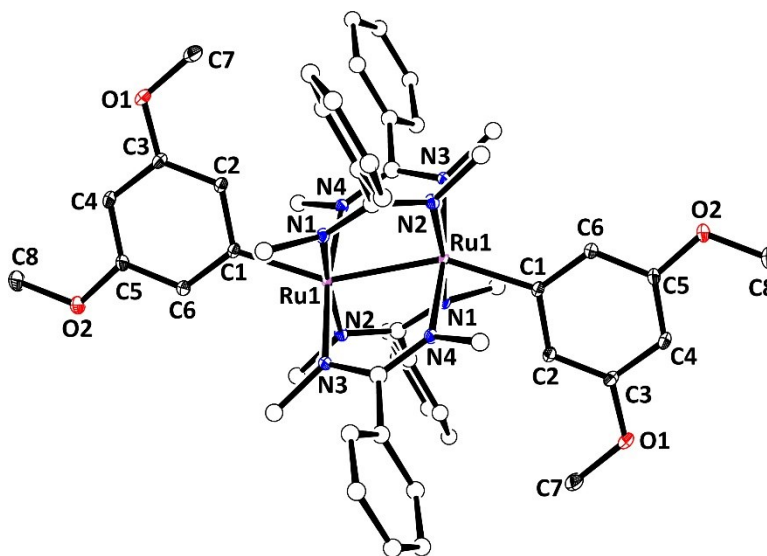


Figure 2.3. Structural plot of **9** at the 30% probability level. Solvent molecules and hydrogens are omitted for clarity.

Compounds **7–9** (Figures 2.1–2.3) exhibit a significant distortion from an octahedral geometry at both ruthenium centers. This is reflected in the disparity in Ru–N/Ru'–N' bond lengths, Ru–Ru–N/Ru–Ru–N' bond angles, and from the fact that C–Ru–Ru bond angles are significantly lesser than the ideal 180° (Figure 2.4). This overall distortion is attributed to a second-order Jahn–Teller (SOJT) effect, which has been documented and analyzed using a Fenske–Hall type MO analysis for the $\text{Ru}_2(\text{DArF})_4(\text{C}_2\text{Ph})_2$ series (DArF = diarylformamidinate)⁷⁵ and subsequently observed in many $\text{Ru}_2^{\text{III,III}}\text{L}_4\text{X}_2$ -type complexes.⁷ It should be noted that SOJT is probably more common than usually perceived because of its subtlety. Power and coworkers have noted pronounced SOJT effects in multiply bonded main group compounds and elaborated it in an excellent account.⁷⁶

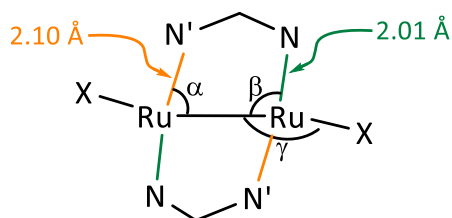


Figure 2.4. Distorted coordination geometry in **7–9**. $\alpha_{\text{ave}} \approx 79.7^\circ$, $\beta_{\text{ave}} \approx 95.2^\circ$, $\gamma_{\text{ave}} \approx 152^\circ$.

The extent of structural distortion depends on the nature of the axial substituents. This is For example, the value of γ in $\text{Ru}_2(\text{dmba})_4\text{X}_2$ species where X is Cl^- , NO_3^- or BF_4^- is *ca.* 180° .⁷⁷ If X is $^-\text{C}\equiv\text{CR}$, γ ranges from 161° – 175° ^{73,74} and if X is Ar^- (compounds **7–9**), $\gamma \approx 152^\circ$. Structural distortion in $\text{Ru}_2^{\text{III,III}}\text{L}_4(\text{C}\equiv\text{CR})_2$ complexes has been previously analyzed using DFT calculations,⁷⁸ and the results are transferrable here with the major difference being the higher dimensionality of aryl compared to alkynyl. Going from a one-dimensional alkynyl to a two-dimensional aryl lowers the symmetry of the molecule from D_{4h} to D_{2h} . From an orbital perspective, the two π^* orbitals are no longer degenerate – one is a combination of the π -system of aryl and $[\text{Ru}_2(\text{dmba})_4]$ whereas the other is purely $[\text{Ru}_2(\text{dmba})_4]$ -based. In model compounds $\text{Ru}_2(\text{NHCHNH})_4(\text{C}\equiv\text{CH})_2$, lowering the symmetry from D_4 to C_2 is accompanied by a significant stabilization of the $\pi^*(xz)$ orbital while the $\pi^*(yz)$ is more or less unaffected – an effect of HOMO–LUMO mixing. Consequently, the HOMO–LUMO gap is increased and the overall molecular structure is stabilized. A similar effect is seen for **7–9**, but to a greater extent presumably because the two $\pi^*(\text{Ru}_2)$ orbitals are inherently non-degenerate.

2.3.3 Electrochemistry

Cyclic and differential pulse voltammetric analyses were carried out for compounds **7–9** in CH_2Cl_2 , and three redox events were observed for each of them, namely two oxidations and one reduction (Figure 2.5 and Table 2.2). For all three compounds, the first oxidation (**B**, $\text{Ru}_2^{7+/6+}$) is a reversible one-electron event that occurs between -0.41 and -0.54 V (all potentials are reported against $\text{Fc}^{+/0}$), while the second oxidation (**C**), is an irreversible one-electron event that occurs between 0.57 and 0.66 V. Unlike more electron-rich aryls such as $\text{C}_6\text{H}_4\text{-4-NR}_2$, those of compounds **7–9** are not necessarily suited to stabilize a cationic charge upon oxidation. Thus, the irreversible nature of **C** suggests that it might be aryl ligand-based. The only reduction event observed for all three compounds (**A**, $\text{Ru}_2^{6+/5+}$) is initially quasi-reversible but becomes irreversible upon repeated scans. Quasi-reversibility is restored upon polishing the working electrode between scans. Such a behavior suggests dissociation of the axial aryls or of the *dmba* ligands.

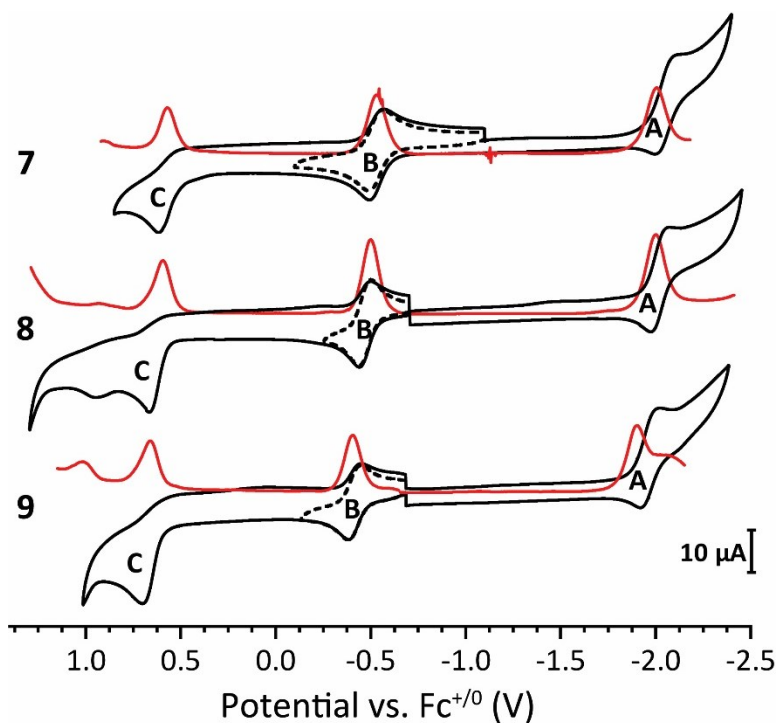


Figure 2.5. Cyclic (black) and differential pulse (gray) voltammograms of compounds **7–9** (1.0 mM) recorded in 0.10 M $n\text{Bu}_4\text{NPF}_6$ in CH_2Cl_2 at a scan rate of 0.10 V/s.

Table 2.2. Electrode Potentials (V, vs. $\text{Fc}^{+/0}$) for $\text{Ru}_2(\text{dmba})_4\text{X}_2$.

X	$E_{1/2}$ (A)	$E_{1/2}$ (B)	E_{pa} (C) ^a
$\text{C}_6\text{H}_4\text{-4-}'\text{Bu}$ (7)	-2.05	-0.53	0.61
C_6H_5 (8)	-2.02	-0.47	0.66
$\text{C}_6\text{H}_3\text{-3,5-}(\text{OCH}_3)_2$ (9)	-1.97	-0.42	0.69
$\text{C}\equiv\text{CPh}$	-1.67	-0.056	-
Cl	-0.89	0.49	-

^a Irreversible couple.

Aryls are much stronger electron donors than alkynyls, and this is reflected in the *ca.* 0.44 V cathodic shift of the reduction potential of event **B** ($\text{Ru}_2^{7+/6+}$) upon going from $\text{Ru}_2(\text{dmba})_4(\text{C}\equiv\text{CPh})_2$ to $\text{Ru}_2(\text{dmba})_4(\text{Ph})_2$. This ability of compounds **7–9** to undergo oxidation at low potentials is noteworthy. While compounds **8** and **9** are stable as $\text{Ru}_2(\text{III,III})$ complexes under ambient conditions, **7** was isolated with a minor paramagnetic impurity. This is seen from the fact that the ^1H NMR peaks (in CDCl_3) of **8** and **9** are sharp and well-defined, whereas those of **7** are

ill-defined and slightly broadened (Figures 2.S5–2.S7). In order to obtain a clean diamagnetic spectrum of **7**, a slight excess of NaBH₄ was added to the NMR tube (Fig. 2.S5b). Thus, even a weakly electron-donating substituent such as *p*-^tBu can result in the facile oxidation of Ru₂^{III,III}(*dmba*)₄(Ar)₂ to [Ru₂^{III,IV}(*dmba*)₄(Ar)₂]⁺. This is an interesting point to consider in terms of ligand design for the isolation of stable Ru₂(III,IV) complexes.

2.3.4 Electronic Absorption Spectroscopy.

Figure 2.6 shows the Vis-NIR absorption spectra of compounds **7–9** in THF. The most intense transitions occur at 390 nm and 490 nm for all three complexes – the latter being the color-producing band, since they all appear to take on a similar shade of red in solution. The spectroscopic features seen here are reminiscent of Ru₂(*dmba*)₄(C≡CR)₂ complexes with a few differences.

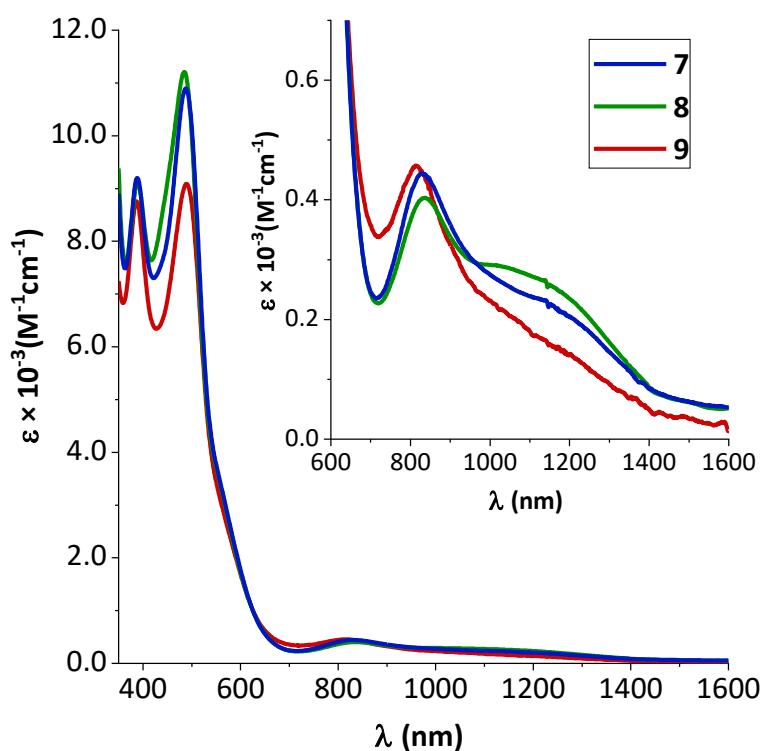


Figure 2.6. Vis–NIR spectra of compounds **7–9** in THF.

The two weakly absorbing transitions seen above 800 nm for compounds **7–9** are different from the one intense absorption at *ca.* 860 nm for $\text{Ru}_2(\text{dmba})_4(\text{C}\equiv\text{CR})_2$ species, which can be explained by the loss of degeneracy of the frontier $\pi^*(\text{Ru}_2)$ orbitals resulting from the two-dimensional aryl ligands. One of the *d* orbitals (d_{xz} or d_{yz}) is perpendicular to the plane of Ar^- while the other is coplanar, and consequently, not affected by it. The lowest energy absorption at *ca.* 1100 nm likely belongs to the HOMO (π^*) \rightarrow LUMO (δ^*) transition as is evident from the slight blueshift upon going from compound **7** to **9**, i.e. from electron-donating 4-*t*Bu to electron-withdrawing 3,5-(OCH₃)₂. The low intensity of the peaks suggests that they are mainly metal-based, and that the dependence on the aryl ligand is likely due to inductive effects. In contrast, the intensity of the absorptions at *ca.* 490 nm, 390 nm, and to a certain extent, the shoulder peak at *ca.* 570 nm suggest that some sort of charge transfer process is at play, either metal-to-ligand (MLCT) or ligand-to-metal (LMCT). To better characterize the nature of these electronic transitions, time-dependent DFT (TD-DFT) calculations were performed on compound **8**, the results of which are discussed below.

2.3.5 Density Functional Theory Calculations.

To understand the ground state electronic structure of these complexes, the molecular orbitals of $\text{Ru}_2(\text{dmba})_4\text{Ph}_2$ were computed using spin-restricted DFT. The optimized geometry **8'** was based on the crystal structure of compound **8**. Figure 2.7 shows the frontier MOs of **8'** based on calculations done using the B3LYP^{35–38} functional, with the def2-TZVP/def2-SVP basis sets,^{79,80} including Grimme's dispersion correction (D3).⁸¹ The optimized geometric parameters agree with the crystallographically determined structure of **8**. Details of the computational methods are provided in section 2.6 (Supporting Information).

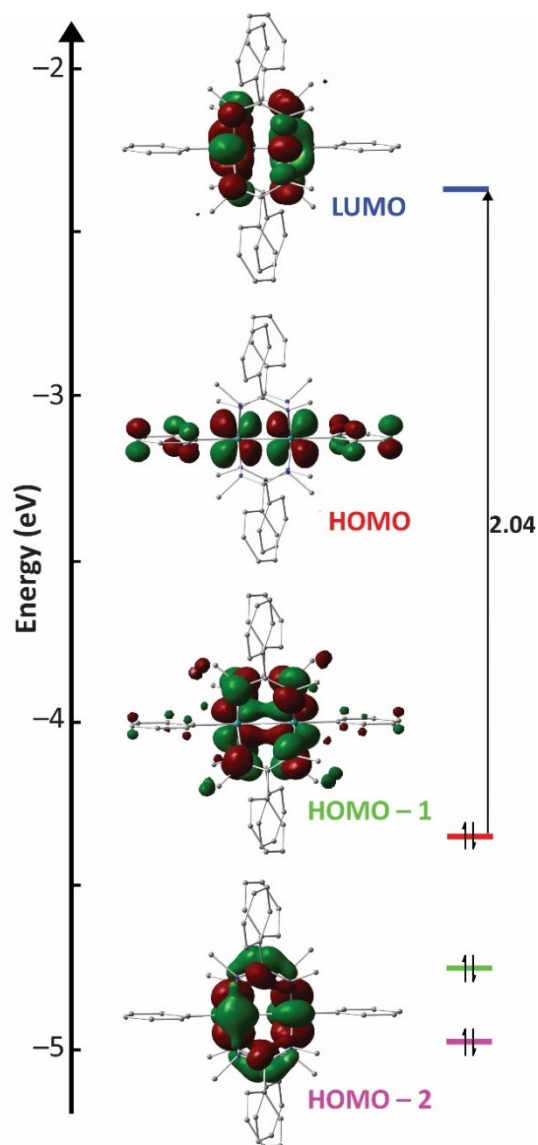


Figure 2.7. Frontier MO diagram of **8'** obtained from DFT calculations; $|\text{isovalue}| = 0.03$.

As expected, the HOMO is a $\pi^*(\text{Ru}_2/\text{Ar})$ orbital with contributions from both the diruthenium core and the aryl ligand, whereas the LUMO is a $\delta^*(\text{Ru}_2)$ orbital with additional contribution from the nonbonding $\pi(\text{N}-\text{C}-\text{N})$ of the *dmba* ligands. Consistent with the energy lowering of one of the two π^* orbitals due to SOJT effects discussed above, and with the fact that aryls are good π -donor ligands, HOMO - 1 lacks π^* character; in its place is the high-lying $\pi(\text{Ru}_2/\text{Ar})$ orbital. HOMO - 2 is the familiar $\delta(\text{Ru}_2)/\pi(\text{Ru}-\text{N})$ orbital, devoid of any contribution from the axial ligand. Hence, across the series **7-9** the δ - δ^* gap is expected to remain invariant.

The effect of the large deviation from linearity of the Ru–Ru–C bond on the electronic structure is readily seen from the HOMO – 4 orbital (Figure 2.8), a $\pi^*(\text{Ru–Ru})$ orbital that has gained some σ -bonding character. As mentioned previously, this phenomenon has been observed with the model compound $\text{Ru}_2(\text{NHCHNH})_4(\text{C}\equiv\text{CH})_2$.⁷⁸ Thus, while the overall ground state d -electron configuration for Ru_2 can be simplified as $\pi^4\delta^2(\pi^*)^4$, the actual ordering of the MOs is certainly more complex, namely $(\pi^*+\sigma)^2\pi^2\delta^2\pi^2(\pi^*)^2$.

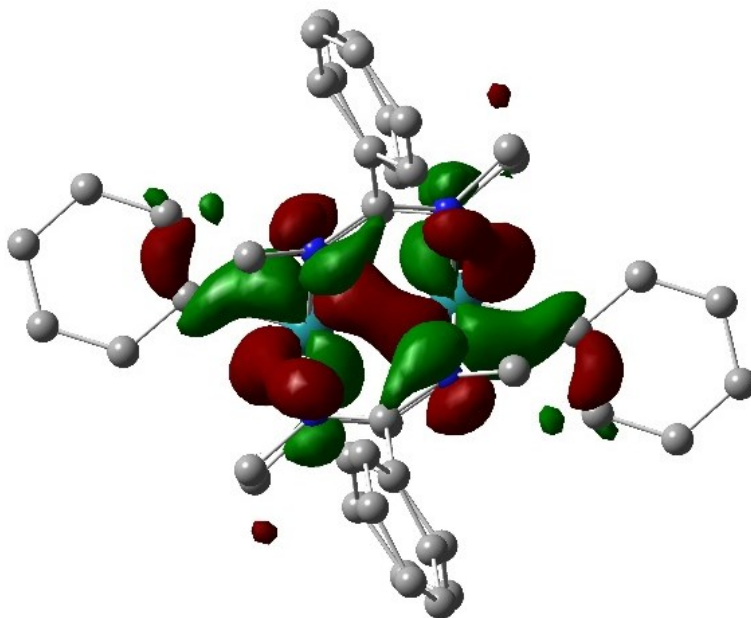


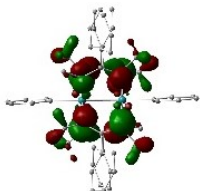
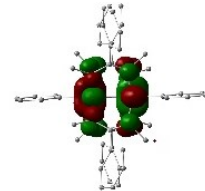
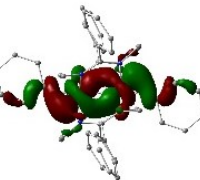
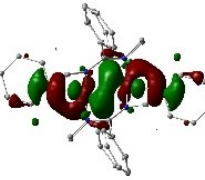
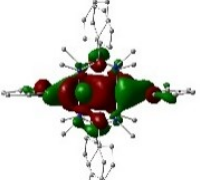
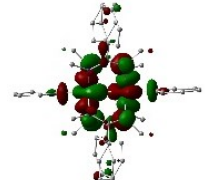
Figure 2.8. HOMO – 4 for the optimized structure **8'**; a $\pi^*(\text{Ru–Ru})$ orbital with σ -bonding character.

In addition to ground state calculations, TD-DFT analysis was carried out on the optimized structure **8'** in order to better understand the nature of its electronic excited states. Table 2.S3 (section 2.6) lists the most significant transitions calculated by TD-DFT and Table 2.3 below depicts the MO diagrams of the natural transition orbitals⁸² (NTOs) calculated based on each of the excited states. Figure 2.9 shows the deconvoluted electronic absorption spectrum of **8** in THF and Figure 2.S4 shows the absorption spectrum of **8'** simulated from TD-DFT results.

Table 2.3. Natural transition orbitals derived from TD-DFT calculations. Transitions are noted as NTO1 \rightarrow NTO2.

Excited state	$\bar{\nu}$ (cm ⁻¹)	NTO1	NTO2
1	6331.45		
4	12958.87		
6	17858.87 (major)		
6	17858.87 (minor)		
7	20500.80 (major)		
7	20500.80 (minor)		
9	21390.32		
10	21892.74 (major)		

Table 2.3 continued

10	21892.74 (minor)		
18	27436.29 (major)		
18	27436.29 (minor)		

While quantitative differences between experiment and theory do exist, TD-DFT is indeed able to qualitatively illustrate the natures of the most important absorptions seen in the Vis-NIR spectrum of **8**. The two low-intensity peaks below 13000 cm^{-1} are both expected to be $d-d$ transitions with minor contributions from both the axial and equatorial ligand. Accordingly, TD-DFT predicts the lowest energy absorption feature observed at *ca.* 8700 cm^{-1} to belong to the HOMO \rightarrow LUMO transition ($\pi^*(\text{Ru}_2/\text{Ar}) \rightarrow \delta^*(\text{Ru}_2)/p(\text{N})$). The second low-intensity peak calculated at *ca.* 13000 cm^{-1} also agrees with the measured value of *ca.* 12000 cm^{-1} and is predicted to be $\pi^*(\text{Ru}_2) \rightarrow \delta^*(\text{Ru}_2)/p(\text{N})$ in nature. This $\pi^*(\text{Ru}_2)$ orbital is coplanar with the aryl ligand and hence unaffected by its π -system. Thus, while the transition at 8700 cm^{-1} is dependent on the nature of the axial substituent, as can be seen from Figure 2.6, the latter peak is invariant at *ca.* 12000 cm^{-1} . The shoulder peak that appears at *ca.* 18000 cm^{-1} agrees well with the predicted value of 17858 cm^{-1} . NTO analysis reveals that this transition has two components, namely $\delta(\text{Ru}_2)/\pi(\text{NCN}) \rightarrow \delta^*(\text{Ru}_2)/p(\text{N})$ (major) and $\pi(\text{Ru}_2) \rightarrow \sigma^*(\text{Ru}-\text{C})$ (minor).

The most intense absorption features observed between 19000 cm^{-1} and 27000 cm^{-1} can be deconvoluted into four peaks of comparable intensities (Figure 2.9). Qualitatively, four similar transitions of comparable oscillator strengths are indeed predicted by TD-DFT, which can be grouped into two categories. The first category consists of the experimentally observed (and calculated by Gaussian deconvolution) peaks at 20264, 21649 and 23145 cm^{-1} . These are in good agreement with the predicted transitions at 20500, 21390 and 21890 cm^{-1} respectively. NTO

analysis suggests that the two major contributors for this category are ligand-to-metal charge transfer $p(\text{N}) \rightarrow \delta^*(\text{Ru}_2)$ and $\pi(\text{Ru}_2) \rightarrow \sigma^*(\text{Ru}-\text{C})$. The second category contains the fourth transition measured at 25560 cm^{-1} , the predicted value for which is *ca.* 27400 cm^{-1} . The major contribution for this peak is predicted to come from a $\pi(\text{Ru}_2) \rightarrow \sigma^*(\text{Ru}-\text{C})$ transition, both of which have metal (major) and aryl ligand (minor) characters.

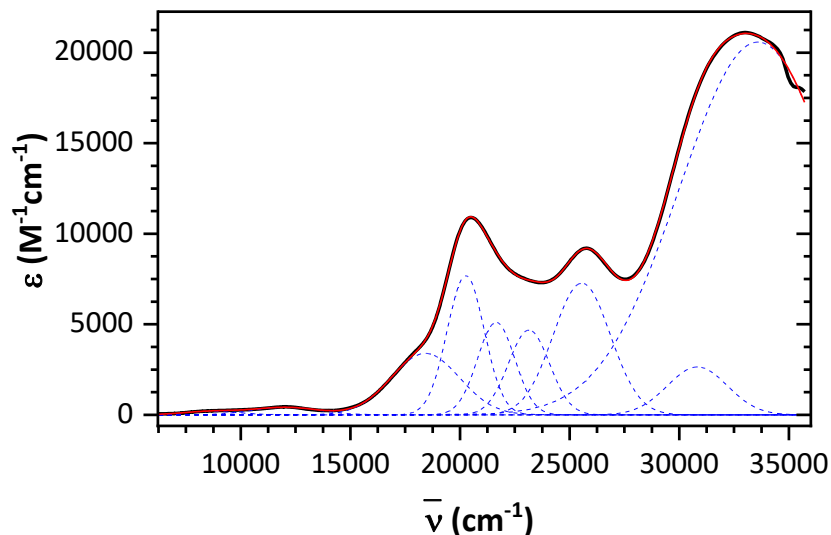


Figure 2.9. Experimental curve (black), fit peaks (blue, dashed) and cumulative fit curve (red) obtained from Gaussian deconvolution of the electronic absorption spectrum of **8** in THF.

2.4 Conclusion

In summary, the isolation of the first examples of M_2 bisaryl paddlewheel complexes with intact $\text{M}-\text{M}$ bonds has been described here. The strong σ -donating ability of the aryl ligands force a change in electronic configuration from $\sigma^2\pi^4\delta^2(\pi^*)^2$ ($S = 1$) in $\text{Ru}_2(\text{dmba})_4\text{Cl}_2$ to “ $\pi^4\delta^2(\pi^*)^4$ ” ($S = 0$) in $\text{Ru}_2(\text{dmba})_4\text{Ar}_2$ (compounds **7–9**), while their strong π -donating ability is evident from both electronic absorption spectroscopy and DFT calculations. The superior electron-donating ability of the aryls as compared to alkynyls is evident from the *ca.* 400–500 mV cathodic shift of $E(\text{Ru}_2^{+7/+6})$, the first oxidation potential, from $\text{Ru}_2(\text{dmba})_4(\text{C}\equiv\text{CAr})_2$ to $\text{Ru}_2(\text{dmba})_4\text{Ar}_2$. Computational modeling of the electronic structure of $\text{Ru}_2(\text{dmba})_4\text{Ar}_2$ -type complexes has been achieved through both ground state DFT and TD-DFT analyses of **8'**, which indicate significant mixing of the metal and ligand (both axial and equatorial) orbitals. Additionally, DFT also sheds

light on the effect of SOJT distortions on the $\pi^*(\text{Ru-Ru})$ orbital, which gains significant σ -character.

Overall, the isolation of $\text{Ru}_2(\text{III,III})$ bisaryls described here marks the expansion of the scope of the $\text{Ru-Ru-C}(sp^2)$ motif from $\text{Ru}_2(\text{II,III})$ monoaryls in Chapter 1, made possible through judicious choice of the paddlewheel ligand.

2.5 Experimental Section

General considerations. Hdmba ⁸³ and $\text{Ru}_2(\text{dmba})_4\text{Cl}_2$ ⁷⁴ were prepared using literature methods. $n\text{BuLi}$ (2.5 M and 1.6 M in hexanes) was purchased from Sigma-Aldrich. Aryl bromide precursors were purchased from commercial sources and used as received. Tetrahydrofuran was freshly distilled over sodium/benzophenone, while dichloromethane was freshly distilled over CaH_2 prior to use. All reactions were performed under a dry N_2 atmosphere implementing standard Schlenk techniques unless otherwise noted. All reagents were thoroughly dried and degassed prior to lithiation. UV-Vis-NIR spectra were obtained with a JASCO V-670 spectrophotometer in THF solutions. ^1H NMR spectra were recorded on a Varian Mercury 300 spectrometer operating at 299.953 MHz. Cyclic and differential pulse voltammograms were recorded in 0.1 M [$n\text{Bu}_4\text{N}$][PF_6] solution (CH_2Cl_2 , Ar-degassed) on a CHI620A voltammetric analyzer with a glassy carbon working electrode (diameter = 3 mm), a Pt-wire auxiliary electrode, and a Ag/AgCl quasi-reference electrode. The concentration of Ru_2 species was always *ca.* 1.0 mM. The $\text{Fc}^{+/0}$ couple was observed at *ca.* 0.51 ± 0.064 V under the noted experimental conditions. Electrospray ionization mass spectra (ESI-MS) were collected on an Advion expression^L mass spectrometer with an m/z range of 10–2000. Elemental analyses were performed by Atlantic Microlab, Inc.

Synthesis of $\text{Ru}_2(\text{dmba})_4(\text{C}_6\text{H}_4\text{-4'-Bu})_2$ (7). To a THF (10 mL) solution of 1-bromo-4-*tert*-butylbenzene (0.60 mL, 3.5 mmol) at -78°C was added, dropwise, 2.2 mL $n\text{BuLi}$ (1.6 M in hexanes). The aryllithium solution was slowly warmed to *ca.* 0°C and transferred cannula to $\text{Ru}_2(\text{dmba})_4\text{Cl}_2$ (75 mg, 0.09 mmol) dissolved in 20 mL THF. The color of the solution immediately changed from brown to deep red. After stirring for *ca.* 30 min under dinitrogen, the solution was concentrated and filtered through a celite plug. The filtrate was collected, solvent removed, and the product recrystallized twice from THF/MeOH and CH_2Cl_2 /hexanes at -20°C . The precipitate was rinsed with *n*-pentane and dried to afford a red brown solid (25 mg, 27% yield).

Crystals suitable for X-ray diffraction analysis were grown by layering hexanes over a solution of **7** in CHCl₃.

Data for **7**. Anal. Found (calcd) for C₅₇H₇₄Cl₂N₈ORu₂ (**7**·CH₂Cl₂·H₂O): C, 58.77 (59.00); H, 6.22 (6.43); N, 9.43 (9.66). ESI-MS (m/z) [**7**⁺] = 1057.4. UV-Vis/NIR (in THF) λ, nm, (ε, M⁻¹cm⁻¹): 388 (9100), 484 (11000), 575 (sh, ~2800), 836 (400), 1132 (270). Electrochemistry (CH₂Cl₂, vs. Fc⁺⁰), E_{1/2}/V, ΔE_p/mV, i_{forward}/i_{backward}: 0.61 (E_{pa}), irrev; -0.53, 77, 1.0; -2.1, ≈2.1. ¹H NMR (CDCl₃, 25°C) δ, ppm: 1.27 (s, 18H, *p*-C(CH₃)₃), 3.02 (br, 24H, *dmba* N-(CH₃)₂), 6.87–7.12 (br, 12H, *dmba* *o*-CH and aryl *o*/*m*-CH), 7.28–7.54 (m, 16H, *dmba* *m*- and *p*-CH, and aryl *m*/*o*-CH).

Synthesis of Ru₂(*dmba*)₄Ph₂ (8**)**. To a THF (15 mL) solution of bromobenzene (0.15 mL, 1.4 mmol) at -78°C was added, dropwise, 0.6 mL ⁿBuLi (2.5 M in hexanes). The aryllithium solution was slowly warmed to *ca.* 0°C and transferred *via* cannula to Ru₂(*dmba*)₄Cl₂ (150 mg, 0.17 mmol) dissolved in 20 mL THF. The color of the solution immediately changed from brown to deep red. After stirring for *ca.* 30 min under dinitrogen, the solution was concentrated and filtered through a deactivated (with triethylamine) silica plug. The red-brown filtrate was collected, solvent removed, and a red microcrystalline solid recrystallized from CH₂Cl₂/hexanes at -20°C. The precipitate was rinsed with cold methanol and *n*-pentane dried to afford a red microcrystalline solid (65 mg, 40% yield). Crystals suitable for X-ray diffraction analysis were grown by layering hexanes over a solution of **8** in CH₂Cl₂.

Data for **8**. Anal. Found (calcd) for C₅₀H₅₈Cl₄N₈Ru₂ (**8**·2CH₂Cl₂): C, 54.28 (53.86); H, 5.35 (5.24); N, 10.18 (10.05). ESI-MS (m/z) [**8**⁺] = 945.7. UV-Vis/NIR (in THF) λ, nm, (ε, M⁻¹cm⁻¹): 388 (9200), 487 (11000), 580 (sh, ~2500), 830 (440), 1132 (220). Electrochemistry (CH₂Cl₂, vs. Fc⁺⁰), E_{1/2}/V, ΔE_p/mV, i_{forward}/i_{backward}: 0.66 (E_{pa}), irrev; -0.47, 60, 1.1; -2.0, 100, 1.4. ¹H NMR (CDCl₃, 25°C) δ, ppm: 3.05 (s, 24H, *dmba* N-(CH₃)₂), 6.61 (br, 2H, aryl *p*-CH), 6.80 (t, 4H, aryl *m*-CH), 6.99 (d, 8H, *dmba* *o*-CH), 7.12 (br, 4H, aryl *o*-CH), 7.30–7.45 (m, 12H, *dmba* *m*- and *p*-CH).

Synthesis of Ru₂(*dmba*)₄(C₆H₃-3,5-(OCH₃)₂)₂ (9**)**. To a THF (15 mL) solution of 1-bromo-3,5-dimethoxybenzene (375 mg, 1.7 mmol) at -78°C was added, dropwise, 0.7 mL ⁿBuLi (2.5 M in hexanes). The aryllithium solution was slowly warmed to *ca.* 0°C and transferred *via* cannula to Ru₂(*dmba*)₄Cl₂ (100 mg, 0.12 mmol) dissolved in 15 mL THF. The color of the solution immediately changed from brown to deep red. After stirring for *ca.* 30 min under dinitrogen, the solution was concentrated and filtered through a celite plug. The red-brown filtrate was collected, solvent removed, and a red-brown solid product twice recrystallized from CH₂Cl₂/hexanes at

-20°C. The microcrystalline precipitate was rinsed with cold methanol and *n*-pentane, and dried (56 mg, 45% yield). Crystals suitable for X-ray diffraction analysis were grown by layering hexanes over a solution of **9** in CH₂Cl₂.

Data for **9**. Anal. Found (calcd) for C₅₄H₆₈Cl₄N₈O₅Ru₂ (**9**·2CH₂Cl₂·H₂O): C, 51.41 (51.76); H, 5.17 (5.47); N, 8.89 (8.94). ESI-MS (m/z) [**9**⁺] = 1065.3. UV-Vis/NIR (in THF) λ, nm, (ε, M⁻¹cm⁻¹): 387 (8700), 489 (9100), 570 (sh, ~2700), 814 (460), 1100 (180). Electrochemistry (CH₂Cl₂, vs. Fc⁺⁰), E_{1/2}/V, ΔE_p/mV, i_{forward}/i_{backward}: 0.69 (E_{pa}), irrev; -0.42, 64, 0.99; -1.9, 104, 2.1. ¹H NMR (CDCl₃, 25°C) δ, ppm: 3.09 (s, 24H, *dmba* N-(CH₃)₂), 3.70 (s, 12H, OCH₃), 5.84 (s, 2H, aryl *p*-CH), 6.33 (s, 4H, aryl *o*-CH), 6.96 (d, 8H, *dmba* *o*-CH), 7.31–7.44 (m, 12H, *dmba* *m*- and *p*-CH).

X-ray Crystallographic Analysis. Single-crystal XRD data for compounds **7–9** at 150 K were collected on a Bruker AXS D8 Quest CMOS diffractometer using Mo-Kα radiation (λ = 0.71073 Å). Data was collected and processed using APEX3,⁴² and the structures were solved using SHELXTL suite of programs^{43,44} and refined using Shelxl2016.^{45,46}

Computational methods. All DFT calculations were carried out using the Gaussian 16 suite.⁵⁴ Geometry optimizations of **8** based on the corresponding crystal structure were done using spin-restricted DFT with the BVP86,⁸⁴ B3LYP, B3PW91⁸⁵ and M06-L⁸⁶ functionals. The electrochemical HOMO–LUMO gap (E_{1/2}(**B**) – E_{1/2}(**A**), Figure 5) was used as an experimental standard to validate the results of DFT calculations. While none of the optimizations with M06-L functionals converged, the BVP86 functional consistently underestimated the HOMO–LUMO gap by *ca.* 1 eV, whereas the B3LYP and B3PW91 slightly overestimated by *ca.* 0.5 eV. Tables 2.S1–2.S2 list the comparison between experimental and DFT-optimized structures (**8** and **8'**, respectively). Since calculations with B3LYP and B3PW91 resulted in better agreement with experiment, further tuning of basis sets was performed using these functionals. Overall, the optimized computational method consists of the B3LYP functional, basis sets def2-TZVP (with ECP) for Ru atoms and def2-SVP for C, H and N atoms along with Grimme's dispersion corrections. TD-DFT calculations were carried out on the ground state DFT-optimized structure **8'** using the same functional and basis sets.

2.6 Supporting Information

Table 2.S1. Selected geometric parameters from X-ray diffraction (**8**) and DFT calculations (**8'**) using a split basis set (DGDZVP^{47,48} for Ru atoms; 6-31G*⁴⁹⁻⁵³ for C, H and N atoms).

Bond length (Å) and Bond angle (°)	Experiment	Functional		
		BVP86	B3LYP	B3PW91
Ru–Ru	2.4940(3)	2.54355	2.56549	2.54328
Ru–C	2.068(1)	2.0951	2.09501	2.07655
Ru–Ru–C	152.42(3)	154.03537	155.114	154.43996
Ru–N1	2.018(1)	2.06673	2.08079	2.06027
Ru–N2	2.1072(9)	2.15562	2.18147	2.14278
Ru–N3	2.0227(9)	2.07068	2.06834	2.0569
Ru–N4	2.1161(8)	2.15241	2.15499	2.13829

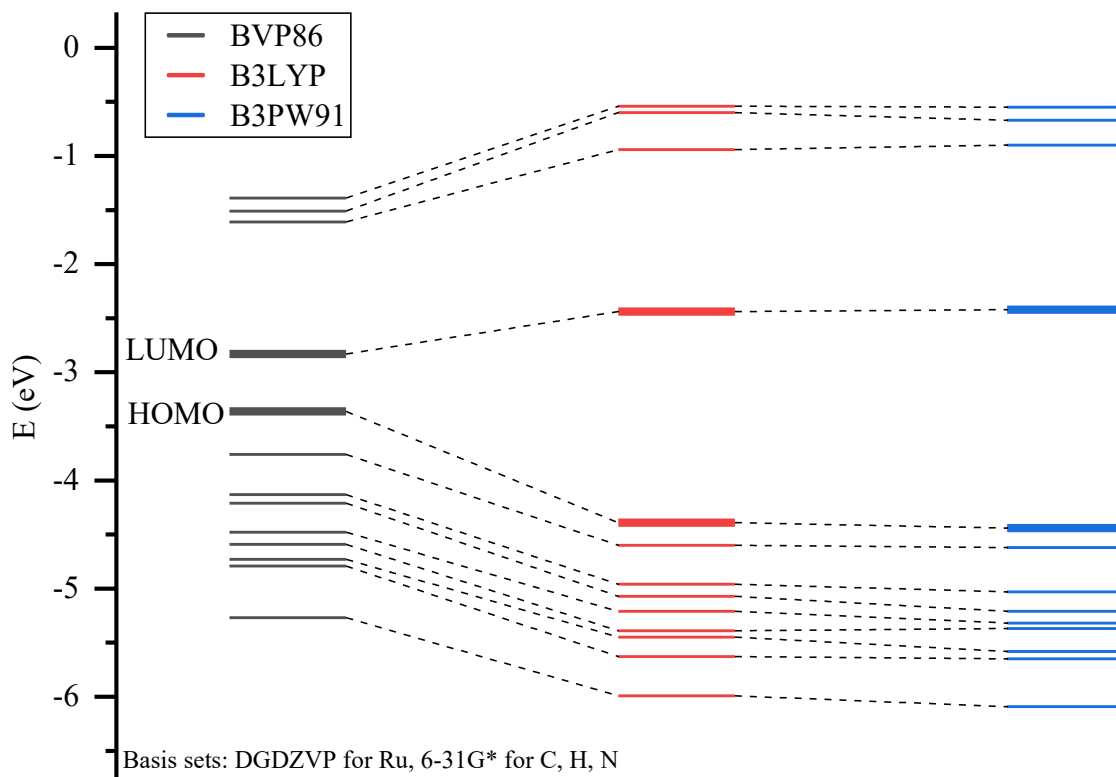


Figure 2.S1. Comparison of DFT-calculated orbital energies for **8'** using the functionals BVP86, B3LYP and B3PW91, and basis sets DGDZVP for Ru atoms and 6-31G* for C,H and N atoms. HOMO and LUMO are shown are highlighted using thicker lines.

Table 2.S2. Selected geometric parameters from X-ray diffraction (**8**) and DFT calculations (**8'**) using the B3LYP functional and different basis sets.

Bond length (Å) and Bond angle (°)	Experiment	Basis sets	
		DGDZVP/6-31G*	def2-TZVP/def2-SVP
Ru–Ru	2.4940(3)	2.56549	2.52797
Ru–C	2.068(1)	2.09501	2.06871
Ru–Ru–C	152.42(3)	155.114	153.10697
Ru–N1	2.018(1)	2.08079	2.02889
Ru–N2	2.1072(9)	2.18147	2.11905
Ru–N3	2.0227(9)	2.06834	2.03313
Ru–N4	2.1161(8)	2.15499	2.12299

Note: Values in bold denote the results from the optimal computational method.

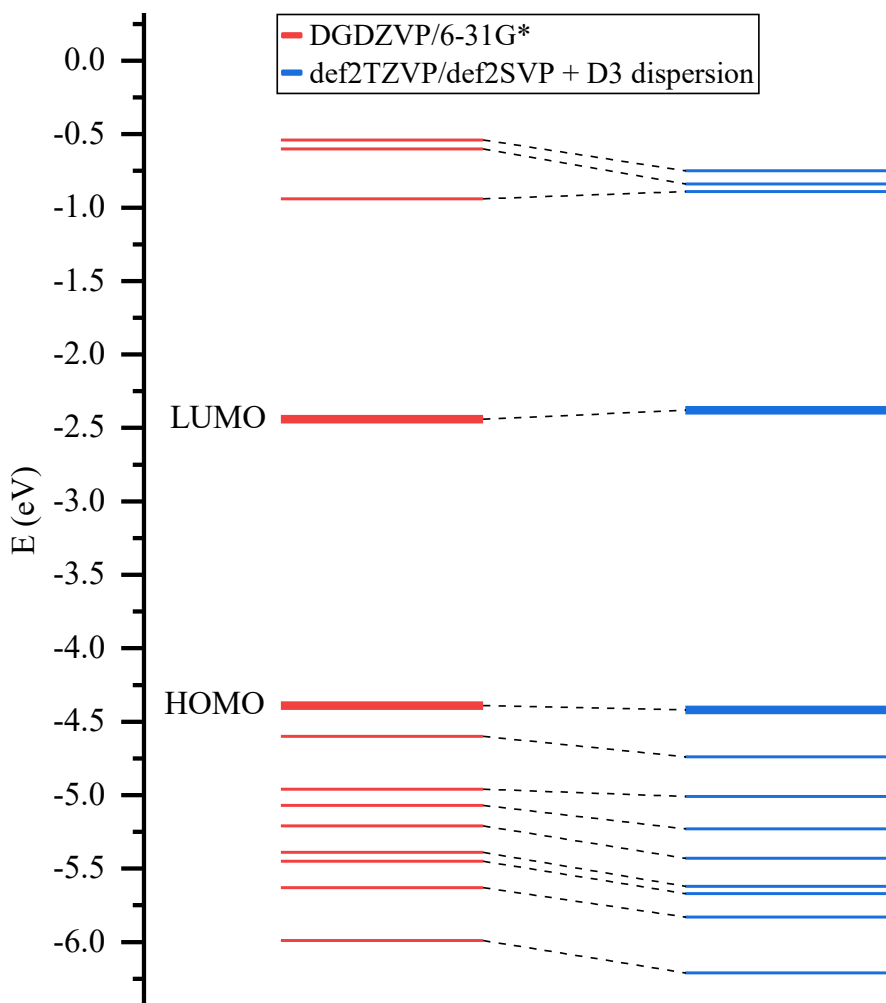


Figure 2.S2. Comparison of DFT-calculated orbital energies for **8'** using the B3LYP functional and different basis sets. HOMO and LUMO are shown are highlighted using thicker lines.

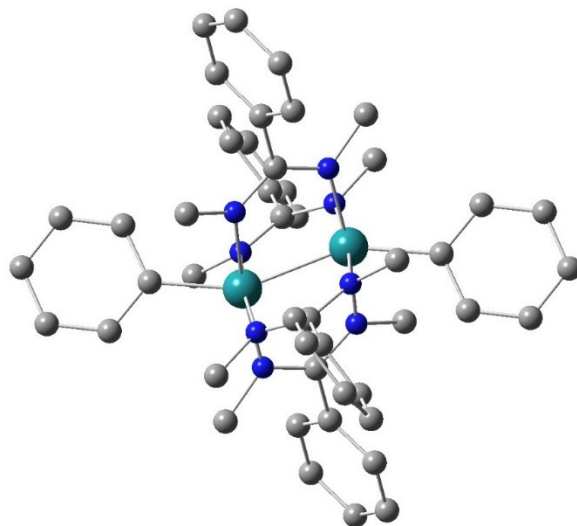


Figure 2.S3. DFT-optimized structure **8'** using the B3LYP functional, def2-TZVP basis set for Ru atoms and def2-SVP basis set for C, H and N atoms. Dispersion forces considered using Grimme's dispersion correction. Covalent radii of all atoms have been scaled by a factor of 0.35, and hydrogens have been omitted for clarity.

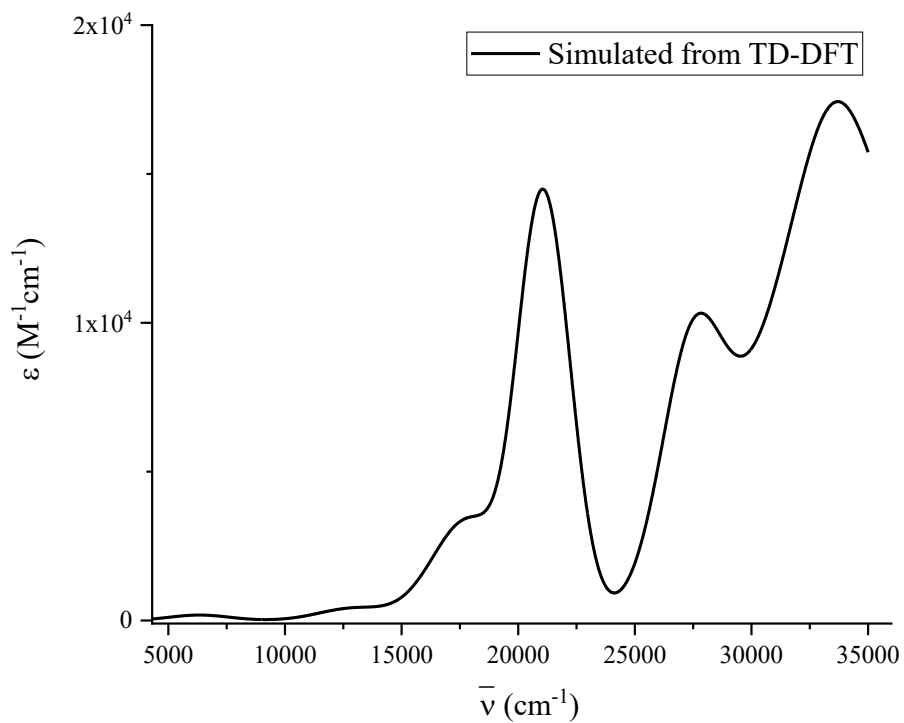


Figure 2.S4. UV-Vis spectrum of **8'** simulated from TD-DFT results, using the most significant transitions.

Table 2.S3. Results of TD-DFT calculations on the optimized structure **8'**.

Excited state	E (eV)	$\bar{\nu}$ (cm ⁻¹)	$f_{\text{oscillator}}$	Transition	%
1	0.7851	6331.45	0.0002	HOMO → LUMO	100
4	1.6069	12958.87	0.0044	HOMO-7 → LUMO	10
				HOMO-4 → LUMO	52
				HOMO-2 → LUMO	37
6	2.2145	17858.87	0.0162	HOMO-7 → LUMO	3
				HOMO-4 → LUMO	28
				HOMO-3 → LUMO+1	13
7	2.5421	20500.80	0.1079	HOMO-2 → LUMO	53
				HOMO-5 → LUMO	77
9	2.6524	21390.32	0.1076	HOMO-1 → LUMO+1	19
				HOMO-7 → LUMO	84
10	2.8147	21892.74	0.0898	HOMO-4 → LUMO	14
				HOMO-3 → LUMO+1	20
18	3.4021	27436.29	0.2218	HOMO-1 → LUMO+1	71
				HOMO-4 → LUMO	3
				HOMO-4 → LUMO+3	2
				HOMO-4 → LUMO+24	2
				HOMO-3 → LUMO+1	66
				HOMO-2 → LUMO	6
57	4.1465	33439.52	0.0987	HOMO-1 → LUMO+4	4
				HOMO-17 → LUMO	2
				HOMO-4 → LUMO+2	4
				HOMO-4 → LUMO+3	68
				HOMO-3 → LUMO+1	4
				HOMO-2 → LUMO+8	3
63	4.2041	33904.03	0.1618	HOMO → LUMO+12	7
				HOMO-4 → LUMO+3	8
				HOMO-4 → LUMO+4	2
				HOMO-1 → LUMO+13	3
				HOMO → LUMO+12	71
				HOMO → LUMO+19	3

Table 2.S4. Fitting results for the Gaussian deconvolution from Figure 2.9.

Peak Index	Peak Type	Area Intg	FWHM	Max Height	Center Grvty	Area IntgP
1	Gaussian	597257.45382	3037.03251	190.46184	8676.51773	0.27102
2	Gaussian	1549493.70511	3530.08901	412.37746	12063.28241	0.70312
3	Gaussian	1.32145E7	3655.45032	3396.07831	18422.1104	5.99638
4	Gaussian	1.63479E7	2000	7678.92662	20264.95717	7.41824
5	Gaussian	1.08755E7	2000	5108.44544	21649.70978	4.93502
6	Gaussian	1.0958E7	2200	4679.24681	23145.86623	4.97244
7	Gaussian	2.38064E7	3074.82463	7273.4668	25557.05535	10.8027
8	Gaussian	9087977.96261	3229.89833	2643.78465	30826.88458	4.12388
9	Gaussian	1.33938E8	8449.64919	20580.50917	33584.73732	60.77721

AR-3-93_NaBH4 added
H1 standard parameters, CDCl3.

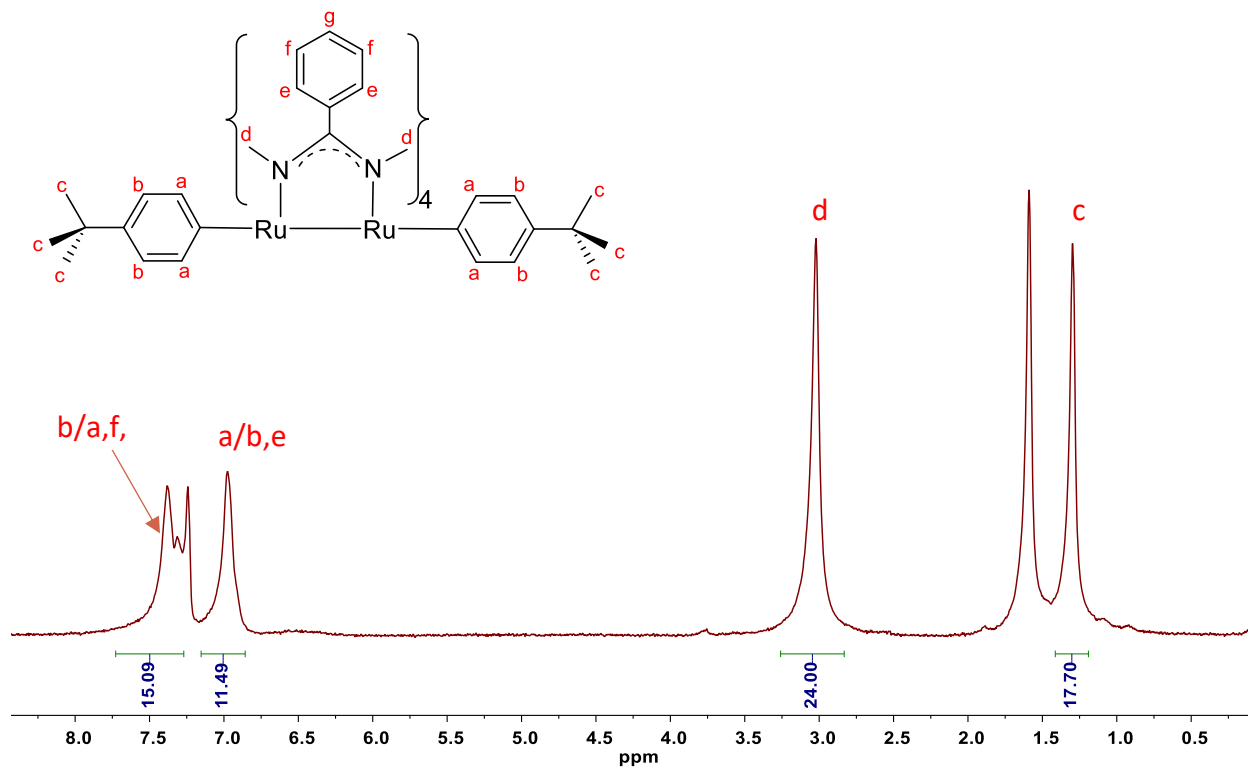


Figure 2.S5a. ¹H NMR spectrum of 7 in CDCl₃, after excess NaBH₄ was added to the NMR tube.

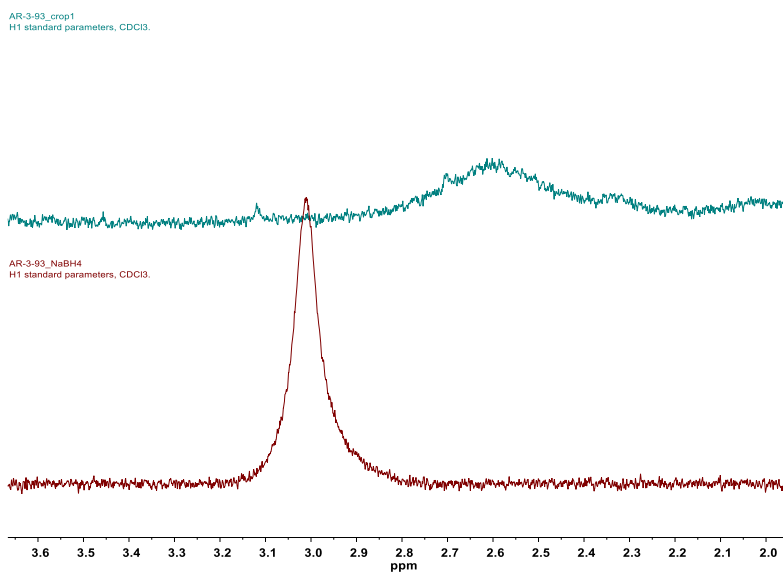


Figure 2.S5b. Difference in NCH₃ peaks in the ¹H NMR spectrum of 7 in CDCl₃ before (top) and after (bottom) addition of excess NaBH₄.

AR-2-279
H1 standard parameters, CDCl₃.

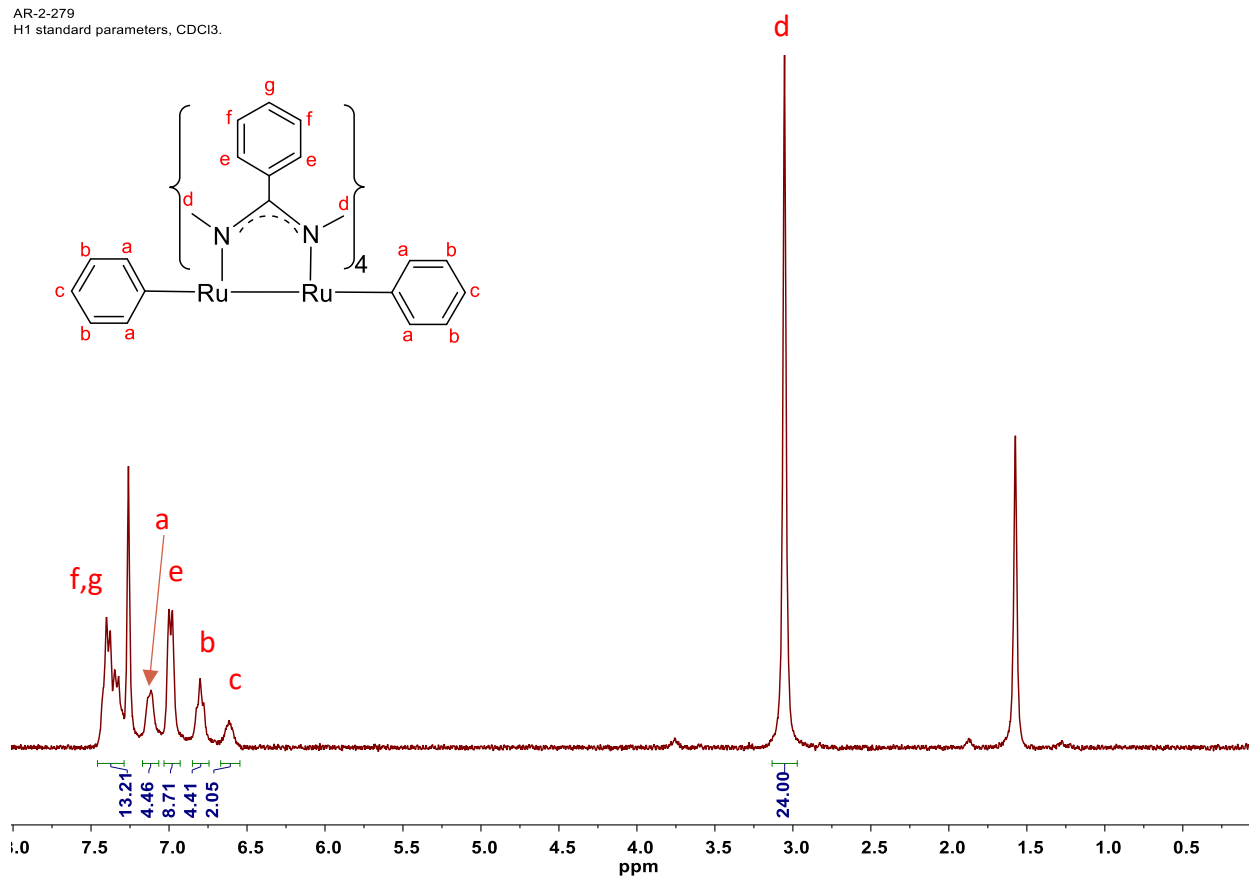


Figure 2.S6. ¹H NMR spectrum of **8** in CDCl₃.

AR-3-27_cleaner
H1 standard parameters, CDCl₃.

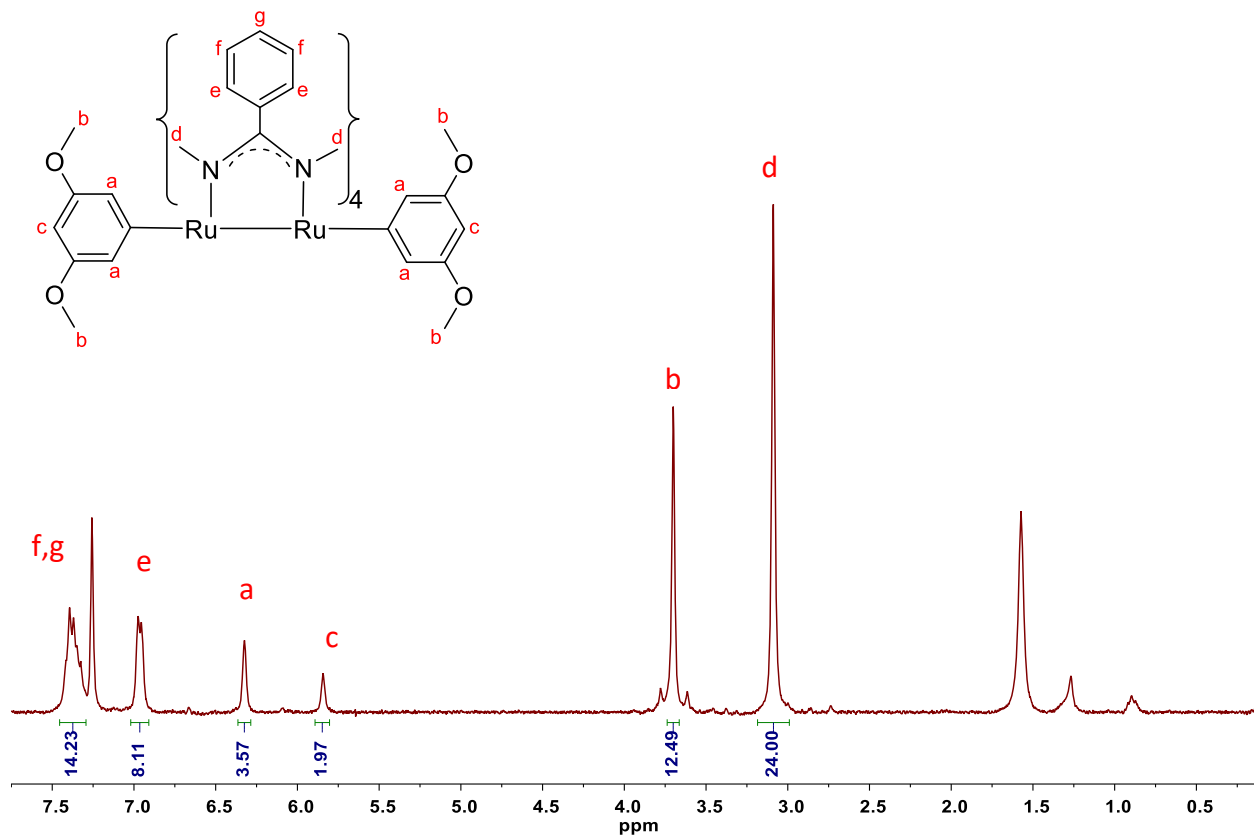


Figure 2.S7. ¹H NMR spectrum of **9** in CDCl₃.

Table 2.S5. Crystallographic details for Ru₂(*dmba*)₄(C₆H₄-4-*t*Bu)₂ (7)

Ru ₂ (<i>dmba</i>) ₄ (C ₆ H ₄ -4- <i>t</i> Bu) ₂ (7)	
Crystal data	
Chemical formula	C ₅₆ H ₇₀ N ₈ Ru ₂
<i>M</i> _r	1057.34
Crystal system, space group	Triclinic, <i>P</i> ⁻ 1
Temperature (K)	150
<i>a</i> , <i>b</i> , <i>c</i> (Å)	10.1861 (13), 11.6696 (15), 13.1497 (16)
α, β, γ (°)	68.519 (5), 70.230 (5), 65.461 (5)
<i>V</i> (Å ³)	1290.7 (3)
<i>Z</i>	1
Radiation type	Mo <i>K</i> α
μ (mm ⁻¹)	0.63
Crystal size (mm)	0.20 × 0.18 × 0.16
Data collection	
Diffractometer	Bruker AXS D8 Quest CMOS diffractometer
Absorption correction	Multi-scan TWINABS 2012/1: Krause, L., Herbst-Irmer, R., Sheldrick G.M. & Stalke D. (2015). <i>J. Appl. Cryst.</i> 48 3-10.
<i>T</i> _{min} , <i>T</i> _{max}	0.655, 0.746
No. of measured, independent and observed [<i>I</i> > 2σ(<i>I</i>)] reflections	61906, 8436, 6179
<i>R</i> _{int}	0.064
(sin θ/λ) _{max} (Å ⁻¹)	0.736
Refinement	
<i>R</i> [<i>F</i> ² > 2σ(<i>F</i> ²)], <i>wR</i> (<i>F</i> ²), <i>S</i>	0.050, 0.134, 1.08
No. of reflections	8436
No. of parameters	445
No. of restraints	972
H-atom treatment	H-atom parameters constrained
Δ _{max} , Δ _{min} (e Å ⁻³)	1.36, -1.05

Table 2.S6. Crystallographic details for Ru₂(*dmba*)₄(Ph)₂ (**8**)

Ru ₂ (<i>dmba</i>) ₄ (Ph) ₂ (8)	
Crystal data	
Chemical formula	C ₄₈ H ₅₄ N ₈ Ru ₂
<i>M_r</i>	945.13
Crystal system, space group	Triclinic, <i>P</i> ⁻ 1
Temperature (K)	150
<i>a</i> , <i>b</i> , <i>c</i> (Å)	9.2185 (6), 10.9852 (7), 11.5781 (8)
α, β, γ (°)	101.828 (2), 93.741 (2), 110.788 (2)
<i>V</i> (Å ³)	1060.61 (12)
<i>Z</i>	1
Radiation type	Mo <i>K</i> α
μ (mm ⁻¹)	0.76
Crystal size (mm)	0.45 × 0.30 × 0.26
Data collection	
Diffractometer	Bruker AXS D8 Quest CMOS diffractometer
Absorption correction	Multi-scan <i>SADABS</i> 2016/2: Krause, L., Herbst-Irmer, R., Sheldrick G.M. & Stalke D. (2015). <i>J. Appl. Cryst.</i> 48 3-10.
<i>T_{min}</i> , <i>T_{max}</i>	0.679, 0.747
No. of measured, independent and observed [<i>I</i> > 2σ(<i>I</i>)] reflections	64164, 8103, 7709
<i>R_{int}</i>	0.025
(sin θ/λ) _{max} (Å ⁻¹)	0.772
Refinement	
<i>R</i> [<i>F</i> ² > 2σ(<i>F</i> ²)], <i>wR</i> (<i>F</i> ²), <i>S</i>	0.019, 0.048, 1.10
No. of reflections	8103
No. of parameters	267
H-atom treatment	H-atom parameters constrained
Δ _{max} , Δ _{min} (e Å ⁻³)	0.92, -0.74

Table 2.S7. Crystallographic details for Ru₂(*dmba*)₄(C₆H₃-3,5-(OMe)₂)₂ (**9**)

Ru ₂ (<i>dmba</i>) ₄ (C ₆ H ₃ -3,5-(OMe) ₂) ₂ (9)	
Crystal data	
Chemical formula	C _{53.43} H _{64.86} Cl _{2.86} N ₈ O ₄ Ru ₂
<i>M</i> _r	1186.69
Crystal system, space group	Triclinic, <i>P</i> ⁻ 1
Temperature (K)	150
<i>a</i> , <i>b</i> , <i>c</i> (Å)	10.8804 (6), 11.2715 (7), 13.1094 (7)
α, β, γ (°)	87.986 (2), 80.142 (2), 69.036 (2)
<i>V</i> (Å ³)	1478.53 (15)
<i>Z</i>	1
Radiation type	Mo <i>K</i> α
μ (mm ⁻¹)	0.69
Crystal size (mm)	0.30 × 0.25 × 0.25
Data collection	
Diffractometer	Bruker AXS D8 Quest CMOS diffractometer
Absorption correction	Multi-scan <i>SADABS</i> 2016/2: Krause, L., Herbst-Irmer, R., Sheldrick G.M. & Stalke D. (2015). <i>J. Appl. Cryst.</i> 48 3–10.
No. of measured, independent and observed [<i>I</i> > 2σ(<i>I</i>)] reflections	98693, 11345, 10300
<i>R</i> _{int}	0.035
(sin θ/λ) _{max} (Å ⁻¹)	0.773
Refinement	
<i>R</i> [<i>F</i> ² > 2σ(<i>F</i> ²)], <i>wR</i> (<i>F</i> ²), <i>S</i>	0.025, 0.067, 1.10
No. of reflections	11345
No. of parameters	417
No. of restraints	204
H-atom treatment	H-atom parameters constrained
Δ _{max} , Δ _{min} (e Å ⁻³)	1.25, -0.75

CHAPTER 3. REACTIVITY OF DIRUTHENIUM MONOARYLS

Reprinted (adapted) with permission from Raghavan, A., Yuan, F., Ren, T., *Inorganic Chemistry*, **2020**, DOI: 10.1021/acs.inorgchem.0c01755. Copyright 2019, American Chemical Society.

3.1 Abstract

Described in this chapter is the use of aryls as axial ligands to elicit reactivity from the distal metal site through metal–metal–ligand interactions in diruthenium paddlewheel complexes. The vacant ruthenium site in $\text{Ru}_2(\text{ap})_4(\text{Ar})$ (**1**, ap = 2-anilinopyridinate, Ar = $\text{C}_6\text{H}_4\text{-4-NMe}_2$), rendered reactive by the axial aryl ligand, is able to bind a specific type of ligands to afford complexes of the form $(\text{Y})[\text{Ru}_2(\text{ap})_4](\text{Ar})$ (Y = CO , **10**; CN^- , **11**; $\text{Me}_3\text{Si-C}\equiv\text{C-C}\equiv\text{C}^-$, **12**; $\text{HC}\equiv\text{C-C}\equiv\text{C}^-$, **12a**; $\text{HC}\equiv\text{C}^-$, **13**), each of which exhibits a distinct electronic structure. While reactions with anionic ligands subsequently result in oxidation of the diruthenium core from $\text{Ru}_2(\text{II,III})$ to $\text{Ru}_2(\text{III,III})$, the reaction with CO yields a rare example of a $\text{Ru}_2^{\text{II,III}}\text{-CO}_{\text{axial}}$ adduct. The latter reaction is particularly interesting in its completely reversible change of ground state from $S = 3/2$ in **1** to $S = 1/2$ in **12** – the first of its kind seen in $\text{Ru}_2(\text{II,III})$ species. In general, this chapter sheds light on the modulation of electronic structure of diruthenium paddlewheel complexes using distinct coordination environments around each of the ruthenium centers.

3.2 Introduction

The chemistry of bimetallic complexes featuring metal–metal multiple bonds is currently an active area of research.^{87–92} Many biological metalloenzymes^{93,94} and synthetic catalysts employ dinuclear cores supported by appropriate ligands to carry out thermodynamically challenging reactions such as dinitrogen reduction,⁹⁵ hydrogen splitting,⁹⁶ group transfer reactions and otherwise difficult catalytic transformations.^{97–99} In many of these cases, both metal–metal and metal–ligand bonding play equally crucial roles to tune sterics and electronics at the active sites. The highly covalent nature of bonding in homobimetallic systems, as opposed to the localization of valence electrons in heterobimetallic systems^{100–103} offers opportunities to study extended metal–metal–ligand (M-M-L) interactions that can often afford very interesting reactivity. A classic example of such metal–metal–ligand (M-M-L) interactions is that of dirhodium acetates,

$\text{Rh}_2(\text{O}_2\text{CR})_4$, and related complexes that perform carbene transfer, where a three-center two-electron interaction between the dirhodium unit and the axial carbene results in increased electrophilicity and enhanced reactivity at the *ipso* carbon.^{104–106} While such interactions have been investigated in dirhodium paddlewheel complexes, inroads have not been made into diruthenium systems, which can benefit from their inherently robust redox chemistry and unique magnetism.^{2,107}

The effort to utilize aryls – a class of σ and π -donating electron-rich axial ligands – in conjunction with M–M multiply bonded paddlewheel scaffolds was outlined in the previous chapters. Using the monoaryl complexes as a template, the aimed of this chapter is to describe a somewhat different type of M–M–L interaction. The ground state configuration of the monoaryl complex $\text{Ru}_2(\text{ap})_4(\text{Ar})$ (**1**, Chapter 1) was proposed as $\sigma^2\pi^4\delta^2(\pi^*\delta^*)^3$, and corroborated by DFT analysis and room temperature magnetic susceptibility data. It was found that much like Rh_2 carbenes, the strong axial ligand Ar^- ($\text{Ar} = \text{aryl}$) forms an extended σ/π interaction with the M_2 unit. However, the absence of an empty p-orbital on the *ipso* carbon and the mixing of $\pi(\text{Ru–Ru})$ and $\pi(\text{Ar})$ manifolds to yield a high-lying $\pi(\text{Ru–Ru–Ar})$ orbital are significant points of divergence from Rh_2 carbenes. It was reasoned that these interactions, taken in combination, should result in an increase in π -basicity, and to a smaller extent, σ -acidity at the vacant ruthenium site. Accordingly, reactivity towards π -acceptors and σ -donors should be enhanced. However, there are severe steric limitations on the types of ligands that can coordinate to the vacant ruthenium site. A spacefill model of **1** (Figure 3.1) shows that only zero- and one-dimensional ligands can fit in this ‘binding pocket’ formed by the four flanking Ph groups of the *ap* ligand. This is best exemplified by the fact that the reaction between $\text{Ru}_2(\text{ap})_4\text{Cl}$ and a large excess of Ar^- still only affords the monoaryl species **1–6**, and not bisaryl species akin to **7–9**.

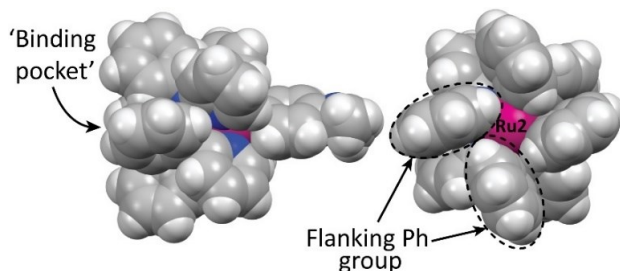


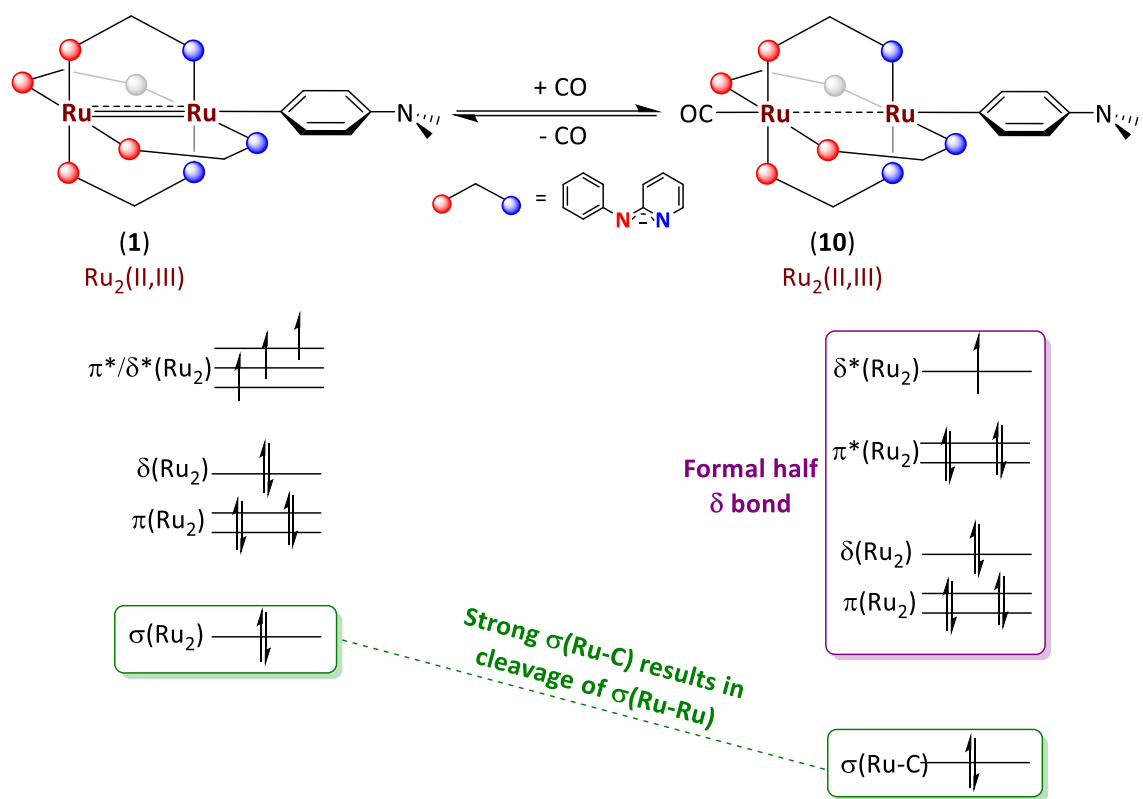
Figure 3.1. Spacefill model of **1** viewed perpendicular to the Ru–Ru–aryl axis (left) and down the Ru–Ru axis (right).

As a representative example of monoaryl Ru₂(II,III) complexes, compound **1** (Ru₂(*ap*)₄(C₆H₄-4-NMe₂)) was chosen. Described in this chapter is the reactivity of **1** towards a series of linear substrates (neutral or anionic) to form (Y)[Ru₂(*ap*)₄](Ar). If Y is neutral (CO), the resulting product is a Ru₂(II,III) species, and if Y is an anion (CN⁻, TMS/H-C₄⁻, HC₂⁻), then in the presence of an oxidant like O₂, the resulting product is a Ru₂(III,III) species. The electronic structure of these complexes is dictated by the interaction between the Ru₂ unit and the axial ligand Y.

3.3 Results and Discussion

3.3.1 Reactivity with neutral substrates (CO)

The reaction of **1** with CO was facile: a solution of **1** in THF turned from black to deep red instantaneously upon CO bubbling (Scheme 3.1). The reaction was complete within one minute and the product (OC)[Ru₂(*ap*)₄](C₆H₄-4-NMe₂) (**10**) was isolated in quantitative yield (99%) upon solvent removal. Compound **10** loses CO slowly under ambient conditions (Figures 3.2–3.3) and needs to be stored under CO as both solution and solid. The lack of reactivity of other monosubstituted [Ru₂(*ap*)₄]X complexes (X = halide, CN⁻, RC≡C⁻, N₃⁻) towards CO (see Experimental Section) suggests that the axial aryl moiety in **1** has a crucial role to play.



Scheme 3.1. Synthesis of **10** from the reaction between **1** and CO.

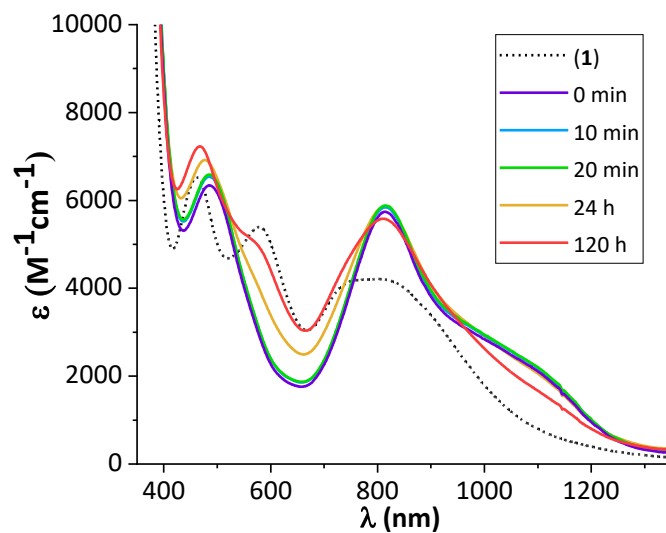


Figure 3.2. UV-Vis/NIR spectrum of **1** (black dotted line), **4** freshly prepared by exposure of **1** for varying lengths of time.

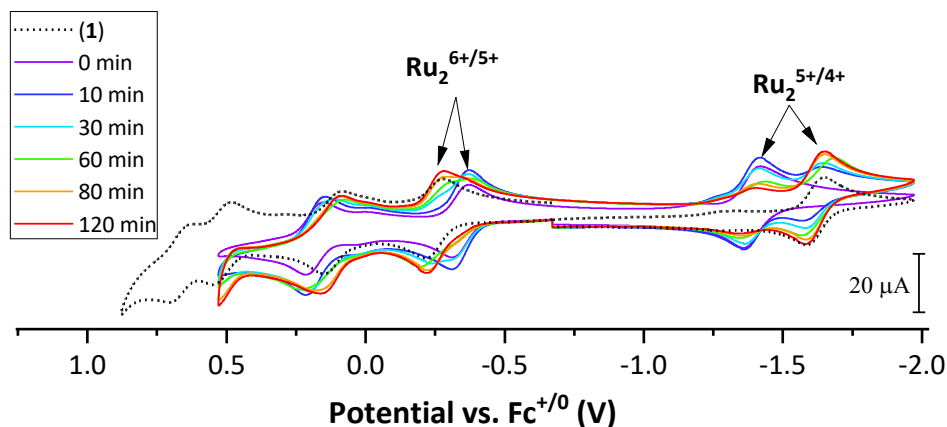


Figure 3.3. Cyclic voltammogram of compound **1** under N₂ (black dotted line), **4** freshly prepared by purging the electrochemical cell with CO (violet line, 0 min), and subsequent scans recorded after the electrochemical cell was purged with N₂ for varying lengths of time.

With CO being a neutral ligand, a minimal perturbation in structure was expected. However, single crystal XRD analysis of **10** (Figure 3.4) revealed very surprising features: a very short Ru–C_{CO} bond (1.877(2) Å), a substantial shortening of the Ru–C_{aryl} bond (2.214(3) Å to 2.053(2) Å) and elongation of the Ru–Ru bond (2.3347(7) Å to 2.5060(3) Å) compared to **1**. In a previously reported Ru₂⁵⁺ CO adduct, [Ru₂^{II,III}(DPhF)₃(OAc)(CO)]⁺ (DPhF = diphenylformamidinate), the Ru–Ru distance (2.450 Å) was comparable to that of the CO-free species.¹⁰⁸ A longer Ru–Ru bond (2.554 Å) was noted for the CO adduct of Ru₂(DPhF)₄ (a Ru₂(II,II) species) with the lengthening from the CO-free species about 0.08 Å.¹⁰⁹ Both of these literature examples provide excellent evidence for the fact that the Ru₂(II,III) core in **1** has been rendered more electron-rich not despite the presence of an axial mono-substitution, but *because* of it. This electron-richness is also reflected in the C≡O stretching frequency of 1950 cm⁻¹ in **10**, a large shift from that of free CO (2143 cm⁻¹). The order of triple bond activation is thus CO > CN⁻, HCC⁻, which reflects the difference in d-electron count of the complexes (Ru₂(II,III), d¹¹ vs Ru₂(III,III), d¹⁰). This is particularly remarkable in a Ru₂(II,III) complex, since all other known examples of Ru₂(II,III) and Ru₂(II,II) species bearing axial CO adducts respectively exhibit a ν(CO) of *ca.* 2016 cm⁻¹ and 1926 cm⁻¹.^{13,108,109} Accordingly, the C–O bond in **10** (1.146(2) Å) is slightly longer than that in free CO (1.128 Å) due to *dπ*–*π* back donation, and is the same as that determined for Ru₂^{II,II}(DPhF)₄(CO) (1.148(11) Å). Electrochemical and infrared spectroscopic data for known Ru₂ⁿ⁺ (n = 3, 4, 5) complexes with axial CO ligands is given in Table 3.2. It is quite clear that for

C≡O activation, having an axial aryl ligand attached to a Ru₂(II,III) core is nearly equivalent to having a Ru₂(II,II) core with no other axial ligands.

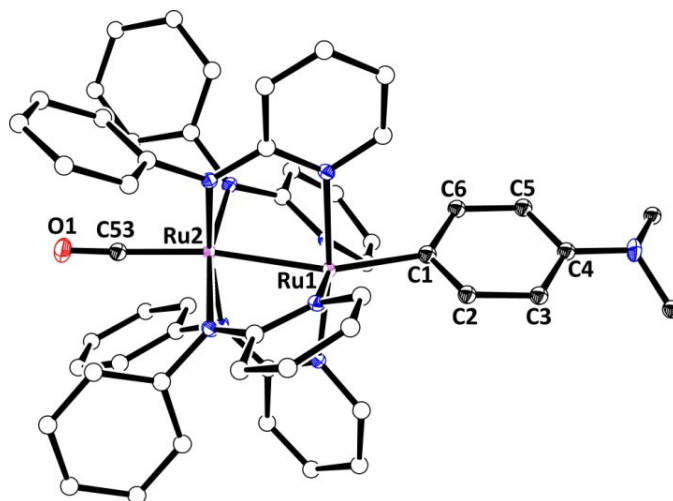


Figure 3.4. Molecular structure of compound **10**. Solvent molecules and hydrogens are omitted for clarity. Selected bond lengths (Å) and angles (deg): Ru1–Ru2, 2.5060(3); Ru1–C1, 2.053(2); Ru2–C53, 1.877(2); Ru2–Ru1–C1, 155.61(6); Ru1–Ru2–C53, 169.50(7).

A striking structural feature of **10**, especially in contrast with the parent compound **1**, is the deviation from an ideal paddlewheel geometry for the [Ru₂(*ap*)₄] core and lowering of symmetry of the whole molecule. Upon closer inspection, this inspection is very similar to the kind observed in compounds **7–9**, where second-order Jahn-Teller (SOJT) effects were invoked. In this case too, we posit that the structural distortions and the heavy mixing of valence MOs are closely related to the need for a stronger Ru–Ru bond. Such a drastic effect surely must manifest as a significant change in its ground state electronic structure. Magnetic susceptibility measurement using Evans method yielded an effective magnetic moment of 1.9 μ_B at 293 K for **10**, indicating a change in ground state from $S = 3/2$ in **1** to $1/2$ in **10** (Figure 3.3). SQUID magnetometry measurements on **1** (Section 1.3.6) clearly established the presence of a classic quartet ground state with large zero-field splitting ($D = 76\text{cm}^{-1}$). However, the SQUID study of **10** did not yield data consistent with a $S = 1/2$ system.

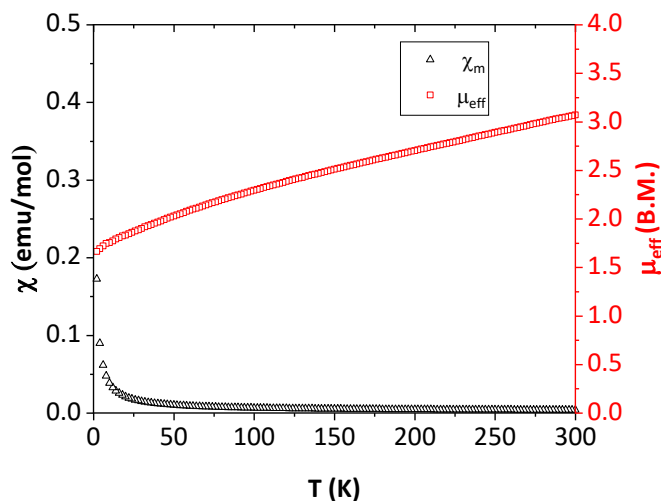


Figure 3.5. SQUID magnetometry of **10** from 2–300 K, courtesy of Dr. Fang Yuan.

For a doublet ground state, the value of χT , and hence μ_{eff} , is expected to be invariant of temperature for most of the higher temperature regime in the 2–300 K window. However, the lability of CO and the associated change in spin-state complicates the issue. Ideally, the SQUID sample holder would be hermetically sealed under a magnetically inert atmosphere. But in the event of leaks wherein the compound gets inadvertently exposed to the low-pressure of the vacuum that is operative during measurements, CO can dissociate from the complex. All attempts to fit the data as a physical mixture of compound **10** ($S = 1/2$) with compound **1** ($S = 3/2$) as an impurity failed. Upon closer inspection, it can be seen that with CO as a labile axial ligand, this system closely resembles $[\text{Ru}_2(\text{DPhF})_3(\text{OAc})(\text{H}_2\text{O})]\text{BF}_4$, which has labile water molecules at the axial positions. This compound displays a very similar temperature-dependent magnetic behavior between 2–300 K, which was attributed to a quantum mechanical spin admixture that takes place through spin-orbit coupling. This phenomenon could be operative in the case of compound **10** as well.

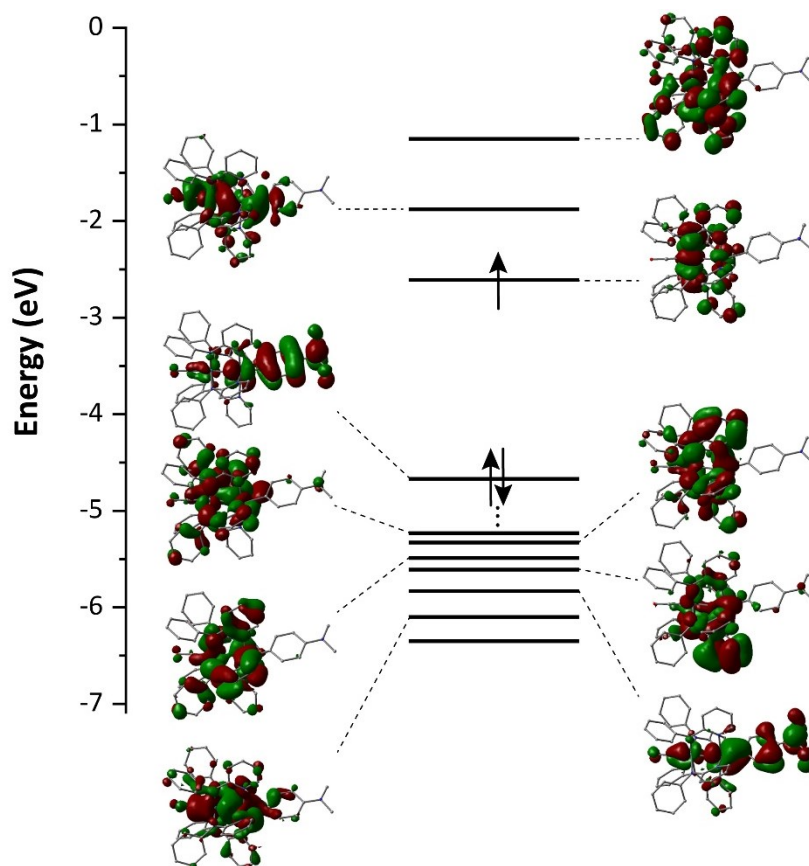


Figure 3.6. Frontier MO plots from ground-state DFT calculations of **4**.

Taken together, the structural and magnetic characteristics suggest that the likely ground state configuration of **10** is $\pi^4\delta^2\pi^*4\delta^*1$. DFT calculations support the idea of one unpaired electron being housed in an orbital of δ^* symmetry (Figure 3.6). Admittedly, the heavy mixing of metal and ligand valence orbitals makes orbital descriptions convoluted, but it is clear the singly occupied MO (SOMO) has δ^* character. Additionally, a spin-density plot (Figure 3.7) also confirms the location of the unpaired electron in the complex. In addition to being $S = 1/2$, compound **10** has a formal bond order of half (δ bond) that is consistent with a very long Ru–Ru bond. Clearly, the formation of a strong Ru–C_{CO} bond occurs at the expense of σ (Ru–Ru), which frees up the other Ru d_z^2 for an enhanced Ru–C_{aryl} bond. The two σ (Ru–Ru) valence electrons in **1** are pushed into the $\pi^*\delta^*$ manifold in **10** (Scheme 3.1).

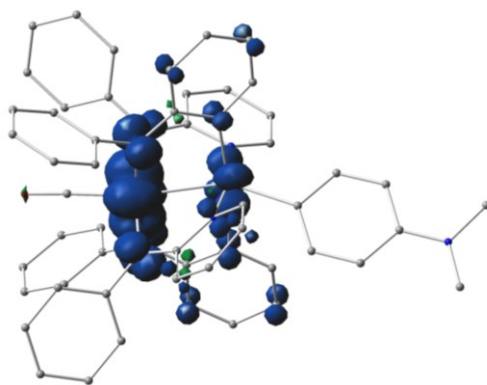
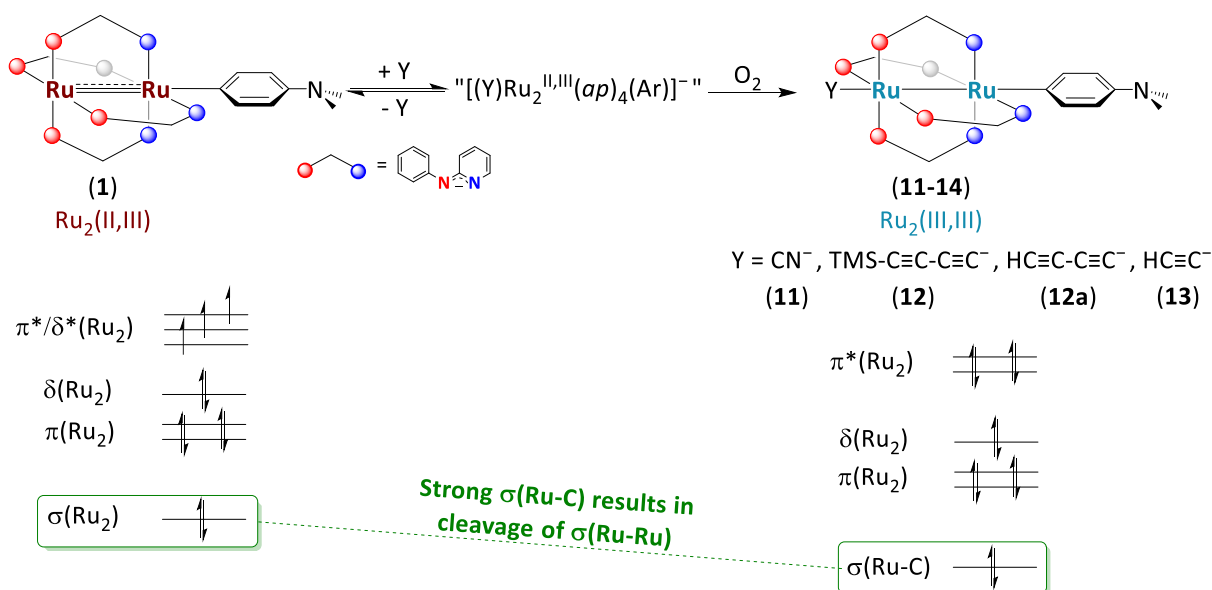


Figure 3.7. Net unpaired electron density calculated from the difference between α and β -spin electron densities in **10'**, represented at $|\text{isovalue}| = 0.003$. The unpaired electron is predominantly localized on the δ^* orbital, per the electronic configuration described in the text.

3.3.2 Reactivity with anionic substrates (CN^- , $\text{RC}\equiv\text{C}-\text{C}\equiv\text{C}^-$ and $\text{HC}\equiv\text{C}^-$)

The reaction of **1** with anionic substrates proceeded in a two-step fashion (Scheme 3.2). First, ligand coordination at the vacant ruthenium site proceeded at a rate dictated by the electronic nature of the ligand. This equilibrium step likely resulted in an (hypothesized based on literature evidence of similar transformations)⁷ anionic $\text{Ru}_2(\text{II,III})$ complex that was deep red in color. Subsequently, when the reaction mixture was exposed to ambient air, the oxidation of this species by O_2 produced the final $\text{Ru}_2(\text{III,III})$ product.



Scheme 3.2. Synthesis of **11–13** from the reaction between **1**, **Y** and O_2 .

CN⁻

Addition of KCN to a THF/MeOH solution of **1** resulted in a deep red solution within a few minutes under inert atmosphere, presumably the $[(\text{NC})\text{Ru}_2(\text{ap})_4(\text{Ar})]^-$ intermediate, which immediately turned deep violet upon exposure to O_2 . Subsequent recrystallization of the crude product in CH_2Cl_2 -hexanes yielded $(\text{NC})[\text{Ru}_2(\text{ap})_4](\text{Ar})$ (**11**) as a dark violet microcrystalline solid in 83% yield. Compound **11** exhibited ^1H NMR spectra in the normal diamagnetic window with clearly identifiable peaks that are consistent with an effective C_{4v} symmetry (Figure 3.8). The N- CH_3 and a couple of other paddlewheel ligand proton peaks are slightly broadened, while all the other peaks are sharp and very well-defined. Lack of any appreciable magnetic moment (Evans method) implies this is either due to exchange, or more likely, a small, immeasurable amount of paramagnetic impurity.

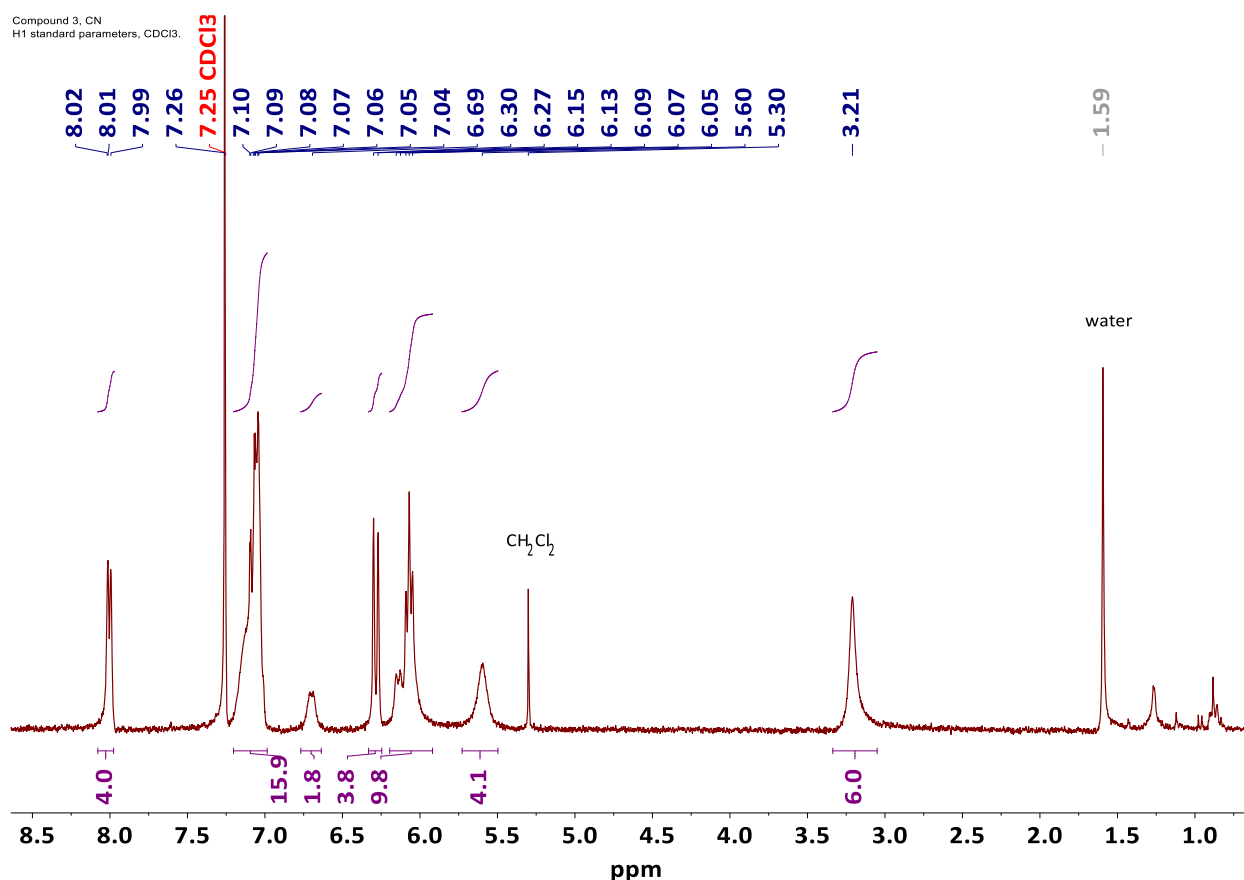


Figure 3.8. ^1H NMR spectrum of **11** in CDCl_3 at 293 K.

Further confirmation of the identity of **11** came from its X-ray structure (Figure 3.9), which revealed a Ru₂ core distorted from an idealized paddlewheel motif. Notably, the Ru–Ru bond is lengthened *ca.* 0.15 Å from that of **1** (2.3347(7) Å to 2.4857(7) Å) and both Ru–Ru–C angles are significantly deviated from 180°, which are signatures of SOJT effects as documented previously for Ru₂^{III,III}(*ap*)₄(CN)₂,¹² many Ru₂(III,III) bis-alkynyl compounds,^{2,7} and Ru₂(III,III) bis-aryl compounds of the form Ru₂(DMBA)₄Ar₂ (compounds **7–9** in Chapter 2). Both the diamagnetic nature of **11** and its structural similarity to these axially disubstituted Ru₂⁶⁺ species point to a ground state configuration of $\pi^4\delta^2\pi^*4$ with a net single Ru–Ru δ bond. This accounts for 10 Ru valence electrons after the loss of σ (Ru–Ru) bond to the formation of two strong σ (Ru–C) bonds.

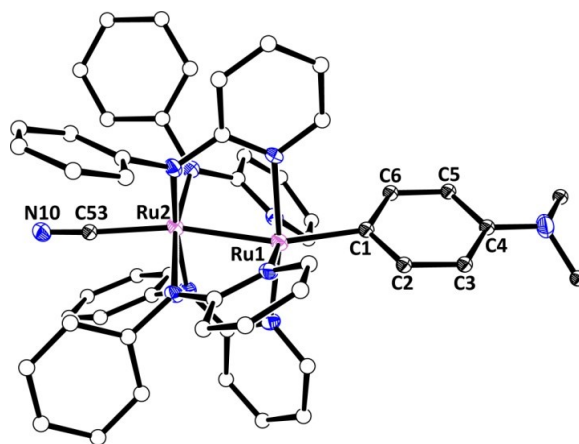


Figure 3.9. Molecular structure of compound **11**. Solvent molecules and hydrogens are omitted for clarity. Selected bond lengths (Å) and angles (deg): Ru1–Ru2, 2.4857(7); Ru1–C1, 2.077(7); Ru2–C53, 2.021(7); Ru2–Ru1–C1, 155.61(6); Ru1–Ru2–C53, 169.50(7).

R-C≡C–C≡C[−] (*R* = TMS, H)

The reaction between **1** and TMS-C≡C–C≡C[−] was significantly slower than that with CN[−]. A slight excess of LiC₄TMS (3–4 equiv.) was added to a THF solution of **1** under inert conditions, and the slow disappearance of starting material was monitored by TLC and ESI-MS over the course of 12 hours. At this juncture, the deep red solution was oxidized by exposing the reaction mixture to O₂, and within a few minutes, the solution turned green. Recrystallization from THF/*n*-pentane afforded **12** as a microcrystalline dark green solid in 64% yield. The ¹H NMR spectrum of **12** in CDCl₃ (Figure 3.10) showed well-resolved peaks in the diamagnetic window with an effective C_{4v} solution symmetry, like **11**. All the NMR peaks are sharp and well-defined and have

been assigned either to the paddlewheel ligands or the axial aryl ligand. Compared to compound **11**, some of the aromatic C–H peaks (both equatorial paddlewheel and axial aryl) are shifted upfield and appear in the range of 4.5–5.8 ppm, while N–CH₃ peaks (axial aryl) have shifted downfield from 3.21 ppm to 4.10 ppm. Considering that the expected ground state of this compound $S = 0$, and the fact that the distribution in NMR peaks is not too drastically different from those of **11**, temperature-independent paramagnetism (TIP)¹¹⁰ was invoked to explain it, until new evidence came to light (see below).

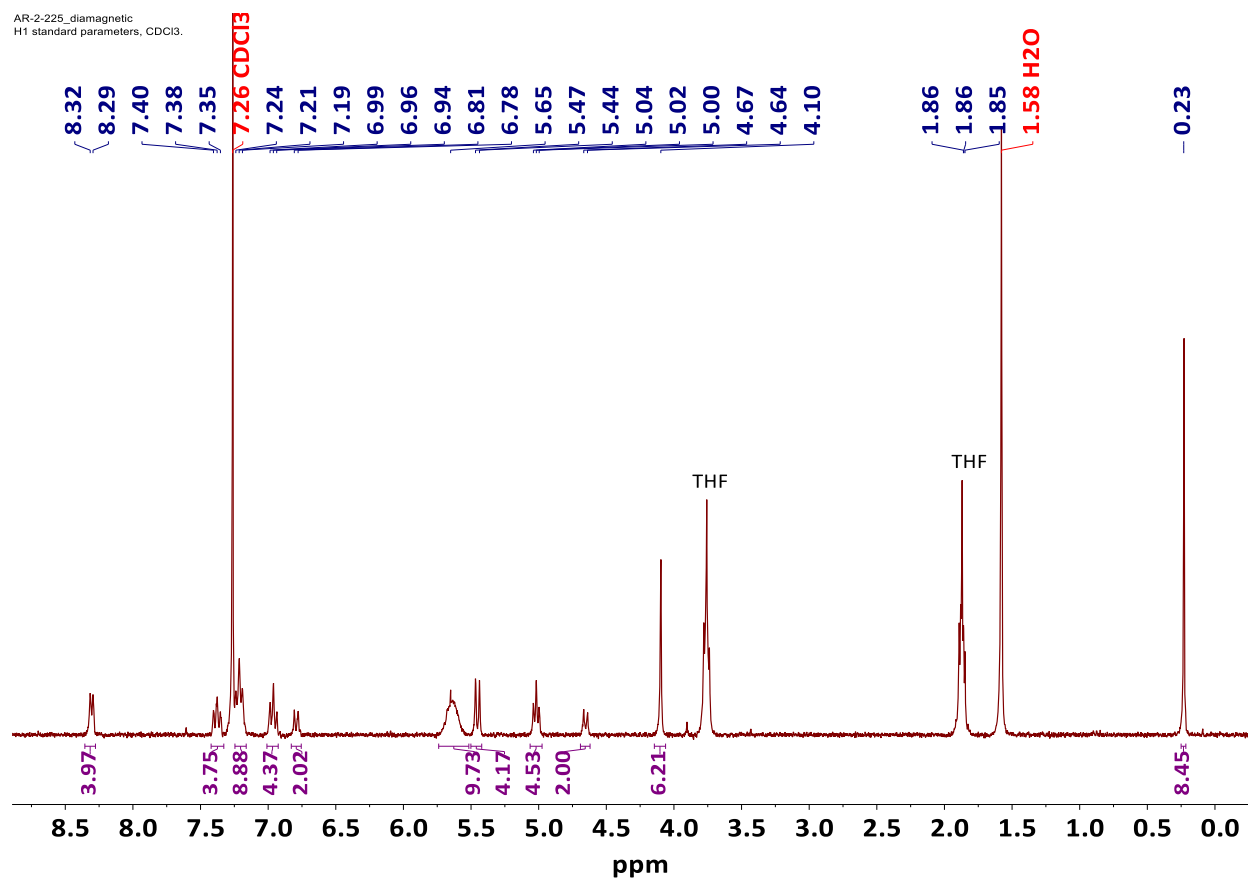


Figure 3.10. ¹H NMR spectrum of **12** in CDCl₃ at 293 K.

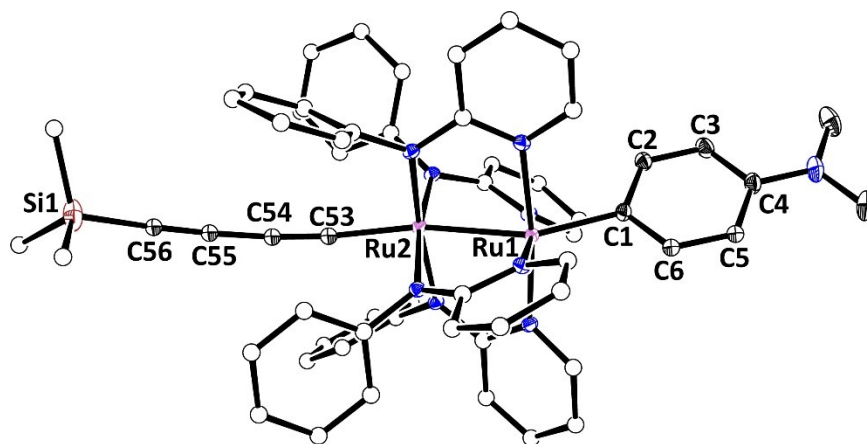


Figure 3.11. Molecular structure of compound **12**. Solvent molecules and hydrogens are omitted for clarity. Selected bond lengths (Å) and angles (deg): Ru1–Ru2, 2.4887(5); Ru1–C1, 2.046(2); Ru2–C53, 1.977(2); Ru2–Ru1–C1, 153.99(6); Ru1–Ru2–C53, 166.22(6).

At first glance, the structural features of **12** (Figure 3.11) are very similar to those of **11**, including the distortions resulting from SOJT effects. While the Ru–Ru bond length is barely any different, both Ru–C bonds are slightly shorter, by about 0.02–0.03 Å. The C53≡C54, C54–C55 and C55≡C56 bond lengths of the –C₄– unit are 1.227(3) Å, 1.370(3) Å and 1.223(3) Å, respectively; this type of bond-length alternation is indicative of some contribution from a cumulenic resonance structure.

The deprotection of the capping TMS with K₂CO₃ was attempted over the course of many days (monitored by TLC and ESI-MS), without success. A stronger desilylating agent like NaOH had to be used, and within 6 hours, the target product (HC≡C–C≡C)Ru₂(*ap*)₄(C₆H₄-4-NMe₂) (**12a**) was formed exclusively. After recrystallization from THF/*n*-pentane, a green solid was isolated in 64% yield. The ¹H NMR spectrum of **12a** is shown in Figure 3.12. Crystallographic characterization was not attempted for this compound, but it is within reason to not expect a major change in the corresponding metrical parameters compared to those of **12**. While there is a small shift of the axial aryl C–H peak from 4.66 ppm (compound **12**) to 5.02 ppm (compound **12a**), it is still a slightly unusual upfield shift for an aromatic C–H resonance. The same applies to the paddlewheel ligand C–H resonances between 5.20–5.80 ppm. The more interesting feature in Figure 3.12, however, is the δ(C≡C–H) at –0.37 ppm – an extreme upfield shift for a terminal alkynyl proton. Two explanations were considered plausible: i) the terminal proton is affected by the ring currents of the four flanking Ph groups that cause a high diamagnetic anisotropy effect or

ii) TIP. As it turned out, there was a third possibility that was solidified by the case of compound **13** (see below).

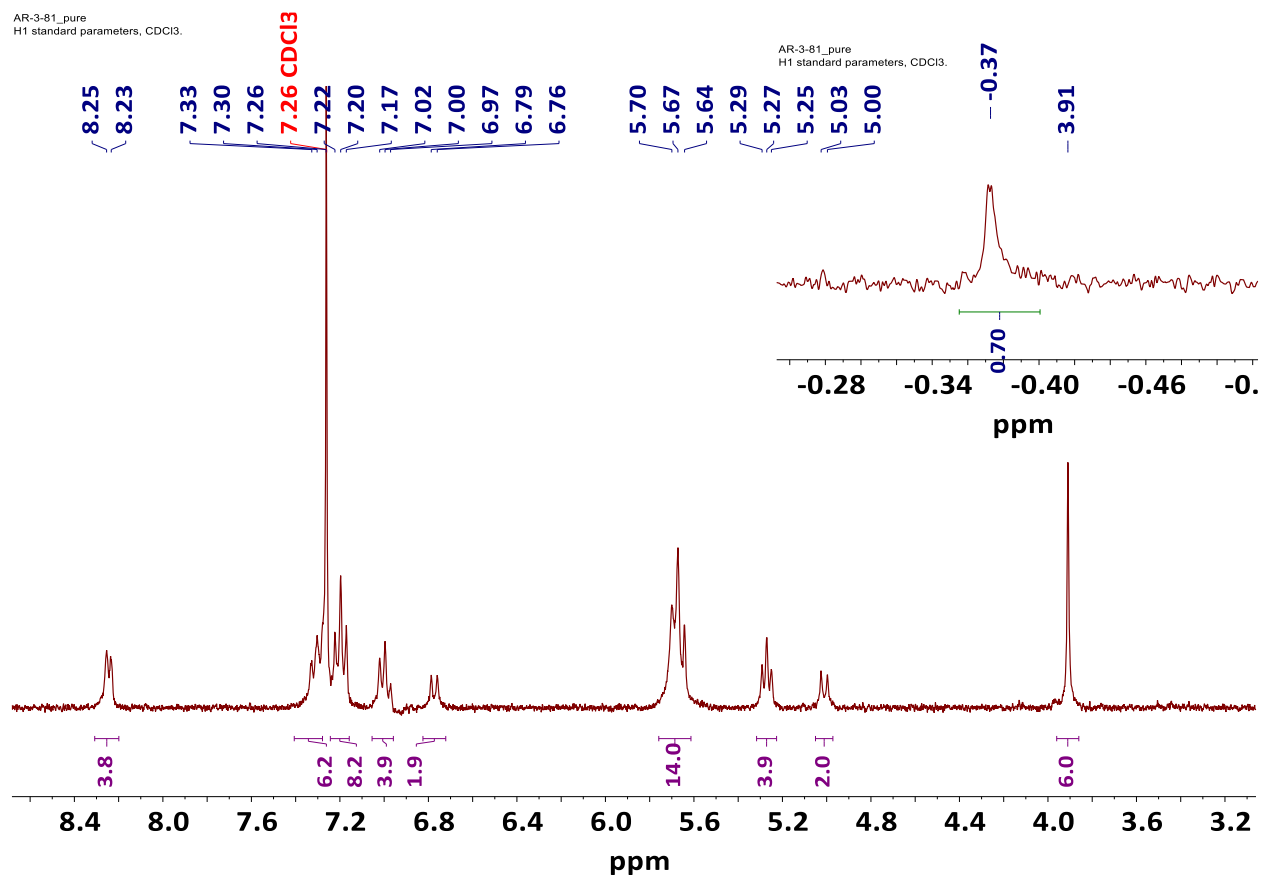


Figure 3.12. ^1H NMR spectrum of **12a** in CDCl_3 at 293 K.

$\text{HC}\equiv\text{C}^-$

The reaction between **1** and $\text{HC}\equiv\text{C}^-$ was surprisingly much slower than that with either CN^- or TMS-C_4^- . The use of a large excess of $\text{NaC}\equiv\text{CH}$ resulted in *ca.* 40% consumption of **1** after 6 days (monitored by TLC and ESI-MS). Subsequent addition of $\text{NaC}\equiv\text{CH}$ under inert conditions did not lead to further conversion. At this juncture the reaction mixture was exposed to O_2 , and the target compound $(\text{HC}_2)[\text{Ru}_2(\text{ap})_4](\text{C}_6\text{H}_4\text{-4-NMe}_2)$ (**13**) isolated after purification by column chromatography as a dark blue crystalline material in 36% yield. The decreased reactivity can be attributed to the strong σ -donating yet weak π -accepting nature of $\text{HC}\equiv\text{C}^-$ compared to CN^- and RC_4^- . In contrast, the addition of the second alkynyl in the formation of $(\text{R}'\text{C}_2)[\text{Ru}_2(\text{ap})_4](\text{C}_2\text{R})$ -type species was more facile (< 3 hr) and higher yielding (75%),⁷⁰ which

is consistent with $[\text{Ru}_2(\text{ap})_4](\text{C}_2\text{R})$ being more electron deficient than $[\text{Ru}_2(\text{ap})_4](\text{Ar})$. The molecular structure of **13** (Figure 3.10) bears strong resemblance to **11** and **12**, and given the structural similarity, we hypothesized that compound **13** has the same ground state Ru_2^{6+} d-electron configuration, namely $\pi^4\delta^2\pi^*4$ (Scheme 3.2).

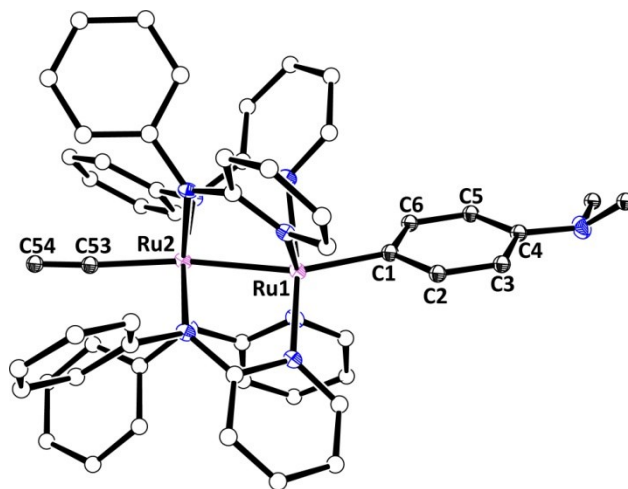


Figure 3.13. Molecular structure of compound **13**. Solvent molecules and hydrogens are omitted for clarity. Selected bond lengths (Å) and angles (deg): Ru1–Ru2, 2.4887(5); Ru1–C1, 2.058(4); Ru2–C53, 2.005(4); Ru2–Ru1–C1, 156.02(9); Ru1–Ru2–C53, 166.45(9).

The ^1H NMR spectrum of **13** (Figure 3.10) consists of sharp peaks, most of which appear in the diamagnetic window (0–9 ppm). However, some unusual chemical shifts are very noteworthy: $\delta(\text{N}(\text{CH}_3)_2)$ is at 5.66 ppm while that of **11** is at 3.21 ppm, $\delta(\text{C}-\text{H}, \text{aryl})$ at 1.40 ppm, and $\delta(\text{C}\equiv\text{C}-\text{H})$ at -10.74 ppm. This is a much wider distribution of NMR chemical shifts compared to both **12** and **12a**. At this juncture, TIP was considered less likely than the alternative – a Boltzmann distribution between a singlet ground state and a thermally accessible low-lying excited state. Variable temperature NMR (VT-NMR) analysis in CDCl_3 within the range of 233–273 K definitively established the temperature-dependence of the chemical shifts, all of which trended toward their respective diamagnetic reference values with decreasing temperature (Figure 3.11). These data are consistent with a thermally accessible low-lying triplet state;¹¹¹ the singlet-triplet gap was calculated to be *ca.* $972 \pm 147 \text{ cm}^{-1}$ ($|2J|$, see below).

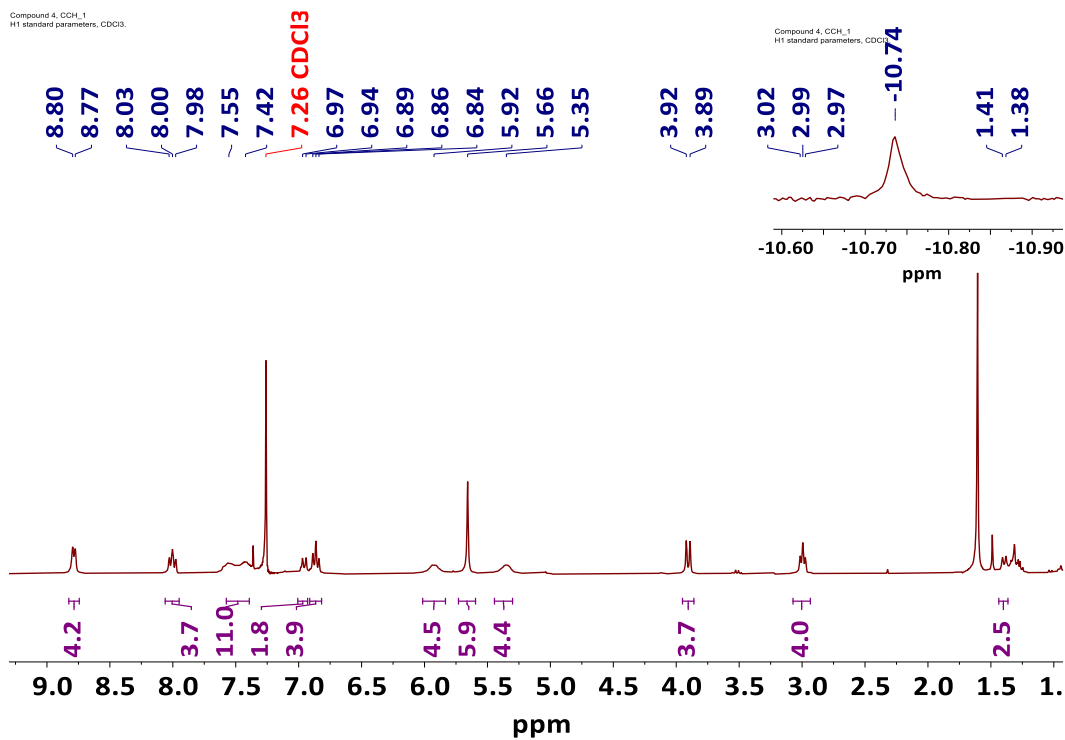


Figure 3.14. ^1H NMR spectrum of **13** in CDCl_3 at 293 K.

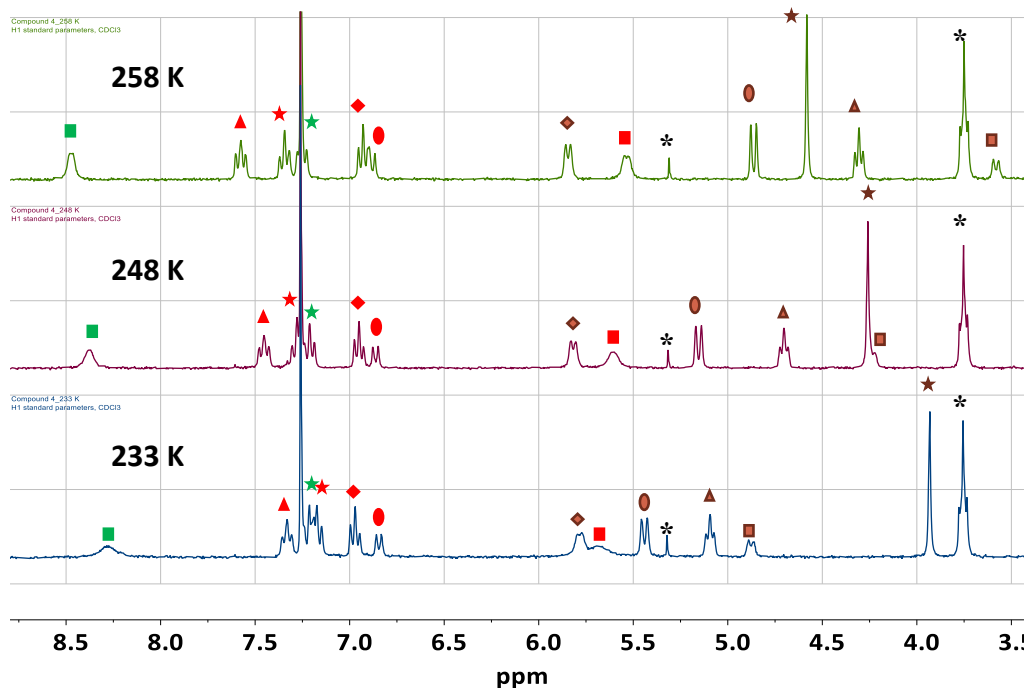


Figure 3.15. VT-NMR spectrum of **13** in CDCl_3 . Black asterisks represent solvent impurities (THF and CH_2Cl_2). Equivalent peaks are denoted by matching shapes and colors.

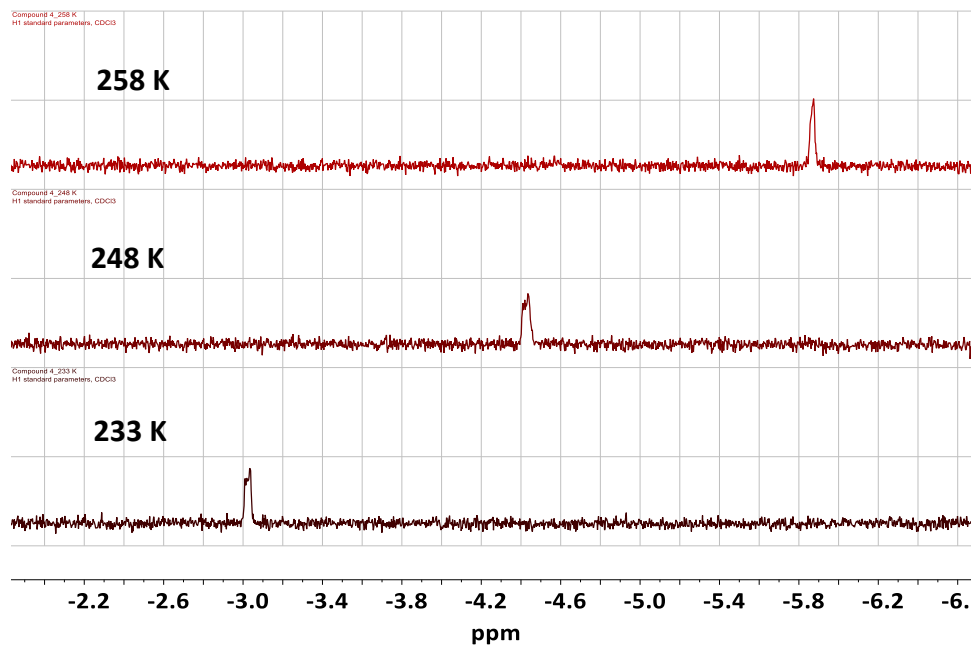


Figure 3.16. VT-NMR spectrum of **13** in CDCl_3 , shown here are the peaks corresponding to the acetylide ($\text{C}\equiv\text{C}-\text{H}$) proton.

It is clear from the above VT-NMR spectra that the chemical shifts for compound **13** are temperature-dependent. As the temperature is decreased, all the peaks trend toward their diamagnetic reference values. Based on this, we hypothesized that compound **13** exists in a singlet ground state ($\lim_{T \rightarrow 0}(S) = 0$) but has a thermally accessible low-lying triplet state ($S = 1$). This can be modelled as the result of a Boltzmann distribution between the states according to equation Eq 3.1.¹¹²

$$\delta(T) = a + \left(\frac{1}{T}\right) \frac{b \cdot e^{\frac{c}{RT}}}{1 + 3e^{\frac{c}{RT}}} \dots (\text{Eq 3.1})$$

$a = \delta_0$, the diamagnetic reference value for the chemical shift of the proton considered,

b = a parameter that is related to the Hyperfine coupling constant,

$c = \Delta E_{s-t} = E_s - E_t$, the energy difference between the singlet ground state and the triplet excited state.

The parametrized equation (Eq 3.1) was used to analyze the chemical shifts of the $\text{C}\equiv\text{C}-\text{H}$, $\text{N}(\text{CH}_3)_2$ and axial aryl($\text{C}-\text{H}$) protons (Figures 3.S8a–c). Accordingly, the singlet-triplet energy gap was calculated to be $|2J| = 972.3 \pm 146.9 \text{ cm}^{-1}$ ($2.78 \pm 0.42 \text{ kcal/mol}$).

3.3.3 UV-Vis/NIR and IR absorption spectroscopy

To better characterize the various oxidation states of $[\text{Ru}_2\text{L}_4]$, electronic absorption spectra of compounds **10–13** were measured in THF (Figure 3.17); the difference between the $\text{Ru}_2(\text{II},\text{III})$ (compounds **1** and **10**) and $\text{Ru}_2(\text{III},\text{III})$ oxidation states (compounds **11–13**) is immediately clear. Characteristic of the former, compounds **1** and **10** both mainly absorb in two regions of the spectrum: 400–450 nm, and 700–850 nm. The peak at 579 nm is an outlier for **1** since it is the result of a para N-substituted aryl ring (section 1.3.4).

For compounds **11–13** (and to an extent **10**, too), the peaks that appear in the NIR region of the spectrum are indicative of low-lying excited states, a fact that is readily corroborated by the VT-NMR spectroscopic data described above. In the 500–800 nm region, interestingly, compounds **11–13** exhibit multiple transitions. This is most pronounced and hence most readily noticeable in the case of **11**, which has at least four peaks in this region. It is likely that the severe structural distortions and the associated heavy mixing between metal and ligand orbitals result in the observation of many allowed electronic transitions.

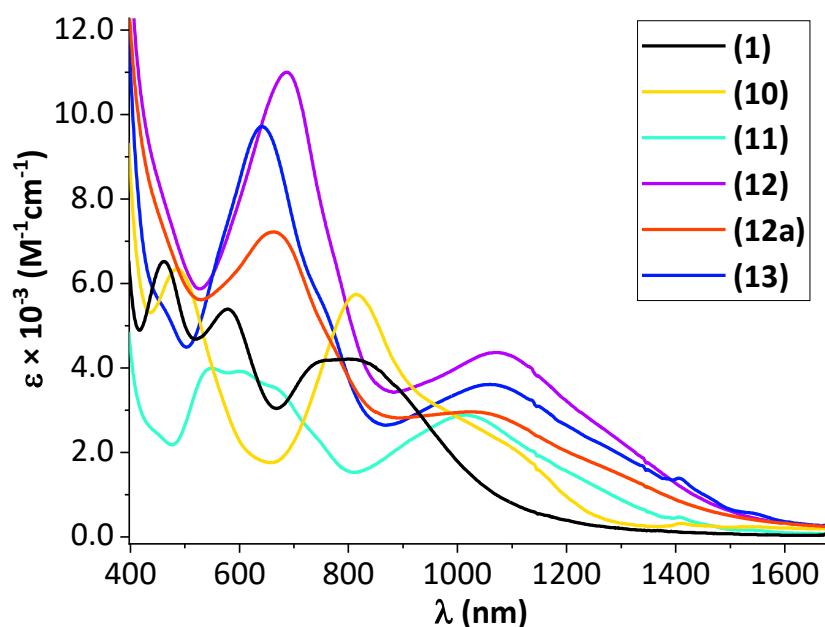


Figure 3.17. Vis/NIR absorption spectrum of compounds **10–13** (and **1** included for comparison) measured in THF.

3.3.4 Electrochemistry

Cyclic and differential pulse voltammograms of compounds **10–13** are shown in Figure 3.18, and the reduction potentials are listed in Table 3.1. Overall, all compounds exhibit two reversible oxidation events (**A** and **B**) and one reversible reduction (**C**). A second reduction does occur in all of these cases, but it is either irreversible (not included in Figure 3.18) or quasi-reversible (**D**). Compound **10** being Ru_2^{5+} , the very first oxidation event **B** is the $\text{Ru}_2^{6+/5+}$ couple (-0.34 V), while for all others, event **B** corresponds to the $\text{Ru}_2^{7+/6+}$ couple. For the latter, there is a clear cathodic shift from -0.11 V to -0.21 V, which reflects the gradient in electron-donating/withdrawing ability of the second axial ligand in each case. The second oxidation event (**A**) was previously ascribed to a predominantly aryl ligand-based oxidation – one that was present only in the cases where the *para* substituent is a tertiary amine functional group. Later in Chapter 4, this will be proven conclusively with the aid of spectro-electrochemical measurements and DFT calculations.

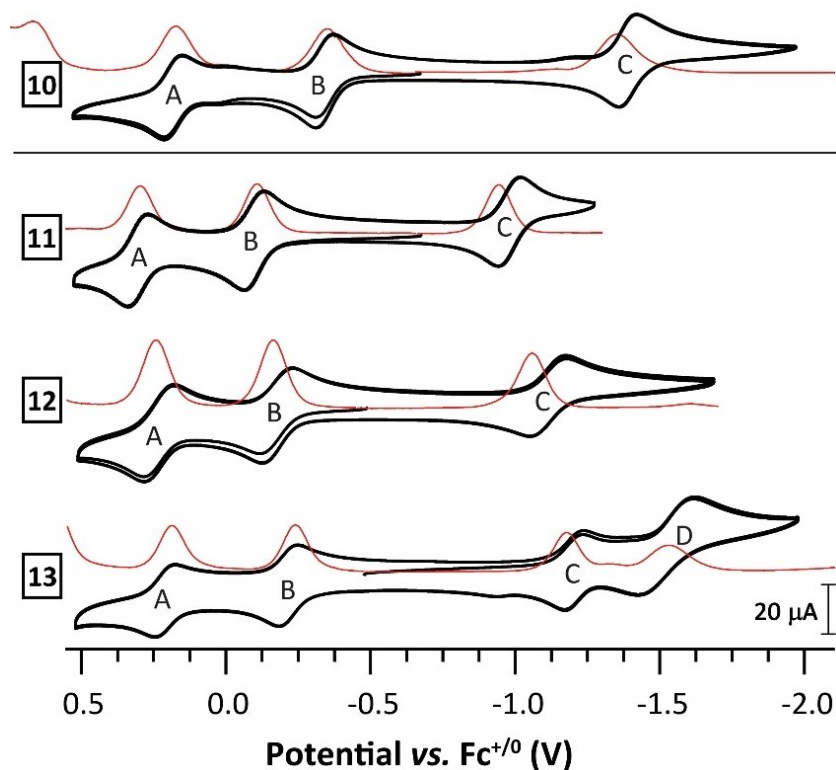


Figure 3.18. CV (black) and DPV (red) of compounds **10–13** recorded in 0.1 M TBAP THF solution. $[\text{Ru}_2] = 1$ mM.

Table 3.1. Redox potentials (V, versus $\text{Fc}^{+/0}$) for $(\text{Y})[\text{Ru}_2(\text{ap})_4](\text{C}_6\text{H}_4\text{-4-NMe}_2)$ in THF.

Y	$E_{1/2}$ (A)	$E_{1/2}$ (B)	$E_{1/2}$ (C)	$E_{1/2}$ (D)
– (1)	0.12	–0.27	–1.62	–
–CO (10)	0.18	–0.34	–1.39	–
–CN (11)	0.30	–0.11	–0.98	–
–C ₄ TMS (12)	0.23	–0.18	–1.11	–
–C ₂ H (13)	0.21	–0.21	–1.20	–1.53

The presence of a stable, reversible reduction event is not surprising for either **10** or **11**. CO binding is strengthened through increased metal-ligand back bonding when the $\text{Ru}_2(\text{II,II})$ oxidation state is reached at event C ($\text{Ru}_2^{5+/4+}$); a similar argument can be extended to **11**. As we move from the more electron-withdrawing CN^- to the more electron-donating HCC^- , this reduction becomes increasingly more difficult, and a cathodic shift of roughly 200 mV is seen. Additionally, this $\text{Ru}_2^{5+/4+}$ couple is less reversible for **12** and **13** than it is for **11** and can perhaps be explained by the occurrence of a small amount of axial ligand dissociation. Beyond C, compounds **11** and **12** do indeed have a second reduction event, however their reversibility was impeded by compound degradation at more negative potentials. Event D is quasi-reversible and cleanly accessed in the case of compound **13** at –1.53 V. The nature of this second reduction is unclear, and the fact that it is seen when the axial ligand is most electron-donating, is counter-intuitive. It is possible that this wave is a result of a degradation product from the previous reduction event (the corresponding DPV peaks have lower amplitudes).

Special mention must be made here about the electrochemical properties of compound **10**. From Table 3.2, which lists voltammetric and IR spectroscopic data of $\text{Ru}_2\text{-CO}$ complexes in the literature, it is clear that the combination of anilinopyridinate equatorial ligands and aryl axial ligand is responsible for increasing the electron density of the $\text{Ru}_2(\text{II,III})$ core to such an extent, that one may now think of it as a ‘masked $\text{Ru}_2(\text{II,II})$ ’ species in terms of $\text{C}\equiv\text{O}$ activation.

Table 3.2. Voltammetry and IR spectroscopy of Ru₂–CO complexes in the literature.

Compound	Oxidation state	E _{1/2} (V vs. Fc ⁺⁰)		ν _{CO} , cm ⁻¹	Reference
		Ru ₂ ^{6+/5+}	Ru ₂ ^{5+/4+}		
[Ru ₂ (dpb) ₄ (CO)] ⁺		0.48	-0.82	2013	(13)
[Ru ₂ (DPhF) ₄ (CO)] ⁺		-	-	2019	(109)
[Ru ₂ (DPhF) ₃ (OAc)(CO)] ⁺	Ru ₂ ⁵⁺	0.31	-0.59	2016	(108)
[(CO)Ru₂(<i>ap</i>)₄Ar]		-0.34	-1.39	1950	This chapter
Ru ₂ (dpb) ₄ (CO)		0.59	-0.37	1924	(13)
Ru ₂ (DPhF) ₄ (CO)	Ru ₂ ⁴⁺	-	-0.20	1929	(109)
[Ru ₂ (dpb) ₄ (CO)] ⁻		-	-	1834	(13)
[Ru ₂ (DPhF) ₄ (CO)] ⁻	Ru ₂ ³⁺	-	-	1840	(109)

3.4 Conclusion

The ligands, CO, CN⁻, RC≡C–C≡C⁻, and HC≡C⁻ differ in their σ-donor and π-acceptor properties, and these differences are accordingly reflected in both the formation and properties of complexes **10–13**. The lack of reactivity of other monosubstituted [Ru₂(*ap*)₄]X complexes (X = halide, CN⁻, RC≡C⁻, N₃⁻) towards CO (see Experimental Section) suggests that the axial aryl moiety in **1** has a crucial role to play. Thus, in addition to tuning the structural, electronic and magnetic properties of a homobimetallic system using relatively simple axial ligands, it is shown that the reactivity of the distal metallic site can be enhanced by an extended metal–metal–ligand interaction between Ru₂ and an aryl ligand. Whereas the reaction of **1** (Ru₂⁵⁺) with CN⁻, RC≡C–C≡C⁻, and HC≡C⁻ was accompanied by facile oxidation by O₂ to afford the Ru₂⁶⁺ complexes **11–13**, the reaction with CO resulted in the isolation of **10**, a rare example of a Ru₂⁵⁺ species possessing a doublet ground state. These reactions are accompanied by changes in molecular and electronic structures, which are completely reversible in the case of **10**. Also interesting is the widely dispersed NMR chemical shifts in **13**, which has been attributed to a low-lying triplet excited state.

Further examination of similar Ru₂⁶⁺ complexes is ongoing. Overall, this chapter highlights the broader scope of reactivity than can be elicited from the vacant metal center in dinuclear paddlewheel systems by manipulating metal–metal–ligand interactions, and also the extreme sensitivity of the electronic structures of these complexes to even minor variations in axial ligands.

3.5 Experimental Section

General considerations. Ru₂(*ap*)₄Cl²⁴ and Ru₂(*ap*)₄(C₆H₄-4-NMe₂) (**1**) were prepared using literature methods. ⁿBuLi (1.6 M in hexanes) was purchased from Sigma-Aldrich. Bis(trimethylsilyl)-1,3-butadiyne was purchased from Alfa Aesar and freshly sublimed before use. Sodium acetylide (18 wt% slurry in xylene, ρ = 0.89 g/mL) was purchased from Sigma-Aldrich. KCN and [ⁿBu₄N][PF₆] were purchased from commercial sources and used as received. Tetrahydrofuran was freshly distilled over sodium/benzophenone prior to use. All reactions were performed under dry N₂ atmosphere implementing standard Schlenk techniques where noted. UV-Vis/NIR spectra were obtained with a JASCO V-670 spectrophotometer in THF solutions. ¹H NMR spectra were recorded on a Varian Inova 300 spectrometer operating at 300 MHz. Cyclic and differential pulse voltammograms were recorded in 0.1 M [ⁿBu₄N][PF₆] solution (THF, Ar or N₂-degassed) on a CHI620A voltammetric analyzer with a glassy carbon working electrode (diameter = 2 mm), a Pt-wire auxiliary electrode, and a Ag/AgCl quasi-reference electrode. The concentration of Ru₂-species is always *ca.* 1.0 mM. The Fc⁺⁰ couple was observed at *ca.* 0.542 ± 0.113 V (vs Ag/AgCl QRE) at the noted experimental conditions. Electrospray ionization mass spectra (ESI-MS) were collected on an Advion expression^L mass spectrometer with an *m/z* range of 10 – 2000. Elemental analyses were performed by Atlantic Microlab, Inc. DC temperature-dependent magnetization was measured from 2 to 300 K using zero-field-cooling (ZFC) mode on a Quantum Design MPMS-3 SQUID magnetometer. Both compound **1** and **10** were measured under a magnetic field of 1000 Oe with a cooling rate of 2 K/min. The whole magnetic measurement was done under vacuum of a few torr.

Synthesis of (O≡C)Ru₂(*ap*)₄(C₆H₄-4-NMe₂) (10**).** Carbon monoxide gas was bubbled through a 20 mL THF solution of **1** (50 mg, mmol) in a Schlenk tube. An immediate colour change from red-black to deep red was observed. Solvent was evaporated and the red solid thus obtained was dried in vacuo. Prior to collecting the solid for analysis, the tube was re-pressurized with CO_(g). Yield: 51 mg, 99 %. Crystals suitable for X-ray diffraction analysis were grown in a tube sealed

with a slight pressure of CO_(g) by layering hexanes over a concentrated solution of **10** in a 1:1 mixture of benzene and toluene.

Data for **10**. Anal. Found (Calcd.) for C₅₃H₅₂N₉O₄Ru₂ (**10**·3H₂O): C, 58.97 (58.88); H, 4.46 (4.85); N, 11.23 (11.66). ESI-MS (m/z, based on ¹⁰¹Ru): [M]⁺ = 1028.2, [M-CO]⁺ = 1000.2. UV-Vis (in THF) λ, nm, (ε, M⁻¹cm⁻¹): 336 (33000, sh), 486 (6300), 815 (5700), 1010 (2800, sh). IR $\bar{\nu}$, cm⁻¹: 1950, ν (C≡O). μ_{eff} (25°C) = 1.9 B.M. Electrochemistry (THF, vs. Fc⁺⁰), E_{1/2}/V, ΔE_p/mV, $i_{\text{forward}}/i_{\text{backward}}$: -0.34, 63, 1.03; 0.18, 57, 1.04; -1.39, 59, 1.00.

Synthesis of (N≡C)Ru₂(ap)₄(C₆H₄-4-NMe₂) (11). To a 20 mL solution of **1** (60 mg, 0.06 mmol) in THF was added a 10 mL solution of KCN 20 mg, 0.31 mmol) in MeOH. A rapid color change from black to deep red/purple was observed. O₂ was bubbled through the reaction mixture for 10 minutes during which a distinct color to violet was observed. The solvents were removed in vacuo and the product was extracted from CH₂Cl₂/H₂O. The organic layers were collected, and the product was recrystallized from a 1:20 (v:v) CH₂Cl₂:hexanes mixture at -20°C, as a dark violet microcrystalline solid. Yield: 51 mg, 83%. Crystals suitable for X-ray diffraction analysis were grown by layering hexanes over a concentrated solution of **11** in THF.

Data for **11**. Anal. Found (Calcd.) for C₅₄H₅₀N₁₀OCl₂Ru₂ (**11**·CH₂Cl₂·H₂O): C, 57.52 (57.49); H, 4.43 (4.47); N, 12.34 (12.42). ESI-MS (m/z, based on ¹⁰¹Ru): [M+H]⁺ = 1027.4. UV-Vis (in THF) λ, nm, (ε, M⁻¹cm⁻¹): 345 (13000), 440 (2500, sh), 550 (4000), 600 (3900), 667 (3500), 740 (2400, sh), 1014 (2900). IR $\bar{\nu}$, cm⁻¹: 2084, ν (C≡N). Electrochemistry (THF, vs. Fc⁺⁰), E_{1/2}/V, ΔE_p/mV, $i_{\text{forward}}/i_{\text{backward}}$: -0.11, 64, 1.1; 0.30, 62, 1.2; -0.98, 65, 1.1. ¹H NMR (300 MHz, 293 K, CDCl₃) δ = 3.21 (s, 6H, N(CH₃)₂), 5.60 (br, 4H, *ap*), 6.07 (t, 8H, *ap*, 6.4 Hz), 6.14 (d, 2H, aryl, 6.6 Hz), 6.28 (d, 4H, *ap*, 9.0 Hz), 6.69 (d, 2H, aryl, 6.6 Hz), 6.77–7.21 (m, 16H, *ap*), 7.99 (d, 4H, *ap*, 6.9 Hz).

Synthesis of (TMS-C₄)Ru₂(ap)₄(C₆H₄-4-NMe₂) (12) and (HC₄)Ru₂(ap)₄(C₆H₄-4-NMe₂).(12a). Freshly prepared (Trimethylsilyl)buta-1,3-diyne-1-yl)lithium (1.4 mmol) was added to **1** (175 mg, 0.18 mmol) at room temperature, and allowed to stir for 12 h under N₂. The reaction was constantly monitored by TLC and ESI-MS to confirm consumption of starting material. After 12 h, the color of the solution had completely turned from black to deep red. At this juncture, after all of **1** had been consumed, the reaction was exposed to air, and O₂ was bubbled through the solution. Within a few minutes, the solution acquired a deep green color, indicating complete oxidation. The crude solution was concentrated and filtered through a deactivated (with triethylamine) silica plug. The filtrate was collected with THF as the sole eluant, and concentrated.

A green microcrystalline solid was obtained by recrystallization from THF/n-pentane. Yield: 125 mg, 64%. Crystals suitable for X-ray diffraction analysis were grown by layering hexanes over a concentrated solution of **12** in CH₂Cl₂. Deprotection of the TMS group was accomplished by adding excess NaOH (1 g, 250 mmol) to a 50 mg sample of **12**. After 6 h, when the reaction had gone to completion, the solvent was removed and the product extracted from CH₂Cl₂/H₂O. The organic layers were combined, and a green microcrystalline solid was recrystallized from THF/n-pentane at -20 °C for 48 h. Yield: 30 mg, 64%.

Data for **12**. ESI-MS (m/z, based on ¹⁰¹Ru): [M+H⁺] = 1121.4. UV-Vis (in THF) λ, nm, (ε, M⁻¹cm⁻¹): 358 (28000, sh), 455 (8300, sh), 570 (7000, sh), 686 (11000), 776 (6500, sh), 1067 (4300). IR $\bar{\nu}$, cm⁻¹: 2070 (sh), 2104, 2166 ν (C≡C). Electrochemistry (THF, vs. Fc⁺⁰), E_{1/2}/V, ΔE_p/mV, i_{forward}/i_{backward}: -0.16, 131, 1.1; 0.72, 129, 2.0; -1.1, 82, 1.1. ¹H NMR (300 MHz, 293 K, CDCl₃) δ = 0.23 (s, 9H, Si(CH₃)₃), 4.10 (s, 6H, N(CH₃)₂), 4.65 (d, 2H, aryl, 9.0 Hz), 5.02 (t, 4H, *ap*, 6.0 Hz), 5.45 d, 4H, *ap*, 9.0 Hz), 5.65 (br, 8H, *ap*), 6.80 (d, 2H, aryl, 9.0 Hz), 6.98 (t, 4H, *ap*, 6.0 Hz), 7.21 (t, 8H, *ap*, 7.5 Hz), 7.38 (t, 4H, *ap*, 7.5 Hz), 8.31 (d, 4H, *ap*, 9.0 Hz).

Data for **12a**. ESI-MS (m/z, based on ¹⁰¹Ru): [M+H⁺] = 1049.2. UV-Vis (in THF) λ, nm, (ε, M⁻¹cm⁻¹): 351 (24000, sh), 451 (7200, sh), 570 (7000, sh), 665 (7300), 777 (4400, sh), 1030 (2900), 1281 (1600, sh). IR $\bar{\nu}$, cm⁻¹: 2118, 2036 ν (C≡C); 3301, ν (C≡C-H). ¹H NMR (300 MHz, 293 K, CDCl₃) δ = -0.37 (br, 1H, C≡CH), 3.91 (s, 6H, N(CH₃)₂), 5.02 (d, 2H, aryl, 9.0 Hz), 5.27 (t, 4H, *ap*, 6.0 Hz), 5.67 (t, 12H, multiple *ap*), 6.78 (d, 2H, aryl), 7.00 (t, 4H, *ap*, 7.5 Hz), 7.20 (t, 8H, *ap*, 7.5 Hz), 7.30 (t, 4H, aryl, 8.1 Hz), 8.24 (t, 4H, *ap*, 6.0 Hz).

Synthesis of (HC≡C)Ru₂(*ap*)₄(C₆H₄-4-NMe₂) (13**).** Sodium acetylide slurry (1.1 mL, 18 wt%, *ca.* 3.7 mmol) was added to a 10 mL THF solution of **1** (60 mg, 0.060 mmol). The color of the solution gradually changed from red-black to blue-black over the course of 24 h under N₂. Aliquots of the reaction mixture were retrieved for TLC analysis. The ratio of the starting material to product (*ca.* 2:3) did not noticeably change after 24–36 h despite addition of excess sodium acetylide. At this juncture, O₂ was bubbled through the reaction mixture for 30 minutes. The crude reaction mixture was purified by column chromatography. The blue fraction was eluted with triethylamine/EtOAc/hexanes (1/10/70, v/v/v). Yield: 22 mg, 36%. Crystals suitable for X-ray diffraction analysis were grown by layering hexanes over a concentrated solution of **13** in THF. Data for **13**. Anal. Found (Calcd.) for C₆₂H₇₁N₉O₆Ru₂ (**13**·2THF·4H₂O): C, 59.78 (60.03); H, 5.45 (5.77); N, 9.90 (10.16). ESI-MS (m/z, based on ¹⁰¹Ru): [M⁺] = 1024.2. UV-Vis (in THF) λ, nm,

(ϵ , $\text{M}^{-1}\text{cm}^{-1}$): 345 (25000, sh), 450 (5600, sh), 570 (7000, sh), 641 (9700), 740 (5800, sh), 1060 (3600). IR $\bar{\nu}$, cm^{-1} : 1947, $\nu(\text{C}\equiv\text{C})$; 3280, $\nu(\text{C}\equiv\text{C}-\text{H})$. Electrochemistry (THF, vs. $\text{Fc}^{+/0}$), $E_{1/2}/\text{V}$, $\Delta E_p/\text{mV}$, $i_{\text{forward}}/i_{\text{backward}}$: -0.21, 66, 1.1; 0.21, 67, 1.2; -1.2, 71, 1.2; -1.53, 188, 1.4. ^1H NMR (300 MHz, 293 K, CDCl_3) δ = -10.74 (s, 1H, $\text{C}\equiv\text{CH}$), 1.39 (d, 2H, aryl, 8.4 Hz), 2.99 (t, 4H, *ap*, 6.3 Hz), 3.90 (d, 4H, *ap*, 8.8 Hz), 5.34 (br, 4H, *ap*), 5.66 (s, 6H, $\text{N}(\text{CH}_3)_2$), 5.92 (br, 4H, *ap*), 6.86 (t, 4H, *ap*, 6.9 Hz), 6.96 (d, 2H, aryl, 8.4 Hz), 7.49 (br, 8H, *ap*), 8.00 (t, 4H, *ap*, 7.5 Hz), 3.90 (d, 4H, *ap*, 6.9 Hz).

Attempted reactions of CO with $[\text{Ru}_2(\text{ap})_4]\text{X}$ ($\text{X} = \text{Cl}, \text{CN}, \text{C}\equiv\text{CR}, \text{N}_3$): The Ru_2 starting materials were prepared via established literature procedures through metathesis reactions of $\text{Ru}_2(\text{ap})_4\text{Cl}$ with KCN,¹² $\text{MC}\equiv\text{CR}$ ($\text{M} = \text{Li}, \text{R} = \text{Ph}, \text{C}_6\text{H}_4\text{-4-NMe}_2, \text{M} = \text{Na}, \text{R} = \text{H}$)^{4,71} and NaN_3 ,¹¹³ respectively. CO was bubbled through THF solutions of $[\text{Ru}_2(\text{ap})_4]\text{X}$ for *ca.* 1 min at room temperature. When no color change was observed, the reaction was attempted at an elevated temperature (50–60 °C) for *ca.* 1 min. No color change was observed, and ESI-MS of the reaction mixtures consistently showed no new product peaks.

Crystallographic details. Single-crystal X-ray diffraction data for compounds **10–13** at 150 K were collected on a Bruker AXS D8 Quest CMOS diffractometer using Mo- $\text{K}\alpha$ radiation ($\lambda = 0.71073 \text{ \AA}$). Data was collected and processed using APEX3,⁴² and the structures were solved using SHELXT suite of programs^{43,44} and refined to convergence on F^2 and against all independent reflections by full-matrix least-squares using SHELXL.^{45,46} All non-hydrogen atoms were refined anisotropically and hydrogen atoms were geometrically placed and allowed to ride on their parent atoms.

Computational details. All Density Functional Theory (DFT) calculations were carried out using Gaussian16 Rev. A03.⁵⁴ Geometry optimizations of **10** based on the corresponding crystal structure were done using the restricted open-shell formalism with the B3LYP^{35,37,38,114} and BP86⁸⁴ functionals. Minima were confirmed through frequency analysis. The output from B3LYP was found to be closer to experimentally determined metrical parameters. Table 3.S6 lists the comparison between experimental and DFT-optimized structures (**10** and **10'**, respectively). All subsequent analyses, therefore, were performed with the B3LYP functional, basis sets def2-TZVP (with ECP) for Ru atoms and def2-SVP for C, H, O and N atoms,^{79,80} and the conductor-like polarizable continuum solvent model (CPCM) for tetrahydrofuran.¹¹⁵ Dispersion effects were modelled using Grimme's empirical dispersion correction parameters.⁸¹

3.6 Supporting Information

Table 3.S1. Selected Bond Lengths (Å) and Angles (deg) for Compounds **10–13**.

	10, CO	11, CN	12	13, CCH
Ru1–Ru2	2.5060(3)	2.4857(7)	2.4887(5)	2.4887(5)
Ru1–C1	2.053(2)	2.077(7)	2.046(2)	2.058(4)
Ru2–C53	1.877(2)	2.021(7)	1.977(2)	2.005(4)
C53–N10/C54/O1	1.146(2)	1.14(1)	1.227(3)	1.181(6)
Ru2–Ru1–C1	155.61(6)	157.0(2)	153.99(6)	156.02(9)
Ru1–Ru2–C53	169.50(7)	166.9(2)	166.22(6)	166.45(9)
Ru1–N1	2.157(2)	2.149(5)	2.170(2)	2.132(2)
Ru1–N3	2.040(1)	2.138(5)	2.133(2)	2.156(2)
Ru1–N5	2.068(2)	2.038(4)	2.023(2)	2.038(2)
Ru1–N7	2.166(1)	2.037(5)	2.046(2)	2.018(3)
Ru2–N2	2.028(2)	1.974(5)	1.978(2)	2.007(2)
Ru2–N4	2.136(2)	1.988(5)	2.005(1)	1.978(3)
Ru2–N6	2.069(2)	2.068(5)	2.158(2)	2.080(2)
Ru2–N8	2.022(1)	2.165(4)	2.061(1)	2.164(2)

Table 3.S2. Crystallographic details for (OC)Ru₂(ap)₄(C₆H₄-4-NMe₂) (**10**)

	AR_3_99_0m (CCDC 2000257)
Crystal data	
Chemical formula	C _{59.39} H _{52.77} N ₉ ORu ₂
<i>M_r</i>	1110.66
Crystal system, space group	Triclinic, <i>P</i> $\bar{1}$
Temperature (K)	150
<i>a</i> , <i>b</i> , <i>c</i> (Å)	12.5822 (9), 12.8242 (9), 17.5440 (11)
α , β , γ (°)	71.387 (3), 73.114 (2), 75.340 (3)
<i>V</i> (Å ³)	2526.7 (3)
<i>Z</i>	2
Radiation type	Mo <i>K</i> α
μ (mm ⁻¹)	0.65
Crystal size (mm)	0.70 × 0.30 × 0.30
Data collection	
Diffractometer	Bruker AXS D8 Quest CMOS diffractometer
Absorption correction	Multi-scan <i>SADABS</i> 2016/2: Krause, L., Herbst-Irmer, R., Sheldrick G.M. & Stalke D., <i>J. Appl. Cryst.</i> 48 (2015) 3-10
<i>T_{min}</i> , <i>T_{max}</i>	0.674, 0.746
No. of measured, independent and observed [<i>I</i> > 2 σ (<i>I</i>)] reflections	83101, 16824, 13493
<i>R_{int}</i>	0.036
($\sin \theta/\lambda$) _{max} (Å ⁻¹)	0.737
Refinement	
<i>R</i> [<i>F</i> ² > 2 σ (<i>F</i> ²)], <i>wR</i> (<i>F</i> ²), <i>S</i>	0.034, 0.075, 1.08
No. of reflections	16824
No. of parameters	707
No. of restraints	204
H-atom treatment	H-atom parameters constrained
Δ) _{max} , Δ) _{min} (e Å ⁻³)	2.81, -1.13

Table 3.S3. Crystallographic details for (NC)Ru₂(ap)₄(C₆H₄-4-NMe₂) (**11**)

	AR_3_21_0m (CCDC 2000255)
Crystal data	
Chemical formula	C ₆₁ H ₆₂ N ₁₀ O ₂ Ru ₂
<i>M</i> _r	1169.34
Crystal system, space group	Monoclinic, <i>P</i> 2 ₁ / <i>c</i>
Temperature (K)	150
<i>a</i> , <i>b</i> , <i>c</i> (Å)	19.0728 (8), 16.6306 (7), 18.7099 (7)
β (°)	117.995 (2)
<i>V</i> (Å ³)	5240.2 (4)
<i>Z</i>	4
Radiation type	Cu <i>K</i> α
μ (mm ⁻¹)	5.10
Crystal size (mm)	0.2 × 0.1 × 0.05
Data collection	
Diffractometer	Bruker AXS D8 Quest CMOS diffractometer
Absorption correction	Multi-scan <i>SADABS</i> 2016/2: Krause, L., Herbst-Irmer, R., Sheldrick G.M. & Stalke D. (2015). <i>J. Appl. Cryst.</i> 48 3-10.
<i>T</i> _{min} , <i>T</i> _{max}	0.477, 0.754
No. of measured, independent and observed [<i>I</i> > 2σ(<i>I</i>)] reflections	35321, 10759, 7585
<i>R</i> _{int}	0.091
(sin θ/λ) _{max} (Å ⁻¹)	0.640
Refinement	
<i>R</i> [<i>F</i> ² > 2σ(<i>F</i> ²)], <i>wR</i> (<i>F</i> ²), <i>S</i>	0.061, 0.174, 1.07
No. of reflections	10759
No. of parameters	678
H-atom treatment	H-atom parameters constrained
Δ _{max} , Δ _{min} (e Å ⁻³)	1.39, -1.37

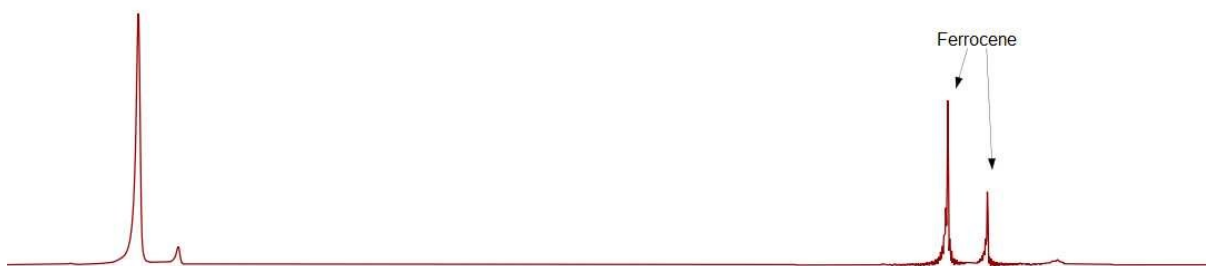
Table 3.S4. Crystallographic details for (TMS-C₄)Ru₂(ap)₄(C₆H₄-4-NMe₂) (**12**)

	AR_3_11_0m
Crystal data	
Chemical formula	C ₆₂ H ₆₂ Cl ₀ N ₉ Ru ₂ Si
<i>M_r</i>	1163.43
Crystal system, space group	Triclinic, <i>P</i> ⁻ 1
Temperature (K)	150
<i>a</i> , <i>b</i> , <i>c</i> (Å)	10.5987 (5), 15.4720 (8), 18.8347 (10)
α, β, γ (°)	105.259 (2), 100.321 (2), 101.425 (2)
<i>V</i> (Å ³)	2831.9 (3)
<i>Z</i>	2
Radiation type	Mo <i>K</i> α
μ (mm ⁻¹)	0.60
Crystal size (mm)	0.65 × 0.40 × 0.22
Data collection	
Diffractometer	Bruker AXS D8 Quest CMOS diffractometer
Absorption correction	Multi-scan <i>SADABS</i> 2016/2: Krause, L., Herbst-Irmer, R., Sheldrick G.M. & Stalke D., <i>J. Appl. Cryst.</i> 48 (2015) 3-10
<i>T_{min}</i> , <i>T_{max}</i>	0.664, 0.747
No. of measured, independent and observed [<i>I</i> > 2σ(<i>I</i>)] reflections	64618, 21104, 17336
<i>R_{int}</i>	0.039
(sin θ/λ) _{max} (Å ⁻¹)	0.772
Refinement	
<i>R</i> [<i>F</i> ² > 2σ(<i>F</i> ²)], <i>wR</i> (<i>F</i> ²), <i>S</i>	0.038, 0.109, 0.97
No. of reflections	21104
No. of parameters	701
No. of restraints	87
H-atom treatment	H-atom parameters constrained
Δ _{max} , Δ _{min} (e Å ⁻³)	1.95, -1.52

Table 3.S5. Crystallographic details for (HCC)Ru₂(ap)₄(C₆H₄-4-NMe₂) (**13**)

	AR_3_173_0m (CCDC 2000256)
Crystal data	
Chemical formula	C ₆₂ H ₆₃ N ₉ O ₂ Ru ₂
<i>M_r</i>	1168.35
Crystal system, space group	Triclinic, <i>P</i> $\bar{1}$
Temperature (K)	150
<i>a</i> , <i>b</i> , <i>c</i> (Å)	11.3227 (5), 14.1697 (6), 17.6704 (7)
α , β , γ (°)	109.063 (2), 102.115 (3), 92.949 (3)
<i>V</i> (Å ³)	2597.70 (19)
<i>Z</i>	2
Radiation type	Cu <i>K</i> α
μ (mm ⁻¹)	5.14
Crystal size (mm)	0.20 × 0.15 × 0.14
Data collection	
Diffractometer	Bruker AXS D8 Quest CMOS diffractometer
Absorption correction	Multi-scan <i>SADABS</i> 2016/2: Krause, L., Herbst-Irmer, R., Sheldrick G.M. & Stalke D. (2015). <i>J. Appl. Cryst.</i> 48 3-10.
<i>T_{min}</i> , <i>T_{max}</i>	0.530, 0.753
No. of measured, independent and observed [<i>I</i> > 2 σ (<i>I</i>)] reflections	29336, 9759, 8521
<i>R_{int}</i>	0.057
($\sin \theta/\lambda$) _{max} (Å ⁻¹)	0.610
Refinement	
<i>R</i> [<i>F</i> ² > 2 σ (<i>F</i> ²)], <i>wR</i> (<i>F</i> ²), <i>S</i>	0.040, 0.114, 1.01
No. of reflections	9759
No. of parameters	724
No. of restraints	216
H-atom treatment	H-atom parameters constrained
Δ _{max} , Δ _{min} (e Å ⁻³)	1.24, -1.30

Compound 1_C6D6
H1 standard parameters, CDCl3.



Compound 2_C6D6
H1 standard parameters, CDCl3.



7.6 7.4 7.2 7.0 6.8 6.6 6.4 6.2 6.0 5.8 5.6 5.4 5.2 5.0 4.8 4.6 4.4 4.2 4.0 3.8 3.6 3.4 3.2 3.0
ppm

Figure 3.S1. ^1H NMR spectra of **1** (top) and **10** (bottom) in C_6D_6 at 293 K, containing capillary inserts for Evans method³⁰ magnetometry.

$$\chi_m = \frac{3000 \times \Delta f \times 300}{F \times 4\pi \times [\text{Ru}_2]}$$

(where F = frequency of the spectrometer in Hz, Δf = difference in chemical shifts of Fc peak in ppm, $[\text{Ru}_2]$ = concentration of the diruthenium species in mol.L^{-1})

Using the above equation and applying appropriate diamagnetic corrections, μ_{eff} for compound **1** and **10** were calculated:

$$\mu_{\text{eff},1} = 4.1 \mu_B; \mu_{\text{eff},4} = 1.9 \mu_B.$$

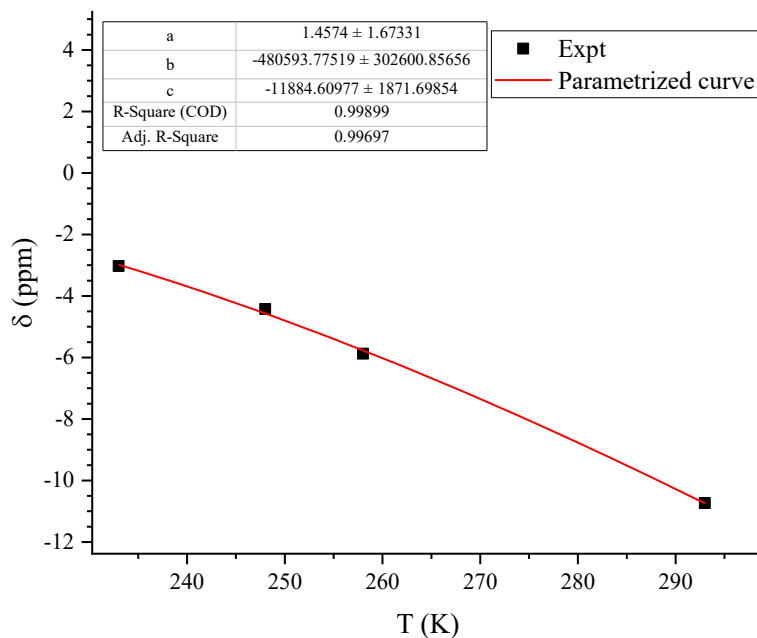


Figure 3.S2a. Experimental VT-NMR chemical shift data for $\delta(\text{C}\equiv\text{C}-\text{H})$ modelled according to the parametrized equation Eq 3.1.

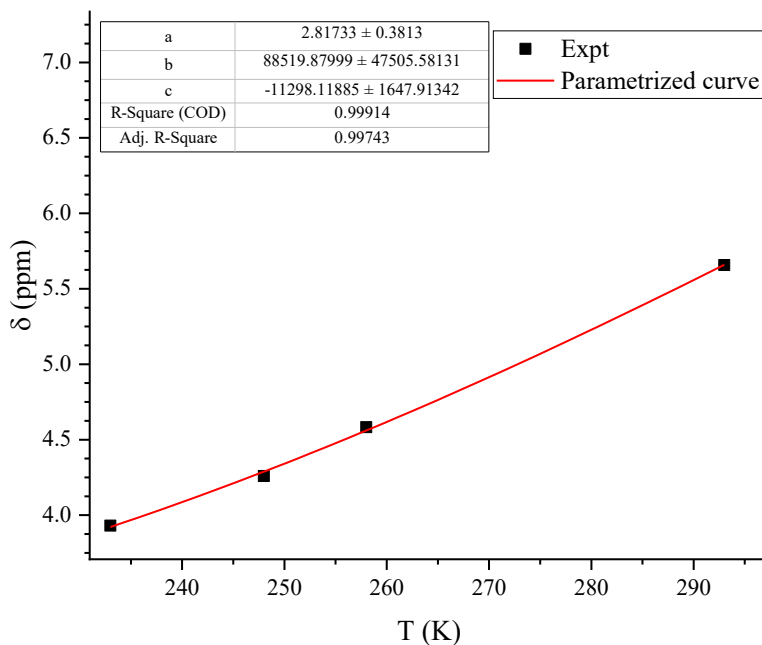


Figure 3.S2b. Experimental VT-NMR chemical shift data for $\delta(\text{N}-(\text{CH}_3)_2)$ modelled according to the parametrized equation Eq 3.1.

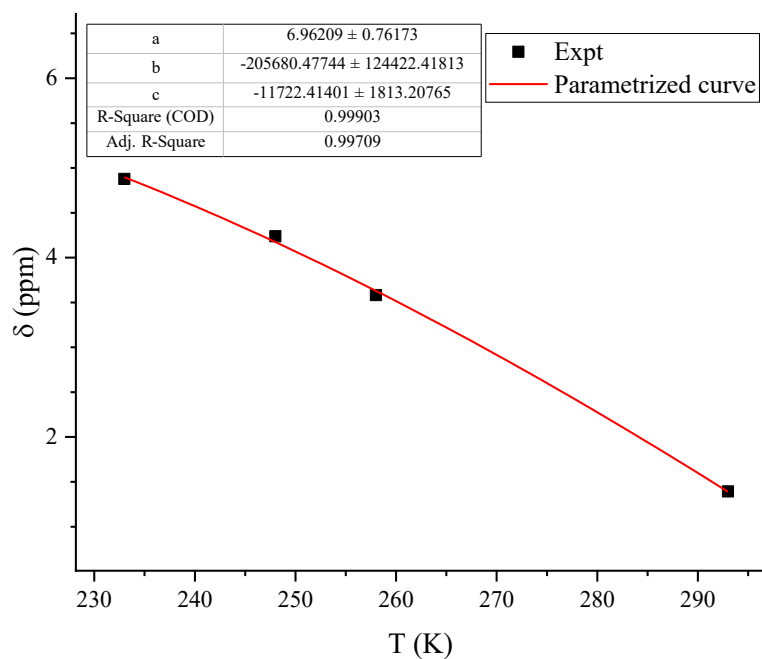


Figure 3.S2c. Experimental VT-NMR chemical shift data for $\delta(\text{Aryl}(\text{CH}))$ modelled according to the parametrized equation Eq 3.1.

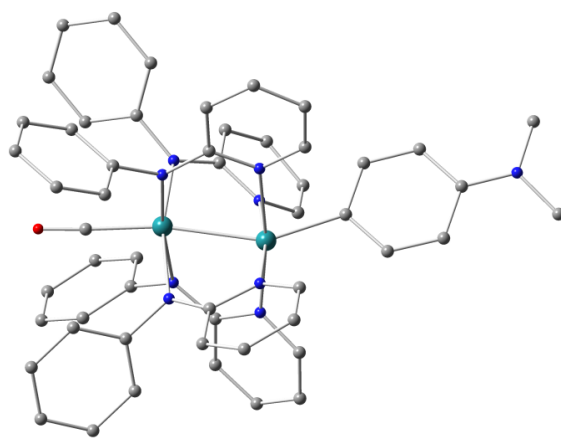


Figure 3.S3. DFT-optimized structure (**10'**) derived from the single crystal X-ray diffraction data of compound **10**.

Table 3.S6. Selected experimental and DFT-optimized metrical parameters of **4** and **4'**.

	10 (XRD)	10' (DFT, B3LYP)	10' (DFT, BP86)
Ru1–Ru2	2.5060(3)	2.52113	2.54806
Ru1–C1	2.053(2)	2.02168	2.03964
Ru2–C53	1.877(2)	1.85911	1.84910
C53–O1	1.146(2)	1.15457	1.17423
Ru2–Ru1–C1	155.61(6)	150.41711	151.40244
Ru1–Ru2–C53	169.50(7)	170.60788	169.55364

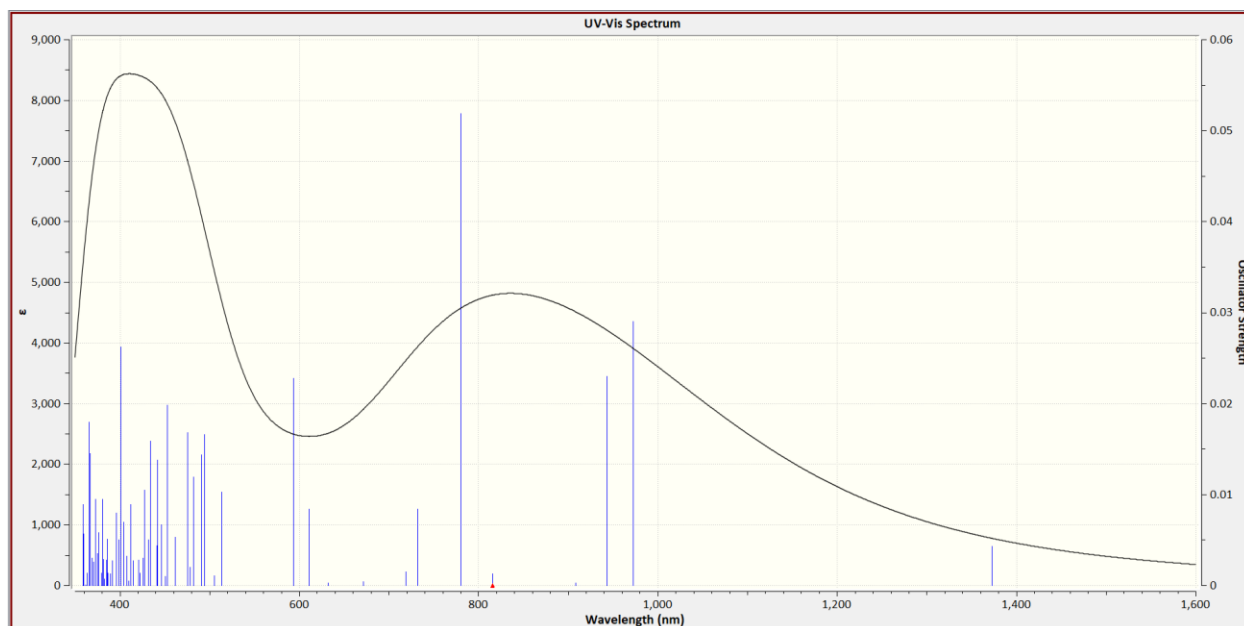


Figure 3.S4. TD-DFT spectrum of DFT-optimized **10'** (compare with experimental spectrum in Figure S10)

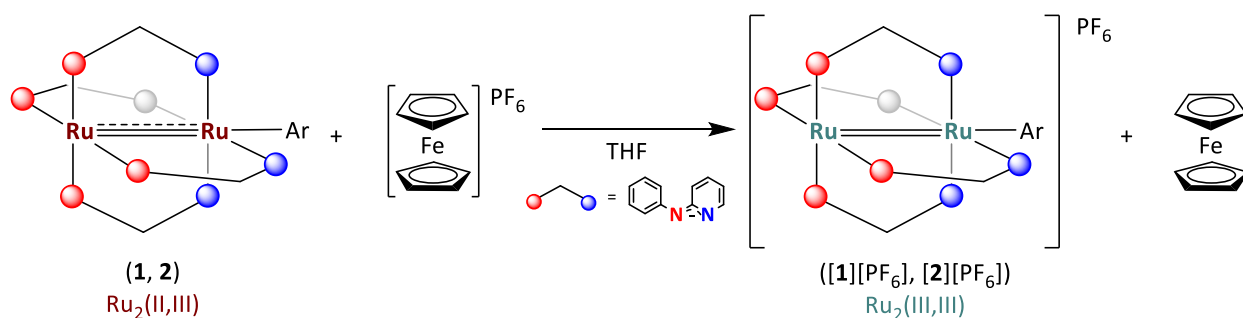
CHAPTER 4. MISCELLANEOUS

4.1 Abstract

In this chapter, some miscellaneous projects that evolved as off-shoots of Chapters 1–3 are discussed. In part (i), the oxidative stability of compounds **1** and **2** has been leveraged to stably access the Ru_2^{6+} oxidation state in these axially monosubstituted compounds both chemically and electrochemically. A second oxidation to form the $\text{Ar}^{+\cdot}$ radical cation has also been achieved electrochemically. In part (ii), some improved DFT and TD-DFT calculations shed light on the nature of the electronic transitions in complexes **1**, $[\mathbf{1}]^+$ and **4**. The role of the para N-substitution in the aryl ligand on the electronic structure of $\text{Ru}_2(\text{II,III})$ monoaryls (Chapter 1) is explained here. Finally, in part (iii), synthetic efforts to link two Ru_2 units together via arylene bridges is discussed.

4.2 Results and Discussion

4.2.1 Redox chemistry and spectroelectrochemistry of $\text{Ru}_2(\text{II,III})$ monoaryls



Scheme 4.1. Synthesis of $[\mathbf{1}]\text{PF}_6$ and $[\mathbf{2}]\text{PF}_6$.

The oxidative stability of the $\text{Ru}_2(\text{II,III})$ compounds **1** ($\text{Ru}_2(\text{ap})_4(\text{C}_6\text{H}_4\text{-4-NMe}_2)$) and **2** ($\text{Ru}_2(\text{ap})_4(\text{C}_6\text{H}_4\text{-4-(N,N-(C}_6\text{H}_4\text{-4-OMe)}_2))$) prompted us to explore their chemical and electrochemical oxidation, while simultaneously monitoring them spectroscopically in order to gain any insight into their electronic structures. The oxidation potential ($\text{Ru}_2^{6+/5+}$ couple) of compounds **1** and **2** are -0.38 V and -0.34 V in CH_2Cl_2 (vs. $\text{Fc}^{+/0}$), respectively. Electrochemically, both processes were found to be reversible (section 1.3.5). So, oxidation of both complexes with

ferrocenium hexafluorophosphate (FcPF₆) was attempted. In particular, compound [2]⁺ was thought to be a slightly more viable target due to the stability provided by extended conjugation through the triarylamine moiety.^{27,116}

The syntheses of [1]PF₆ and [2]PF₆ were attempted by oxidation with FcPF₆ (Scheme 4.1). While the stability of [1]PF₆ was questionable, and the reaction led to somewhat intractable product mixtures, [2]PF₆ was more reliably isolated as a red solid upon reaction with a slight excess of FcPF₆, added in two stages. Addition of 1.3 equivalents of FcPF₆ allowed for the consumption for most of the starting material (**2**), which turned the color of the reaction mixture from blue-green to deep red. Further addition of 1.7 equivalents of Fc⁺ resulted in complete reaction and intensifying of the deep red color. After solvent removal and recrystallization, a deep red solid was isolated. Characterization by TLC was precluded by active decomposition of the compound on silica gel, and ESI-MS was not useful to differentiate between **2** and [2]⁺. However, electronic absorption spectroscopy was able to clearly differentiate between starting material and product (Figure 4.1). Additionally, room temperature solid-state magnetometry measurements of [2][PF₆] suggested the presence of two unpaired electrons ($\mu_{\text{eff}} = 2.9 \mu_B$). Despite the inability to isolate [1][PF₆] as a stable compound, it was found possible to oxidize both **1** and **2** to [1]⁺ and [2]⁺, respectively, *in situ* during UV-Vis/NIR absorption measurements by adding an excess of FcPF₆ to the cuvette. Remarkably, it was also found that the oxidation was reversible; addition of NaBH₄ reduced the oxidized complexes back to their neutral, Ru₂(II,III) forms.

Clearly, [1]⁺ and [2]⁺ are very similar complexes; both compounds take on a deep red/purple color in solution. This is accompanied by the disappearance of bands centered around 430 nm, 579–615 nm, and 710–900 nm. A very prominent ‘double-humped’ feature of much higher intensity appears between 800–1500 nm for both complexes, along with a band at around 500 nm, one that is of comparable intensity to the peaks observed in the starting materials. To a loose first approximation, these spectral features are very similar to those of [Ru₂(*ap*)₄(C≡CSiMe₃)]⁺, also produced *in situ* during spectroelectrochemistry of the neutral species.⁵ Both the bands were assigned as ligand-to-metal charge-transfer (LMCT) transitions that red-shift upon oxidation of the Ru₂ core and subsequent stabilization of the d-orbitals. Upon reduction with NaBH₄, the original spectroscopic features are restored, and this is also reflected in the restoration of the colors of the THF solutions (black for **1** and blue-green for **2**).

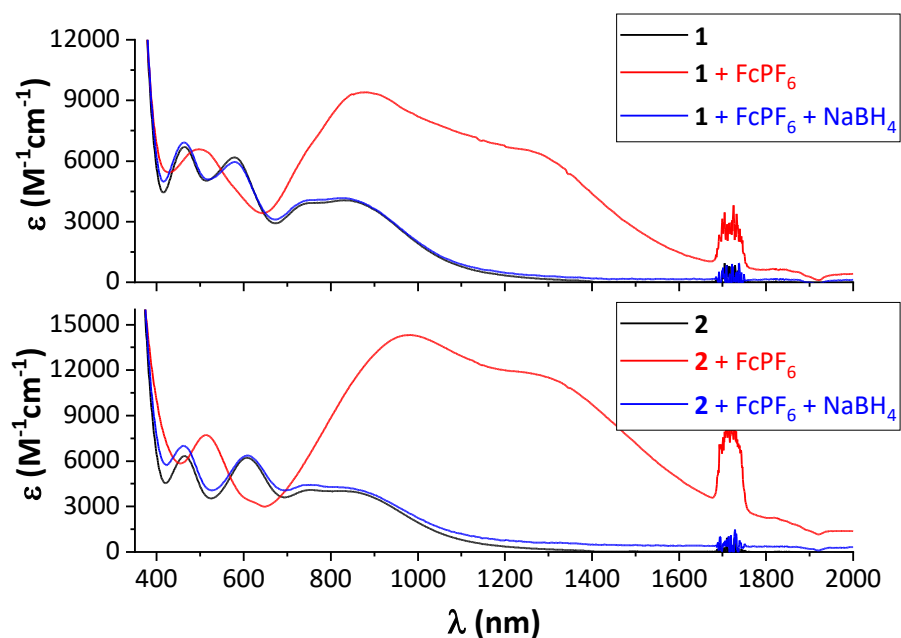


Figure 4.1. UV-Vis/NIR absorption spectrum of **1** and **1**⁺, and **2** and **2**⁺.

The first oxidation event is expected to be localized mainly to the Ru₂ core, going from Ru₂(II,III) to Ru₂(III,III) and back to Ru₂(II,III). The para amino substituent on the aryl ligands in **1** and **2** makes possible the existence of metal–ligand multiple bonding in the oxidized complexes [**1**]⁺ and [**2**]⁺. Unfortunately, the lack of an X-ray structure of these species limits any further conclusions from being drawn. Nonetheless, encouraged by these spectroscopic results, spectroelectrochemical characterization of compound **2** was attempted. The results are shown in Figures 4.2–4.3.

As the potential was slowly swept in the positive direction, the differences between the first and second oxidation events became clear. Figure 4.2 (left) shows the first oxidation event, which is likely Ru₂-based; Ru₂⁵⁺ to Ru₂⁶⁺. Three isosbestic points at 499 nm, 544 nm and 753 nm suggest that this is a clean process with no other intermediates or decomposition by-products. This agrees well with the fact that this oxidation event is electrochemically reversible (section 1.3.5) and that the product of chemical oxidation by ferrocenium can be stably isolated. Notably, the spectroscopic features seen here are almost exactly the same as those observed for the chemically oxidized [**2**][PF₆] complex (Figure 4.4). Further, upon increasing the potential to more positive values, new spectroscopic features begin to appear while the ones for [**2**]⁺ disappear at the same rate. The isosbestic points at *ca.* 1209 nm and *ca.* 1487 nm are occluded by instrumental noise, but

the ones at 338 nm and 396nm (Figure 4.S1) are much more clearly discernable. Once again, these point to a clean oxidation process without significant decomposition or other intermediates. The second oxidation event in the voltammetric analysis of compounds **1** and **2** was assigned as aryl ligand-based, specifically localized on the para amino moiety. Figure 4.2 (right) provides confirmation of this based on spectra of triarylamino radical cations in the literature.^{117,118}

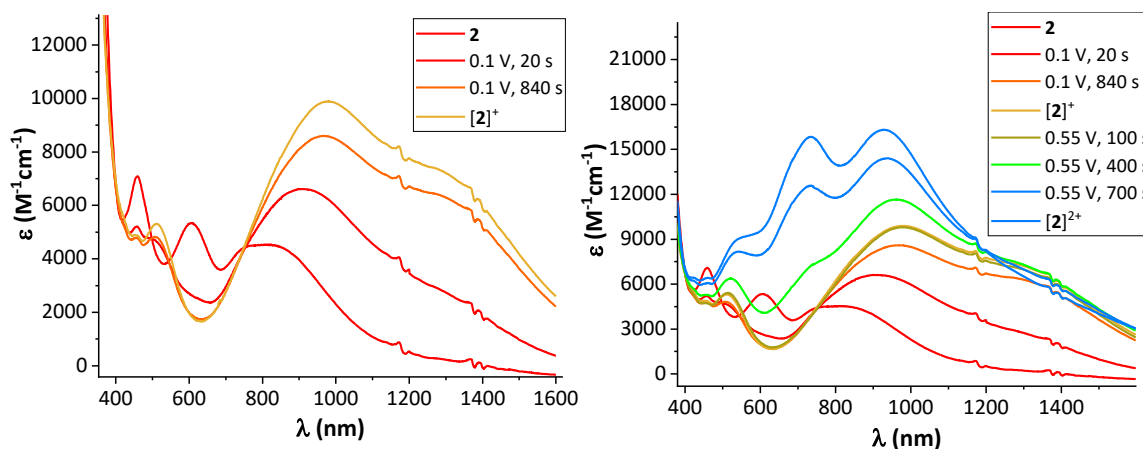


Figure 4.2. Oxidation of **2** to $[2]^+$ (left) and oxidation of $[2]^+$ to $[2]^{2+}$ (right).

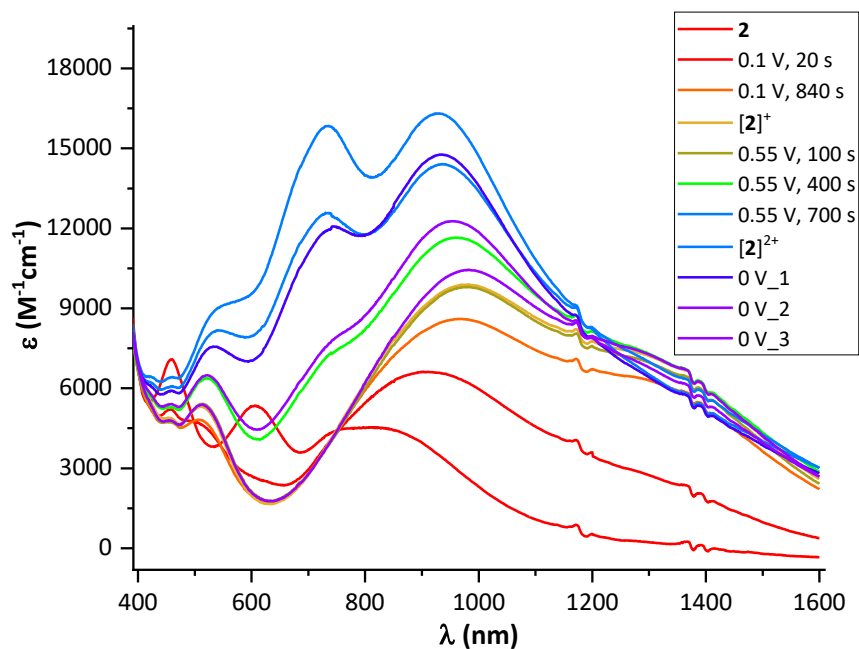


Figure 4.3. The oxidation of compound **2** to $[2]^+$ and $[2]^{2+}$, and subsequent reduction of $[2]^{2+}$ to $[2]^+$ upon removal of the positive bias.

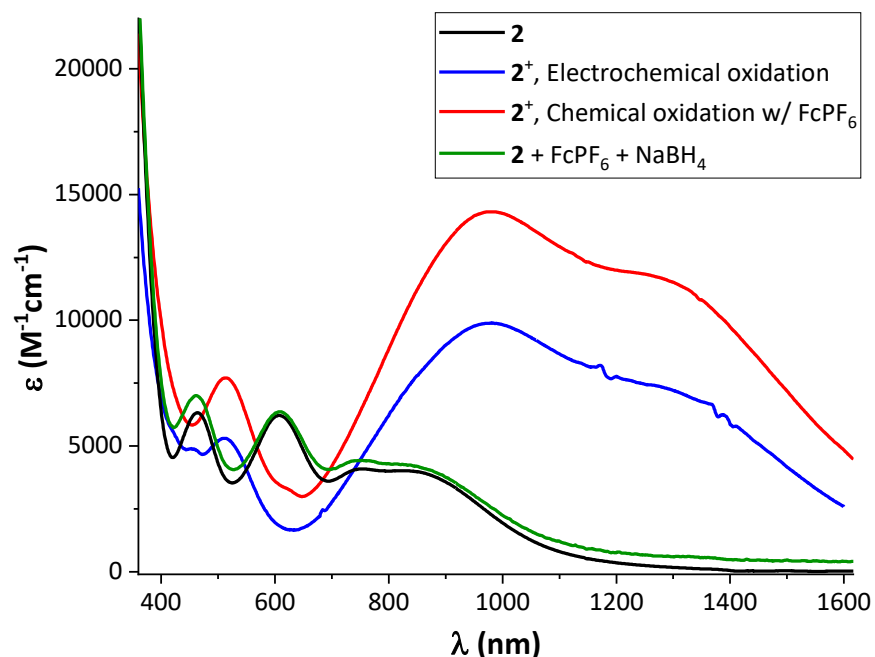


Figure 4.4. Similarities between the chemical and electrochemical oxidation of **2**.

As expected, $[\mathbf{2}]^{2+}$ was found to be much less stable compared to $[\mathbf{2}]^+$, and this can be seen from Figure 4.3; upon removal of the positive bias, $[\mathbf{2}]^{2+}$ is rapidly reduced to $[\mathbf{2}]^+$ (likely due to diffusion of **2** from other parts of the OTTLE cell, and comproportionation of **2** and $[\mathbf{2}]^{2+}$). Finally, based on magnetic susceptibility measurements (see above), the d-electron configuration $\sigma^2\pi^4\delta^2(\pi^*\delta^*)^2$ or, more likely, $\sigma^2\pi^4\delta(\pi^*)^2$, is proposed. Both a reliable X-ray structure (pending) and DFT calculations (below) should provide more evidence.

4.2.2 Improved ground state and excited state DFT calculations of $\text{Ru}_2(\text{II,III})$ and $\text{Ru}_2(\text{III,III})$ monoaryls

Ground state calculations

After the ‘quick and dirty’ analysis outlined in Chapter 1, multiple attempts were made to improve computational accuracy to more accurately model the $\text{Ru}_2(\text{ap})_4\text{Ar}$ systems, and each attempt met with varying degrees of success. Having chosen the density functional for these calculations (B3LYP seemed to perform well), the choice of basis sets, solvent model and empirical dispersion correction factors were systematically varied to fine-tune and optimize the results. Geometry optimization and frequency analysis were carried out using both the unrestricted

and ROS formalism for compound **1** as a test example. Since there was no significant difference in the optimized geometries (or frequencies) between the two methods, the unrestricted formalism was applied to all future calculations because it was computationally less expensive. The results of these calculations are given in Table 4.1.

Table 4.1. Comparison between experimental and DFT-optimized (improved) structural parameters

	1	1'(ROS)	1'(U)	[1']⁺	2	2'	4	4'
Ru–Ru	2.3343(7)	2.34070	2.34102	2.37657	2.338(1)	2.3398	2.3380(5)	2.3396
Ru–C	2.214(3)	2.13967	2.14122	2.08572	2.260(8)	2.14427	2.16(1)	2.15349
Ru–Ru–C	179.3(1)	179.839	179.840	169.433	177.8(2)	179.912	173.9(3)	179.998
Ru–N _{py}	2.106[3]	2.1327	2.1311	2.1234	2.111[4]	2.1316	2.118[2]	2.1309
Ru–N _{an}	2.044[3]	2.0433	2.044	2.0079	2.037[4]	2.0426	2.039[2]	2.0421

The biggest and most obvious improvement from the DFT calculations presented in Chapter 1 is correct estimation of the Ru–Ru bond length, which is probably *the* most important descriptor of the M–M valence manifold. As a result, remarkable improvement, especially in TD-DFT-simulated spectra was seen. Although the price to be paid for this accuracy is the slight underestimation of the Ru–C bond length, overall, this level of agreement between experiment and theory is desired for further calculations. Since both chemical and electrochemical oxidation of **1** and **2** were performed successfully, to fully characterize these oxidized species, DFT calculations for **[1]⁺** and **[2]⁺** were performed; the spectra of **1** and **2**, and by extension, **[1]⁺** and **[2]⁺** were found to be very similar, so for the sake of computational simplicity, calculations were focused on **1** and **[1]⁺**. Only those results are discussed here.

Figure 4.5 shows the optimized structures **1'** and **[1']⁺**. To date, there have been two structurally characterized Ru₂⁶⁺ compounds with only one axial ligand – [Ru₂(*ap*)₄Cl][FeCl₄],¹¹⁹ prepared by chemical oxidation with FcPF₆, and [Ru₂(*dm*at)₄Cl][PF₆] (*dm*at = 4,5-dimethyl-2-methylaminothiazolate),¹²⁰ by electrochemical oxidation. Because of its close relation to compound **[1']⁺**, a closer look into the structural characteristics of [Ru₂(*ap*)₄Cl][FeCl₄] is warranted. Going from Ru₂(*ap*)₄Cl to [Ru₂(*ap*)₄Cl]⁺, the Ru–Ru bond length increases by about 0.026 Å whereas the Ru–Cl distance decreases by ca. 0.018 Å. The shortening of the bond that would result

from removal of an electron from a δ^* orbital is outweighed by the lengthening that results from increased Ru–Ru repulsion upon oxidation from Ru_2^{5+} to Ru_2^{6+} . DFT calculations aptly reproduce this result; there is a roughly 0.035 Å elongation of the Ru–Ru bond upon oxidation of **1'** to $[\mathbf{1}']^+$. However, two striking structural features of $[\mathbf{1}']^+$ were unexpected: the Ru–C bond is dramatically shortened in $[\mathbf{1}']^+$ compared to **1'** by around 0.13 Å, and the overall paddlewheel geometry is distorted, not unlike those of **10–13**. At ca. 169°, the Ru–Ru–C angle is significantly distorted from linearity. These distortions were not present in the molecular structure of $[\text{Ru}_2(\text{ap})_4\text{Cl}]^+$. Clearly then, the aryl ligand plays a big role in forcing the structural deformations. The exact nature of these interactions (whether there is Ru–C multiple bonding, etc.) is unclear at this point.

Excited state calculations

Equipped with good models to describe the ground state, it was important to simulate the excited states of compounds **1**, $[\mathbf{1}]^+$ and **4** to better understand the electronic structure and support our putative assignments (Section 1.3.4) for the electronic transitions. While it is accepted practice, in the interest of saving on computational expenses, to use slightly different levels of theory for ground and excited state calculations, for the sake of rigor, consistency has been maintained here. Thus, the same functional, basis sets and solvent model applied for ground state calculations were used for TDDFT analysis. TD-DFT calculations were performed both using linear-response TD-DFT (TD) and with the Tamm-Dancoff approximation (TDA),¹²¹ and the results are shown below.

While some quantitative differences do exist between experimental and computational results, qualitatively, the results are in good agreement. This, in fact, is what led to the choice of optimal functional/basis set/solvent model/dispersion correction from a library of permutations and combinations. First, for the optimized structure **1'**, we see that the three major absorption features are faithfully reproduced by TD-DFT calculations (Figure 4.5): the peaks at around 460 nm and 600 nm, and even the transitions between 800–1000 nm. This latter region admittedly has a ‘double-humped’ feature in the experimental spectrum (Figure 1.9); while calculations do not quite capture this intricate detail, they do predict the presence of multiple transitions of very similar intensity. Similarly, for the optimized structure **4'**, TD-DFT accurately predicts intense transitions centered around 460 nm and 800–900 nm, including the shoulder peak at ca. 650 nm. It is in the latter that the success of TD-DFT calculations of both **1'** and **4'** lies. The differences in the experimental spectra of compounds **1** and **4** are accurately captured by these calculations; the band

unique to para-amino aryls at around 570–620 nm (compounds **1** and **2**) is present in the calculated spectrum of **1'** and is absent in both the experimental spectrum of **4** and the calculated spectrum of **4'**. The shoulder peak at around 650 nm in the spectrum of compound **4** is also faithfully reproduced in the calculated spectrum of **4'**.

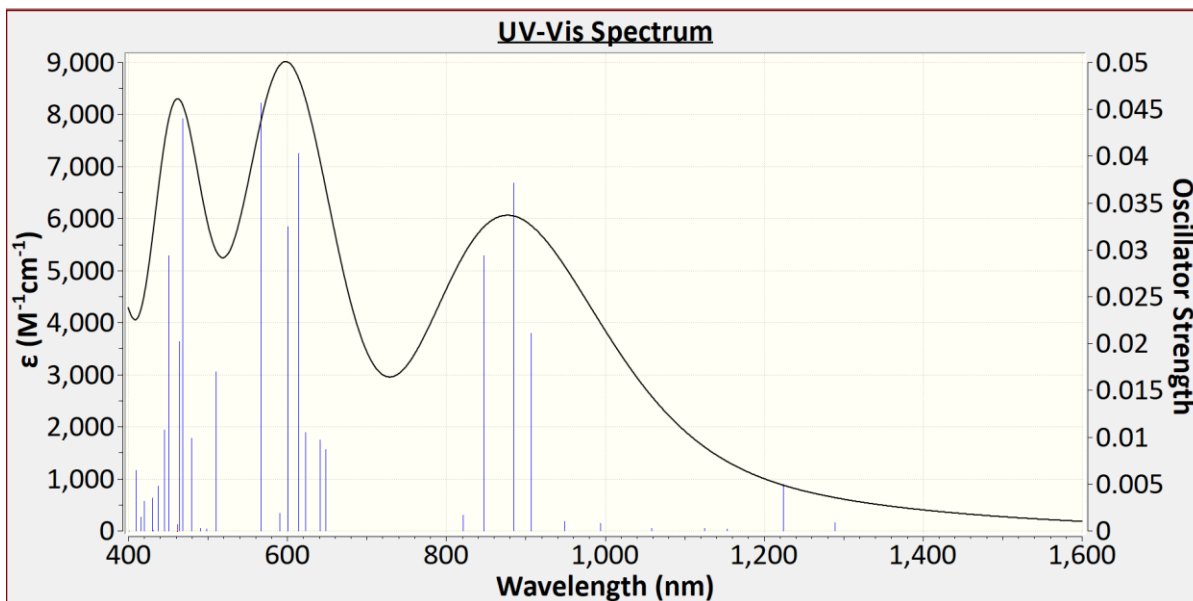


Figure 4.5. TD-DFT calculated UV-Vis/NIR spectrum of [**1'**] in THF.

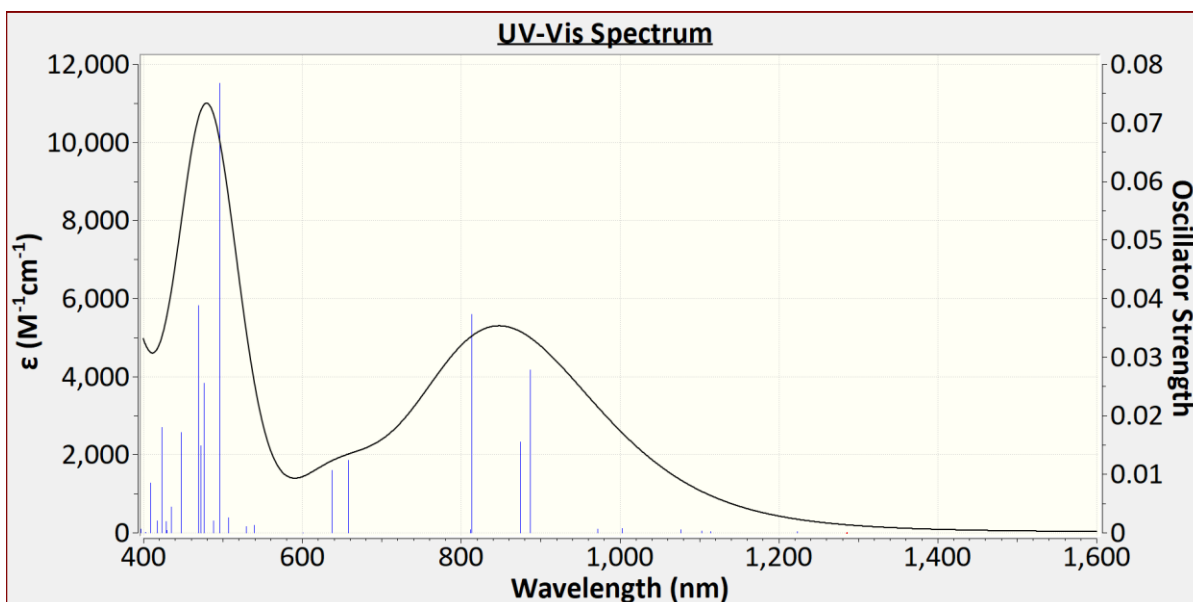


Figure 4.6. TD-DFT calculated UV-Vis/NIR spectrum of [**4'**] in THF.

A more detailed analysis of the electronic transitions can indeed be made using orbital descriptions. However, mixing between the ligand and metal orbitals convolutes these assignments. Hence natural transition orbitals⁸² were computed to simplify the picture to a qualitative one that describes “where the electron was and where it ended up after excitation” (a paraphrasing from ref 82). The results of these calculations for DFT-optimized **1'** and **4'** are shown in Table 4.2–4.3, and a brief qualitative discussion is provided below.

Table 4.2. Natural transition orbitals* derived from TD-DFT analysis of **1'**

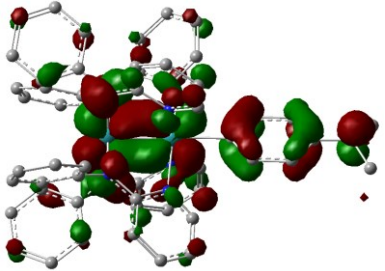
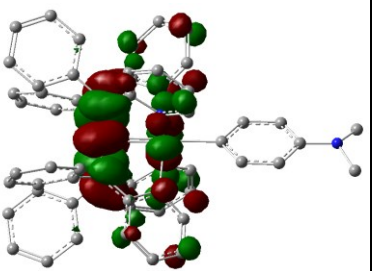
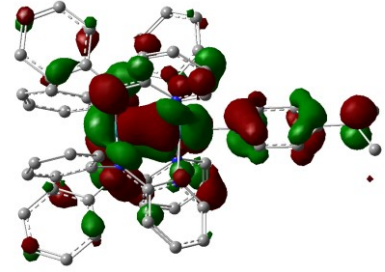
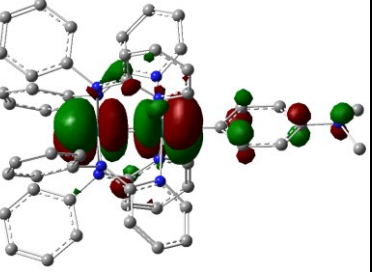
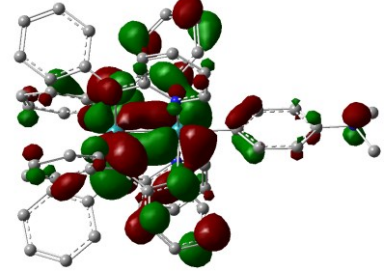
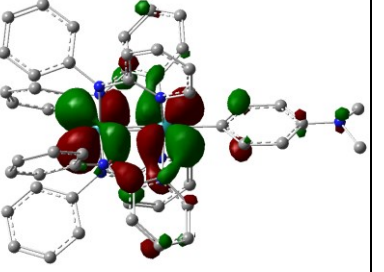
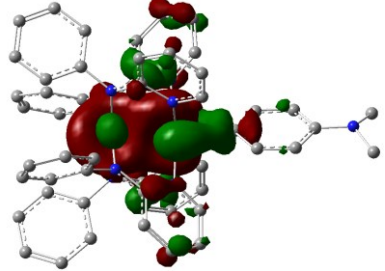
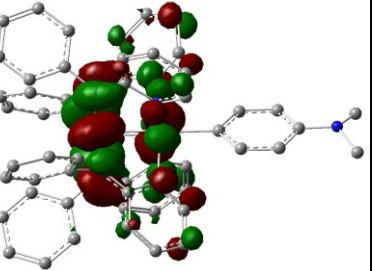
Excited states and energies	Oscillator strength (f_{oscil})	NTO1	NTO2	λ
Q8 11024.5 cm^{-1} 907.0 nm	0.021			1.98
Q9 11307.6 cm^{-1} 884.3 nm	0.037			0.85
				0.70
				0.44

Table 4.2 continued

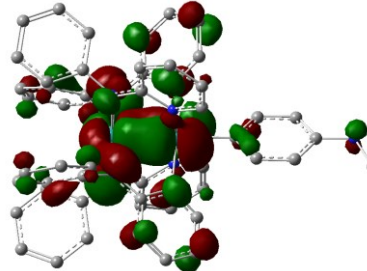
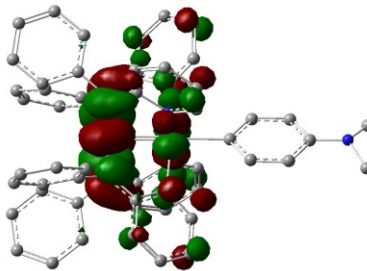
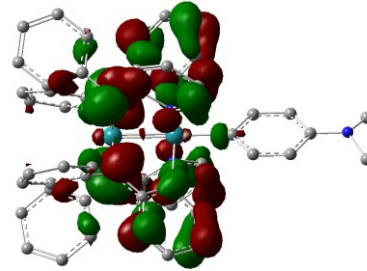
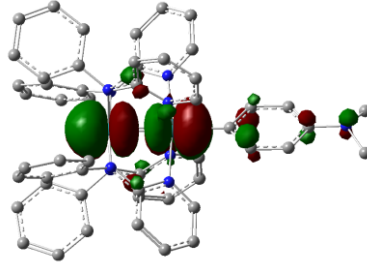
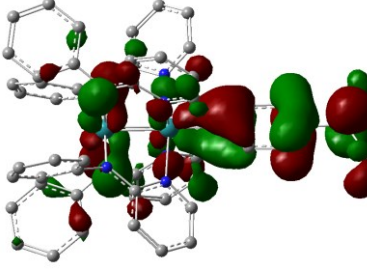
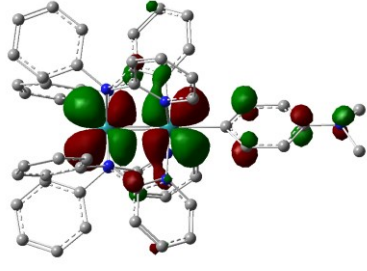
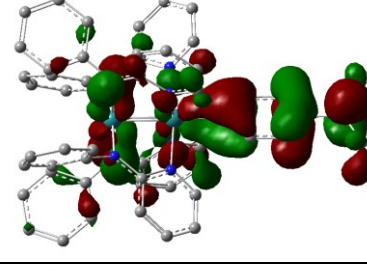
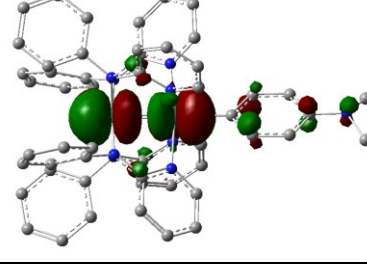
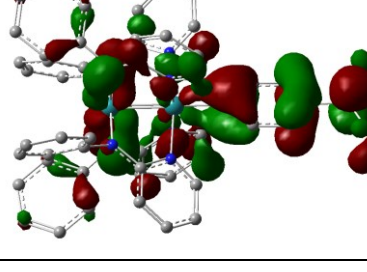
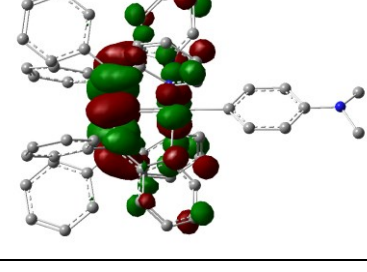
Excited states and energies	Oscillator strength (f_{oscil})	NTO1	NTO2	λ
Q10 11797.0 cm^{-1} 847.6 nm	0.029			1.99
Q14 16050.1 cm^{-1} 623.1 nm	0.010			1.99
Q15 16284.5 cm^{-1} 614.1 nm	0.040			1.96
Q16 16648.4 cm^{-1} 600.7 nm	0.033			1.93
Q18 17656.3 cm^{-1} 566.4 nm	0.046			1.98

Table 4.2 continued

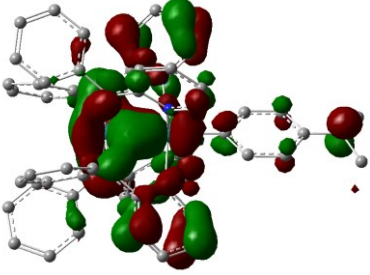
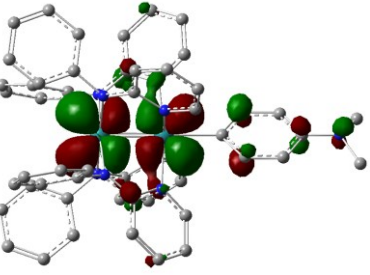
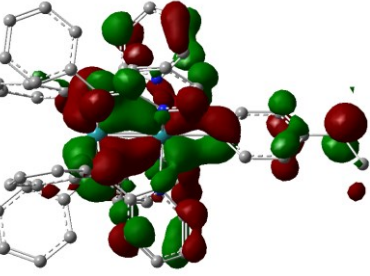
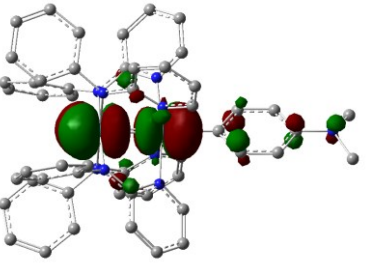
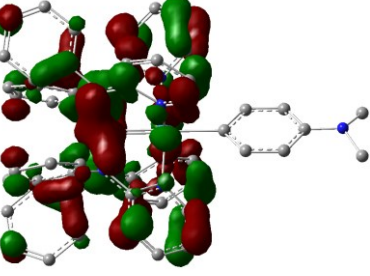
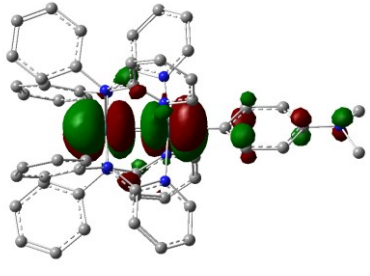
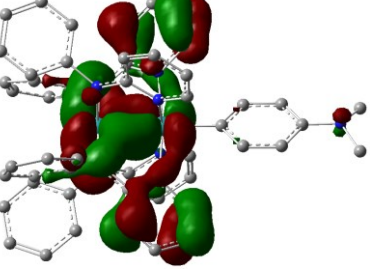
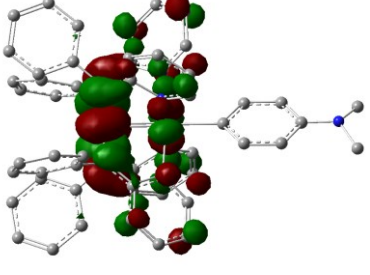
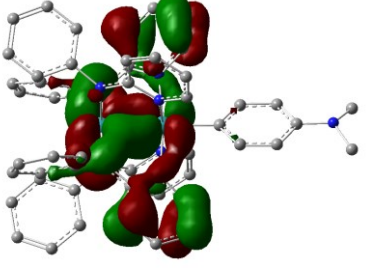
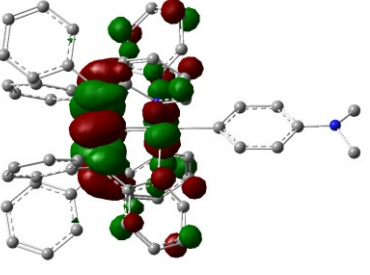
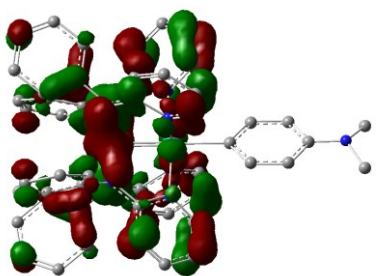
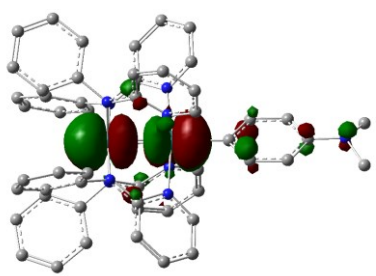
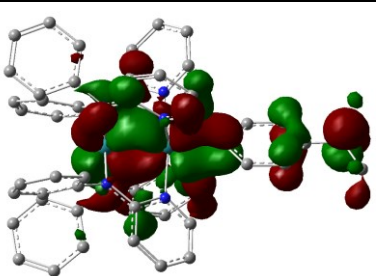
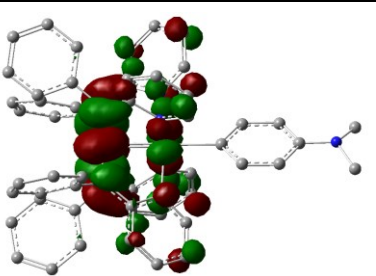
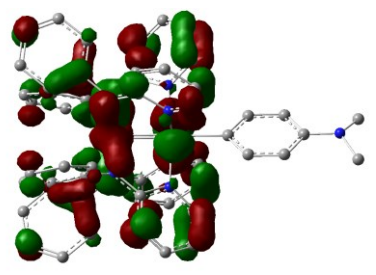
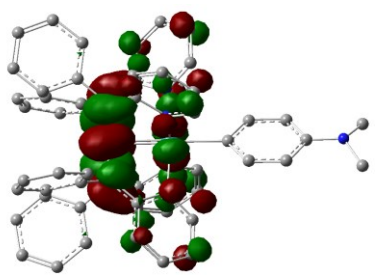
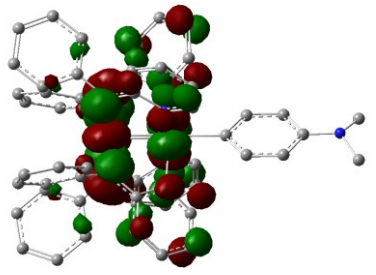
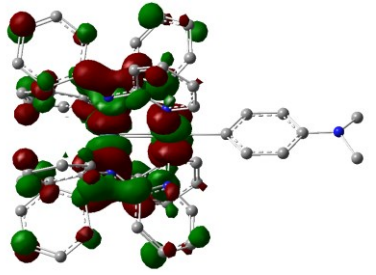
Excited states and energies	Oscillator strength (f_{oscil})	NTO1	NTO2	λ
Q19 19607.8 cm^{-1} 510.0 nm	0.017			1.73
				0.23
Q23 21358.8 cm^{-1} 468.2 nm	0.044			1.41
				0.55
Q24 21530.8 cm^{-1} 464.5 nm	0.020			1.34

Table 4.2 continued

Excited states and energies	Oscillator strength (f_{oscil})	NTO1	NTO2	λ
Q24 21530.8 cm^{-1} 464.5 nm	0.020			0.57
Q26 22202.9 cm^{-1} 450.4 nm	0.029			1.87
Q27 22454.7 cm^{-1} 445.3 nm	0.011			0.92
				0.77

*Transitions are noted as NTO1 \rightarrow NTO2

Table 4.3. Natural transition orbitals* derived from TD-DFT analysis of 4'

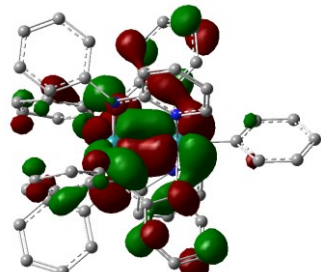
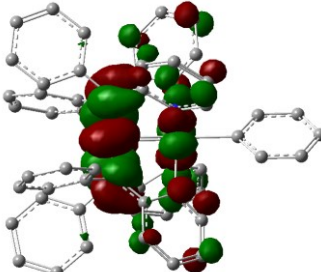
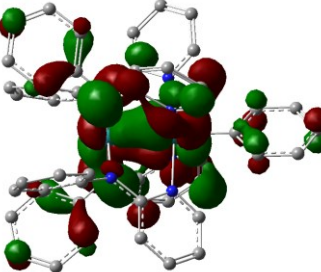
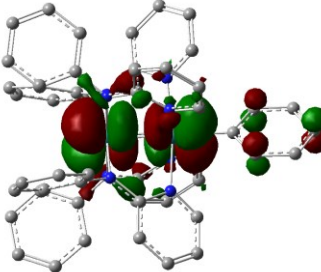
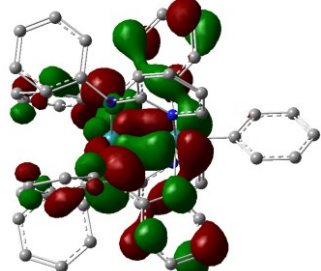
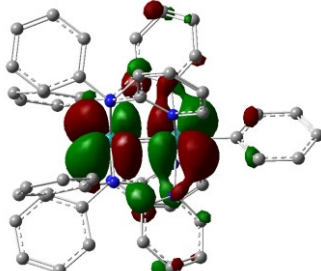
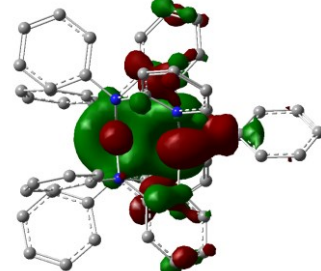
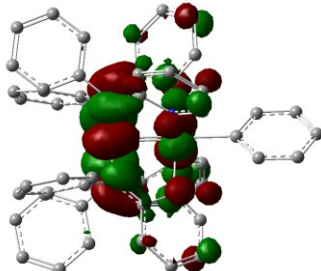
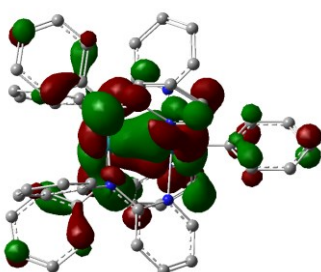
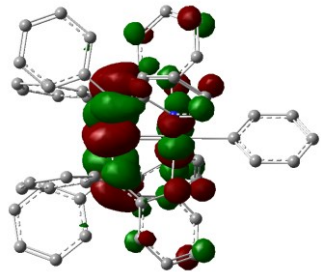
Excited states and energies	Oscillator strength (f_{oscil})	NTO1	NTO2	λ
Q8 11272.6 cm^{-1} 887.1 nm	0.028			1.99
Q9 11434.8 cm^{-1} 874.52 nm	0.016			1.02
				0.53
				0.44
Q10 12294.1 cm^{-1} 813.4 nm	0.037			1.99

Table 4.3 continued

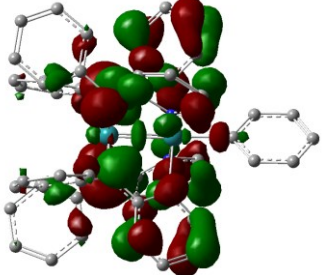
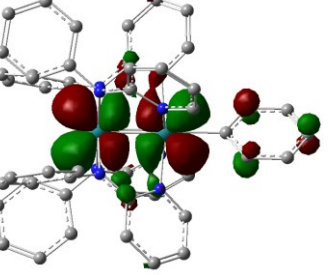
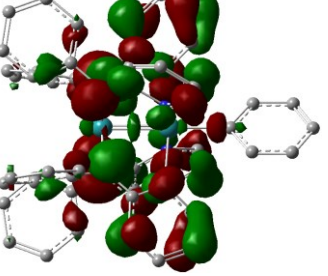
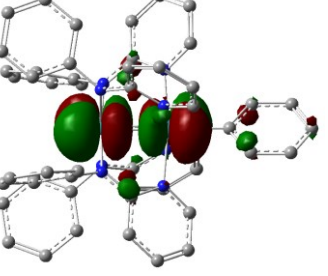
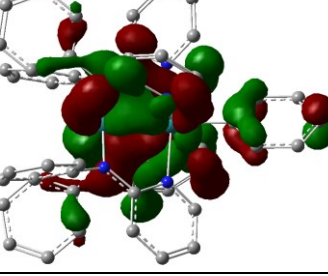
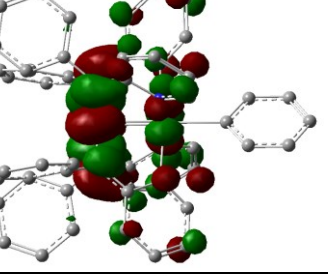
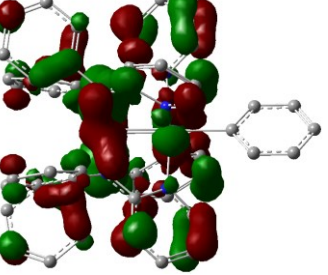
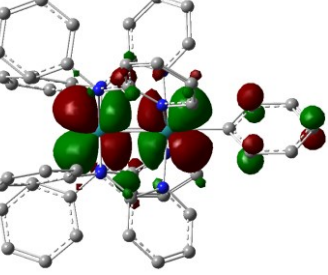
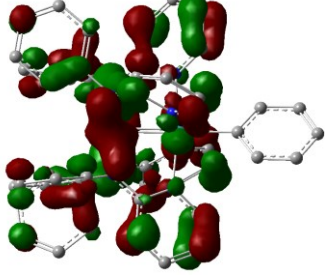
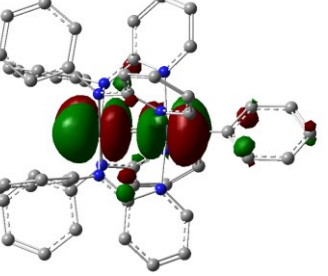
Excited states and energies	Oscillator strength (f_{oscil})	NTO1	NTO2	λ
Q13 15204.5 cm^{-1} 657.7 nm	0.012			1.99
Q14 15691.2 cm^{-1} 637.3 nm	0.011			1.99
Q19 20145.0 cm^{-1} 496.4 nm	0.077			1.81
				0.15
Q21 21017.2 cm^{-1} 475.8 nm	0.026			1.82

Table 4.3 continued

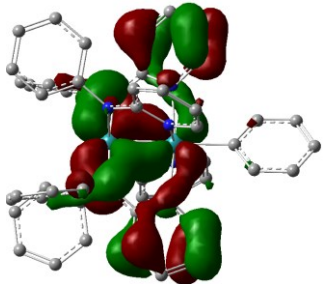
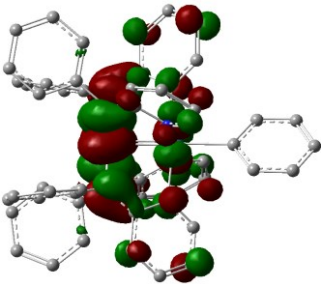
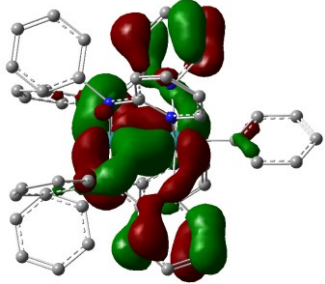
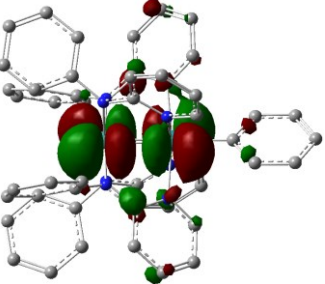
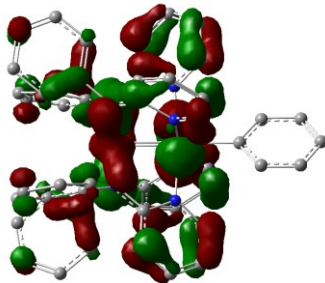
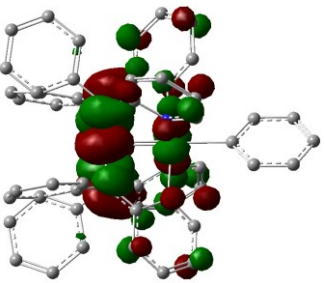
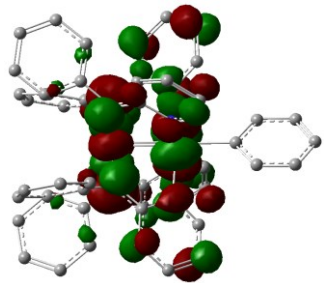
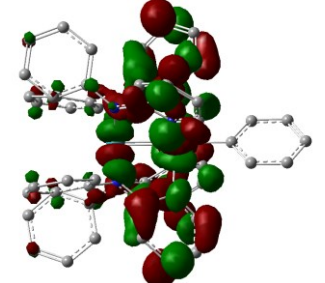
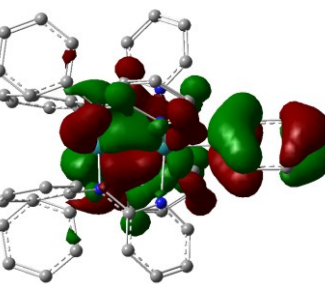
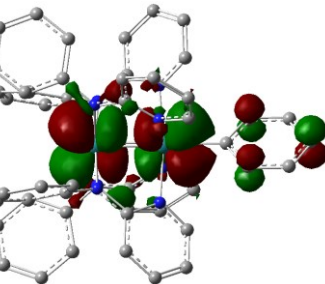
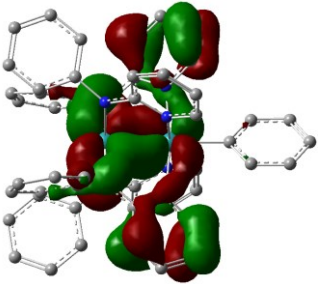
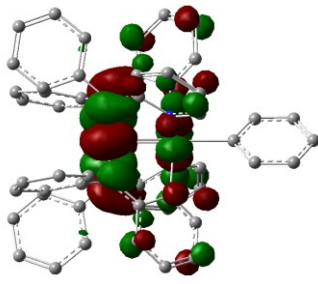
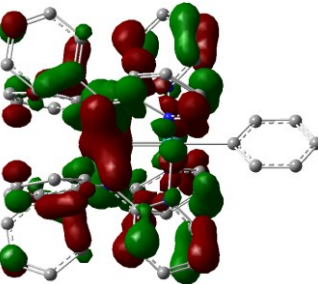
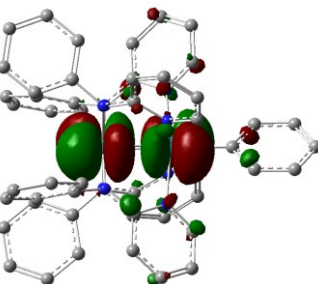
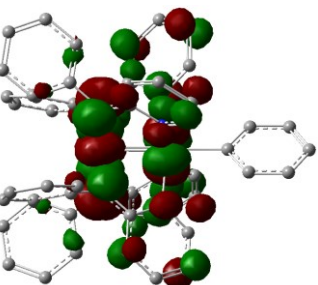
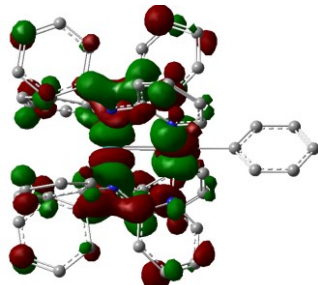
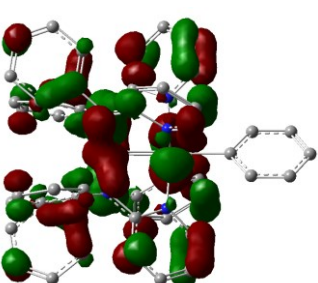
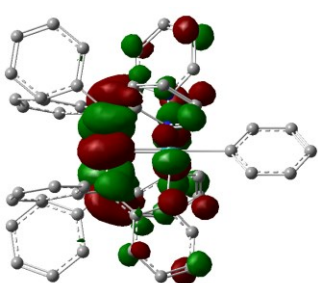
Excited states and energies	Oscillator strength (f_{oscil})	NTO1	NTO2	λ
Q21 21017.2 cm^{-1} 475.8 nm	0.026			0.16
Q22 21177.5 cm^{-1} 472.2 nm	0.015			0.68
				0.61
				0.32
				0.25

Table 4.3 continued

Excited states and energies	Oscillator strength (f_{oscil})	NTO1	NTO2	λ
Q23 21331.1 cm^{-1} 468.8 nm	0.039			1.76
				0.16
Q24 22326.4 cm^{-1} 447.9 nm	0.017			1.19
				0.53

*Transitions are noted as NTO1 \rightarrow NTO2.

Comparing the natural transition orbital contributions to the electronic transitions of **1'** and **4'**, many similarities, and a few stark differences become apparent. Low-energy transitions (800–950 nm, Figures 4.5 and 4.6) **1'** and **4'** have nearly identical NTO contributions: states Q8–Q10 for both complexes result from a movement of electron density from either a $\pi(\text{Ru}_2)$, $\pi(\text{Ru}_2)/\pi(\text{Ar})$

orbital (major contributors) or $\delta(\text{Ru}_2)$ (minor contributor) to orbitals which are primarily just Ru_2 based, either $\pi^*(\text{Ru}_2)$ or $\delta^*(\text{Ru}_2)$. This imparts a significant amount of LMCT character to what are primarily MMCT transitions, particularly for compound **1'**, since $-\text{C}_6\text{H}_4-4\text{-NMe}_2$ has a more extensive and higher-energy π -system compared to Ph. As a result, the transitions in this region of the spectrum for compound **4'** are consistently blue-shifted compared to those of **1'** (887 nm vs. 907 nm, 874 nm vs. 884 nm, and 813 nm vs. 847 nm, respectively). The shoulder peak between 640–660 nm for compound **4'** is a result of transitions that are almost entirely LMCT in character, and while at first glance they are seemingly absent in **1'**, upon closer inspection it can be seen that they are blue-shifted to about 600–630 nm. This trend is opposite to what is seen with states Q8–Q10, and this is because the electronic transitions corresponding to Q12–Q14 all originate in the equatorial *ap* ligands, and end in Ru_2 -based orbitals with a minor contribution from the axial ligand. More importantly, there are other more prominent bands in the spectrum of **1'** that overlap with (and outweigh) the above-mentioned peaks.

The 560–615 nm region of the spectrum is unique to and characteristic of the *para*-amino substituent on the aryl ligand in the monoaryl $\text{Ru}_2(\text{II,III})$ compounds (compounds **1** and **2**, Figure 1.9). From Table 4.2, it is clear that transitions belonging to states Q15–Q18 arise as a result of the high-lying $\pi(\text{C}_6\text{H}_4-4\text{-NMe}_2)$ orbitals mixing with $\pi^*(\text{Ru}_2)$. Accordingly, three relatively closely spaced intense transitions (614 nm, 601 nm and 566 nm) dominate this region of the spectrum exclusively for **1'**, which are absent for **4'**. Higher energy transitions in the range of 440–520 nm (Q19–Q27 in **1'** and Q21–Q24 in **4'**) seem to involve the $\pi(\text{Ru}_2/\text{ap})$, $\delta(\text{Ru}_2)/\pi(\text{ap})$ and $\delta^*(\text{Ru}_2)$ orbitals, with little to no contribution from the aryl ligands. This is evident from the relatively unchanged peak position at ca. 445 nm for both **1'** and **4'** (also seen experimentally, Figure 1.9).

Having assigned the electronic transitions of the $\text{Ru}_2(\text{II,III})$ mono aryls, the more complicated absorption spectrum of $[\mathbf{1}]^+$ was targeted for excited state calculations, based on the optimized geometry of $[\mathbf{1}']^+$. Calculations furnished a simulated UV-Vis spectrum (Figure 4.7) with features very similar to the experimental ones in Figures 4.1 (top) and 4.2 (left). The very broad, ‘double-humped’ spectral shape in the region 800–1500 nm is faithfully reproduced, as is the sharp peak close to 500 nm. Overall, both these bands are red-shifted from those of **1'**, which accurately reflect the experimental trend in going from **1** to $[\mathbf{1}]^+$. The structure of $[\mathbf{1}']^+$ is more distorted from an idealized paddlewheel geometry than that of **1'**, resulting in an increased mixing of metal and ligand (both axial and equatorial) orbitals. The lowering of overall symmetry and

significant charge transfer character of many of the transitions described above for **1'** and **4'** translate into an increased ‘allowedness’, and hence increased oscillator strength, for a greater number of electronic transitions in $[1']^+$. The qualitative description of donor→acceptor NTOs in $[1']^+$ plotted in Table 4.4 .

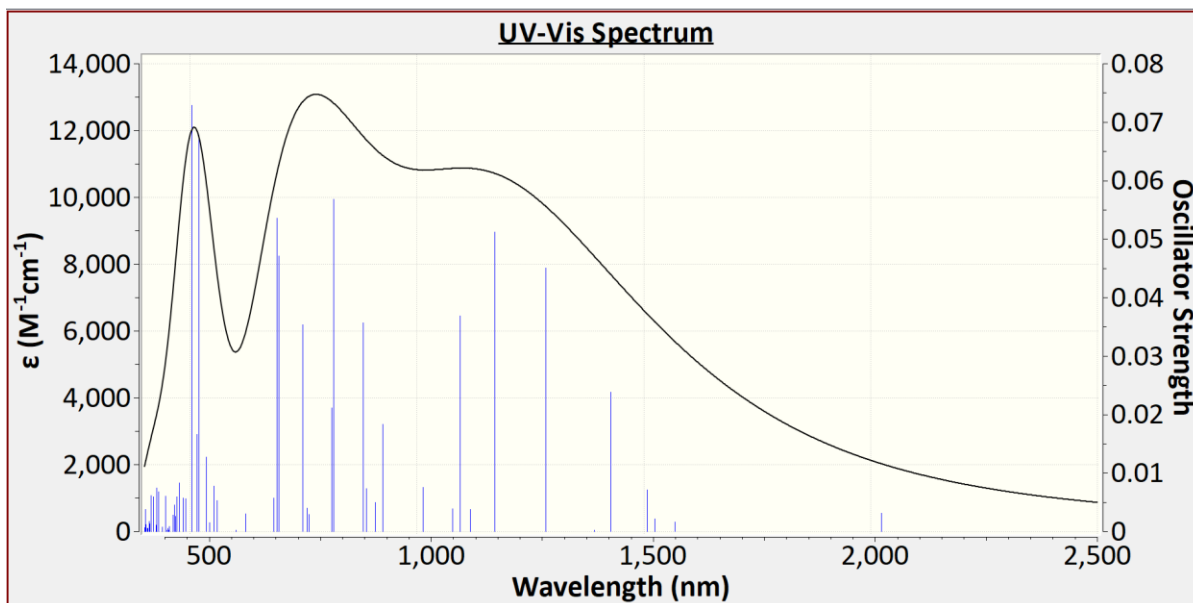


Figure 4.7. TD-DFT calculated UV-Vis/NIR spectrum of $[1']^+$ in THF.

Table 4.4. Natural transition orbitals* derived from TD-DFT analysis of $[1']^+$

Excited states and energies	Oscillator strength (f_{oscil})	NTO1	NTO2	λ
T6 7007.8 cm^{-1} 1426.9 nm	0.024			1.35

Table 4.4 continued

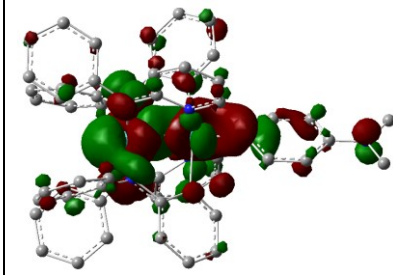
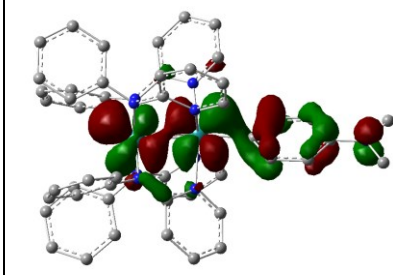
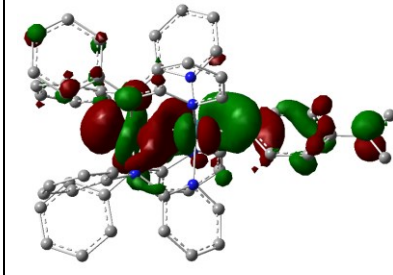
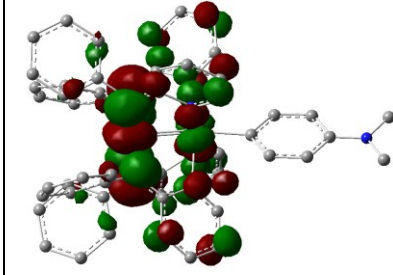
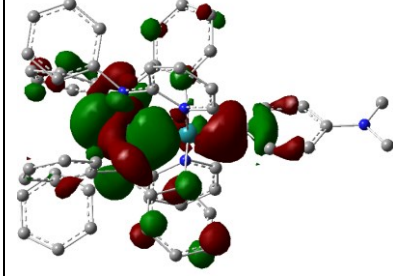
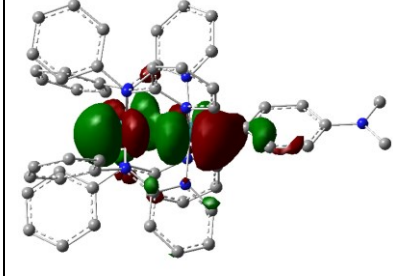
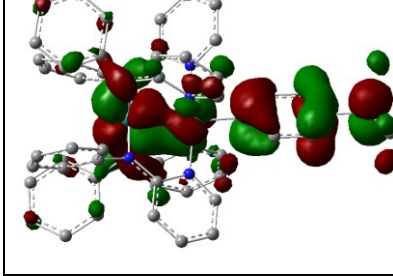
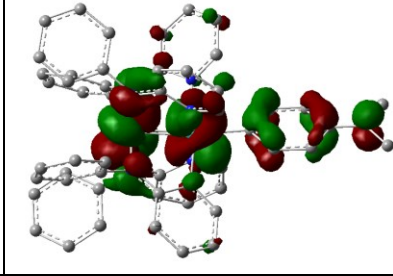
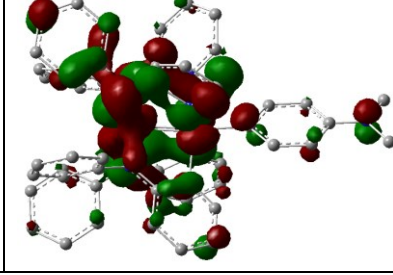
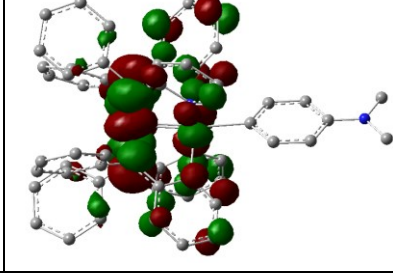
				0.37
				0.32
T8 7784.7 cm ⁻¹ 1284.6 nm	0.045			1.05
				0.66
				0.28

Table 4.4 continued

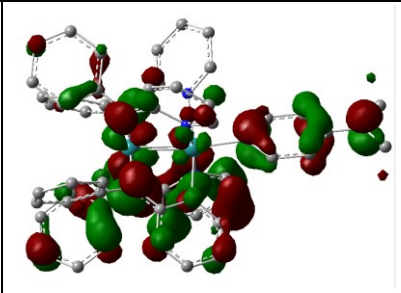
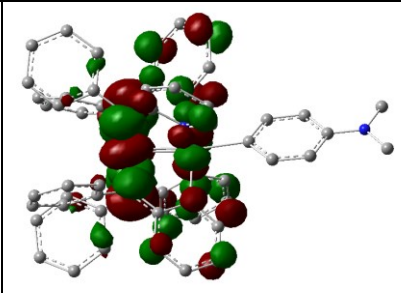
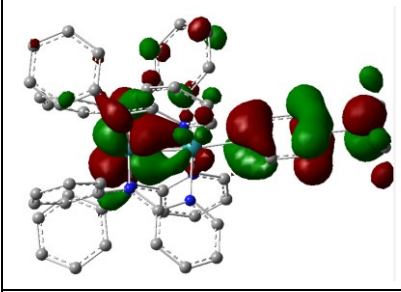
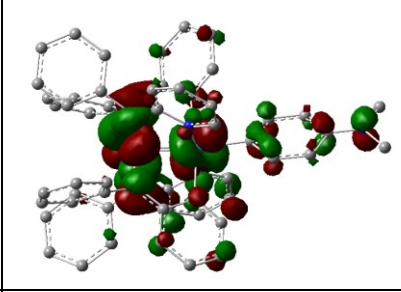
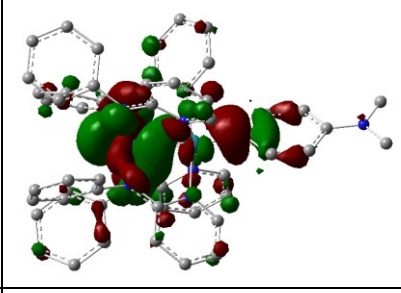
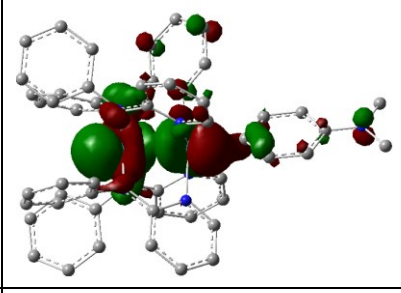
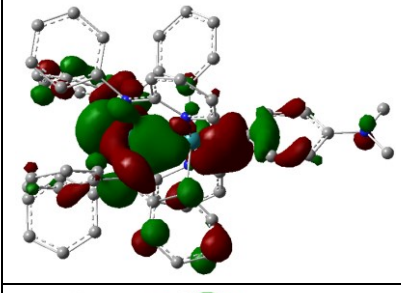
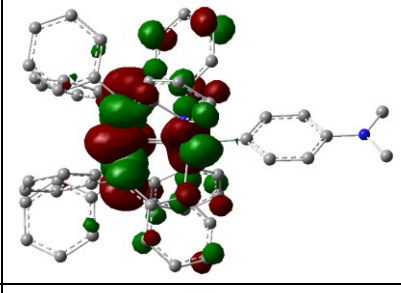
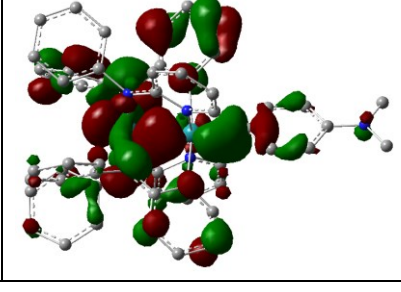
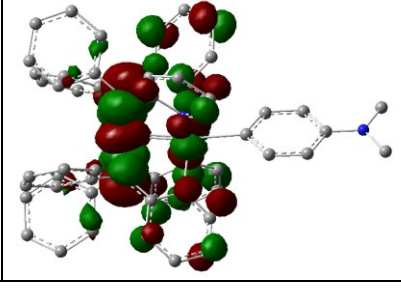
<p>T9 8533.1 cm^{-1} 1171.9 nm</p>	<p>0.051</p>			<p>0.97</p>
				<p>0.81</p>
				<p>0.18</p>
<p>T11 9130.1 cm^{-1} 1095.3 nm</p>	<p>0.037</p>			<p>1.02</p>
				

Table 4.4 continued

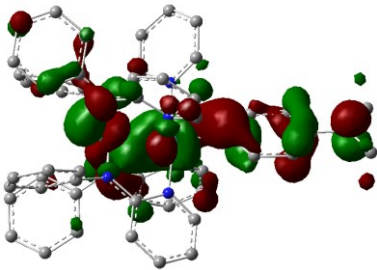
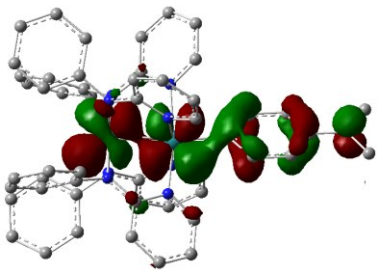
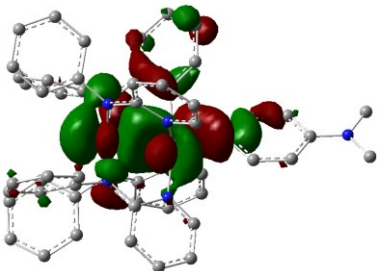
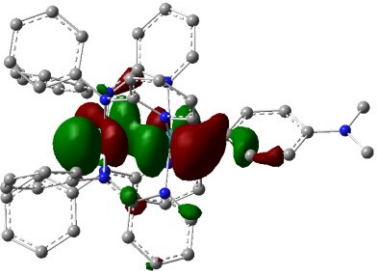
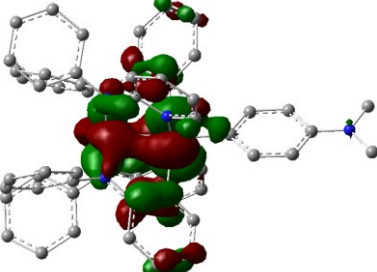
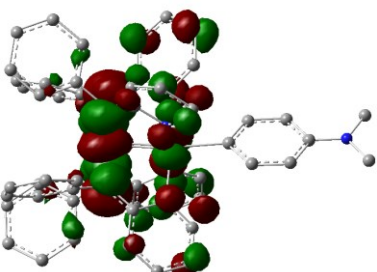
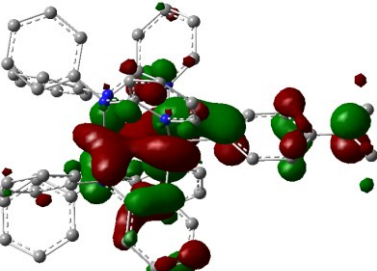
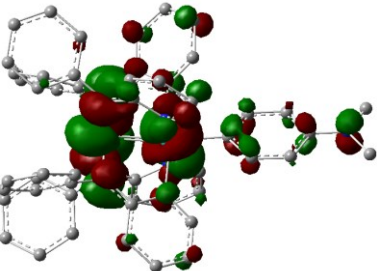
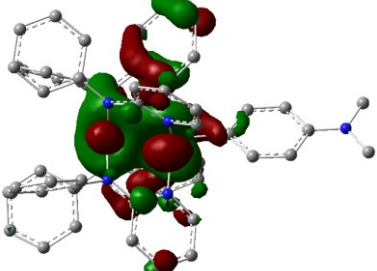
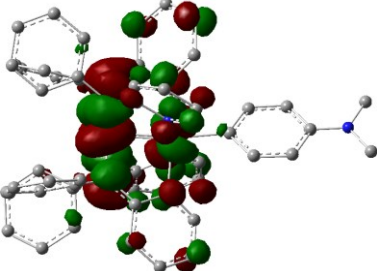
<p>T11 9130.1 cm^{-1} 1095.3 nm</p>	0.037			
<p>T14 10813.5 cm^{-1} 924.8 nm</p>	0.018			1.14
				0.60
				0.19
<p>T17 11338.0 cm^{-1} 881.9 nm</p>	0.036			0.84

Table 4.4 continued

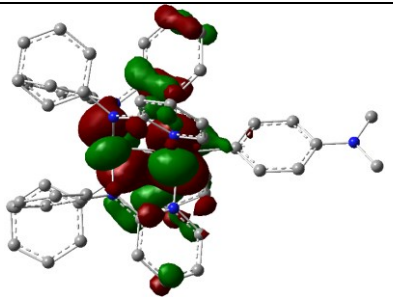
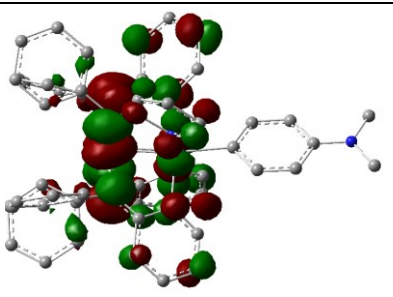
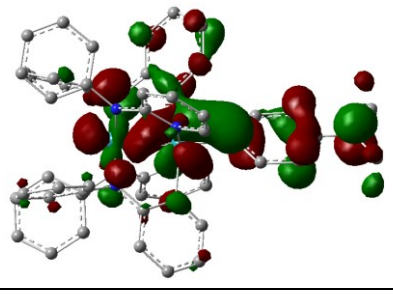
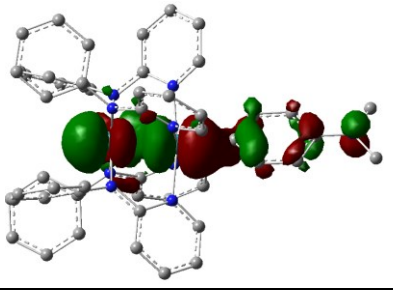
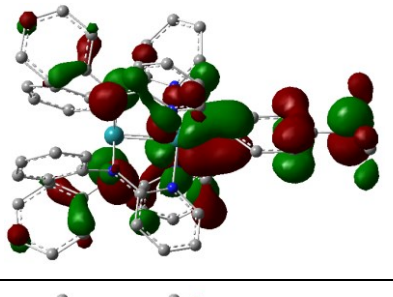
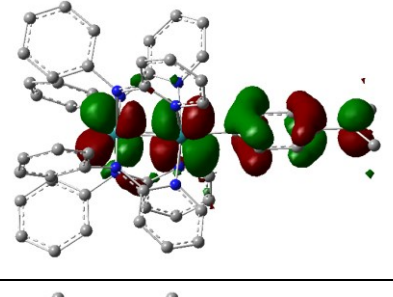
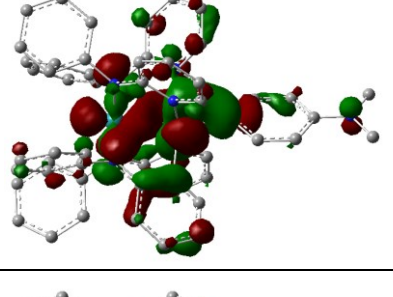
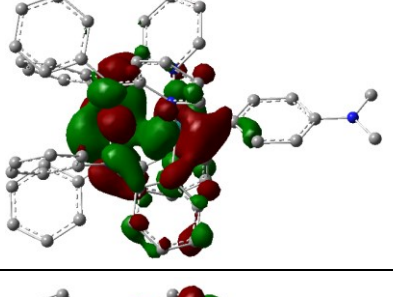
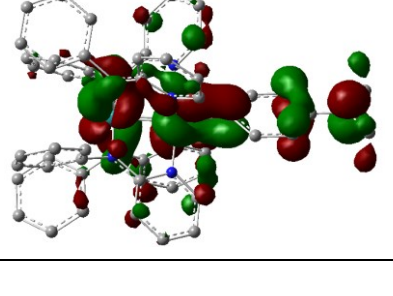
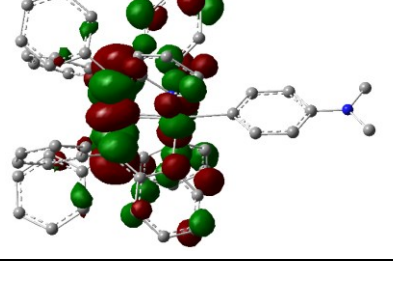
<p>T17 11338.0 cm^{-1} 881.9 nm</p>	0.036			0.54
				0.37
	<p>T18 12246.7 cm^{-1} 816.5 nm</p>	0.057		
				0.29
				0.29

Table 4.4 continued

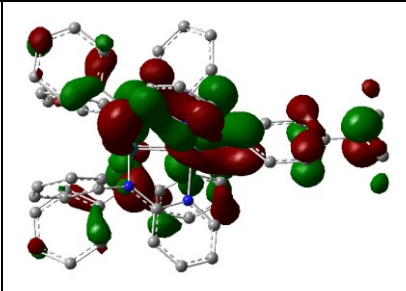
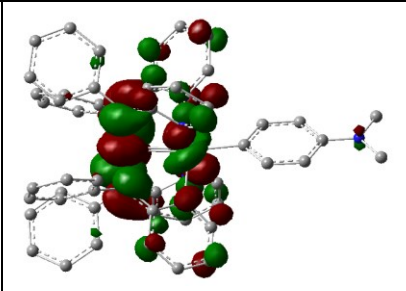
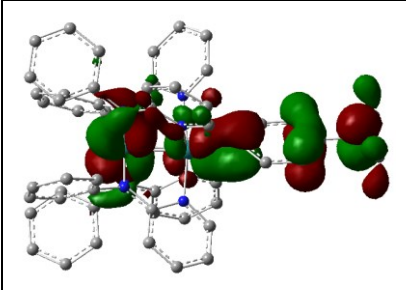
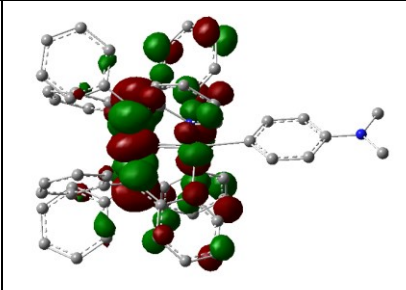
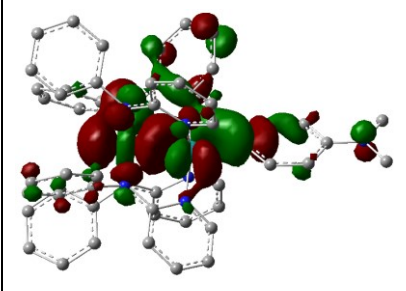
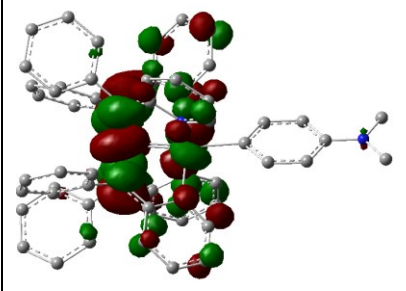
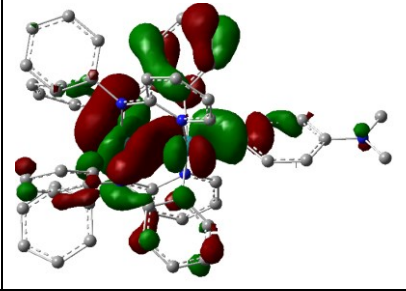
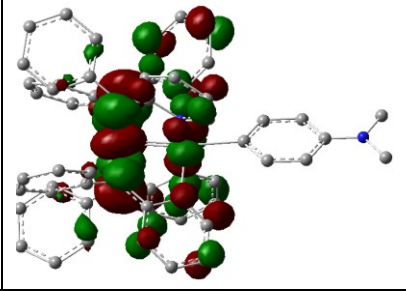
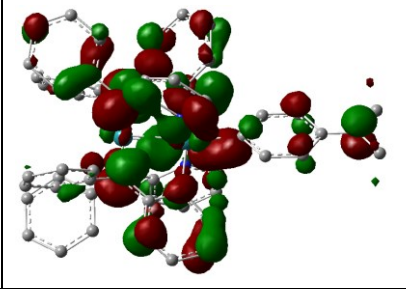
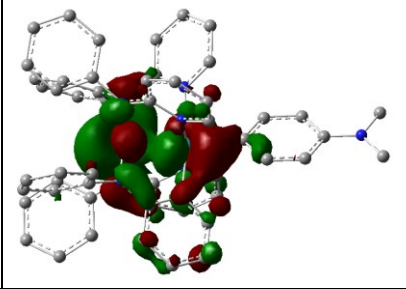
T19 12321.3 cm^{-1} 811.6 nm	0.021			1.00
				0.92
T22 13359.4 cm^{-1} 748.5 nm	0.035			0.89
				0.76
T23 14371.2 cm^{-1} 695.8 nm	0.047			1.09

Table 4.4 continued

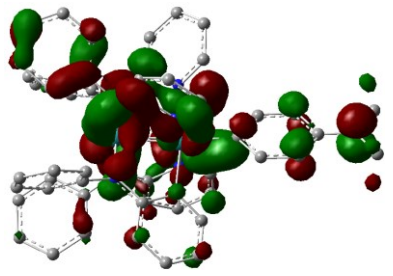
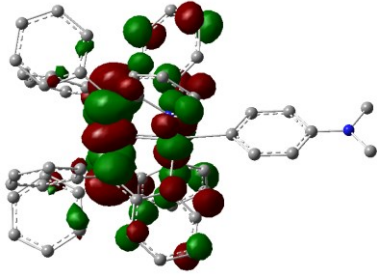
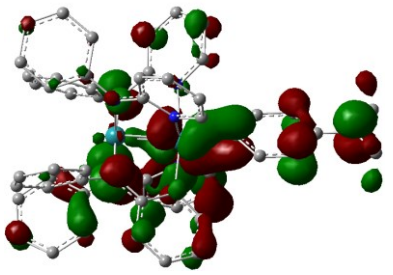
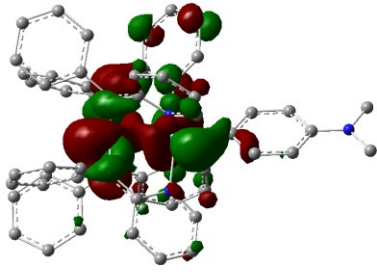
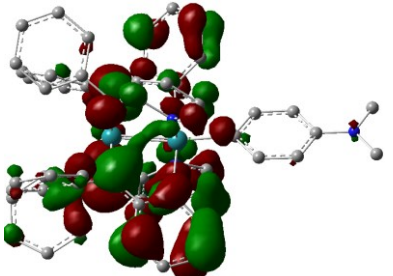
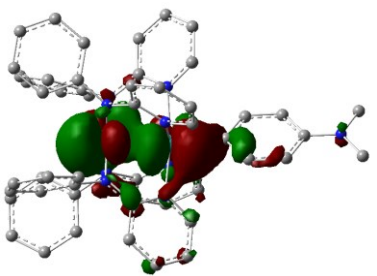
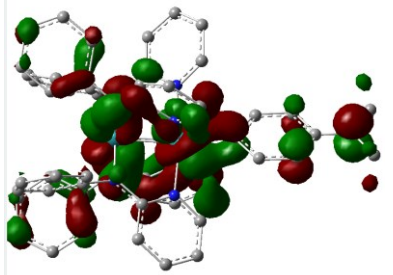
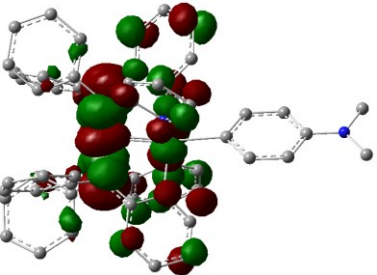
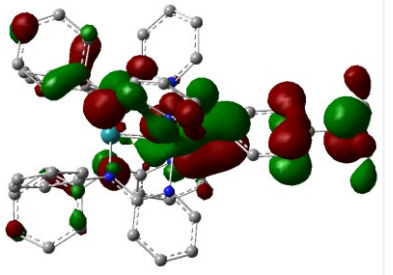
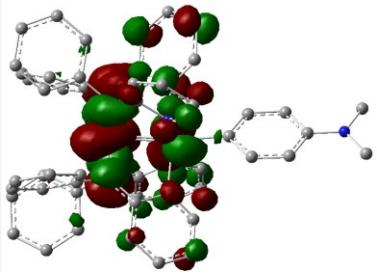
<p>T23 14371.2 cm^{-1} 695.8 nm</p>	<p>0.047</p>			0.49
				0.40
<p>T24 14456.8 cm^{-1} 691.7 nm</p>	<p>0.054</p>			1.05
				0.50
				0.44

Table 4.4 continued

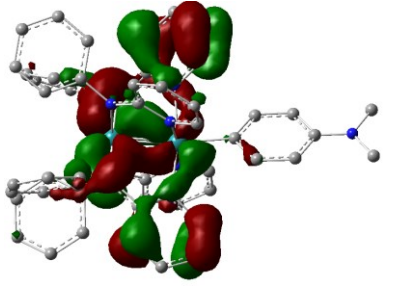
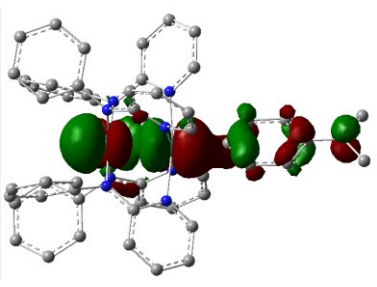
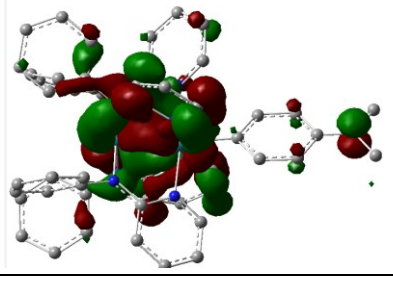
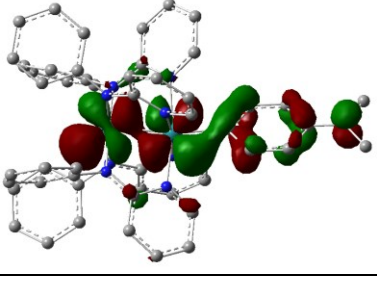
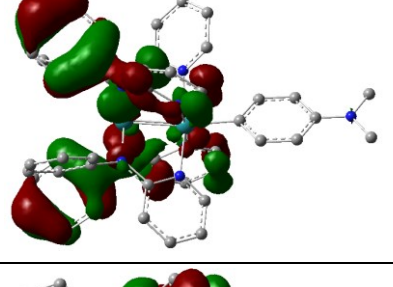
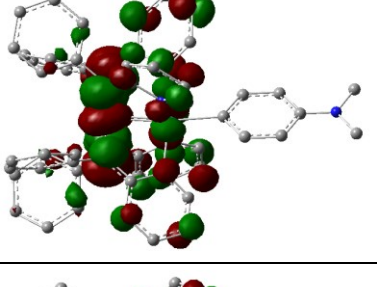
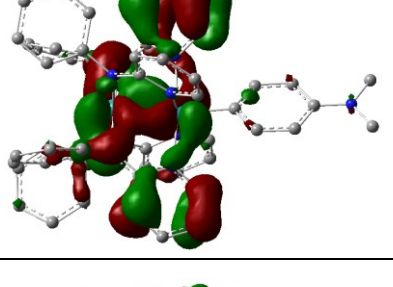
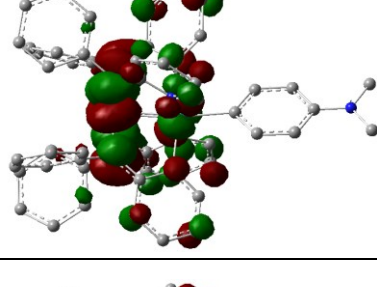
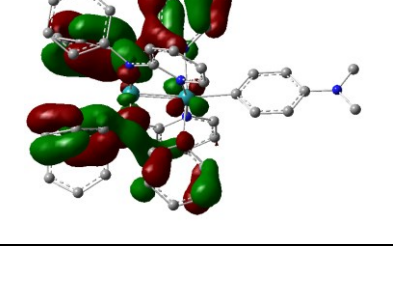
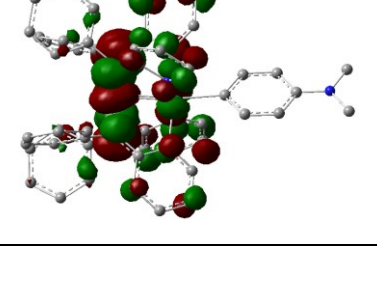
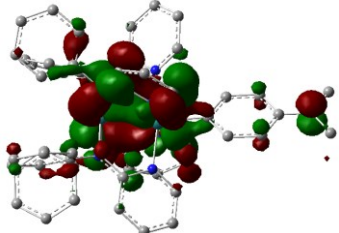
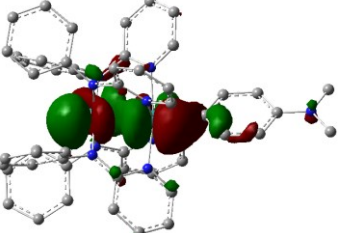
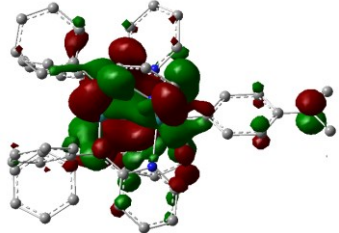
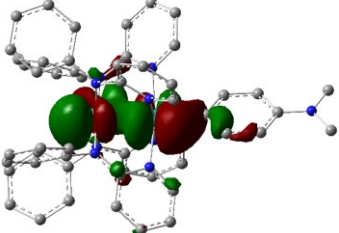
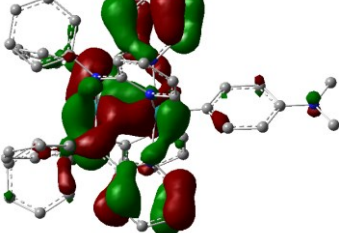
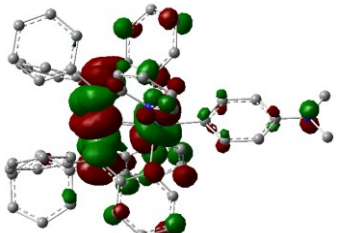
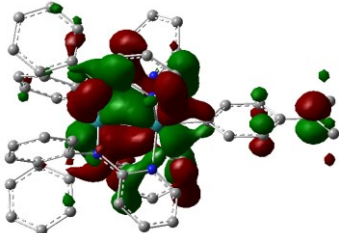
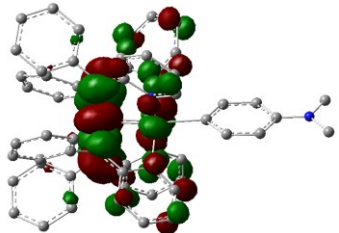
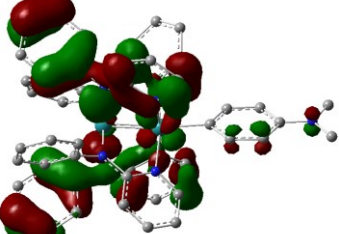
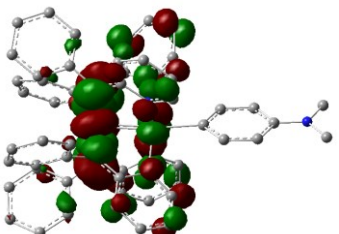
<p>T31 18648.7 cm^{-1} 536.2 nm</p>	<p>0.012</p>			<p>0.83</p>
				<p>0.71</p>
				<p>0.45</p>
<p>T32 19258.9 cm^{-1} 519.2 nm</p>	<p>0.068</p>			<p>1.18</p>
				<p>0.41</p>

Table 4.4 continued

T32 19258.9 cm^{-1} 519.2 nm	0.068			0.40
T33 19392.8 cm^{-1} 515.7 nm	0.017			1.56
				0.35
T34 19840.5 cm^{-1} 504.0 nm	0.073			1.51
				0.42

*Transitions are noted as $\text{NTO1} \rightarrow \text{NTO2}$.

Based on the NTO populations shown in Table 4.4, it is clear that the structural distortion that accompanies the oxidation of $\mathbf{1}'$ to $[\mathbf{1}']^+$ results in the heavy mixing of metal and ligand orbitals to the extent where it is difficult to clearly delineate the contributions of either metal or ligand to

the MO picture. On account of bearing a *para*-amino substituent on the aryl ligand, the spectra of both $[1]^+$ and $[2]^+$ are very similar, hence the nature of electronic transitions, orbital contributions and NTO populations are expected to be similar too.

Mention must be made here of two things: (i) employing the Tamm-Dancoff approximation (TDA) for excited state calculations improved the agreement in energies of the transitions between experiment and computation (Figures 4.S2–4.S4). However, since TDA inherently violates the oscillator sum rule, the predicted extinction coefficients are not in the same ballpark as experimental values. and (ii) while other functionals (like BP86) gave egregious results for the TD-DFT calculations of $1'$, slightly better agreement was found for $[1]^+$ (Figures 4.S5–4.S6).

Overall, DFT calculations (both ground and excited state) for the above mentioned $Ru_2(II,III)$ and $Ru_2(III,III)$ monoaryls provide reliable information about the electronic structure of the complex that is in good agreement with both experiment and chemical intuition. However, a true test of theory is whether it can predict a property that can be experimentally verified. To this end, the following predictions are made about the molecular structure of $[1]^+$, which can be verified by XRD analysis of the corresponding $[1][X]$ compound ($X =$ suitable anion). First, the Ru–Ru bond length in $[1]^+$ should be elongated by about 0.035 Å, whereas the Ru–C_{aryl} bond should be drastically shortened by about 0.12 Å. Additionally, severe distortion from an idealized paddlewheel geometry might be seen, culminating in a Ru–Ru–C bond angle significantly less than 180°. These changes upon going from $1'$ to $[1]^+$ are quite different from what has been observed before ingoing from $Ru_2^{II,III}(ap)_4Cl$ to $[Ru_2^{III,III}(ap)_4Cl][FeCl_4]$, and are doubly interesting because of the differences. The validity of these predictions depends on being able to obtain a quality X-ray structure of the compound, a result that is much awaited.

4.2.3 Phenylene bridged diruthenium complexes of the form $[\text{Ru}_2(\text{ap})_4]\text{-Ar-}[\text{Ru}_2(\text{ap})_4]$

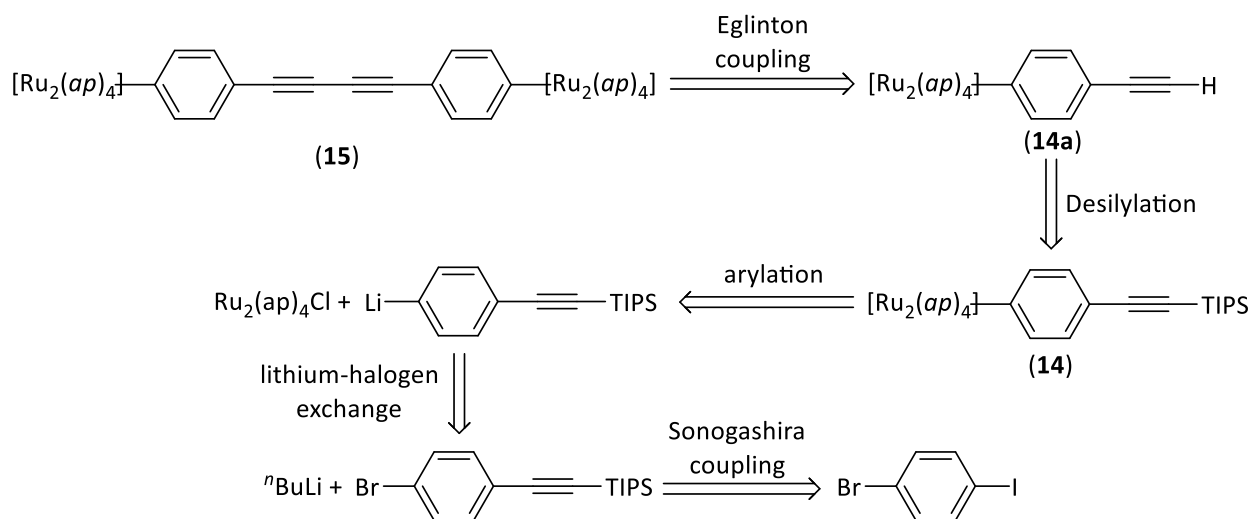
The electronic communication between diruthenium termini across polyyndiyl bridges has been thoroughly investigated by our laboratory.^{5,8} We have been able to vary the length of this polyalkynyl bridge to show that the extent of coupling between the two termini varies, as expected, inversely. Electrochemical and spectroelectrochemical characterization of these species has led to the conclusion that polyene bridges are as efficient as polyynes in mediating electron transfer between metal centers. Further, the $[\text{Ru}_2(\text{ap}')_4]_2(\mu\text{-C}_{2m})$ ($m \geq 4$) systems were revealed to be class II Robin–Day mixed valence systems, while DFT calculations revealed extensive mixing between the filled $\pi^*(\text{Ru-Ru})$ and $\pi(\text{C}\equiv\text{C})$ orbitals. Given that aryls are better electron donors than alkynyls, we sought to explore the coupling between two $[\text{Ru}_2(\text{ap})_4]$ units bridged by either a stand-alone phenylene moiety, or a phenylene linker extended interspersed with polyalkynyl chains.

$\text{Ru}_2(\text{II,III})$ termini bridged by a mixed phenylene/polyyndiyl unit $(-\text{C}_6\text{H}_4\text{-C}\equiv\text{C-C}\equiv\text{C-C}_6\text{H}_4-)$

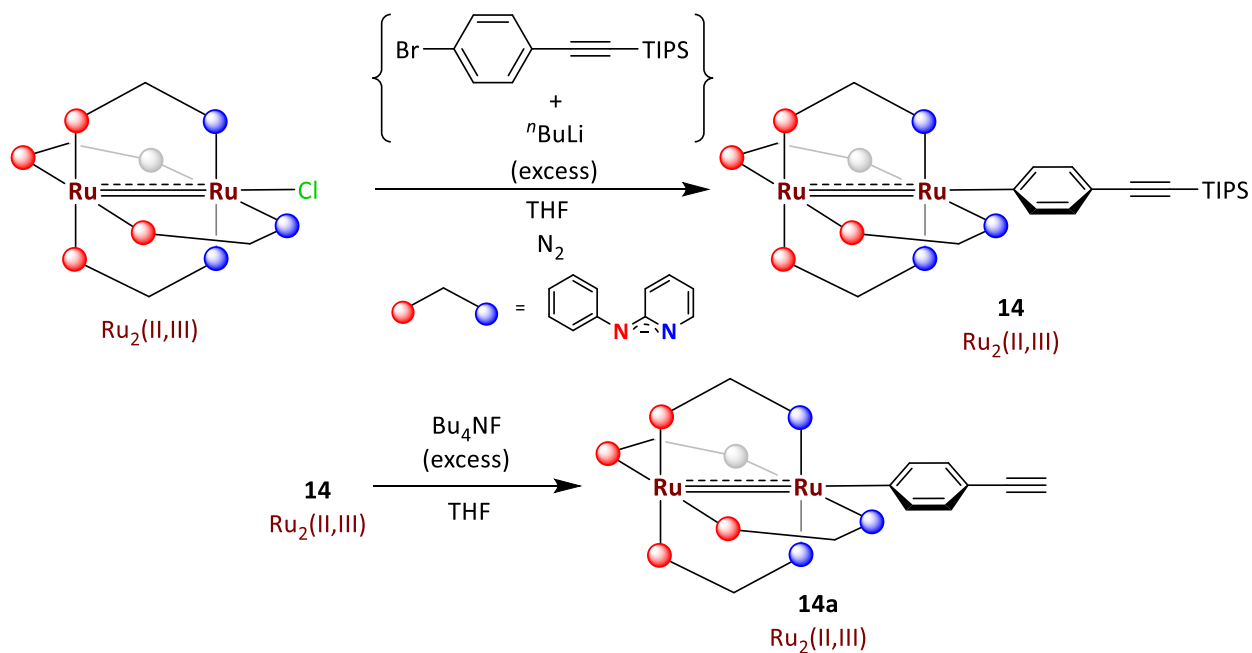
The synthesis of the target compound $[\text{Ru}_2(\text{ap})_4]\text{-}\{\text{C}_6\text{H}_4\text{-C}\equiv\text{C-C}\equiv\text{C-C}_6\text{H}_4\}\text{-}[\text{Ru}_2(\text{ap})_4]$ (**15**) was attempted based on the retrosynthetic route shown in Scheme 4.2. To begin with, 1-bromo-4-iodobenzene was chosen keeping in mind that only one position needed to be subjected to Sonogashira coupling (iodide is a much better leaving group than bromide), while the other needed to be left untouched. Second, TIPS (triisopropylsilyl) was chosen as the protecting agent, since other groups like TMS react with $n\text{BuLi}$ to produce $n\text{Bu-TMS}$ during the lithium-halogen exchange step. After desilylation of the TIPS group to make the terminal acetylide compound, the next step was to stitch two monomeric units together via a cross-coupling reaction. A variety of copper-catalyzed cross-coupling reactions were considered to effect this transformation.¹²² However, many popular strategies like Glaser oxidative coupling under Hay conditions, or Ullmann coupling involve metal halides at one point or other in the mechanism. It was found that these halides react with compound **14a** to produce $\text{Ru}_2(\text{ap})_4\text{X}$ ($\text{X} = \text{halide}$) under the reaction conditions. The Eglinton reaction, which only uses $\text{Cu}(\text{OAc})_2$ and pyridine, was found to be a much more viable alternative.¹²³

The syntheses of **14** was accomplished in a manner similar to the syntheses of the monoaryls mentioned in Chapter 1. The TIPS-protected product was obtained in good yield (77%) after purification by filtration of the reaction mixture on a silica plug, and subsequent

recrystallization from THF/MeOH. The deprotection of the TIPS group was accomplished by addition of an excess of Bu₄NF and subsequent purification, and the end product (**14a**) was isolated in after recrystallization in good yields (80–90%).



Scheme 4.2. Retrosynthesis for **15**



Scheme 4.3. Syntheses of **14** and **14a**.

The X-ray structure of **14** (Figure 4.8) presents all the characteristic features of the Ru₂(II,III) monoaryls (compounds **1–6**). A full list of bond metrics is given in the supporting information (Section 4.4).

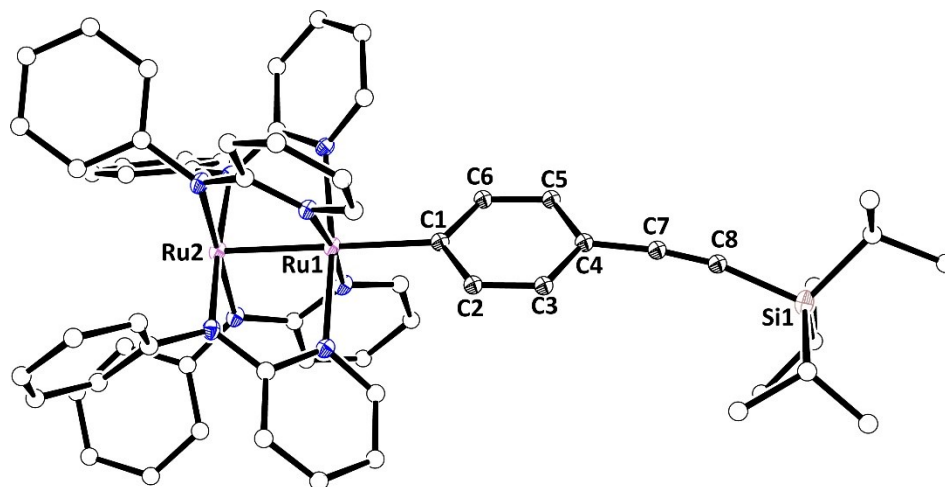
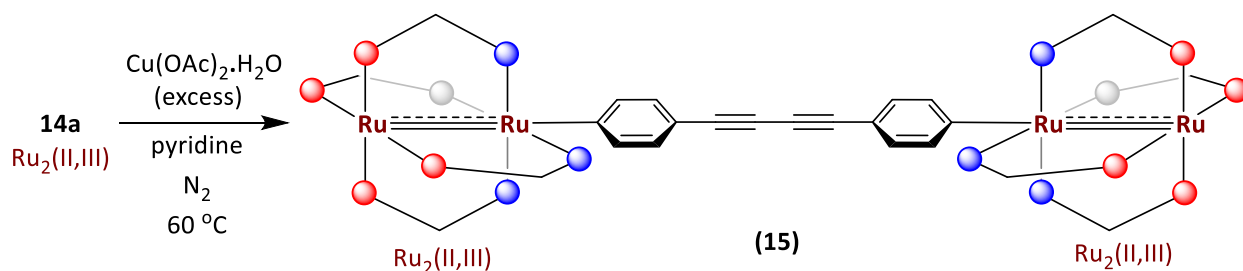


Figure 4.8. Molecular structure of **14** represented at the 30% probability level (one of the two disordered TIPS moieties shown). Hydrogens and solvents have been removed for clarity.

The dimer compound **15** was prepared from **14a** according to Scheme 4.4. The reaction was monitored over the course of 36 h, during which the starting material (**14a**) slowly disappeared. After solvent removal and subsequent filtration of a THF solution of the crude reaction mixture through a celite plug, the product was recrystallized from THF/MeOH in roughly 50% yield as a brown solid (Yields vary depending on the length of the reaction and the temperature. Lower yields were obtained at higher temperatures, longer reactions times, or a combination of both). High resolution mass spectrometry (HR-MS) was required to characterize compound **15**, which, due to the presence of four Ru atoms has a markedly different isotopic distribution from compound **14a**, which only has two Ru atoms. Using collision-induced dissociation (CID), the molecular ion peaks at $m/z = 1958 \pm 15$ were fragmented, and this confirmed the identity of **15** (Figure 4.9).



Scheme 4.4. Synthesis of **15** through a modified Eglinton reaction.

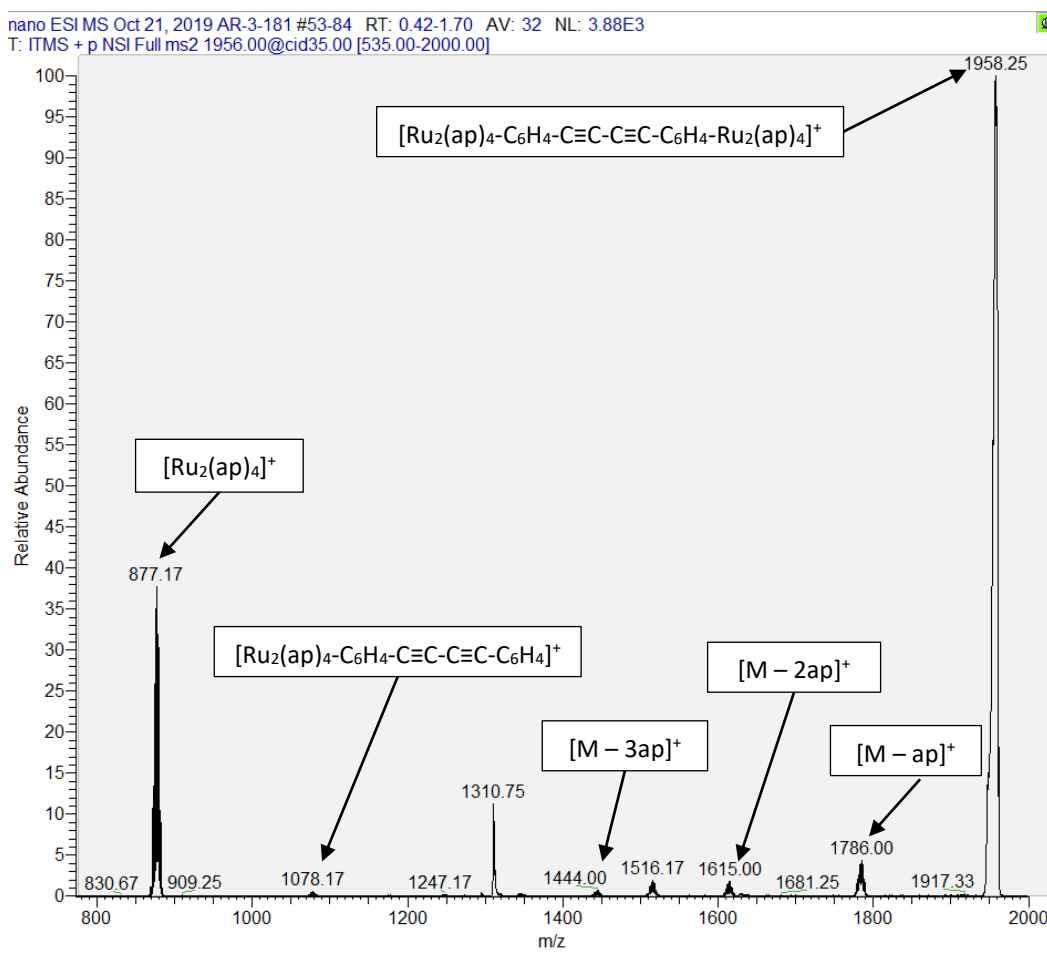


Figure 4.9. HR-MS spectrum of **15** in an acetone solution; CID performed for peaks at $m/z = 1958 \pm 15$.

Having isolated both the monomer and dimer, voltammetric studies were performed to probe for signs of electronic communication between the diruthenium termini. If the mixed arylene polyndiyl bridge does indeed mediate electron transfer, a distinct separation between the redox

couples of the corresponding monomer would be seen in either the cyclic or the differential pulse voltammogram. Unfortunately, from Figure 4.10 it is clear that the redox couples of **14a** and **15** overlap. The potentials of the one-electron events in **14a** and what are expected to be two-electron events in **15** are listed in Table 4.5. The lack of interaction between the Ru₂ termini can also be seen from the similarity of the electronic absorption spectra of **14a** and **15** (Figure 4.S9).

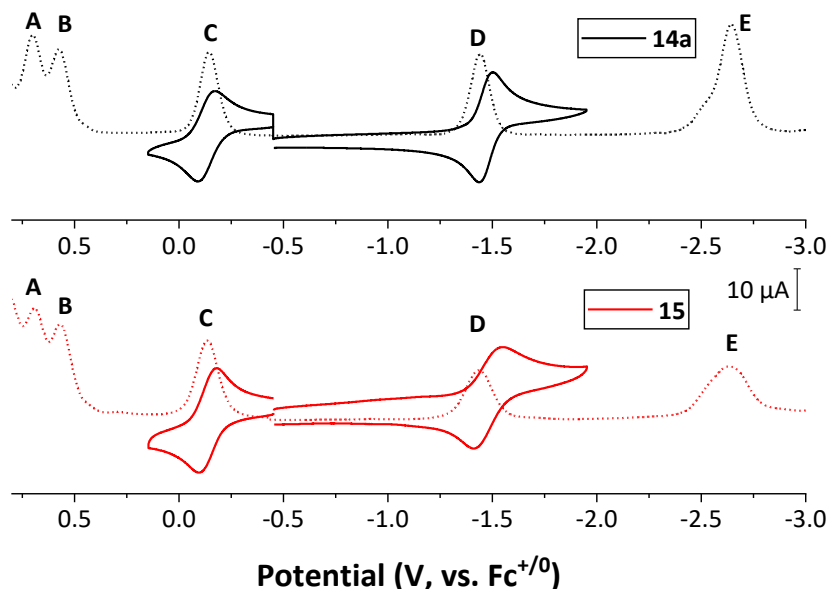


Figure 4.10. CV and DPV of compounds **14a** and **15** recorded in 0.2 M TBAP THF solution. [**14a**] = 1 mM, [**15**] < 1mM due to solubility issues.

Table 4.5. Redox potentials of compounds **14a** and **15** (from DPV)*

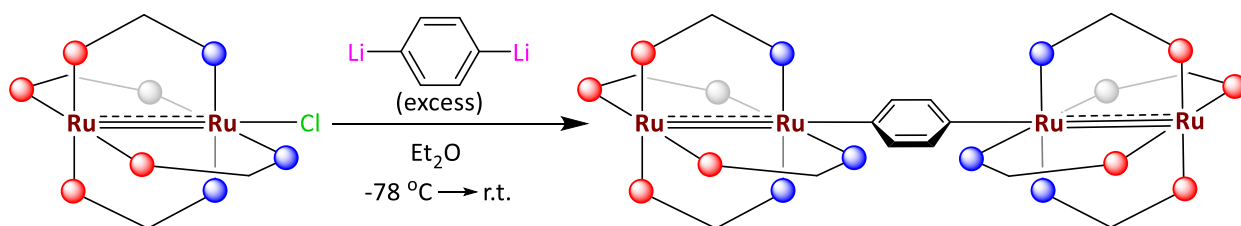
Compound	A	B	C (Ru ₂ ^{6+/5+})	D (Ru ₂ ^{5+/4+})	E
14a	0.70	0.57	-0.14	-1.44	-2.64
15	0.69	0.57	-0.14	-1.44	-2.64

*Note that since **15** did not fully dissolve in THF, the concentration in solution is less than 1 mM. But this should not affect peak splitting/resolution.

It is reasonable to assume that the reason for the lack of electronic communication is the incorrect (non-coplanar) arrangement of the phenylene groups relative to each other, but in the absence of an X-ray structure, this is merely speculative. At this juncture, in the interest of more closely tethering the two Ru₂(II,III) termini, a bridging unit was sought that would obviate the need for the right orientation of two or more phenylene rings.

Ru₂(II,III) bridged by a phenylene unit (-C₆H₄-)

Para-phenylene (1,4-disubstituted C₆H₄ unit) as a linker is commonly used to mediate electron transfer in conjugated organic systems, preferred due to its rigidity and planarity. Commonly used in conjugated organic wire-like molecules, *para*-phenylene connects two substituents with π -conjugation and plays an important role in the electronics of the molecule. In the context of our exploration of aryls as axial ligands, para-phenylene is the simplest aryl that can bridge two diruthenium cores. The target molecule is [Ru₂(*ap*)₄]-{C₆H₄}-[Ru₂(*ap*)₄] (**16**). A few synthetic strategies were attempted in vain, until recently, a simple method was found to work (Scheme 4.5).



Scheme 4.5. Synthesis of **16** from Ru₂(*ap*)₄Cl and 1,4-dilithiobenzene.

1,4-dilithiobenzene reacts with THF, so its synthesis was accomplished by reacting excess ⁿBuLi (*ca.* 3 equivalents) with 1,4-diiodobenzene in ether. The solution took on a distinctive cloudy white appearance, indicating the formation of the target dilithiobenzene, which is likely less soluble in ether than the monolithium congener. Reaction with Ru₂(*ap*)₄Cl was performed stepwise, with sequential addition of increasing equivalents of dilithiobenzene. The reaction was surprisingly slightly slower than expected: after 5 min at low temperature, an aliquot of the reaction retrieved for TLC analysis showed no consumption of the Ru₂ starting material. Upon warming to room temperature, and allowing the reaction to proceed for 30 minutes, it was found that a new product was indeed formed, but in a 1:1 ratio with Ru₂(*ap*)₄Cl. At this juncture, multiple equivalents of dilithiobenzene were added (4–5 equivalents), which led to complete consumption of the starting material. Preliminary ESI-MS of the crude reaction mixture strongly suggests that the new product is indeed compound **16** (Figure 4.11). A small amount of side product was noted on the TLC plate and confirmed by ESI-MS to be Ru₂(*ap*)₄Ph (**4**), which is reasonable.

Fragmentation of both product ions under higher voltages resulted in the same fragment species, namely $[\text{Ru}_2(\text{ap})_4]^+$ and $[\text{Ru}_2(\text{ap})_4(\text{MeCN})]^+$ (Figure 4.S10).

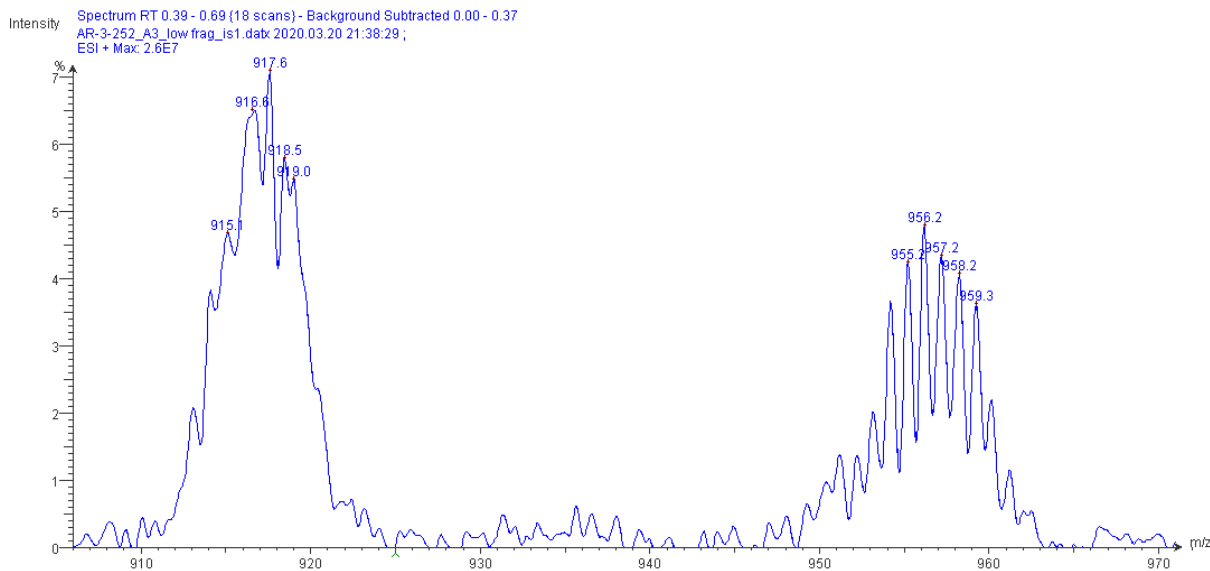


Figure 4.11. ESI-MS of the crude reaction mixture of Scheme 4.5 at low fragmentation voltages. Isotopic distribution characteristic of $(\text{Ru}_2)_2$ corresponding to $[\mathbf{16}]^{2+}$ ($m/z = 1834.0/2 = 917$, left). Side-product $\text{Ru}_2(\text{ap})_4(\text{Ph})$ (compound **4**, right).

More recent attempts at this synthesis have yielded an optimized synthetic procedure, which involves adding a slight excess of dilithiobenzene to $\text{Ru}_2(\text{ap})_4\text{Cl}$. The reaction is rapid, and complete within a few minutes. The product can be purified by recrystallization and repeated washing with THF/hexanes (1/1, v/v) to remove $\text{Ru}_2(\text{ap})_4\text{Ph}$ (compound **4**), which is formed as an impurity in the product mixture. Further washing with cold methanol and hexanes affords compound **16** as a dark brown solid in high yield (ca 70%). While preliminary characterization by electronic absorption spectroscopy and voltammetry (Figures 4.S11–4.S13) has provided some promising insights into the electronic structure and the nature of electronic coupling between the diruthenium termini, further characterization and analyses of compound **16** are pending.

4.3 Conclusions and Future Directions

The sections outlined above each have interesting consequences for diruthenium aryl chemistry. Spectroelectrochemistry and DFT calculations have shed more light on the electronic structure of these complex molecules. More importantly, DFT could become a reliable predictor

of properties (bond metrics, UV-Vis/NIR spectra) in these systems for future analysis. For instance, while XRD analysis of compounds $[1]^+$ and $[2]^+$ are pending, one can make the (not entirely unreasonable) prediction that the Ru–Ru bond length in these complexes will be longer, accompanied by a shortening of the Ru–C bond and deviation of Ru–Ru–C bond length from linearity. Further, it has also been shown that it is synthetically possible to access a phenylene bridged complex of the form $[Ru_2]-C_6H_4-[Ru_2]$. While polyalkynediyl bridges have been explored in these systems previously, aryene bridges directly connecting bimetallic termini are unknown.

4.4 Supporting Information

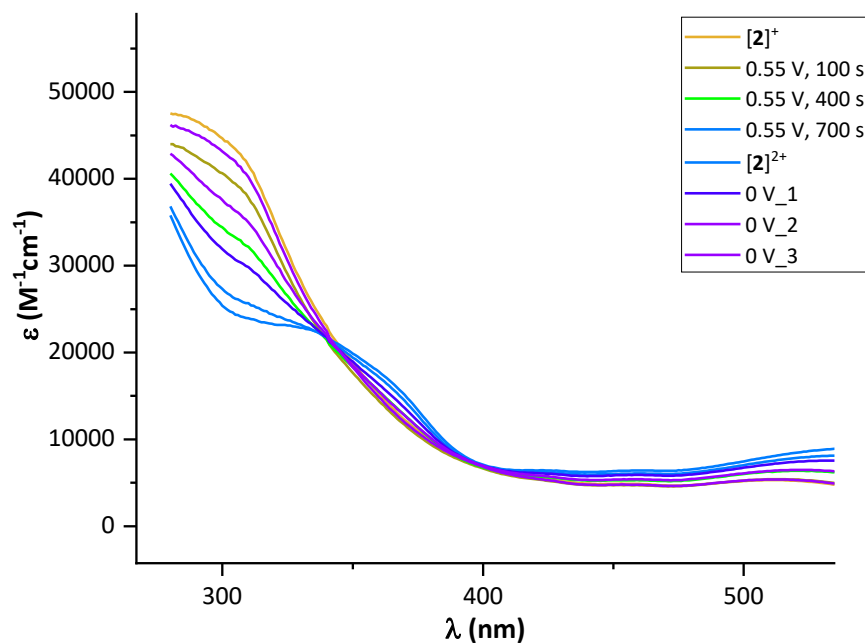


Figure 4.S1. Electrochemical oxidation of [2]⁺ to [2]²⁺, showing the existence of isosbestic points.

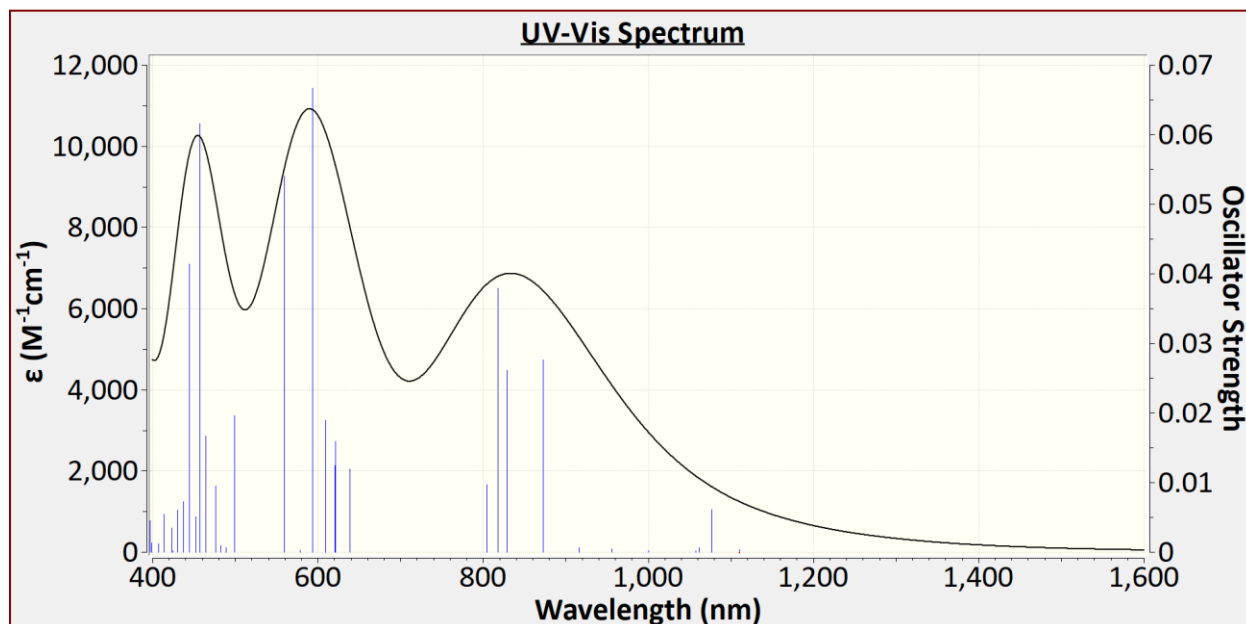


Figure 4.S2. TD-DFT/TDA calculated UV-Vis/NIR spectrum of 1'.

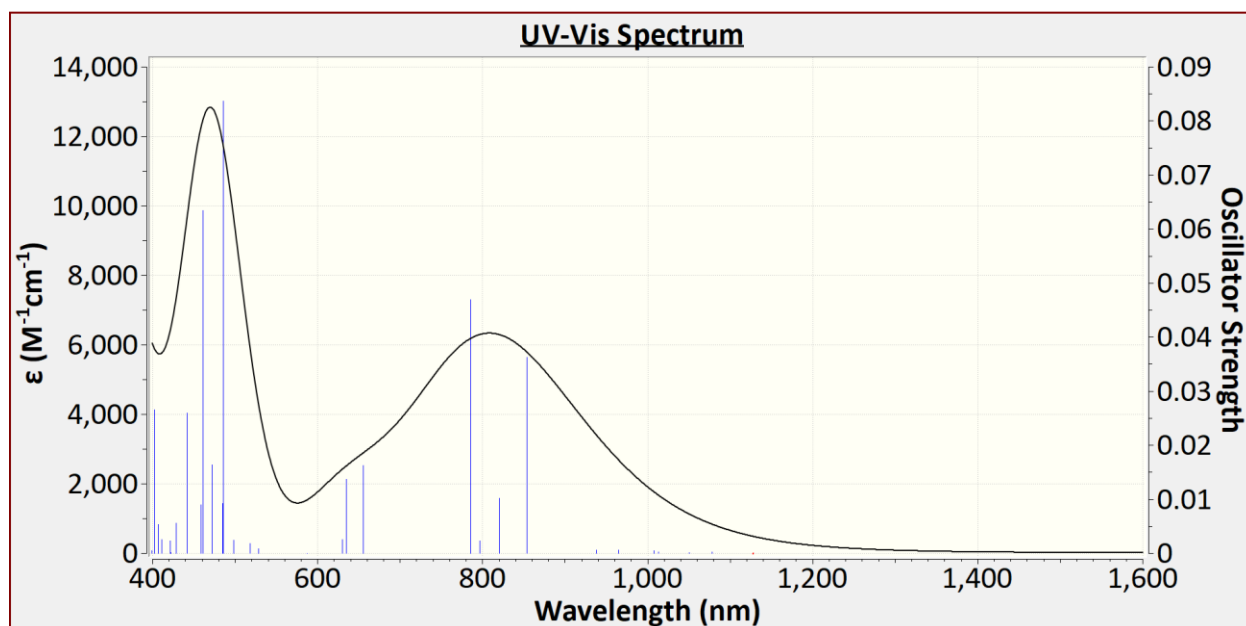


Figure 4.S3. TD-DFT/TDA calculated UV-Vis/NIR spectrum of 4'.

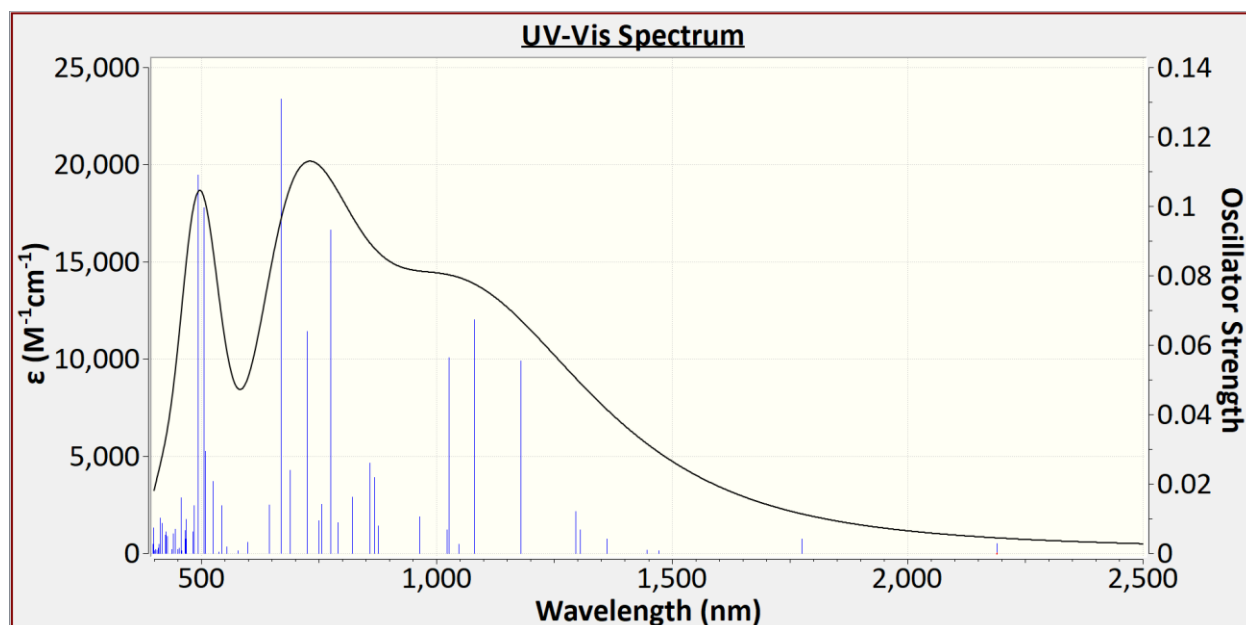


Figure 4.S4. TD-DFT/TDA calculated UV-Vis/NIR spectrum of [1']⁺.

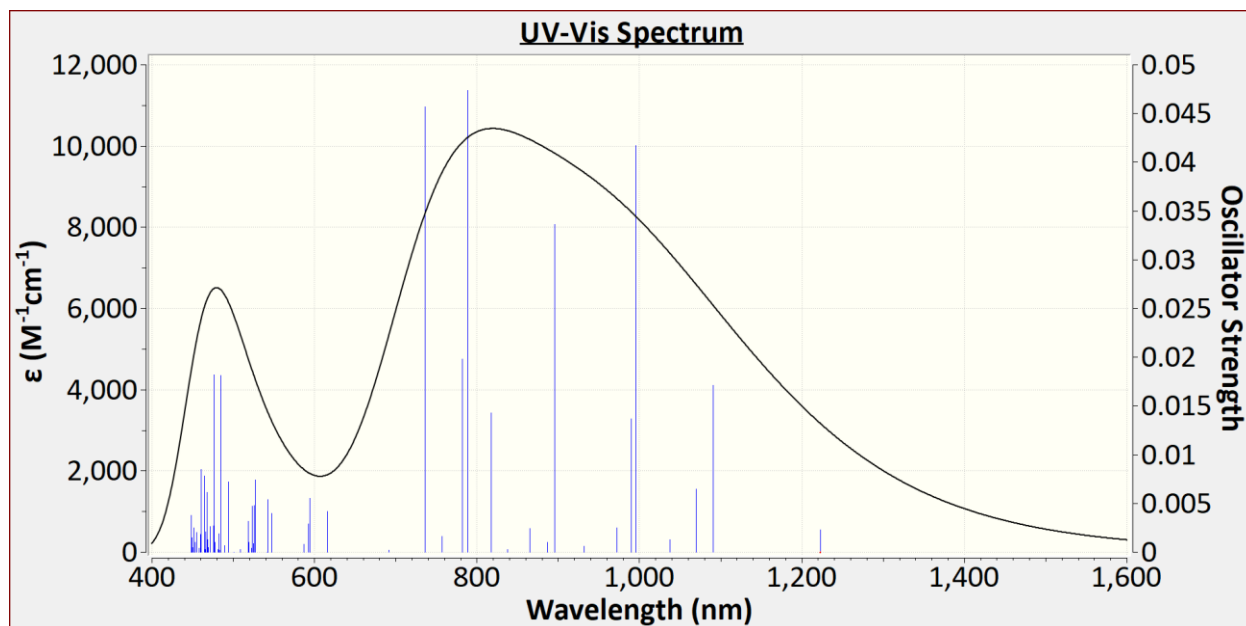


Figure 4.S5. TD-DFT (BP86) calculated UV-Vis/NIR spectrum of **1'**.

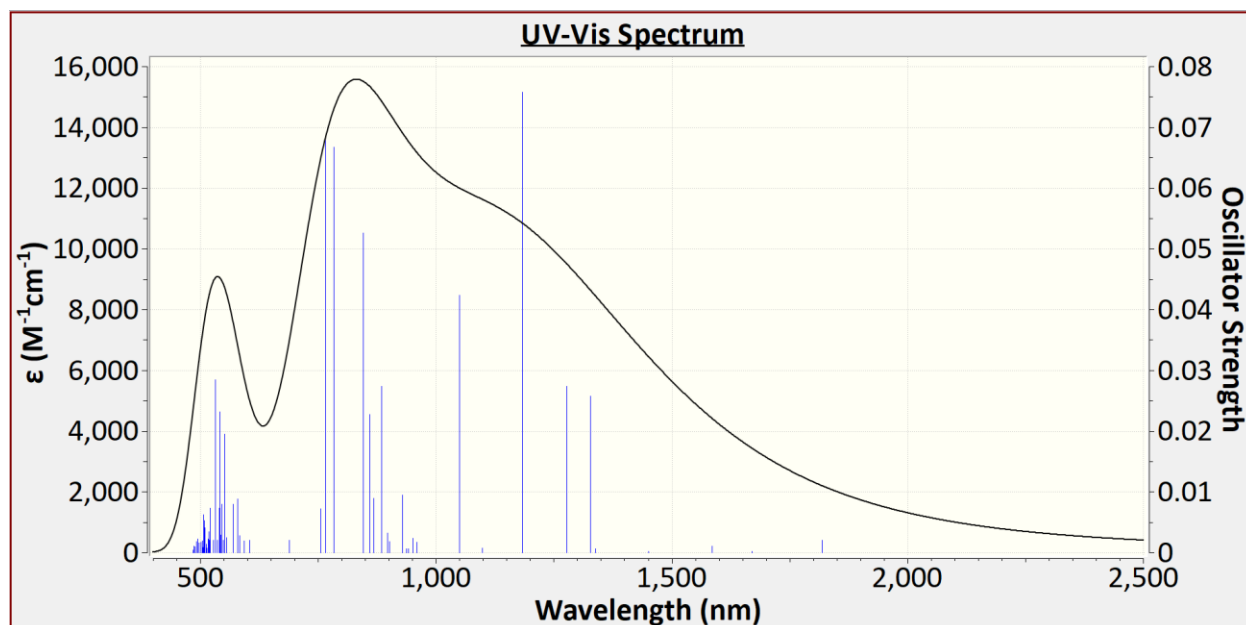


Figure 4.S6. TD-DFT (BP86) calculated UV-Vis/NIR spectrum of **[1']⁺**.

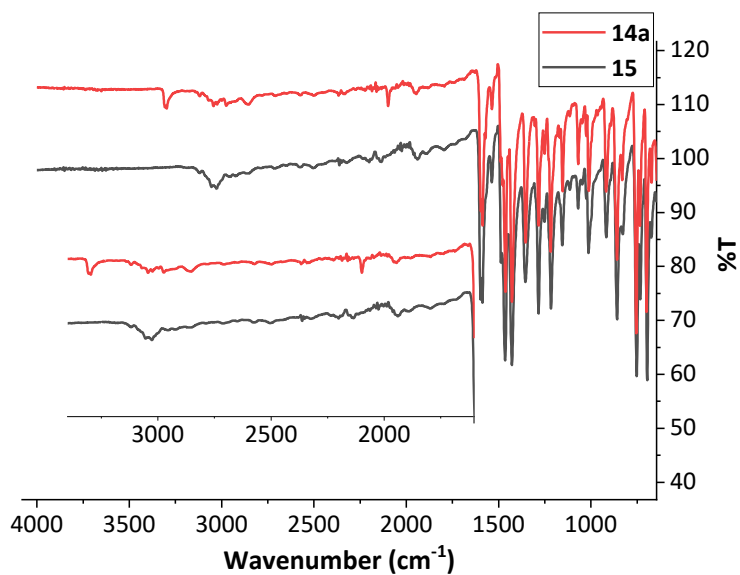


Figure 4.S7. IR spectra of compounds **14a** and **15**.

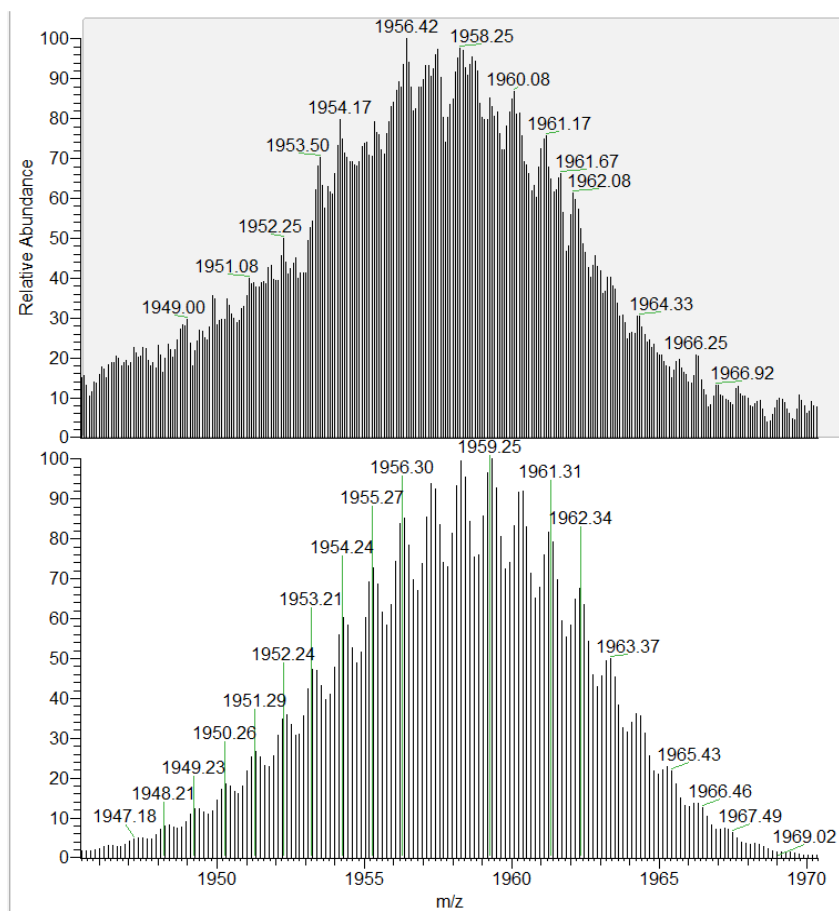


Figure 4.S8. Experimental (top) and simulated (bottom) Nano ESI-MS spectrum of **15** (only molecular ion peak shown).

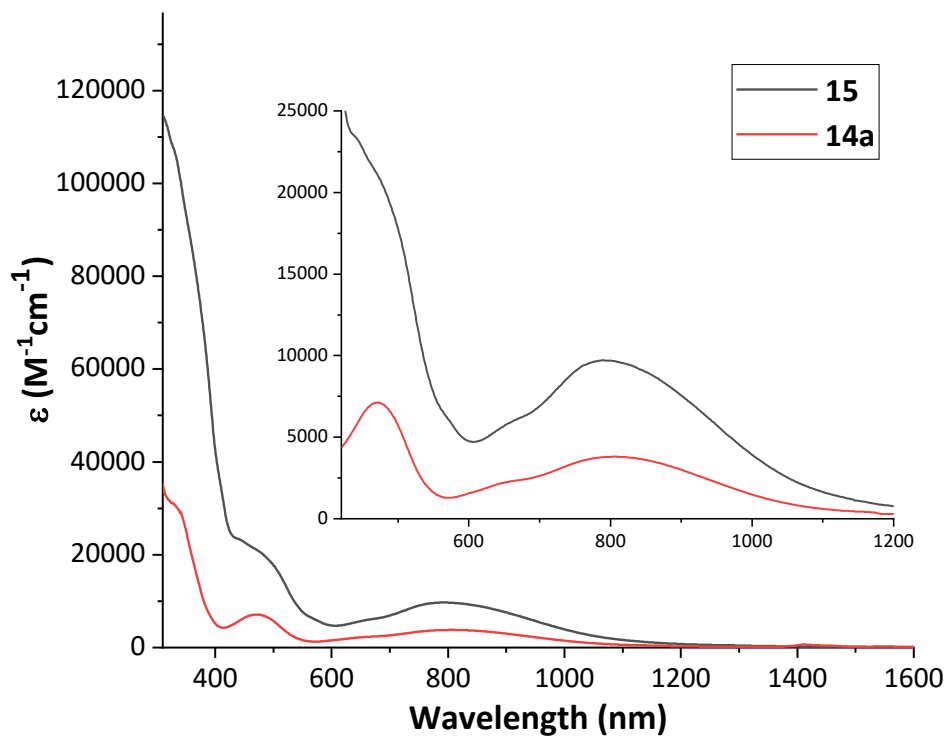


Figure 4.S9. UV-Vis/NIR spectrum of **14a** and **15** in THF.

Table 4.S1. Selected bond lengths (Å) and angles (deg) for compound **14**

Metric	Å/deg
Ru1–Ru2	2.3297(5)
Ru1–C1	2.173(3)
C7–C8	1.204(5)
Ru2–Ru1–C1	179.30(8)
Ru1–N _{py}	2.105[1]
Ru2–N _{an}	2.048[1]

Table 4.S2. Crystallographic details for Ru₂(ap)₄(C₆H₄-4-C≡C-TIPS) (**14**)

	AR_3_143_0m
Crystal data	
Chemical formula	C ₇₀ H ₇₀ N ₈ Ru ₂ Si
<i>M_r</i>	1253.57
Crystal system, space group	Monoclinic, <i>P2₁/c</i>
Temperature (K)	150
<i>a</i> , <i>b</i> , <i>c</i> (Å)	18.2446 (8), 15.4836 (7), 21.4979 (10)
β (°)	93.7359 (17)
<i>V</i> (Å ³)	6060.1 (5)
<i>Z</i>	4
Radiation type	Mo <i>K</i> α
μ (mm ⁻¹)	0.57
Crystal size (mm)	0.50 × 0.30 × 0.15
Data collection	
Diffractometer	Bruker AXS D8 Quest CMOS diffractometer
Absorption correction	Multi-scan <i>SADABS</i> 2016/2: Krause, L., Herbst-Irmer, R., Sheldrick G.M. & Stalke D., <i>J. Appl. Cryst.</i> 48 (2015) 3-10
<i>T_{min}</i> , <i>T_{max}</i>	0.648, 0.746
No. of measured, independent and observed [<i>I</i> > 2σ(<i>I</i>)] reflections	116515, 18563, 12951
<i>R_{int}</i>	0.061
(sin θ/λ) _{max} (Å ⁻¹)	0.716
Refinement	
<i>R</i> [<i>F</i> ² > 2σ(<i>F</i> ²)], <i>wR</i> (<i>F</i> ²), <i>S</i>	0.050, 0.135, 1.11
No. of reflections	18563
No. of parameters	906
No. of restraints	468
H-atom treatment	H-atom parameters constrained
Δ _{max} , Δ _{min} (e Å ⁻³)	2.43, -1.21

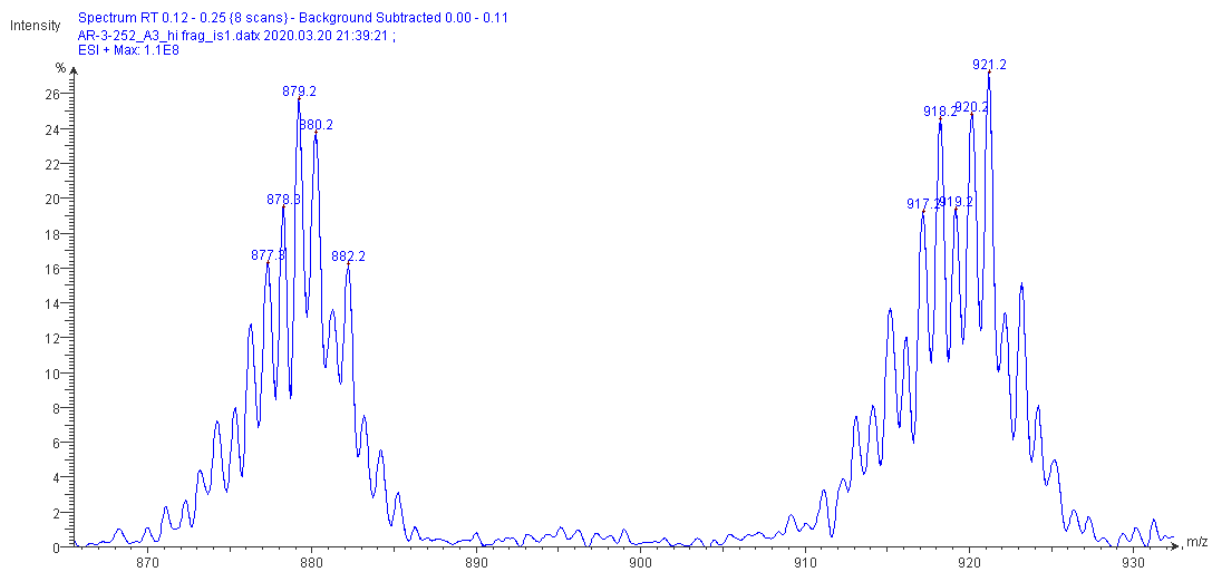


Figure 4.S10. ESI-MS of the crude reaction mixture of Scheme 4.5 at high fragmentation voltage, showing $[\text{Ru}_2(\text{ap})_4]^+$ (left) and $[\text{Ru}_2(\text{ap})_4(\text{MeCN})]^+$ (right). MeCN is the carrier solvent for the mass spectrometer.

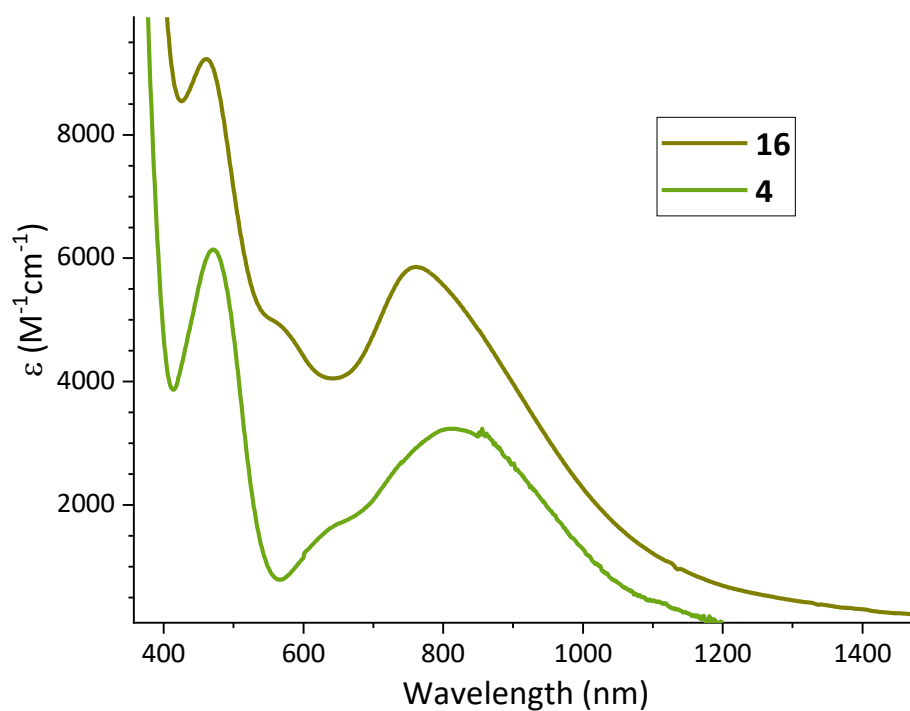


Figure 4.S11. UV-Vis/NIR spectrum of compounds **4** and **16** in THF.

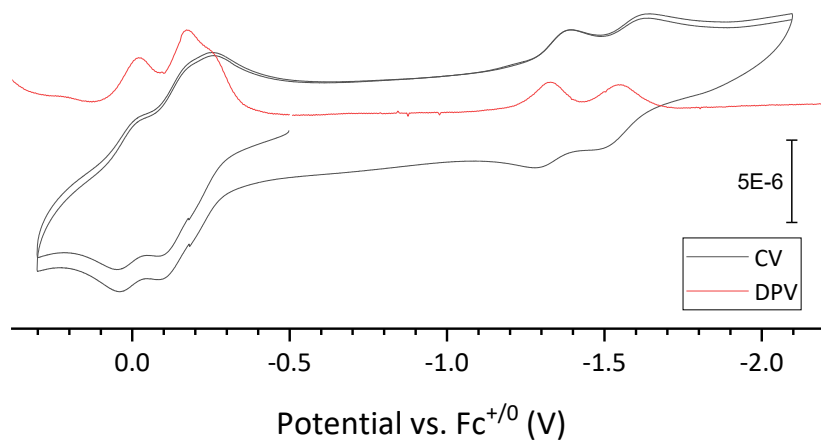
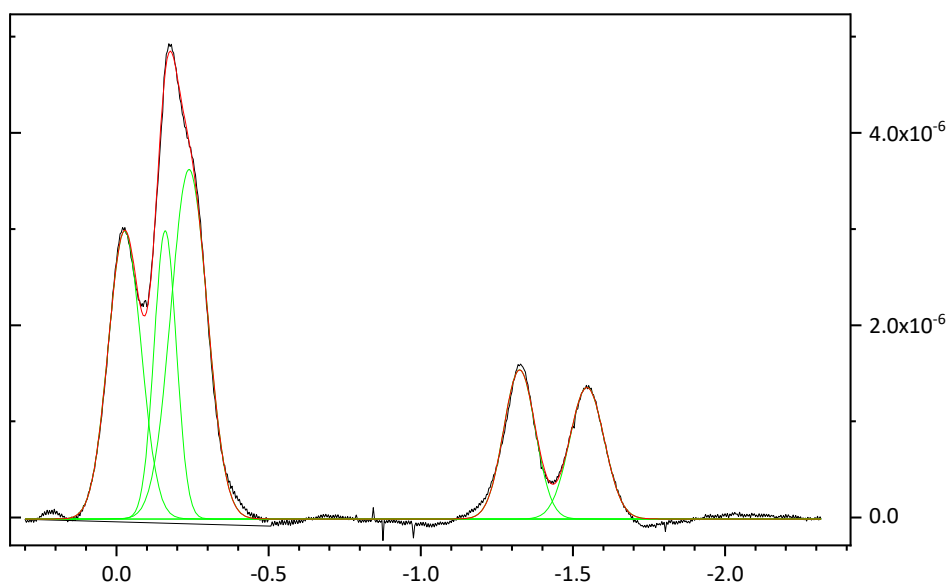


Figure 4.S12. Cyclic (black) and differential pulse (gray) voltammograms of compound **16** (0.5 mM) recorded in 0.15 M $n\text{Bu}_4\text{NPF}_6$ in THF at a scan rate of 0.10 V/s.



Fitting Results

Peak Index	Peak Type	Area Intg	FWHM	Max Height	Center Grvty	Area IntgP
1	Gaussian	1.94281E-7	0.13347	1.36746E-6	-1.54629	12.06724
2	Gaussian	2.0129E-7	0.12209	1.54883E-6	-1.3248	12.50262
3	Gaussian	5.40261E-7	0.13977	3.63127E-6	-0.23876	33.55685
4	Gaussian	2.72666E-7	0.0855	2.99597E-6	-0.16026	16.9359
5	Gaussian	4.01489E-7	0.12597	2.99404E-6	-0.02687	24.93739

Figure 4.S13. Gaussian deconvolution of the differential pulse voltammogram of compound **16** in THF.

Improved computational methods: Geometry optimizations of structures **1**, **2** and **4** were performed using both the unrestricted and restricted open-shell formalism using the B3LYP^{35–38,114} functional. The basis set 6-31G(d,p) was used for C, H, N and O atoms while the basis set def2-tzvp (with ECP, effective core potential) was used for Ru atoms.⁸⁰ Dispersion corrections were applied using Grimme's empirical dispersion (GD3) and the Becke-Johnson (BJ) damping parameters.⁸¹ The calculations were performed in a conductor-polarizable continuum solvent model (CPCM).¹¹⁵ In order to ensure stationary points, force constants were calculated at the first point of the optimization method and subsequent frequency analyses were performed to ensure that there were indeed 3N–6 positive, real (positive) normal vibrational modes.

All TD-DFT calculations were performed at either the same level of theory as ground state DFT. Calculations were performed by either with the Tamm-Dancoff approximation (TD-DFT/TDA) or without it.¹²¹ A total of 60 excited states were calculated. The UV-Vis spectra generated from TDDFT analysis were done so with a half-width and half-maximum (HWHM) of 1600 cm⁻¹.

REFERENCES

- 1 T. A. Stephenson and G. Wilkinson, *J. Inorg. Nucl. Chem.*, 1966, **28**, 2285–2291.
- 2 P. Angaridis, in *Multiple Bonds Between Metal Atoms*, Springer-Verlag, New York, pp. 377–430.
- 3 A. R. Chakravarty, D. A. Tocher and F. A. Cotton, *Inorg. Chem.*, 1985, **24**, 172–177.
- 4 A. R. Chakravarty and F. A. Cotton, *Inorganica Chim. Acta*, 1986, **113**, 19–26.
- 5 G.-L. Xu, G. Zou, Y.-H. Ni, M. C. DeRosa, R. J. Crutchley and T. Ren, *J. Am. Chem. Soc.*, 2003, **125**, 10057–10065.
- 6 B. Xi, I. P. C. Liu, G. L. Xu, M. M. R. Choudhuri, M. C. Derosa, R. J. Crutchley and T. Ren, *J. Am. Chem. Soc.*, 2011, **133**, 15094–15104.
- 7 T. Ren, *Organometallics*, 2005, **24**, 4854–4870.
- 8 Z. Cao, B. Xi, D. S. Jodoin, L. Zhang, S. P. Cummings, Y. Gao, S. F. Tyler, P. E. Fanwick, R. J. Crutchley and T. Ren, *J. Am. Chem. Soc.*, 2014, **136**, 12174–12183.
- 9 A. S. Blum, T. Ren, D. A. Parish, S. A. Trammell, M. H. Moore, J. G. Kushmerick, G. L. Xu, J. R. Deschamps, S. K. Pollack and R. Shashidhar, *J. Am. Chem. Soc.*, 2005, **127**, 10010–10011.
- 10 S. Pookpanratana, H. Zhu, E. G. Bittle, S. N. Natoli, T. Ren, C. A. Richter, Q. Li and C. A. Hacker, *J. Phys. Condens. Matter*, 2016, **28**, 094009.
- 11 H. Zhu, S. J. Pookpanratana, J. E. Bonevich, S. N. Natoli, C. A. Hacker, T. Ren, J. S. Suehle, C. A. Richter and Q. Li, *ACS Appl. Mater. Interfaces*, 2015, **7**, 27306–27313.
- 12 J. L. Bear, W. Z. Chen, B. Han, S. Huang, L. L. Wang, A. Thuriere, E. Van Caemelbecke,

- K. M. Kadish and T. Ren, *Inorg. Chem.*, 2003, **42**, 6230–6240.
- 13 M. Manowong, B. Han, T. R. McAloon, J. Shao, I. A. Guzei, S. Ngubane, E. Van Caemelbecke, J. L. Bear and K. M. Kadish, *Inorg. Chem.*, 2014, **53**, 7416–7428.
- 14 J. M. Nichols, J. Wolf, P. Zavalij, B. Varughese and M. P. Doyle, *J. Am. Chem. Soc.*, 2007, **129**, 3504–3505.
- 15 J. H. Xie, J. M. Nichols, C. Lubek and M. P. Doyle, *Chem. Commun.*, 2008, 2671–2673.
- 16 M. P. Doyle, D. Shabashov, L. Zhou, P. Y. Zavalij, C. Welch and Z. Pirzada, *Organometallics*, 2011, **30**, 3619–3627.
- 17 D. Angelone, A. Draksharapu, W. R. Browne, M. M. R. Choudhuri, R. J. Crutchley, X. Xu, X. Xu and M. P. Doyle, *Inorganica Chim. Acta*, 2015, **424**, 235–240.
- 18 J. Wolf, R. Poli, J. H. Xie, J. Nichols, B. Xi, P. Zavalij and M. P. Doyle, *Organometallics*, 2008, **27**, 5836–5845.
- 19 J.-H. Xie, L. Zhou, C. Lubek and M. P. Doyle, *Dalt. Trans.*, 2009, 2871.
- 20 J. L. Bear, B. Han, Y. Li, S. Ngubane, E. Van Caemelbecke and K. M. Kadish, *Polyhedron*, 2009, **28**, 1551–1555.
- 21 A. R. Chakravarty, F. A. Cotton and D. A. Tocher, *J. Am. Chem. Soc.*, 1984, **106**, 6409–6413.
- 22 A. R. Chakravarty and F. A. Cotton, *Inorg. Chem.*, 1985, **24**, 3584–3589.
- 23 B. Cordero, V. Gómez, A. E. Platero-Prats, M. Revés, J. Echeverría, E. Cremades, F. Barragán and S. Alvarez, *Dalt. Trans.*, 2008, 2832.
- 24 G. Zou, J. C. Alvarez and T. Ren, *J. Organomet. Chem.*, 2000, **596**, 152–158.

- 25 A. R. Corcos, M. D. Roy, M. M. Killian, S. Dillon, T. C. Brunold and J. F. Berry, *Inorg. Chem.*, 2017, **56**, 14662–14670.
- 26 C. Hansch, A. Leo and R. W. Taft, *Chem. Rev.*, 1991, **91**, 165–195.
- 27 S. Dapperheld, E. Steckhan, K. G. Brinkhaus and T. Esch, *Chem. Ber.*, 1991, **124**, 2557–2567.
- 28 T. Ren, *Coord. Chem. Rev.*, 1998, **175**, 43–58.
- 29 A. R. Chakravarty, F. A. Cotton, D. A. Tocher and J. H. Tocher, *Polyhedron*, 1985, **4**, 1475–1478.
- 30 D. F. Evans, *J. Chem. Soc.*, 1959, 2003–2005.
- 31 W. Z. Chen, F. A. Cotton, N. S. Dalal, C. A. Murillo, C. M. Ramsey, T. Ren and X. Wang, *J. Am. Chem. Soc.*, 2005, **127**, 12691–12696.
- 32 P. Angaridis, F. A. Cotton, C. A. Murillo, D. Villagrán and X. Wang, *Inorg. Chem.*, 2004, **43**, 8290–8300.
- 33 F. Albert Cotton and T. Ren, *Inorg. Chem.*, 1995, **34**, 3190–3193.
- 34 E. I. Solomon and A. B. P. Lever, *Inorganic Electronic Structure and Spectroscopy: Applications and Case Studies*, 2006.
- 35 P. J. Stephens, F. J. Devlin, C. F. Chabalowski and M. J. Frisch, *J. Phys. Chem.*, 1994, **98**, 11623–11627.
- 36 C. Lee, W. Yang and R. G. Parr, *Phys. Rev. B*, 1988, **37**, 785–789.
- 37 S. H. Vosko, L. Wilk and M. Nusair, *Can. J. Phys.*, 1980, **58**, 1200–1211.

- 38 A. D. Becke, *J. Chem. Phys.*, 1993, **98**, 5648–5652.
- 39 S. P. Cummings, Z. Cao, P. E. Fanwick, A. Kharlamova and T. Ren, *Inorg. Chem.*, 2012, **51**, 7561–7568.
- 40 D. Xiang, X. Wang, C. Jia, T. Lee and X. Guo, *Chem. Rev.*, 2016, **116**, 4318–4440.
- 41 A. K. C. Mengel, B. He and O. S. Wenger, *J. Org. Chem.*, 2012, **77**, 6545–6552.
- 42 *Apex3 v2016.9-0, Saint V8.34A, Saint V8.37A*, Bruker AXS Inc., Madison, WI, 2016.
- 43 *SHELXTL, version 6.14*, Bruker AXS Inc.: Madison, WI, 2000–2003.
- 44 G. M. Sheldrick, *Acta Crystallogr. Sect. A Found. Crystallogr.*, 2008, **64**, 112–122.
- 45 G. M. Sheldrick, *Acta Crystallogr. Sect. C Struct. Chem.*, 2015, **71**, 3–8.
- 46 G. M. Sheldrick, *SHELXL 2016*, University of Göttingen, Göttingen, Germany, 201.
- 47 N. Godbout, D. R. Salahub, J. Andzelm and E. Wimmer, *Can. J. Chem.*, 1992, **70**, 560–571.
- 48 C. Sosa, J. Andzelm, B. C. Elkin, E. Wimmer, K. D. Dobbs and D. A. Dixon, *J. Phys. Chem.*, 1992, **96**, 6630–6636.
- 49 M. M. Francl, W. J. Pietro, W. J. Hehre, J. S. Binkley, M. S. Gordon, D. J. DeFrees and J. A. Pople, *J. Chem. Phys.*, 1982, **77**, 3654–3665.
- 50 R. Ditchfield, W. J. Hehre and J. A. Pople, *J. Chem. Phys.*, 1971, **54**, 720–723.
- 51 W. J. Hehre, K. Ditchfield and J. A. Pople, *J. Chem. Phys.*, 1972, **56**, 2257–2261.

- 52 P. C. Hariharan and J. A. Pople, *Theor. Chim. Acta*, 1973, **28**, 213–222.
- 53 P. C. Hariharan and J. A. Pople, *Mol. Phys.*, 1974, **27**, 209–214.
- 54 M. J. Frisch, G. W. Trucks, H. B. Schlegel, G. E. Scuseria, M. A. Robb, J. R. Cheeseman, G. Scalmani, V. Barone, G. A. Petersson, H. Nakatsuji, X. Li, M. Caricato, A. V. Marenich, J. Bloino, B. G. Janesko, R. Gomperts, B. Mennucci, H. P. Hratchian, J. V. Ortiz, A. F. Izmaylov, J. L. Sonnenberg, D. Williams-Young, F. Ding, F. Lipparini, F. Egidi, J. Goings, B. Peng, A. Petrone, T. Henderson, D. Ranasinghe, V. G. Zakrzewski, J. Gao, N. Rega, G. Zheng, W. Liang, M. Hada, M. Ehara, K. Toyota, R. Fukuda, J. Hasegawa, M. Ishida, T. Nakajima, Y. Honda, O. Kitao, H. Nakai, T. Vreven, K. Throssell, J. J. A. Montgomery, J. E. Peralta, F. Ogliaro, M. J. Bearpark, J. J. Heyd, E. N. Brothers, K. N. Kudin, V. N. Staroverov, T. A. Keith, R. Kobayashi, J. Normand, K. Raghavachari, A. P. Rendell, J. C. Burant, S. S. Iyengar, J. Tomasi, M. Cossi, J. M. Millam, M. Klene, C. Adamo, R. Cammi, J. W. Ochterski, R. L. Martin, K. Morokuma, O. Farkas, J. B. Foresman and D. J. Fox, *Gaussian 16 Rev. A.03*.
- 55 Y. Li, B. Han, K. M. Kadish and J. L. Bear, *Inorg. Chem.*, 1993, **32**, 4175–4176.
- 56 J. L. Bear, B. Han and S. Huang, *J. Am. Chem. Soc.*, 1993, **115**, 1175–1177.
- 57 C. K. Kuo, J. C. Chang, C. Y. Yeh, G. H. Lee, C. C. Wang and S. M. Peng, *Dalt. Trans.*, 2005, 3696–3701.
- 58 J.-L. Zuo, E. Herdtweck, F. Fabrizi de Biani, A. M. Santos and F. E. Kühn, *New J. Chem.*, 2002, **26**, 889–894.
- 59 J.-L. Zuo, E. Herdtweck and F. E. Kühn, *J. Chem. Soc. Dalt. Trans.*, 2002, 1244.
- 60 J. L. Bear, B. Han, S. Huang and K. M. Kadish, *Inorg. Chem.*, 1996, **35**, 3012–3021.
- 61 A. K. Mahapatro, J. Ying, T. Ren and D. B. Janes, *Nano Lett.*, 2008, **8**, 2131–2136.
- 62 A. K. M. Long, G. H. Timmer, J. S. Pap, J. L. Snyder, R. P. Yu and J. F. Berry, *J. Am. Chem. Soc.*, 2011, **133**, 13138–13150.

- 63 J. E. Barker and T. Ren, *Inorg. Chem.*, 2008, **47**, 2264–2266.
- 64 L. Villalobos, Z. Cao, P. E. Fanwick and T. Ren, *Dalt. Trans.*, 2012, **41**, 644–650.
- 65 A. R. Corcos, J. S. Pap, T. Yang and J. F. Berry, *J. Am. Chem. Soc.*, 2016, **138**, 10032–10040.
- 66 M. C. Barral, S. Herrero, R. Jiménez-Aparicio, M. R. Torres and F. A. Urbanos, *Angew. Chemie - Int. Ed.*, 2004, **44**, 305–307.
- 67 M. C. Barral, T. Gallo, S. Herrero, R. Jiménez-Aparicio, M. R. Torres and F. A. Urbanos, *Inorg. Chem.*, 2006, **45**, 3639–3647.
- 68 C.-S. Tsai, I. P.-C. Liu, F.-W. Tien, G.-H. Lee, C.-Y. Yeh, C. Chen and S.-M. Peng, *Inorg. Chem. Commun.*, 2013, **38**, 152–155.
- 69 K.-N. Shih, M.-J. Huang, H.-C. Lu, M.-D. Fu, C.-K. Kuo, G.-C. Huang, G.-H. Lee, C. Chen and S.-M. Peng, *Chem. Commun.*, 2010, **46**, 1338.
- 70 T. Ren, *Organometallics*, 2002, **21**, 732–738.
- 71 G. Xu and T. Ren, *Organometallics*, 2001, **20**, 2400–2404.
- 72 M. H. Chisholm, D. L. Clark, J. C. Huffman, W. G. Van Der Shiys, E. M. Kober, D. L. Lichtenberger and B. E. Bursten, *J. Am. Chem. Soc.*, 1987, **109**, 6796–6816.
- 73 S. K. Hurst, G. L. Xu and T. Ren, *Organometallics*, 2003, **22**, 4118–4123.
- 74 G. Xu, C. Campana and T. Ren, *Inorg. Chem.*, 2002, **41**, 3521–3527.
- 75 C. Lin, T. Ren, E. J. Valente and J. D. Zubkowski, *J. Chem. Soc. Dalt. Trans.*, 1998, 571–576.

- 76 H. B. Wedler, P. Wendelboe and P. P. Power, *Organometallics*, 2018, **37**, 2929–2936.
- 77 G.-L. Xu, C. G. Jablonski and T. Ren, *Inorganica Chim. Acta*, 2003, **343**, 387–390.
- 78 I. P. C. Liu and T. Ren, *Inorg. Chem.*, 2009, **48**, 5608–5610.
- 79 D. Andrae, U. Häußermann, M. Dolg, H. Stoll and H. Preuß, *Theor. Chim. Acta*, 1990, **77**, 123–141.
- 80 F. Weigend and R. Ahlrichs, *Phys. Chem. Chem. Phys.*, 2005, **7**, 3297–3305.
- 81 S. Grimme, J. Antony, S. Ehrlich and H. Krieg, *J. Chem. Phys.*, 2010, **132**, 154104.
- 82 R. L. Martin, *J. Chem. Phys.*, 2003, **118**, 4775–4777.
- 83 W. Z. Chen, G. L. Xu, C. G. Jablonski and T. Ren, *J. Mol. Struct.*, 2008, **890**, 90–94.
- 84 J. P. Perdew, *Phys. Rev. B*, 1986, **33**, 8822–8824.
- 85 Y. Wang and J. P. Perdew, *Phys. Rev. B*, 1991, **43**, 8911–8916.
- 86 Y. Zhao and D. G. Truhlar, *J. Chem. Phys.*, 2006, **125**, 194101.
- 87 S. T. Liddle, *Molecular Metal-Metal Bonds: Compounds, Synthesis, Properties*, Wiley-VCH Verlag GmbH & Co. KGaA, Weinheim, Germany, Germany, 2015.
- 88 J. F. Berry, *J. Chem. Sci.*, 2015, **127**, 209–214.
- 89 J. A. Chipman and J. F. Berry, *Chem. Rev.*, 2020, **120**, 2409–2447.
- 90 Q. Wang, S. Zhang, P. Cui, A. B. Weberg, L. M. Thierer, B. C. Manor, M. R. Gau, P. J.

- Carroll and N. C. Tomson, *Inorg. Chem.*, 2020, **59**, 4200–4214.
- 91 J. A. Hlina, J. R. Pankhurst, N. Kaltsoyannis and P. L. Arnold, *J. Am. Chem. Soc.*, 2016, **138**, 3333–3345.
- 92 C. M. Thomas, *Comments Inorg. Chem.*, 2011, **32**, 14–38.
- 93 P. A. Lindahl, *J. Inorg. Biochem.*, 2012, **106**, 172–178.
- 94 R. H. Holm, P. Kennepohl and E. I. Solomon, *Chem. Rev.*, 1996, **96**, 2239–2314.
- 95 R. B. Siedschlag, V. Bernales, K. D. Vogiatzis, N. Planas, L. J. Clouston, E. Bill, L. Gagliardi and C. C. Lu, *J. Am. Chem. Soc.*, 2015, **137**, 4638–4641.
- 96 R. C. Cammarota, L. J. Clouston and C. C. Lu, *Coord. Chem. Rev.*, 2017, **334**, 100–111.
- 97 C. M. Farley and C. Uyeda, *Trends Chem.*, 2019, **1**, 497–509.
- 98 I. G. Powers and C. Uyeda, *ACS Catal.*, 2017, **7**, 936–958.
- 99 T. J. Steiman and C. Uyeda, *J. Am. Chem. Soc.*, 2015, **137**, 6104–6110.
- 100 B. Wu, M. J. T. Wilding, S. Kuppaswamy, M. W. Bezpalko, B. M. Foxman and C. M. Thomas, *Inorg. Chem.*, 2016, **55**, 12137–12148.
- 101 R. J. Eisenhart, P. A. Rudd, N. Planas, D. W. Boyce, R. K. Carlson, W. B. Tolman, E. Bill, L. Gagliardi and C. C. Lu, *Inorg. Chem.*, 2015, **54**, 7579–7592.
- 102 R. J. Eisenhart, L. J. Clouston and C. C. Lu, *Acc. Chem. Res.*, 2015, **48**, 2885–2894.
- 103 H. Zhang, G. P. Hatzis, C. E. Moore, D. A. Dickie, M. W. Bezpalko, B. M. Foxman and C. M. Thomas, *J. Am. Chem. Soc.*, 2019, **141**, 9516–9520.

- 104 M. P. Doyle, R. Duffy, M. Ratnikov and L. Zhou, *Chem. Rev.*, 2010, **110**, 704–724.
- 105 K. P. Kornecki, J. F. Briones, V. Boyarskikh, F. Fullilove, J. Autschbach, K. E. Schrote, K. M. Lancaster, H. M. L. L. Davies and J. F. Berry, *Science (80-.)*, 2013, **342**, 351–354.
- 106 J. F. Berry, *Dalt. Trans.*, 2012, **41**, 700–713.
- 107 S. J. Tereniak and C. C. Lu, in *Molecular Metal-Metal Bonds: Compounds, Synthesis, Properties*, Wiley-VCH Verlag GmbH & Co. KGaA, Weinheim, Germany, Germany, 2015, pp. 225–278.
- 108 M. C. Barral, S. Herrero, R. Jiménez-Aparicio, M. R. Torres and F. A. Urbanos, *J. Organomet. Chem.*, 2008, **693**, 1597–1604.
- 109 K. M. Kadish, B. Han, J. Shao, Z. Ou and J. L. Bear, *Inorg. Chem.*, 2001, **40**, 6848–6851.
- 110 S. C. Bart, K. Chłopek, E. Bill, M. W. Bouwkamp, E. Lobkovsky, F. Neese, K. Wieghardt and P. J. Chirik, *J. Am. Chem. Soc.*, 2006, **128**, 13901–13912.
- 111 F. A. Cotton, J. L. Eglin, B. Hong and C. A. James, *Inorg. Chem.*, 1993, **32**, 2104–2106.
- 112 B. Le Guennic, T. Floyd, B. R. Galan, J. Autschbach and J. B. Keister, *Inorg. Chem.*, 2009, **48**, 5504–5511.
- 113 W. Z. Chen, V. De Silva, C. Lin, J. Abellard, D. M. Marcus and T. Ren, *J. Clust. Sci.*, 2005, **16**, 151–165.
- 114 A. D. Becke, *Phys. Rev. A*, 1988, **38**, 3098–3100.
- 115 M. Cossi, N. Rega, G. Scalmani and V. Barone, *J. Comput. Chem.*, 2003, **24**, 669–681.
- 116 O. Akintola, M. Böhme, M. Rudolph, A. Buchholz, H. Görls and W. Plass, *ChemistryOpen*, 2019, **8**, 271–284.

- 117 S. Amthor, B. Noller and C. Lambert, *Chem. Phys.*, 2005, **316**, 141–152.
- 118 C. Lambert and G. Nöll, *J. Am. Chem. Soc.*, 1999, **121**, 8434–8442.
- 119 F. A. Cotton and A. Yokochi, *Inorg. Chem.*, 1997, **36**, 567–570.
- 120 M. Ebihara, N. Nagaya, N. Kawashima and T. Kawamura, *Inorganica Chim. Acta*, 2003, **351**, 305–310.
- 121 S. Hirata and M. Head-Gordon, *Chem. Phys. Lett.*, 1999, **314**, 291–299.
- 122 P. Siemsen, R. C. Livingston and F. Diederich, *Angew. Chemie - Int. Ed.*, 2000, **39**, 2632–2657.
- 123 S. Claude, J. M. Lehn and J. P. Vigneron, *Tetrahedron Lett.*, 1989, **30**, 941–944.

VITA

Adharsh Raghavan hails from Chennai, India. He majored in Chemistry and Mathematics and obtained dual M.Sc. (Hons.) degrees from Birla Institute of Technology and Science, Pilani – Hyderabad campus. During his summers, he did internships at IISER-Trivandrum and IISc-Bangalore. For his Masters thesis, he performed research under the guidance of Prof. Vivek Polshettiwar at the Tata Institute of Fundamental Research – Mumbai.

Adharsh began his graduate education at Purdue in the fall of 2015 under the supervision of Prof. Suzanne C. Bart from Dec 2015–Mar 2017. During this time, he performed research on uranium tris(imido) complexes supported by a redox-active ligand. Subsequently, he joined Prof. Tong Ren’s lab in April 2017, where he began working on diruthenium chemistry. Since then, he has become a big fan of the field of metal-metal bonding. Between April 2017 and July 2020, he has published three papers on diruthenium aryl chemistry detailing his graduate work. Apart from this, he has also collaborated as both an experimentalist and amateur computational chemist on publications co-authored with his colleagues.

PUBLICATIONS

- (1) A. G. Porter, H. Hu, X. Liu, A. Raghavan, S. Adhikari, D. R. Hall, B. Liu, Y. Xia, T. Ren, *Dalton Trans.*, 2018, **47**, 11882–11887.
- (2) B. Mash, A. Raghavan, T. Ren, *Eur. J. Inorg. Chem.*, 2019, **2019**, 2065–2070.
- (3) A. Raghavan, B. Mash, T. Ren, *Inorg. Chem.*, 2019, **58**, 2618–2626.
- (4) A. Raghavan, T. Ren, *Organometallics*, 2019, **38**, 3888–3896.
- (5) A. Raghavan, F. Yuan, T. Ren, *Inorg. Chem.*, 2020, **59**, 13, 8663–8666.